

FUNDAMENTAL PHYSICS WITH GRAVITATIONAL WAVES

**TESTING GENERAL RELATIVITY AND STUDYING NEUTRON STARS
WITH CURRENT AND FUTURE DETECTORS**

Anna Puecher

ISBN: 978-90-393-7605-8

DOI: <https://doi.org/10.33540/2119>

Printed by: Gildeprint – www.gildeprint.nl

Copyright: © 2023 Anna Puecher



Utrecht
University



This work originates as part of the research program of the Foundation for Fundamental Research on Matter (FOM), and falls as of April 1, 2017 under the responsibility of the Foundation for Nederlandse Wetenschappelijk Onderzoek Instituten (NWO-I), which is part of the Dutch Research Council (NWO).

Fundamental physics with gravitational waves

Testing general relativity and studying neutron stars
with current and future detectors

Fundamentele fysica met zwaartekrachtsgolven

Het testen van de algemene relativiteitstheorie en het bestuderen van
neutronensterren met huidige en toekomstige detectoren

(met een samenvatting in het Nederlands)

Proefschrift

ter verkrijging van de graad van doctor aan de Universiteit Utrecht op gezag van de rector
magnificus, prof.dr. H.R.B.M. Kummeling, ingevolge het besluit van het college voor promoties in
het openbaar te verdedigen op woensdag 7 februari 2024 des middags te 4.15 uur

door

Anna Puecher
geboren op 28 november 1994
te Trento, Italië

Promotor:

Prof. dr. C.F.F. van den Broeck

Co-promotor:

Dr. S.E. Caudill

Assessment Committee:

Prof. dr. J.F.J. van den Brand

Dr. N.E. Chisari

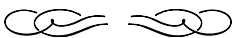
Prof. dr. S. Hild

Prof. dr. R.J.M. Snellings

Prof. dr. N. Stergioulas

*Lock up your libraries if you like;
but there is no gate, no lock, no bolt that
you can set upon the freedom of my mind.*

—Virginia Woolf, A Room of One's Own.



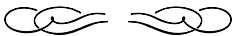
Contents

Introduction	1
1 Gravitational waves in general relativity: from sources to detection	7
1.1 General Relativity	7
1.2 Linearized theory of gravity	9
1.2.1 Solution in vacuum: gravitational waves	11
1.2.2 The effect of gravitational waves	12
1.2.3 Generation of gravitational waves	15
1.2.4 Multipolar expansion	18
1.3 Sources	18
1.3.1 Binary systems in the Newtonian framework	19
1.3.2 Inspiral of compact objects binaries	20
1.3.3 Binary black holes	22
1.3.4 Binary neutron stars	25
1.4 Detection	28
1.4.1 Interferometers	28
1.4.2 Noise characterization	30
1.4.3 Extracting signals from noise	32
1.4.4 Existing and planned detectors	34
2 Data analysis tools	37
2.1 Waveforms	37
2.1.1 Numerical Relativity	38
2.1.2 Post-Newtonian expansion	39
2.1.3 Effective one body	43
2.1.4 Phenomenological models	44
2.2 Bayesian inference	53
2.2.1 Probabilities and Bayes theorem	53
2.2.2 Parameter estimation	54

2.2.3	Characterizing and combining posteriors	55
2.2.4	Hypothesis ranking and model selection	57
2.3	Computational methods	58
2.3.1	Nested sampling	59
2.3.2	Markov chain Monte Carlo	63
2.3.3	Reducing the computational cost	66
3	Testing general relativity using higher-order modes of gravitational waves from binary black holes	71
3.1	Introduction	71
3.2	Properties of higher harmonics and waveform model	73
3.3	Analysis framework and setup of simulations	74
3.3.1	Analysis framework	74
3.3.2	Setup of the simulations	76
3.4	Results of simulations, and analyses of GW190412 and GW190814	76
3.4.1	More massive binary black holes	77
3.4.2	Injections with parameters similar to those of GW190412 and GW190814	79
3.4.3	Results for GW190412 and GW190814	79
3.5	Summary and conclusions	81
4	Comparing gravitational waveform models for binary black hole mergers through a hypermodels approach	85
4.1	Introduction	85
4.2	Methods	86
4.2.1	Waveform models	86
4.2.2	Bayesian framework	88
4.2.3	Hypermodels	88
4.3	Results	91
4.3.1	Single events	95
4.3.2	Combined events	100
4.4	Injection runs	104
4.5	Summary	106
5	Unraveling information about supranuclear-dense matter from the complete binary neutron star coalescence process using future gravitational-wave detector networks	109
5.1	Introduction	109
5.2	The waveform model	110
5.2.1	Inspiral-merger-postmerger model construction	111
5.2.2	Mismatch	115
5.3	Methods and setup	116
5.3.1	Detector networks	116
5.3.2	Parameter estimation	118

5.3.3	Simulations	118
5.3.4	Parameter estimation with future detectors	118
5.3.5	Relative binning settings and validity	121
5.4	Results	123
5.4.1	Best-case scenario	124
5.4.2	Detector network performances in zero noise	126
5.4.3	Detector network performances in non-zero noise	129
5.4.4	Results for the free-parameter model	130
5.4.5	Numerical relativity injections	131
5.5	Conclusions	134
6	Measuring tidal effects with the Einstein Telescope: A design study	137
6.1	Introduction	137
6.2	Methods	138
6.2.1	Sources and configurations	139
6.3	Results	142
6.3.1	Detector configuration comparison	142
6.3.2	Effect of varying PSDs	143
6.3.3	Effect of varying minimum frequency	144
6.4	Summary	146
7	Conclusions	149
Public summary		153
Openbare samenvatting		165
Sintesi per il pubblico		177
Curriculum vitae		189
List of acronyms		191
Acknowledgments		193
Bibliography		194

Contents



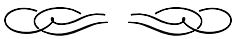
List of Figures

I.1	Black hole image obtained by EHT compared with a simulated image.	2
I.2	LIGO-Virgo-KAGRA observing runs.	3
I.3	Sensitivity curves for different detectors together with the frequency spectra of gravitational-wave signals emitted by various sources.	5
1.1	Displacement induced by a gravitational wave on a ring of test masses.	14
1.2	Example of chirping effect in the time-frequency map of GW170817.	22
1.3	Mass-radius profiles for different equations of state.	26
1.4	Schematic representation of a laser interferometer.	29
1.5	Example of sensitivity curves for different detectors.	35
2.1	Example of gravitational waveform.	38
2.2	Schematic representation of likelihood evolution in a Nested sampling algorithm.	61
3.1	Absolute value of the spin-weighted spherical harmonics of weight -2 as a function of the inclination angle.	74
3.2	Relative signal power of higher-order modes in gravitational waves compared to the dominant mode.	75
3.3	$\ln \mathcal{B}_{\text{GR}}^{\text{NonGR}}$ for non-GR c_{21} and c_{33} injections in the case of heavy BBH simulations.	77
3.4	Violin plots for the posterior density distributions of c_{21} and c_{33} in the case of heavy BBH injections.	78
3.5	$\ln \mathcal{B}_{\text{GR}}^{\text{NonGR}}$ for injections with GR parameters similar to those of GW190412 and GW190814.	79
3.6	Violin plots for c_{21} and c_{33} posterior density distributions, for injections similar to GW190412 and GW190814.	80
3.7	c_{21} and c_{33} posterior density functions for GW190412 and their mismatch contour with the inclination angle.	82
3.8	The same as in Fig. 3.7 but for GW190814.	83
4.1	Posteriors of the source parameters as recovered with the different models.	93
4.2	Evolution of the joint odds ratio for each approximant with respect to SEOBNRv4PHM as events are added.	101

4.3	Posterior probability for the different approximants as a function of the estimated source parameters.	103
4.4	Probability density distribution of the log-likelihood recovered for the different models from the analysis of simulated signals.	105
5.1	Mismatches between our postmerger model and hybrid waveforms from the CoRe and SACRA databases.	114
5.2	Location and sensitivity curves of the detectors considered in the study.	117
5.3	Posterior probability density of the source parameters obtained from the analysis with different detector networks.	121
5.4	Comparison between the posteriors of the source parameters obtained using relative binning with different precision requirements.	122
5.5	$\tilde{\Lambda}$ posteriors recovered with both our postmerger models and the model without postmerger for our best-case-scenario injections.	124
5.6	Comparison between the QU-PM injected signal and the NO-PM waveform obtained with both the injection parameters and the recovered maximum-likelihood ones.	125
5.7	c_1 posteriors obtained with the FREE-PM model in our best-case scenario.	126
5.8	Injected QU-PM waveform compared to the corresponding NR waveform and to the waveforms recovered with both the QU-PM and the NO-PM models.	127
5.9	Width of the 90% confidence interval of the $\tilde{\Lambda}$ posterior recovered with different detector networks for injections in zero noise.	128
5.10	Width of the 90% confidence interval of the $\tilde{\Lambda}$ posterior recovered with different detector networks for injections in Gaussian noise, comparing results for two different noise realizations.	130
5.11	c_1 posteriors recovered with different detector networks for FREE-PM injections in Gaussian noise.	132
5.12	$\tilde{\Lambda}$ posteriors recovered with both our postmerger models and with the model without postmerger for injections of NR waveforms in Gaussian noise.	133
5.13	Frequency-domain waveform of the injected NR signal, compared to the waveforms generated from the maximum-likelihood parameters recovered with each model.	134
6.1	Location, sensitivity, and design considered for the ET detector.	138
6.2	Posterior density distribution of $\tilde{\Lambda}$ for the five reference detector configurations and for all three sources investigated.	141
6.3	Posteriors of the intrinsic source parameters for Source B as recovered with the different detector configurations.	142
6.4	Comparison between posteriors of the source parameters for Source C considering different arm lengths for the various detector's shapes.	143
6.5	Posteriors of \mathcal{M}_c , $\tilde{\Lambda}$, q , and χ_{eff} , for Source C and the $\Delta 10\text{km}$ configuration, recovered with the different PSDs.	144
6.6	Comparison between a typical injected GW signal with the amplitude spectral densities corresponding to the PSDs optimized in different frequency ranges.	145

6.7	Posterior distributions for \mathcal{M}_c , q , $\tilde{\Lambda}$, and χ_{eff} , and the width of their 90% confidence interval, for different choices of f_{low}	148
S.1	Artistic representation of the curvature induced in spacetime by objects with different compactness.	154
S.2	Schematic representation of destructive interference between two laser beams.	155
S.3	Representation of balance between gravity and the pressure from nuclear reactions in a star.	156
S.4	Example of a gravitational-wave signal emitted by a binary black hole coalescence.	158
S.5	Example of gravitational-wave signals produced by the same waveform model for different values of masses.	159
S.6	Schematic representation of the orbital plane precession effect.	160
Sn.1	Artistieke weergave van de kromming die in de ruimtetijd wordt veroorzaakt door objecten met verschillende compactheid.	166
Sn.2	Schematische weergave van destructieve interferentie tussen twee laserstralen.	167
Sn.3	Weergave van het evenwicht tussen zwaartekracht en de druk van nucleaire reacties in een ster.	168
Sn.4	Voorbeeld van een gravitatiegolfsignaal uitgezonden door de samensmelting van een binair zwart gat.	170
Sn.5	Voorbeeld van gravitatiegolfsignalen geproduceerd door hetzelfde golfvormmodel voor verschillende waarden van massa's.	171
Sn.6	Schematische voorstelling van het effect van precessie in het baanvlak.	173
Si.1	Rappresentazione artistica della curvatura indotta nello spaziotempo da oggetti con compattezze diverse.	178
Si.2	Rappresentazione schematica dell'interferenza distruttiva tra due raggi laser.	179
Si.3	Rappresentazione dell'equilibrio tra la gravità e la pressione generata dalle reazioni nucleari in una stella.	180
Si.4	Esempio di segnale di onda gravitazionale emesso dalla coalescenza di una binaria di buchi neri.	182
Si.5	Esempio di segnali di onde gravitazionali prodotti dallo stesso modello di forma d'onda per diversi valori delle masse.	183
Si.6	Rappresentazione schematica dell'effetto di precessione del piano orbitale.	185

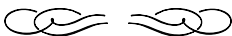
List of Figures



List of Tables

2.1	Main features of the discussed waveform models.	52
3.1	Values of $\ln \mathcal{B}_{\text{GR}}^{\text{NonGR}}$ for analyses of the real events GW190412 and GW190814.	81
4.1	Mass parameters recovered for the various events with the different models.	89
4.2	Spin parameters recovered for the various events with the different models.	90
4.3	Log-likelihood values recovered for the various events with the different models.	92
4.4	Jensen-Shannon divergence between the χ_p posterior recovered with the different models and the χ_p prior conditioned to χ_{eff}	94
4.5	Jensen-Shannon divergence between the posteriors of the mass and spin parameters recovered with our analysis and the LVK results.	96
4.6	Probability percentages recovered for the different models for each event.	99
4.7	Joint odds ratios.	102
4.8	Approximant model and parameters used for injections.	104
5.1	Properties of the sources used for injections.	119
5.2	SNR of the whole signal and of the postmerger part only, for the NR waveforms employed in our analysis, at a distance of 68 Mpc.	120
5.3	SNR values for zero-noise injections in the different networks and for different values of luminosity distance.	120
5.4	Number of frequency bins employed in the relative binning method for different precision requirements.	123
5.5	Recovered and injected values of c_0 and c_2 for FREE-PM injections in our best-case scenario.	126
5.6	Median values with 90% confidence interval of the posterior probability density of $\tilde{\Lambda}$ recovered with two different noise realizations.	131
6.1	Source properties used for injections.	139
6.2	Priors employed in the parameter estimation analysis.	140
6.3	Features of the studied detector configurations.	140

6.4 Recovered $\tilde{\Lambda}$ for different values of f_{low} , comparing zero-noise and Gaussian-noise runs. 146



Introduction

For more than two centuries, the description of gravity relied on the theory elaborated by Isaac Newton in his work “*Philosophiae Naturalis Principia Mathematica*”. The Newtonian law of gravity provides an extremely accurate description of the phenomena observable on Earth, where gravity is relatively weak. However, in 1859, the observation of the anomalous precession of Mercury’s perihelion began to question the reliability of Newton’s theory. In 1887, Michelson and Morley performed an experiment to measure the speed of light in different inertial frames [1]: at the time, light was supposed to travel only through a specific medium, called ether, and Maxwell’s equations, which predict the speed of light to be equal to c , were thought to be valid only in the rest frame of such medium, while the velocity in the other frames could be obtained through the Galilean formulas for the addition of velocities. Nonetheless, Michelson and Morley’s experiment ended up showing that light propagates always with the same speed. While the scientific community started discussing possible flaws in the experiment, Albert Einstein adopted a different approach: assuming that the experiment results were correct, he formulated a new theory to explain them. The theory of *special relativity*, published in 1905, was therefore based on the assumption that the speed of light c is a universal constant and nothing can travel faster than that. This highlighted another issue within the Newtonian theory, in which the gravitational interaction was instantaneous, hence meaning that gravity would propagate with infinite speed. Ten years later, in 1915, Einstein proposed a relativistic theory of gravity, the theory of *general relativity* [2], in which gravity is no longer regarded as a force, but as an effect of matter, or energy, on the geometry of spacetime. General relativity (GR) could explain the precession of perihelion, but it lead also to more “exotic” predictions, difficult to prove experimentally, like the existence of black holes, the expansion of the universe, and the production of gravitational waves.

Black holes (BHs) are extremely compact objects, which curve spacetime to such an extent that a boundary, called *event horizon*, is formed, after which everything, even light, is forced to fall onto the black hole. This implies that direct electromagnetic observations of black holes are not possible: however, we can still aim at detecting the signal emitted by the accretion disk of matter around them. Indirect evidence of the existence of these objects was found by investigating the motion of stars and galaxies, whose trajectories can sometimes be explained only by the presence of very massive, but not visible, objects. Starting from the 1960s, further evidence was provided by the detection of

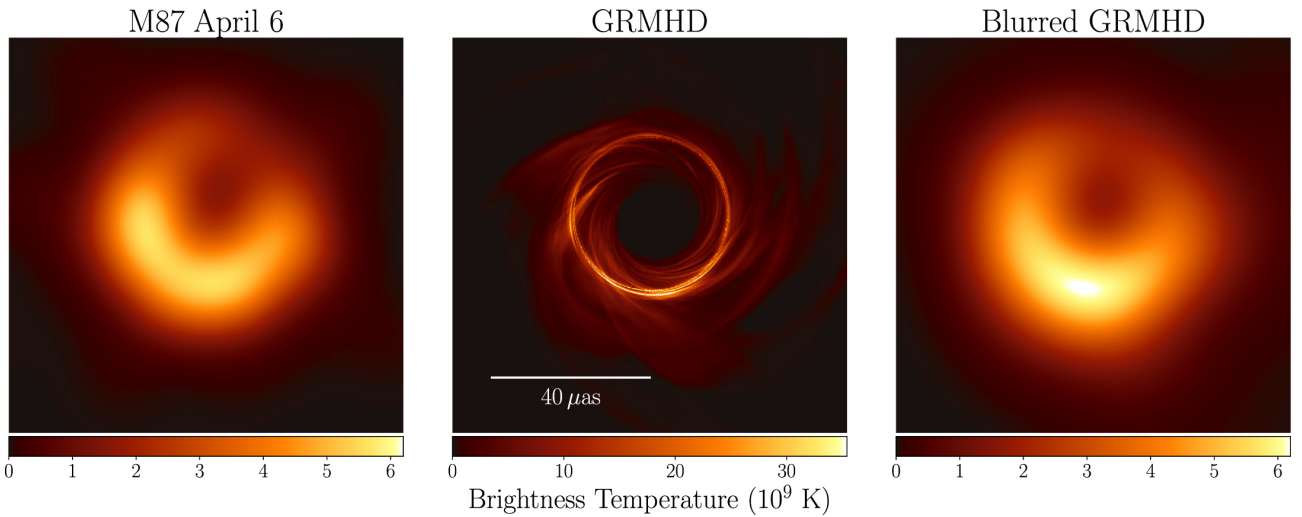


Figure I.1: Image of the M87 supermassive black hole obtained by EHT (*left*), compared with a simulated image obtained from general relativistic magnetohydrodynamic (GRMHD) models (*center and right*). Figure from Ref. [3].

X-ray signals emitted by their accretion disk. In 2019, the first image of a BH was captured, obtained by the Event Horizon Telescope (EHT) collaboration from radio telescopes' data [3–8]. This image is in remarkably good agreement with the predictions of general relativity and with the computer simulations derived from them, as shown in Fig. I.1. According to GR, the heated matter accreting onto the BH emits photons, whose trajectories are curved by the strong gravitational field surrounding it; this results in a bright *photon ring*, with, at its center, a *shadow* corresponding to the line where the photons' trajectories fall into the horizon. The pictures obtained by EHT reveal an outstanding agreement with such prediction, but still they show the shadow of the BH: only gravitational signals can supply a direct observation of these objects.

According to general relativity, gravitational waves (GWs) are perturbations, or ripples, in the spacetime fabric that originate from the acceleration of masses and propagate with the speed of light. As we shall see later, they can be detected by observing the change in distance between two or more test masses. However, spacetime is quite rigid and also the most catastrophic events, like the coalescence of a binary black hole (BBH) system, cause displacements of the order $\mathcal{O}(10^{-18}\text{m})$ or smaller. Therefore, building an experiment able to detect gravitational waves posed a huge challenge. Although indirect evidence of GWs already existed, e.g., from the orbital decay of the Hulse-Taylor binary pulsar [9], after their prediction it took a hundred years to actually detect GWs. The design and, later, construction of laser interferometers for the detection of GWs began in the 1970s, but the numerous technological challenges required over forty years to obtain the first measurement. On the 14th of September 2015, the two LIGO (Laser Interferometer Gravitational-wave Observatory) interferometers detected for the first time a GW signal emitted by a coalescing binary black hole system [10], opening a new window on the Universe. Since then, the two LIGO detectors in the United States, one in Livingston and one in Hanford, and, since 2017, also the Virgo detector in Italy, have been periodically taking data during *observing runs* (see Fig. I.2) alternated with periods of detectors maintenance, during which various technological improvements are applied in order to increase their sensitivity. While the first

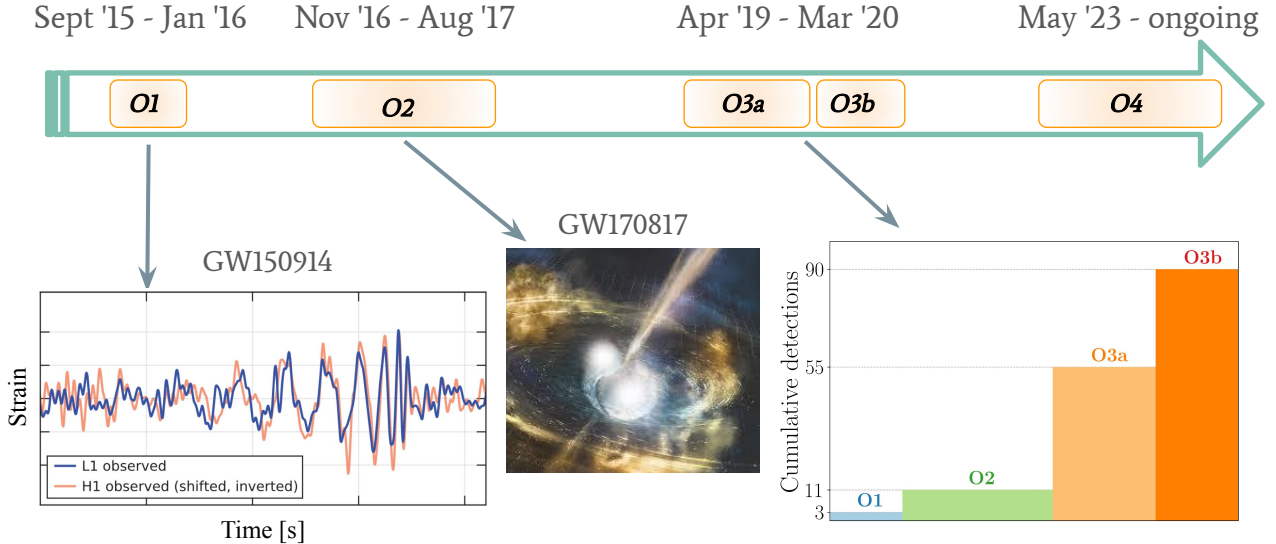


Figure I.2: Schematic representation of the LIGO-Virgo-KAGRA observing runs: O1, from the 12th September 2015 until the 19th January 2016, with the signal (*left*) of the first GW detection GW150914 (figure from Ref. [10]); O2, from the 30th November 2016 until the 20th August 2017, which lead to the first detection of a GW signal from a BNS system, with an artistic illustration (*center*) of the merger of two neutron stars (credit: *NSF/LIGO/Sonoma State University/A. Simonnet*); O3, which lasted almost one year, bringing the total number of events to 90 (*right*); and, finally, O4 that is currently ongoing. In the plot on the right, reporting the cumulative number of detections, the width of the bar corresponding to each observing run is proportional to its duration in days; this plot shows a sharp increase in the number of detections during O3.

observing run, O1, lead to the first GW detection ever, during the second one, O2, the first signal from a binary neutron star (BNS) system was detected, GW170817 [11]. Thanks to the joint detection of the γ -ray burst GRB 170817A and of transient counterparts in the whole electromagnetic spectrum, this extraordinary event inaugurated the era of *multi-messenger astronomy* [12, 13]. The effect of the interferometers' improvements introduced between one observing run and the other is clearly visible from the plot on the right in Fig. I.2, showing the increase in the number of detections. The last observing run, O3¹, lead to the detection of 49 new events, bringing the total to 90, collected in third *Gravitational-Wave Transient Catalog*, GWTC-3 [14]. At the moment, the LIGO-Virgo-KAGRA (LVK) collaboration efforts are focused on O4, started on 24th May 2023 and currently ongoing.

The increasing number of detections enables us to study the features of GW sources at a population level and to combine information from multiple events. However, it also implies a higher probability to observe events outside the expected “vanilla” populations. During O3, for the first time GW

¹The O3 observing run was divided into O3a, from 1st April 2019 until 1st October 2019, and O3b, from 1st November 2019 until 27th March 2020, with a month in-between to upgrade the detectors.

signals emitted by neutron star-black hole systems were detected, GW200105 and GW200115 [15], providing the first direct evidence of the existence of such systems. Furthermore, some detections displayed such particular features to deserve the label of “special events”, which we briefly describe below. GW190412 [16] provided the first detection of a signal from a binary black hole system with unequal masses, including the contribution of higher-order modes. The source of GW190521 [17] is the heaviest system detected so far: the mass of the final BH produced classifies it as an intermediate mass black hole, thus providing the first direct detection of such an object; in addition, the masses of the component BHs fall in the so-called *pair-instability mass gap*, and their existence cannot be explained with the current theory of stellar evolution. GW190425 [18] represented the second observation of a BNS signal; this time no electromagnetic counterpart was detected, probably due to the large distance of the source and the poor sky localization.² Interestingly, the total mass of the system was estimated to be roughly $3.4 M_{\odot}$, much larger than the mass of BNS systems in the population known from electromagnetic observations so far. Finally, GW190814 [19] was the detection of a signal produced by the coalescence of a BH with mass $\sim 23.2 M_{\odot}$ and an object with mass $\sim 2.6 M_{\odot}$, which is larger than the current estimates of the maximum mass that can be supported by a neutron star (NS), but, based on previous X-ray and GW observations, we also do not expect BHs with masses lower than $\sim 5 M_{\odot}$.

As one can see from these examples, the information extracted from GW data already started challenging our current knowledge and models of GWs sources.

The analysis of GW signals emitted by the coalescence of binaries of compact objects, like black holes or neutron stars, allows us to infer information about the sources and their population, but also to probe fundamental physics, by testing the predictions of general relativity or constraining the equation of state of supranuclear-dense matter inside neutron stars. The theory of general relativity is expected to break down at Planck scales, because of significant quantum fluctuations in the classical spacetime geometry, but an universally accepted quantum theory of gravity is still missing. Therefore, we want to test GR, not only to prove its validity, but also to look for hints regarding what is needed in a quantum formulation. Gravitational waves allow us to probe GR in the strong field regime. Different kinds of tests have been developed, investigating various aspects of generation and propagation of GWs, but also the features of possible non-GR sources. Up to now, no evidence of GR violations has been found [20–22].

The sensitivity of current earth-based laser interferometers allows them to detect signals emitted during the coalescence of binary systems of neutron stars or stellar mass black holes. However, different detectors are expected to survey other regions in the frequency band, as shown in Fig. I.3. The Laser Interferometer Space Antenna (LISA) will be a laser interferometer in space, composed by three spacecrafts orbiting around the Sun, with a distance of roughly 10^9 m between each other. It will allow to detect GW signals in the frequency band $[10^{-5} - 1]$ Hz, produced, for example, by supermassive BHs, or during the inspiral of binary systems with extreme mass ratios, like BHs and

²GW170817 was detected with three detectors, the two LIGO ones and Virgo, and therefore the sky position of the source was constrained with great accuracy, $\sim 28 \text{ deg}^2$.

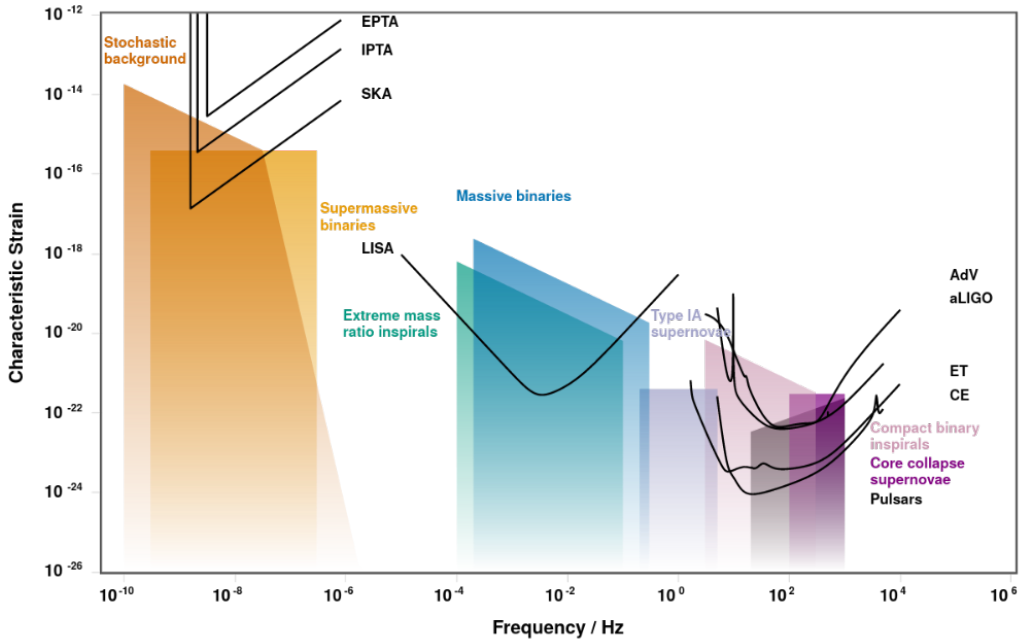


Figure I.3: Sensitivity curves for different detectors together with the frequency spectra of GW signals emitted by various sources. Plot generated via <http://rhcole.com/apps/GWplotter> [24].

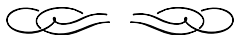
white dwarfs. On the other hand, pulsar timing array detectors can measure GW signals from the stochastic background by looking for their effect on the very precise radio signals emitted by pulsars. Recently, the NANOGrav collaboration announced the evidence of such signals in the released pulsar timing data set from the last 15 years [23].

Moreover, a next generation of ground-based laser interferometers is planned to be built in the upcoming years: the Einstein Telescope in Europe and the Cosmic Explorer in the United States. Their increased sensitivity promises to provide more and louder signals, for all kinds of sources emitting in the region $[5 - 10^3]$ Hz. This will allow us to put tighter constraints on the neutron stars' equation of state and on possible deviations from GR, to infer more information about the populations of compact objects binaries and their origin, and possibly to observe new phenomena. However, it will also present numerous challenges from the data analysis point of view. We will start detecting overlapping signals, i.e., multiple signals, from different sources, at the same time. The loudness of the detections will highlight possible systematic errors in the analysis, starting from the ones induced by the waveform models employed; therefore, it is necessary to build more accurate models and possibly to evaluate their systematics beforehand. Finally, the large amount of signals, together with their increased loudness and longer duration, imply a huge increase in the computational cost for their analysis, which will represent one of the main challenges and potential bottlenecks for future analyses.

This thesis is organized as follows: in Chapter 1, we introduce gravitational waves in the framework of general relativity, including their generation, sources, and detection. In Chapter 2, we discuss the data analysis tools: waveform models, Bayesian analysis, and computational techniques, with a focus on possible methods to reduce the computational cost of the analyses. In Chapter 3, we introduce a

new test of general relativity, based on the amplitude of subdominant modes in the GW signals and the measurement of possible deviations of their values from the predictions of general relativity. In Chapter 4, we perform a *hypermodes* study of the heaviest binary-black-hole signals detected so far, with the goal to study potential systematic biases deriving from the use of different waveform models. In Chapter 5, we present a new frequency-domain waveform model that describes the GW signal emitted during the full coalescence of a binary neutron star system, including the postmerger, and its application in parameter estimation analyses with future detectors to try and unravel information about the supranuclear-dense matter equation of state in NSs. Finally, in Chapter 6, we investigate the influence of the different designs proposed for the Einstein Telescope detector on the study of GW signals from binary neutron star systems, focusing on the extraction of the tidal deformability parameters. In Chapter 7, we conclude and summarize the research presented in this thesis.

Chapter 1



Gravitational waves in general relativity: from sources to detection

Gravitational waves are predicted and described by general relativity. In this chapter, we provide a summary of the basic concepts of general relativity that are needed to understand the theory of gravitational waves, from their generation to the detection. We then focus on the compact objects which can generate them, black holes and neutron stars, and we conclude with a general overview of gravitational-wave detectors.

1.1 General Relativity

In general relativity, gravity is no longer regarded as a force, but as an effect of the spacetime geometry: the presence of mass, or energy, induces a curvature in spacetime, and moving test bodies are forced to follow the trajectories created by such curvature. Mathematically, this connection between mass and spacetime geometry is described by the Einstein field equations (EFEs). The idea of a curved spacetime originates from the experiment on gravitational redshift, born as a thought experiment in Einstein's theory and later carried out in 1960 [25]: according to Einstein's equivalence principle, a uniform gravitational field cannot be distinguished from a uniform acceleration; when applied to photons, it translates to the fact that a gravitational field affects the frequency of a photon in the same way a moving source does. This effect cannot be explained in a flat spacetime and therefore lead to the idea of a non-flat geometry.

In the following, Greek letters represent spacetime coordinates, and Latin letters the space ones. Moreover, we use the *Einstein summation convention*, i.e., we sum over repeated upper and lower indices

$$x_\alpha y^\alpha = \sum_\alpha x_\alpha y^\alpha. \quad (1.1)$$

In general, to characterize a 4-dimensional spacetime geometry we need (i) a system of coordinates $x^\alpha = (x^0, x^1, x^2, x^3)$, through which we can uniquely describe an event, and (ii) the line element describing the physical distance between two points separated by a coordinate distance dx^α

$$ds^2 = g_{\alpha\beta} dx^\alpha dx^\beta, \quad (1.2)$$

where $g_{\alpha\beta}$ is the *metric tensor*, in the form of a 4×4 symmetric matrix. The *proper distance* $\sqrt{ds^2}$ provides a way to measure physical distances on the metric.

In a curved spacetime, vectors and vectorial quantities can be defined only locally. At a given point x^α , a vector a is defined in terms of basis vectors e_α as

$$a(x) = a^\alpha(x) e_\alpha(x), \quad (1.3)$$

where $a^\alpha(x)$ are the vector components with coordinates x . The metric tensor \mathbf{g} is defined as the tensor that takes two basis vectors into a real number

$$\mathbf{g}(e_\alpha, e_\beta) = e_\alpha \cdot e_\beta = g_{\alpha\beta} \quad (1.4)$$

and is used to raise and lower indices, for example $x_\alpha = g_{\alpha\beta} x^\beta$.

With this description of spacetime, the trajectory of a particle can be characterized by a curve $x^\mu(\lambda)$, parametrized by λ . The motion of free-falling test masses follows trajectories referred to as *geodesics*, defined as the path that minimizes the distance $\sqrt{ds^2}$, and is described by the geodesic equation

$$\frac{d^2 x^\beta}{d\lambda^2} + \Gamma_{\mu\nu}^\beta \frac{dx^\mu}{d\lambda} \frac{dx^\nu}{d\lambda} = 0. \quad (1.5)$$

In Eq. 1.5, $\Gamma_{\mu\nu}^\beta$ are the Christoffel symbols, defined as

$$\Gamma_{\mu\nu}^\beta \equiv \frac{1}{2} g^{\alpha\beta} (\partial_\mu g_{\alpha\nu} + \partial_\nu g_{\mu\alpha} - \partial_\alpha g_{\mu\nu}), \quad (1.6)$$

where $\partial_\sigma = \partial/\partial x^\sigma$ is the partial derivative with respect to the coordinates x^σ . The Christoffel symbols are symmetric in the lower indices, i.e., $\Gamma_{\mu\nu}^\beta = \Gamma_{\nu\mu}^\beta$.

Despite the overall curvature, in GR spacetime is locally flat: if we consider sufficiently small patches, each one of them can be adequately described by a flat metric, like the Minkowski one $\eta_{\mu\nu} = (-1, 1, 1, 1)$. This *local flatness* property states that, for each point P in the spacetime, we can always find a *local inertial frame* (LIF), i.e., a coordinate system in which

$$g_{\mu\nu}|_P = \eta_{\mu\nu} \quad (1.7a)$$

$$\left. \frac{\partial g_{\mu\nu}}{\partial x^\alpha} \right|_P = 0. \quad (1.7b)$$

A measure of the space-time curvature in GR is given by the Riemann tensor

$$R_{\beta\gamma\delta}^\alpha = \partial_\gamma \Gamma_{\delta\beta}^\alpha - \partial_\delta \Gamma_{\gamma\beta}^\alpha + \Gamma_{\gamma\sigma}^\alpha \Gamma_{\delta\beta}^\sigma - \Gamma_{\delta\sigma}^\alpha \Gamma_{\gamma\beta}^\sigma. \quad (1.8)$$

The Riemann tensor has various symmetry properties, and can be contracted into the Ricci tensor

$$R_{\alpha\beta} = g^{\mu\nu} R_{\mu\nu\alpha\beta}, \quad (1.9)$$

which can be further contracted into the Ricci scalar

$$R = g^{\alpha\beta} R_{\alpha\beta}. \quad (1.10)$$

The Einstein field equations, as mentioned, describe how mass and energy modify the spacetime geometry generating curvature. The Ricci tensor and the Ricci scalar describe the spacetime curvature term in the EFEs, through the Einstein tensor

$$G_{\alpha\beta} = R_{\alpha\beta} - \frac{1}{2} R g_{\alpha\beta}. \quad (1.11)$$

The source of the curvature, instead, is described by the *energy momentum tensor* $T^{\alpha\beta}$, where T^{00} gives the energy density, T^{i0} and T^{0i} represent, respectively, the energy flux and the momentum density, and T^{ij} is the stress tensor. In a flat spacetime, the energy-momentum conservation is expressed as $\partial_\mu T^{\mu\nu} = 0$. In GR, the generalization of the energy-momentum conservation is obtained with $\nabla_\mu T^{\mu\nu} = 0$, where ∇_μ is the covariant derivative, defined as

$$\nabla_\mu V^\sigma = \partial_\mu V^\sigma + \Gamma_{\mu\rho}^\sigma V^\rho, \quad (1.12)$$

for a generic tensor V^σ .

Finally, with the quantities defined above, the Einstein field equations take the form

$$G_{\alpha\beta} = \frac{8\pi G}{c^4} T_{\alpha\beta}, \quad (1.13)$$

with G and c being the universal gravitational constant and the speed of light in vacuum, respectively.

1.2 Linearized theory of gravity

In regions of spacetime where the gravitational field is weak, for example in absence of very massive objects, the EFEs can be studied more easily in their linearized version, obtained with a perturbation approach.

In the *weak-field limit*, we consider spacetime as described by small perturbations around the flat metric

$$g_{\mu\nu} = \eta_{\mu\nu} + h_{\mu\nu}, \quad (1.14)$$

with $|h_{\mu\nu}| \ll 1$. In this limit, the *linearized theory of gravity* originates from an expansion of Einstein's equations around the flat metric and to the linear order in $h_{\mu\nu}$.

In general, under a coordinate transformation $x^\mu \rightarrow x'^\mu$, the metric $g_{\mu\nu}$ transforms as

$$g'_{\mu\nu} = \frac{\partial x^\rho}{\partial x'^\mu} \frac{\partial x^\sigma}{\partial x'^\nu} g_{\rho\sigma}. \quad (1.15)$$

However, the values of the metric components depend on the reference frame; therefore, in the weak field limit, to preserve the condition $|h_{\mu\nu}| \ll 1$, we need to restrict ourselves to coordinate transformations

$$x^\mu \rightarrow x'^\mu = x^\mu + \xi^\mu, \quad (1.16)$$

with small ξ^μ , meaning that the derivative $\partial_\mu \xi_\nu$ must be of the same order of $|h_{\mu\nu}|$ or smaller. Under such coordinate transformations, Eq. 1.15 becomes

$$g'_{\mu\nu} = \eta_{\mu\nu} + h'_{\mu\nu}, \quad (1.17)$$

with

$$h'_{\mu\nu} = h_{\mu\nu} - (\partial_\mu \xi_\nu + \partial_\nu \xi_\mu). \quad (1.18)$$

Equation 1.18, which describes how the metric perturbation transforms, derives just from constraints imposed on the coordinate transformations, and therefore it does not change the physics of $|h_{\mu\nu}|$. Equation 1.17 shows that, in the weak-field limit, metric perturbations can be treated as a tensor propagating on the flat spacetime. Moreover, since we ignore effects $\mathcal{O}(h^2)$ or higher, in this limit the Minkowski metric $\eta_{\mu\nu}$ can be used to raise and lower indices.

To linearize the Einstein field equations, we start by expanding the Riemann tensor to the first order in $|h_{\mu\nu}|$:

$$R_{\mu\nu\rho\sigma} = \frac{1}{2} (\partial_\nu \partial_\rho h_{\mu\sigma} + \partial_\mu \partial_\sigma h_{\nu\rho} - \partial_\mu \partial_\rho h_{\nu\sigma} - \partial_\nu \partial_\sigma h_{\mu\rho}). \quad (1.19)$$

From Eq. 1.19 we can obtain the linearized Ricci tensor and Ricci scalar, which lead to the following expression for the linearized Einstein tensor

$$G_{\alpha\beta} = \frac{1}{2} (\partial_\alpha \partial^\mu h_{\mu\beta} + \partial^\mu \partial_\beta h_{\alpha\mu} - \partial^\mu \partial_\mu h_{\alpha\beta} - \partial_\alpha \partial_\beta h_\mu^\mu) - \frac{1}{2} \eta_{\alpha\beta} (\partial^\nu \partial^\mu h_{\mu\nu} - \partial^\mu \partial_\mu h_\nu^\nu). \quad (1.20)$$

We now define the *inverse trace*

$$\bar{h}_{\mu\nu} = h_{\mu\nu} - \frac{1}{2} \eta_{\mu\nu} h, \quad (1.21)$$

where

$$h = \eta^{\mu\nu} h_{\mu\nu}. \quad (1.22)$$

Substituting this into Eq. 1.20, and recalling the Einstein field equations in Eq. 1.13, we find the linearized Einstein equations

$$\square \bar{h}_{\alpha\beta} + \eta_{\alpha\beta} \partial^\mu \partial^\nu \bar{h}_{\mu\nu} - \partial^\mu \partial_\beta \bar{h}_{\alpha\mu} - \partial^\mu \partial_\alpha \bar{h}_{\beta\mu} = -\frac{16\pi G}{c^4} T_{\alpha\beta}, \quad (1.23)$$

where $\square \equiv \partial_\alpha \partial^\alpha$ represents the d'Alambertian operator.

The weak-field condition, in which spacetime is described by a perturbed metric $g_{\mu\nu} = \eta_{\mu\nu} + h_{\mu\nu}$, with $|h_{\mu\nu}| \ll 1$, is satisfied in an infinite number of coordinate systems. Since a coordinate transformation like the gauge transformations in Eq. 1.18 does not change the value of a tensor components, a solution of the linearized Einstein equations remains a solution in every coordinate system obtained from such transformations. Therefore, when imposing gauge conditions to fix the coordinate system in which we want to solve the Einstein equations, we have the freedom to choose the coordinate system that simplifies Eq. 1.23 the most.

Applying Eq. 1.18 to the inverse-trace $\bar{h}_{\mu\nu}$ we get

$$\bar{h}'_{\mu\nu} = \bar{h}_{\mu\nu} - (\partial_\mu \xi_\nu + \partial_\nu \xi_\mu - \eta_{\mu\nu} \partial_\sigma \xi^\sigma). \quad (1.24)$$

In particular, for each $\bar{h}_{\alpha\beta}$, we can always find a $\bar{h}'_{\alpha\beta}$ that satisfies the *Lorentz gauge*

$$\partial^\alpha \bar{h}'_{\alpha\beta} = 0 \quad (1.25)$$

and for which the linearized Einstein equations become

$$\square \bar{h}'_{\alpha\beta} = -\frac{16\pi G}{c^4} T_{\alpha\beta}. \quad (1.26)$$

One can show that it is always possible to find a gauge transformation like Eq. 1.24 to a coordinate system that satisfies the Lorentz gauge by choosing ξ_ν such that

$$\square \xi^\nu = \partial_\mu \bar{h}^{\mu\nu}. \quad (1.27)$$

Since the d'Alambertian \square is an invertible operator, Eq. 1.27 always has a solution that can be found via a Green's function. Moreover, any further gauge transformation does not spoil the Lorentz gauge, provided that the functions ξ^μ satisfy the homogeneous equation

$$\square \xi^\mu = 0. \quad (1.28)$$

This means that, also after imposing the Lorentz gauge, we are left with some gauge freedom.

1.2.1 Solution in vacuum: gravitational waves

We study gravitational signals as measured by the detectors, thus far from the source that produced them. Therefore, we now look for solutions of Eq. 1.26 outside the source, in vacuum, i.e. for $T_{\mu\nu} = 0$, where, dropping the prime for convenience, the equation becomes

$$\square \bar{h}_{\alpha\beta} = \left(-\frac{1}{c^2} \frac{\partial^2}{\partial t^2} + \nabla^2 \right) \bar{h}_{\alpha\beta} = 0. \quad (1.29)$$

Equation 1.29 is a wave equation and its general solution is a linear combination of plane waves in the form

$$\bar{h}_{\mu\nu} = A_{\mu\nu} \cos(k_\sigma x^\sigma) = A_{\mu\nu} \cos(\omega t - \mathbf{k} \cdot \mathbf{x}). \quad (1.30)$$

Therefore, in the weak-field limit, perturbations of spacetime propagate on the flat spacetime background as plane waves, and thus we call them *gravitational waves*.

In order to satisfy the wave equation, we need $k_\alpha k^\alpha = 0$, which yields $\omega = c|\mathbf{k}|$, meaning that gravitational waves propagate with the speed of light. Furthermore, from the Lorentz gauge, we get $k_\mu A^{\mu\nu} = 0$, which implies that they are transverse waves.

We saw that imposing the Lorentz gauge does not completely fix the coordinate system. We can use the gauge freedom left to impose further constraints on the components of $\bar{h}_{\alpha\beta}$:

$$\bar{h}_{0\mu} = 0 \quad (1.31a)$$

$$\bar{h}_\mu^\mu = 0. \quad (1.31b)$$

Such choice of coordinates is called the *transverse-traceless (TT) gauge*. In this coordinate system, the Lorentz gauge becomes $\partial_\beta h_\alpha^\beta = 0$. The perturbation $\bar{h}_{\alpha\beta}$ is a 4×4 symmetric matrix, with 10 independent components. However, after imposing the Lorentz gauge and the conditions deriving from the TT gauge, we are left with only two degrees of freedom, which correspond to the two independent polarizations of gravitational waves, usually called *plus* and *cross* polarizations, and denoted as h_+ and h_\times , respectively. Assuming, without loss of generality, that the waves direction of propagation is along the z -axis, the metric perturbation in the TT gauge can be written as

$$\bar{h}^{TT} = \begin{pmatrix} 0 & 0 & 0 & 0 \\ 0 & h_+ & h_\times & 0 \\ 0 & h_\times & -h_+ & 0 \\ 0 & 0 & 0 & 0 \end{pmatrix} = \begin{pmatrix} 0 & 0 & 0 & 0 \\ 0 & A_+ & A_\times & 0 \\ 0 & A_\times & -A_+ & 0 \\ 0 & 0 & 0 & 0 \end{pmatrix} \cos \left[\omega \left(t - \frac{z}{c} \right) \right] \quad (1.32)$$

The most general solution of Eq. 1.29 is a superposition of plane-wave solutions as Eq. 1.32, with different amplitudes, frequencies, and propagation directions.

1.2.2 The effect of gravitational waves

To understand the physical effect of gravitational waves, we look at their influence on the motion of bodies. Particles with a rest mass, i.e., forced to have a velocity smaller than c , must follow *timelike* directions, for which $ds^2 < 0$. In this case, the *proper time* τ , i.e., the time measured by an observer in their own reference frame, can be defined as the time measured by a clock carried by the particle along its trajectory, which we can parametrize with τ as $x^\mu = x^\mu(\tau)$. Defining the *four-velocity* u^μ as

$$u^\mu = \frac{dx^\mu}{d\tau}, \quad (1.33)$$

the geodesic equation in Eq. 1.5 can be rewritten as

$$\frac{du^\mu}{d\tau} + \Gamma_{\alpha\beta}^\mu u^\alpha u^\beta = 0. \quad (1.34)$$

In the TT gauge, if we consider a particle initially at rest, its four-velocity will be $u^\alpha = (1, 0, 0, 0)$. Writing $g_{\mu\nu} = \eta_{\mu\nu} + h_{\mu\nu}$, and expanding to the first order in $h_{\mu\nu}$, Eq. 1.34 becomes

$$\begin{aligned} \frac{du^\mu}{d\tau} &= -\frac{1}{2} \eta^{\mu\sigma} (\partial_\alpha h_{\beta\sigma} + \partial_\beta h_{\alpha\sigma} - \partial_\sigma h_{\alpha\beta}) \\ &= -\left(\partial_0 h_{\mu 0} - \frac{1}{2} \partial_\mu h_{00} \right), \end{aligned} \quad (1.35)$$

where in the last line we used $u^\alpha = (1, 0, 0, 0)$. However, since we are in the TT gauge, according to the condition in Eq. 1.31a, $h_{00} = h_{\mu 0} = 0$, and hence $du^\mu/d\tau = 0$. This means that, for a particle initially at rest, i.e., for which $\frac{dx^i}{d\tau} \Big|_{\tau=0} = 0$, the derivatives $dx^i/d\tau$ remain zero at all times, therefore the coordinates do not change, and particles remain at rest also after the arrival of a gravitational wave. This does not imply that gravitational waves have no physical effect on particles, but that coordinates in the TT gauge have been chosen in such a way that they remain invariant after a GW passes by. To observe the physical effect of GWs, we need to look at two or more particles and how their proper distance changes.

Interaction of gravitational waves with matter

Let us consider two nearby particles, each one in free-falling motion and therefore moving along time-like geodesics, one parametrized by $x^\mu(\tau)$ and the other one by $x^\mu(\tau) + \xi^\mu(\tau)$, where the separation vector $\xi^\mu(\tau)$ connects points with the same proper time τ on the two geodesics. The relative acceleration between the two particles can be computed as the second time derivative of ξ^μ . Assuming that the separation vector is smaller than the typical scale on which the gravitational field changes significantly, the relative acceleration is given by

$$\frac{D^2\xi^\mu}{D\tau^2} = -R_{\nu\rho\sigma}^\mu \xi^\rho \frac{dx^\nu}{d\tau} \frac{dx^\sigma}{d\tau}, \quad (1.36)$$

where the covariant derivative $DV^\mu/D\tau$ of a vector $V^\mu(x)$ along the curve $x^\mu(\tau)$ is defined as

$$\frac{DV^\mu}{D\tau} \equiv \frac{dV^\mu}{d\tau} + \Gamma_{\nu\rho}^\mu V^\nu \frac{dx^\rho}{d\tau}. \quad (1.37)$$

In Eq. 1.36, $R_{\nu\rho\sigma}^\mu$ is the Riemann tensor, hence in a flat spacetime the relative acceleration is zero.

For two particles initially at rest, the geodesic deviation equation in the TT gauge becomes

$$\frac{d^2\xi^i}{d\tau^2}\Big|_{\tau=0} = -\left[\dot{h}_{ij} \frac{d\xi^i}{d\tau}\right]_{\tau=0}, \quad (1.38)$$

meaning that, if the coordinates of masses initially at rest remain constant, also their coordinate separation must remain constant. Therefore, the arrival of a GW does not affect the coordinate distance between two particles, because we specifically built the coordinate system to ensure that coordinates do not change. To see the effects of GWs we need to look at the changes in proper distance or proper time.

Gravitational-wave detectors, however, cannot be described in the TT gauge, because in real laboratories coordinates are fixed by rigid rulers, and hence a passing GW will cause a displacement in the position of test masses. The easiest coordinate system that we can define for a laboratory is a LIF one, for an experimental setup shielded from any gravitational fields and possible GWs. In principle, if we consider sufficiently small regions of spacetime, finding such coordinates is always possible, thanks to the local flatness property. However, ground-based detectors cannot be shielded from the Earth's gravitational field. Therefore, the coordinate system defining these detectors can be found from a LIF through a coordinate transformation that takes into account the Earth's gravitational acceleration and the effects of Earth's rotation [26]. In this new frame, called *proper detector frame*, the equation for geodesic deviation Eq. 1.36 becomes

$$\frac{d^2\xi^i}{d\tau^2} + \xi^\sigma \partial_\sigma \Gamma_{00}^i \left(\frac{dx^0}{d\tau} \right)^2 = 0. \quad (1.39)$$

Moreover, since at the LIF expansion point P we have $\partial_0 \Gamma_{00}^i = 0$, $\Gamma_{\nu\rho}^\mu = 0$ and $\partial_0 \Gamma_{0j}^i = 0$, Eq. 1.39 can be rewritten as

$$\frac{d^2\xi^i}{d\tau^2} = -R_{0j0}^i \xi^j \left(\frac{dx^0}{d\tau} \right)^2. \quad (1.40)$$

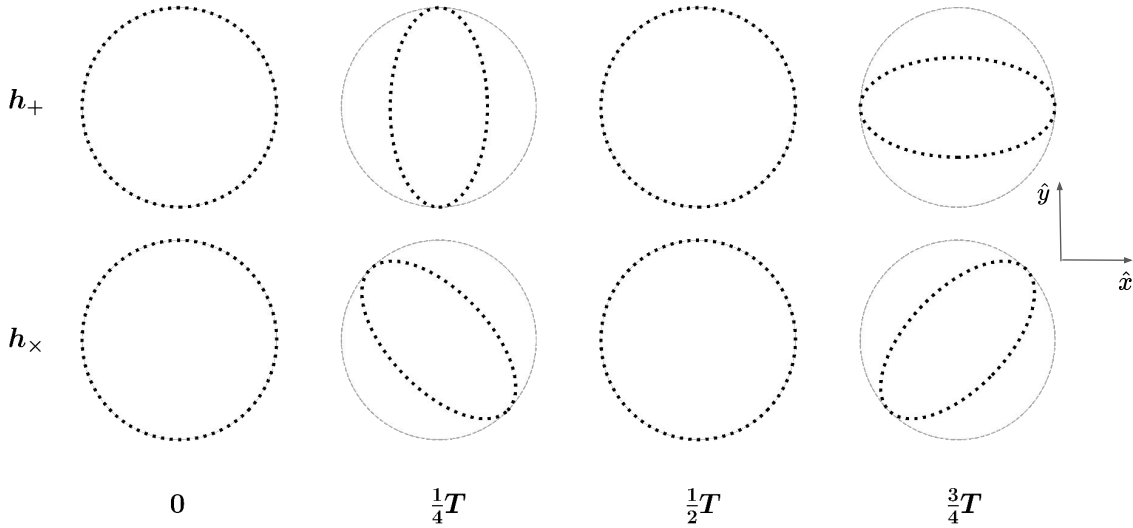


Figure 1.1: Displacement induced on a ring of test masses by a GW travelling perpendicular to the plane of the ring, on top for the plus polarization h_+ and at the bottom for the cross polarization h_x ; $T = 2\pi$ represents the period.

Considering that $dt^2 = d\tau^2 [1 + O(h^2)]$, to the linear order in h we can use the derivative with respect to the coordinate time instead of the proper time. Finally, the Riemann tensor is invariant, hence, for convenience, we can compute it in the TT gauge, finding

$$\ddot{\xi}^i = \frac{1}{2} \ddot{h}_{ij}^{TT} \xi^j, \quad (1.41)$$

which implies that in the *proper detector frame* the physics effects of a GW passing by can be described in terms of a Newtonian force. We remind here that the geodesic deviation equation, Eq. 1.36, was derived under the assumption that the separation vector is much smaller than the typical scale of variation of the gravitational field, which can be characterized by the wavelength λ ; therefore, Eq. 1.41 is valid only for $L \ll \lambda$, with L the length of the detector.

To understand the effect of GWs on test masses, let us consider particles in the (x, y) plane, and a GW propagating along the z direction. Initially the test masses are at (x_0, y_0) , and a GW causes a displacement $(\delta x, \delta y)$. From Eq. 1.32, if we consider a GW with *plus* polarization only, Eq. 1.41 gives

$$\delta \ddot{x} = \frac{\ddot{h}_+}{2} (x_0 + \delta x) = \frac{A_+}{2} (x_0 + \delta x) \omega^2 \cos \omega t \quad (1.42a)$$

$$\delta \ddot{y} = -\frac{\ddot{h}_+}{2} (y_0 + \delta y) = -\frac{A_+}{2} (y_0 + \delta y) \omega^2 \cos \omega t. \quad (1.42b)$$

Since δx and δy are of order $O(h)$, integrating and keeping terms up to the linear order in h , we find

$$\delta x(t) = \frac{h_+}{2}x_0 = \frac{A_+}{2}x_0 \cos \omega t \quad (1.43a)$$

$$\delta y(t) = -\frac{h_+}{2}y_0 = -\frac{A_+}{2}y_0 \cos \omega t. \quad (1.43b)$$

Similarly, for a GW with *cross* polarization only, we obtain

$$\delta x(t) = \frac{h_\times}{2}y_0 = \frac{A_\times}{2}y_0 \cos \omega t \quad (1.44a)$$

$$\delta y(t) = \frac{h_\times}{2}x_0 = \frac{A_\times}{2}x_0 \cos \omega t. \quad (1.44b)$$

This displacement induced by GWs is shown in Fig. 1.1 for the case of a ring of test masses. Such configuration helps visualize why the two polarizations are called *plus* and *cross*: while the *plus* polarization causes simultaneously a stretch along the x (y) direction and a compression along the y (x) one, the *cross* polarization produces this periodic stretch and compression along directions rotated by 45° with respect to the x, y -axes. This is different with respect to electromagnetism, where the two polarizations are shifted by $\pi/2$, not $\pi/4$.

1.2.3 Generation of gravitational waves

In order to understand how gravitational waves are produced, we start from the Einstein field equations, which in the weak-field limit read

$$\square \bar{h}_{\mu\nu} = -\frac{16\pi G}{c^4}T_{\mu\nu}. \quad (1.45)$$

The solution of Eq. 1.45 can be found via the Green's function satisfying

$$\square_x G(x - x') = \delta^4(x - x') \quad (1.46)$$

as

$$\bar{h}_{\mu\nu} = \frac{-16\pi G}{c^4} \int d^4x' G(x - x') T_{\mu\nu}(x'). \quad (1.47)$$

In particular, since we assume that the radiation emitted by the source is outgoing and that there is no incoming radiation from past infinity, the solution is given by the retarded Green's function, which takes into account the time needed for the effect of the source to propagate, considering that the interaction is not instantaneous.

As we saw in Sec. 1.2.1, GWs propagating outside the source, in vacuum, take a simple form in the TT gauge. As part of the TT gauge, we have $\bar{h}_{0\mu} = 0$ (see Eq. 1.31a), therefore in the following we can focus on the spatial components only. Outside the source, we can always find coordinate transformations to the TT gauge. In particular, for a generic wave $h_{\mu\nu}$ propagating in the $\hat{\mathbf{n}}$ direction, we define the operator $\Lambda_{ij,kl}(\hat{\mathbf{n}})$ to extract the TT part of the perturbation, such that

$$h_{ij}^{TT} = \Lambda_{ij,kl}(\hat{\mathbf{n}}) h^{kl}. \quad (1.48)$$

This operator is built from the projector operators

$$P_{ij}(\hat{\mathbf{n}}) = \delta_{ij} - n_i n_j \quad (1.49)$$

as

$$\Lambda_{ij,kl}(\hat{\mathbf{n}}) = P_{ik}P_{jl} - \frac{1}{2}P_{ij}P_{kl}. \quad (1.50)$$

The operator $\Lambda_{ij,kl}(\hat{\mathbf{n}})$ exhibits various properties, among which symmetry, i.e. $\Lambda_{ij,kl} = \Lambda_{kl,ij}$, and tracelessness, i.e. $\Lambda_{ii,kl} = \Lambda_{ij,kk} = 0$. In particular, the latter one implies $h_{ij}^{TT} = \Lambda_{ij,kl}h_{kl} = \Lambda_{ij,kl}\bar{h}_{kl}$. Therefore, the general solution to Eq. 1.45 is

$$h_{ij}^{TT}(t, \mathbf{x}) = \frac{4G}{c^4} \Lambda_{ij,kl}(\hat{\mathbf{n}}) \int d^3x' \frac{1}{|\mathbf{x} - \mathbf{x}'|} T_{kl} \left(t - \frac{|\mathbf{x} - \mathbf{x}'|}{c}, \mathbf{x}' \right). \quad (1.51)$$

Normally, Eq. 1.51 cannot be solved analytically. However, we are interested in studying the gravitational waves that we measure, i.e., that reach our detectors at a distance from the source r much larger than the typical size of the source d .¹ This allows us to expand $|\mathbf{x} - \mathbf{x}'| \simeq r - \mathbf{x}' \cdot \hat{\mathbf{n}}$, with $r = |\mathbf{x}|$, and $\hat{\mathbf{n}} = \mathbf{x}/|\mathbf{x}|$. For $r \gg d$, we can take the limit $r \rightarrow \infty$, and to the leading order in $\mathcal{O}(1/r)$ Eq. 1.51 simplifies to:

$$h_{ij}^{TT}(t, \mathbf{x}) = \frac{1}{r} \frac{4G}{c^4} \Lambda_{ij,kl}(\hat{\mathbf{n}}) \int d^3x' T_{kl} \left(t - \frac{r}{c} + \frac{\mathbf{x}' \cdot \hat{\mathbf{n}}}{c}, \mathbf{x}' \right). \quad (1.52)$$

Now, let us consider non-relativistic sources, for which velocities inside the source are much smaller than the speed of light, $v \ll c$, and, consequently, the reduced wavelength of the radiation emitted is much larger than the typical size of the system. For such sources, we can Taylor-expand the time dependence of T_{kl} in the parameter $\frac{\mathbf{x}' \cdot \hat{\mathbf{n}}}{c}$ as

$$T_{kl} \left(t - \frac{r}{c} + \frac{\mathbf{x}' \cdot \hat{\mathbf{n}}}{c}, \mathbf{x}' \right) \simeq T_{kl} \left(t - \frac{r}{c}, \mathbf{x}' \right) + \frac{x'^i n^i}{c} \partial_t T_{kl} + \frac{1}{2c^2} x'^i x'^j n^i n^j \partial_t^2 T_{kl} + \dots \quad (1.53)$$

If we define the moments of the stress tensor T^{ij} as

$$S^{ij}(t) = \int d^3x T^{ij}(t, \mathbf{x}), \quad (1.54a)$$

$$S^{ij,k}(t) = \int d^3x T^{ij}(t, \mathbf{x}) x^k, \quad (1.54b)$$

$$S^{ij,kl}(t) = \int d^3x T^{ij}(t, \mathbf{x}) x^k x^l, \quad (1.54c)$$

$$(1.54d)$$

and so on, Eq. 1.52 can be written as

$$h_{ij}^{TT}(t, \mathbf{x}) = \frac{1}{r} \frac{4G}{c^4} \Lambda_{ij,kl}(\hat{\mathbf{n}}) \left[S^{kl} + \frac{1}{c} n_m \dot{S}^{kl,m} + \frac{1}{2c^2} n_m n_p \ddot{S}^{kl,mp} + \dots \right]_{t_{\text{ret}}}, \quad (1.55)$$

where everything is evaluated at the retarded time $t_{\text{ret}} = t - r/c$. We notice that the expansion in Eq. 1.55 is equivalent to expanding in terms of (v/c) . This can be seen by considering that, for example, when going from the term S^{kl} to $\frac{1}{c} n_m \dot{S}^{kl,m}$, the x^m in the momentum integral brings an additional factor $\mathcal{O}(d)$, which, combined with the time derivatives, leads to a factor $\mathcal{O}(v)$. This, together with the pre-factor $1/c$, results in an overall difference $\mathcal{O}(v/c)$ between the two terms; the same holds for

¹The typical size of a binary system, for example, is the distance between the two objects in the binary, while for an isolated body is its radius.

the following ones.

To grasp the physical meaning of such expansion, we resort to energy-momentum conservation. Since we are working in the linearized theory, we can use the conservation law in the flat spacetime $\partial_\mu T^{\mu\nu} = 0$ to rewrite the T^{ij} in terms of the energy density T^{00} and the linear momentum T^{0i}/c , finding their respective moments

$$\begin{aligned} M &= \frac{1}{c^2} \int d^3x T^{00}(t, \mathbf{x}) & - \\ M^i &= \frac{1}{c^2} \int d^3x T^{00}(t, \mathbf{x}) x^i & P^i = \frac{1}{c} \int d^3x T^{0i}(t, \mathbf{x}) \\ M^{ij} &= \frac{1}{c^2} \int d^3x T^{00}(t, \mathbf{x}) x^i x^j & P^{i,j} = \frac{1}{c} \int d^3x T^{0i}(t, \mathbf{x}) x^j \\ M^{ijk} &= \frac{1}{c^2} \int d^3x T^{00}(t, \mathbf{x}) x^i x^j x^k & P^{i,j,k} = \frac{1}{c} \int d^3x T^{0i}(t, \mathbf{x}) x^j x^k, \end{aligned}$$

and similarly for the higher-order ones. If we consider a volume \mathcal{V} enclosing and larger than the source, the linearized energy-momentum conservation equation $\partial_\mu T^{\mu\nu} = 0$ leads to the following identities for the time derivatives of the moments found above:

$$\dot{M} = 0 \tag{1.56a}$$

$$\dot{M}^i = P^i \tag{1.56b}$$

$$\dot{M}^{ij} = P^{i,j} + P^{j,i} \tag{1.56c}$$

$$\dot{M}^{ijk} = P^{i,jk} + P^{jk,ki} + P^{k,ij} \tag{1.56d}$$

and

$$\dot{P}^i = 0 \tag{1.57a}$$

$$\dot{P}^{i,j} = S^{ij} \tag{1.57b}$$

$$\dot{P}^{i,jk} = S^{ij,k} + S^{ik,j}. \tag{1.57c}$$

Equations 1.56a and 1.57a simply express the mass and linear momentum conservation. Using the identities above, we can write $S^{ij} = \frac{1}{2} \ddot{M}^{ij}$ and, to leading order, Eq. 1.55 becomes

$$h_{ij}^{TT} = \frac{4}{r} \Lambda_{ij,kl} \ddot{M}^{kl} \left(t - \frac{r}{c} \right). \tag{1.58}$$

Therefore, to the leading order, the gravitational-wave emission is produced by the variation of the mass quadrupole moment; for this reason, Eq. 1.58 is also called the *quadrupole formula*. This is different from electromagnetism, where the lowest order emission is provided by the dipole moment. In GR, the dipole moment depends on P^i , as shown in Eq. 1.56b, but the total momentum is conserved, and hence the dipole variation is zero. If we consider a wave propagating along the $\hat{\mathbf{n}} = \hat{\mathbf{z}}$ direction, from Eqs. 1.58 and 1.32, and computing explicitly the components of $\Lambda_{ij,kl} \ddot{M}^{kl}$, we find the two polarizations as

$$h_+ = \frac{1}{r c^4} \left(\ddot{M}_{11} - \ddot{M}_{22} \right), \tag{1.59a}$$

$$h_\times = \frac{2}{r c^4} \ddot{M}_{12}. \tag{1.59b}$$

1.2.4 Multipolar expansion

In the last section, we saw how GWs' generation can be understood in terms of a multipole expansion of the stress-energy tensor moments. In the following, we will explicitly discuss only the leading-order term, but in general a gravitational-wave signal includes also all the higher-order harmonics [27]. The multipolar expansion of the GW strain can be decomposed in terms of the spherical harmonic modes $h_{\ell m}$ as [28]

$$h(t, \iota, \phi; \Xi) = \sum_{\ell=2}^{\infty} \sum_{m=-\ell}^{\ell} h_{\ell m}(t, \Xi) Y_{\ell m}^{-2}(\iota, \phi), \quad (1.60)$$

where $Y_{\ell m}^{-2}(\iota, \phi)$ are the spin-weighted spherical harmonics of weight -2 , (ι, ϕ) two angles describing the direction of the GW radiation in the frame of the source, and Ξ includes all the other binary parameters influencing the signal. We denote each mode with (ℓ, m) , with the $(2, 2)$ mode being the fundamental one, corresponding to the mass-quadrupole moment. While, as we will see in the next section, the GW fundamental mode has a frequency twice the orbital one, the other harmonics correspond to frequencies that are integer multiples of the orbital frequency [29, 30]. The higher-order modes' amplitude is usually suppressed with respect to the dominant mode one [31–33]; however, the subdominant modes amplitude depends both on the intrinsic and extrinsic parameters of the binaries, and the contribution of higher-order harmonics becomes non-negligible for specific values of the inclination angle ι , and for increasing total mass and mass ratio [34]. Measuring the higher-order modes' contribution in a GW signal helps to break the degeneracy between some of the binary parameters, for example between distance and inclination [35]. Moreover, the presence of higher-order modes provides new ways to test the theory of general relativity, as we shall see in detail in Chapter 3. Among the events detected so far, clear evidence of the presence of higher-order harmonics was found in GW190412 [16] and GW190814 [19].

1.3 Sources

As we saw in Sec. 1.2.3, gravitational waves are produced by time variations of the mass quadrupole and higher moments. Physically, this translates into different possible GW signals and sources: continuous waves emitted, for example, by isolated spinning neutron stars with an irregularity on their surface; the stochastic background produced by unresolved binaries, or the relic of GWs in the early Universe, before recombination; bursts from supernovae explosions; chirping signals generated by the coalescence of binary systems of compact objects, like neutron stars or black holes. The latter is what current detectors have been observing and will be the focus of the work presented in this thesis.

The coalescence of binary systems is usually divided into three phases (see for example Fig. 2.1). During the *inspiral*, the two objects orbit around each other, emitting energy via GWs, until they plunge into one another in the *merger* phase; finally, during the *ringdown* or *postmerger* phase, a new stable configuration is reached. In this section, we present a first approximate description of the system dynamics and the GW emission during the inspiral phase. We shall see later how accurate waveforms for the GW emission during the full coalescence are built. We briefly describe the compact

objects forming these binaries, BHs and NSs, and we provide an overview of their main features and how they affect the emitted GW signals.

1.3.1 Binary systems in the Newtonian framework

Let us approximate a binary as two point-like particles with mass m_1 and m_2 orbiting around each other in circular orbits, separated by a distance R , in a Newtonian framework. In the center-of-mass frame, assuming that the z -axis points towards the observer, and that the perpendicular to the orbit plane can be tilted with respect to \hat{z} by an angle ι , one can show that the position of the two objects is described by

$$\mathbf{x}_1(t) = \frac{\mu}{m_1} R \hat{\mathbf{e}}(t) \quad (1.61a)$$

$$\mathbf{x}_2(t) = -\frac{\mu}{m_2} R \hat{\mathbf{e}}(t), \quad (1.61b)$$

where $\mu = m_1 m_2 / (m_1 + m_2)$ is the reduced mass and $\hat{\mathbf{e}}(t)$ is a unit vector pointing from the center of mass to m_1

$$\hat{\mathbf{e}}(t) = (\cos(\omega_{\text{orb}} t), \cos(\iota) \sin(\omega_{\text{orb}} t), \sin(\iota) \sin(\omega_{\text{orb}} t)), \quad (1.62)$$

with ω_{orb} being the orbital angular frequency. The mass density is

$$\frac{T^{00}}{c^2} = m_1 \delta^3(\mathbf{x} - \mathbf{x}_1) + m_2 \delta^3(\mathbf{x} - \mathbf{x}_2), \quad (1.63)$$

and, computing the mass-quadrupole elements, from Eqs. 1.59a-1.59b we find

$$h_+ = -\frac{4}{r} \frac{G \mu R^2 \omega_{\text{orb}}^2}{c^4} \frac{1 + \cos^2(\iota)}{2} \cos(2\omega_{\text{orb}} t_{\text{ret}}) \quad (1.64a)$$

$$h_\times = -\frac{4}{r} \frac{G \mu R^2 \omega_{\text{orb}}^2}{c^4} \cos(\iota) \sin(2\omega_{\text{orb}} t_{\text{ret}}). \quad (1.64b)$$

From Kepler's third law

$$\omega_{\text{orb}}^2 = \frac{G (m_1 + m_2)}{R^3}, \quad (1.65)$$

therefore, defining the *chirp mass*

$$\mathcal{M}_c = \frac{(m_1 m_2)^{3/5}}{(m_1 + m_2)^{1/5}}, \quad (1.66)$$

we can rewrite Eqs. 1.64a-1.64b for the plus and cross polarizations as

$$h_+ = -\frac{4}{r} \left(\frac{G \mathcal{M}_c}{c^2} \right)^{5/3} \left(\frac{\omega_{\text{orb}}}{c} \right)^{2/3} \frac{1 + \cos^2(\iota)}{2} \cos(2\omega_{\text{orb}} t_{\text{ret}}) \quad (1.67a)$$

$$h_\times = -\frac{4}{r} \left(\frac{G \mathcal{M}_c}{c^2} \right)^{5/3} \left(\frac{\omega_{\text{orb}}}{c} \right)^{2/3} \cos(\iota) \sin(2\omega_{\text{orb}} t_{\text{ret}}). \quad (1.67b)$$

These expressions highlight some important aspects:

- To the leading order, i.e., for the quadrupolar mode, gravitational waves are emitted with a frequency that is twice the orbital one. This follows from the fact that the mass quadrupole is quadratic in $\hat{\mathbf{e}}$ and therefore remains the same when, after half an orbital period, $\hat{\mathbf{e}} \rightarrow -\hat{\mathbf{e}}$. Hence, the quadrupole moment period is half the orbital one, and the GW emission frequency is twice the orbital frequency.

- The masses of the objects in the binary enter the expression for h_+ and h_\times only through the \mathcal{M}_c combination.
- The inclination of the orbital plane with respect to the line of observation plays a crucial role in determining what we can measure. For example, for an edge-on orbit, i.e., with $\iota = 90^\circ$, the cross polarization h_\times becomes zero; on the other hand, for $\iota = 0^\circ$ or $\iota = 180^\circ$, the two polarizations are present with the same amplitude.

1.3.2 Inspiral of compact objects binaries

Until now, we assumed that the two objects follow a fixed Newtonian, circular orbit, ignoring the backreaction of gravitational waves onto the background spacetime. However, in reality, GWs carry energy and therefore contribute to the spacetime curvature. To take this into account, we cannot work anymore in the approximation of linearized gravity, which describes GWs as perturbations propagating on a flat background metric. If we expand the EFEs to the quadratic order, the quadratic corrections will describe the metric modifications induced by the linear order ones, i.e., the emitted GWs. In this second-order expansion, we can derive some “effective” EFEs that describe the average effect of GWs with an effective energy-momentum tensor $t_{\alpha\beta}$, which includes gravitational waves as an effective source of spacetime curvature. If we are studying GWs far away from the source, the TT gauge is valid, and, for a Minkowski background metric, we can write the GW radiated power, or *luminosity*, in terms of the h_+ and h_\times polarizations as

$$P_{\text{gw}} = \frac{dE_{\text{gw}}}{dt} = \frac{c^3 r^2}{16\pi G} \int d\Omega \left\langle \dot{h}_+^2 + \dot{h}_\times^2 \right\rangle, \quad (1.68)$$

with Ω being the solid angle. Substituting h_+ and h_\times with Eqs. 1.67a and 1.67b, and defining $\omega_{\text{gw}} = 2\omega_{\text{orb}}$ ², the radiated power can be rewritten as

$$\frac{dE_{\text{gw}}}{dt} = \frac{32}{5} \frac{c^5}{G} \left(\frac{G\mathcal{M}_c \omega_{\text{gw}}}{2c^3} \right)^{10/3}. \quad (1.69)$$

Therefore, the emission of GWs causes energy loss from the binary. The total energy of the binary system is the sum of its potential and kinetic energy

$$E = E_{\text{kin}} + E_{\text{pot}} = -\frac{Gm_1 m_2}{2R}. \quad (1.70)$$

In order for this energy to become more and more negative, as a consequence of the emission of GWs, the orbital radius R needs to decrease, and thus the orbit shrinks. However, if R decreases, from Kepler’s law (Eq. 1.65) we have that the frequency ω_{orb} increases, and, from Eq. 1.69, more power is radiated through GWs, so the binary’s energy and separation R decrease further, leading to an even larger ω_{orb} and so on, until R becomes so small that the two objects finally merge.

²We saw before that, for the quadrupolar mode, the frequency of the emitted gravitational waves is twice the orbital one.

In the adiabatic, or “quasi-circular motion”, regime, i.e., as long as the orbital velocity’s change over one period is small compared to the orbital velocity itself

$$\dot{\omega}_{\text{orb}} \ll \omega_{\text{orb}}^2, \quad (1.71)$$

orbits can still be approximated as circular and with a slowly-varying radius. Under this approximation, if we assume that the energy radiated by GWs corresponds to the energy lost by the system, we can equate the time derivative of energy in Eq. 1.70 to Eq. 1.69, and, using $f_{\text{gw}} = \omega_{\text{gw}}/2\pi$, we obtain

$$\dot{f}_{\text{gw}} = \frac{96}{5} \pi^{8/3} \left(\frac{G\mathcal{M}_c}{c^3} \right)^{5/3} f_{\text{gw}}^{11/3}. \quad (1.72)$$

Solving Eq. 1.72 leads to the following expression for the frequency of GWs:

$$f_{\text{gw}} = \frac{1}{\pi} \left(\frac{5}{256} \frac{1}{t - t_c} \right)^{3/8} \left(\frac{G\mathcal{M}_c}{c^3} \right)^{-5/8}, \quad (1.73)$$

with t_c being the *coalescence time*, i.e., the time at which f_{gw} diverges. In practice, we never witness the frequency reaching infinity, because when the two objects get close enough, they plunge one into the other. More specifically, in a fully relativistic derivation, one would find that there exists an *innermost stable circular orbit* (ISCO), a minimum value of the radial distance between the two objects after which, in the Schwarzschild geometry, stable circular orbits are no longer allowed. At this point, the adiabatic, quasi-circular motion approximation does not hold anymore. If $M = m_1 + m_2$ is the total mass of the binary, this distance is given by

$$R_{\text{ISCO}} = \frac{6MG}{c^2}, \quad (1.74)$$

and the GW frequency at ISCO is

$$f_{\text{gw,ISCO}} = \frac{c^3}{6^{3/2} \pi GM}. \quad (1.75)$$

After this point, the merger phase of the coalescence begins, but its description requires completely different tools. For example, since we are dealing with compact objects, at such short distances strong-field effects become important, and the flat-spacetime approximation for the background does not hold anymore.

Keeping our focus on the inspiral phase, Eq. 1.73 shows how the frequency increases with time, producing the *chirping effect* typical of compact binary coalescence (CBC) signals; an example of this effect is visible in the time-frequency map of GW170817 shown in Fig. 1.2. Another useful quantity to understand the current GW observations is the time T that a CBC signal spends in a frequency band $[f_{\min}, f_{\max}]$, which can be derived from Eq. 1.72 as

$$T \approx 2.18s \left(\frac{1.21M_{\odot}}{\mathcal{M}_c} \right)^{5/3} \left[\left(\frac{100\text{Hz}}{f_{\min}} \right)^{8/3} - \left(\frac{100\text{Hz}}{f_{\max}} \right)^{8/3} \right]. \quad (1.76)$$

The inverse dependence on \mathcal{M}_c shows clearly that lighter systems spend more time in band than heavier ones. Moreover, if we focus on the inspiral part and thus take $f_{\max} = f_{\text{gw,ISCO}}$, this difference is accentuated by the fact that heavier systems have a lower ISCO frequency (see Eq. 1.75). This is the reason why the binary neutron star signals we detect are longer than the binary black hole ones.

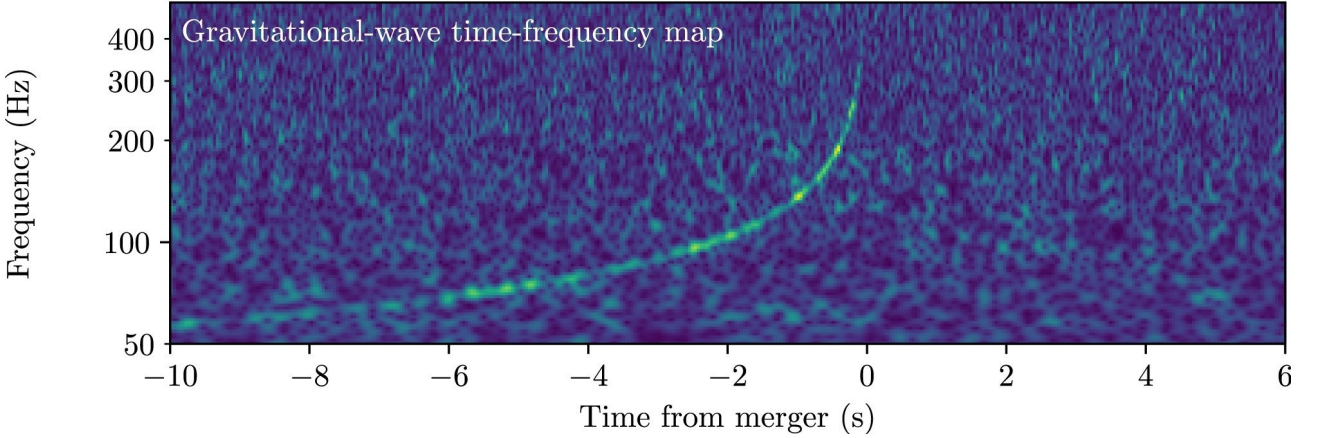


Figure 1.2: Time-frequency map for GW170817 in the LIGO detectors, where the color scale from blue to yellow means smaller to larger amplitude values, respectively. The GW signal with its chirping effect, i.e., its frequency increasing with time, is clearly visible. Figure from Ref. [12]

Finally, we can derive an expression for the waveform describing the inspiral GW emission in this adiabatic, Newtonian, and quadrupolar approximation. With respect to Eqs. 1.67a-1.67b, where the amplitudes of h_+ and h_\times , having R and ω_{orb} fixed, were constant, taking into account the GWs backreaction, and therefore the time evolution of $R(t)$ and $\omega_{\text{orb}}(t)$, means that the argument $(\omega_{\text{orb}} t_{\text{ret}})$ must be substituted by the phase $\Phi(t_{\text{ret}})$, whose time evolution is given by $\dot{\Phi}(t) = \omega_{\text{orb}}(t)$. The contributions related to \dot{R} can be neglected during inspiral, because of the adiabatic approximation. The inspiral waveform for the two polarizations therefore reads

$$h_+ = -\frac{4}{r} \left(\frac{GM_c}{c^2} \right)^{5/3} \left(\frac{\omega_{\text{orb}}(t_{\text{ret}})}{c} \right)^{2/3} \frac{1 + \cos^2(\iota)}{2} \cos(2\Phi(t_{\text{ret}})) \quad (1.77a)$$

$$h_\times = -\frac{4}{r} \left(\frac{GM_c}{c^2} \right)^{5/3} \left(\frac{\omega_{\text{orb}}(t_{\text{ret}})}{c} \right)^{2/3} \cos(\iota) \sin(2\Phi(t_{\text{ret}})), \quad (1.77b)$$

with

$$\Phi(t) = \left(\frac{c^3(t_c - t)}{5GM_c} \right)^{5/8} + \Phi_c, \quad (1.78)$$

where Φ_c is an integration constant, representing the phase at $t = t_c$.

1.3.3 Binary black holes

Most of the GW events detected until now [14, 36–38] originated from binary black hole systems. In this section, we discuss how we can use GWs to investigate the properties of these objects and to probe the theory of general relativity.

Current detectors can measure signals produced by binaries of stellar mass BHs, i.e., with a mass below $\sim 100M_\odot$. Studying the properties of these systems allows us to gather information about their population and hence about the physics processes behind their formation [39, 40]. The events detected so far already challenged our knowledge about this topic. The inferred mass distribution of BBH systems now includes more low-mass and unequal-mass binaries than the predictions by previous models. Moreover, the event GW190521 [17, 41] formed a remnant BH of roughly $140 M_\odot$, i.e., an

intermediate mass BH (IMBH). IMBHs are heavier than stellar BHs and lighter than supermassive ones, with a mass between 10^2 and $10^5 M_\odot$. Although there was indirect evidence of the existence of these objects, GW190521 provided the first direct observation. In addition, the mass of the heavier BH component in the binary was confidently estimated to lie in the so-called *pair-instability mass gap*. According to stellar evolution theory, if the core formed at the end of a star’s life has mass greater than a certain threshold value,³ an electron-positron pair production process initiates, which removes part of the radiation pressure supporting the star against gravitational collapse. As a consequence, the core starts contracting and it heats up, leading to a supernova explosion that blows the star away, leaving no compact remnant behind. This process is expected to prevent the formation via stellar evolution of BHs with masses between roughly 50 and $120 M_\odot$ [42, 43]. Despite the uncertainty about the precise limits of this gap, according to the current estimates the primary component of GW190521, with an estimated mass $m_1 \simeq 85 M_\odot$, could not be formed as the result of a stellar evolution process. This raises the question of how a system like the one that generated GW190521 is created.

There are two main formation channels predicted for binary systems of compact objects [44]:

- *Isolated binary evolution*: in a binary system of massive stars, both of them, at the end of their lives, become a compact object, thus creating a compact binary [45–53];
- *Dynamical capture*: formation of a binary by encounter and gravitational capture of two compact objects [54–62].

Since *dynamical capture* processes require dense environments, like globular clusters, they are expected to be less common than the formation by evolution of an isolated binary. However, this channel can lead to *hierarchical mergers*, in which two “light” BHs merge to form a heavier one, which can then merge again with another BH or NS. Such process could explain the formation of the primary component of GW190521 and offers also a sensible explanation for the formation of IMBHs. The way in which the binary is formed influences its properties and hence leaves an imprint in the emitted GW signal. Besides the components and remnant masses, the strongest signature is embedded in the spin [63], i.e., the rotation axis of the binary’s components, and in particular their orientation with respect to the axis of the orbit. If BHs spins are non-zero, they interact with the orbital angular momentum and with each other, causing visible effects in the emitted gravitational waves. While compact binaries formed by the evolution of isolated systems are expected to have spins aligned with the orbital angular momentum, compact binaries produced by dynamical capture can have spins pointing in random directions. The latter will cause precession of the orbital plane and the spin vectors themselves [64], causing phase and frequency modulations in the emitted GWs [65, 66]. Two effective spin parameters are usually employed to describe the spin of a BBH system: the *effective inspiral spin* [67, 68] and the *effective precessing spin* [66, 69]. The *effective inspiral spin* describes the spin aligned with the orbital angular momentum and is defined as a mass-weighted combination of the aligned component spins

$$\chi_{\text{eff}} = \frac{m_1 \chi_1 + m_2 \chi_2}{m_1 + m_2} \cdot \mathbf{L}, \quad (1.79)$$

³Pair instability supernovae are predicted to happen for core masses greater than $\sim 65 M_\odot$, but the exact threshold value is still subject to great uncertainty.

where \mathbf{L} is the instantaneous orbital angular momentum, m_i with $i = 1, 2$ are the component masses, and $\chi_i = c\mathbf{S}_i/(Gm_i^2)$, with \mathbf{S}_i being the spin angular momentum, represent the dimensionless component spins, which for BHs have values in the range $[0, 1]$. Measuring a non-zero value for χ_{eff} proves the presence of spin in the system, and its sign provides information about alignment or misalignment with respect to the orbital angular momentum.

On the other hand, the *effective precessing spin* describes the in-plane spin components, which cause the precession, and is defined as

$$\chi_p = \max \left[\chi_1 \sin(\theta_1), \left(\frac{3+4q}{4+3q} \right) q \chi_2 \sin(\theta_2) \right], \quad (1.80)$$

where $q = m_2/m_1$ is the *mass ratio*, and θ_i are the angles of \mathbf{S}_i with respect to the orbital angular momentum \mathbf{L} . A non-zero value of χ_p would indicate precession, providing evidence in support of formation via dynamical capture.

Until now, the analyses performed by the LVK collaboration do not show strong evidence of precession for a specific event. However, on a population level, the analyzed BBH systems show some misalignment of the spins with respect to the orbital angular momentum [39, 40].

General relativity provides precise predictions of the GW signal emitted by BBH systems during the full coalescence. Therefore, we can use GWs to perform tests of the theory of general relativity. Before the detection of GWs, general relativity could be tested only in the weak-field regime, for example from the precession of Mercury perihelion, or the orbit decay of binary pulsars due to the emission of GWs. However, gravitational-wave signals from CBCs allow us to probe GR in the strong-field regime, because of the short distance between the two objects and the relativistic speeds they reach at the end of the inspiral.

A wide range of GR tests are currently performed [20–22], e.g., to probe the consistency between data and GR predictions from our waveforms, but also the no-hair theorem [70, 71] and the properties of the remnant. Some other analyses investigate the propagation of GWs, looking for potential evidence of dispersion and putting constraints on the graviton mass, or try to measure possible deviations from the values of post-Newtonian coefficients (which will be discussed in detail in Sec. 2.1.2) predicted by GR. One can also look for the presence of polarizations different from the two tensor modes that we label as *plus* and *cross*. Finally, some analyses inquire the nature of the compact objects involved in the merger, which might not be general-relativistic BHs, for example by measuring the spin-induced quadrupole moment. Furthermore, *exotic compact objects*, including fuzzballs, gravastars, bosons stars, and other objects described by exotic physics, all have in common the lack of an horizon, which leads to the emission of gravitational waves echoes; finding evidence of GW echoes would be a smoking-gun pointing to the existence of such objects.

Until now, no evidence for deviations from GR has been found, but there is an ongoing effort to develop new analyses and improve the current ones. Deviations from GR like the ones listed above produce deviations in the GW signal from what we would expect in GR, and hence we can measure these effects in different ways. However, multiple kinds of systematics can mimic deviations of GR, therefore a very accurate modeling of the waveforms is required.

1.3.4 Binary neutron stars

Neutron stars are formed by the collapse of massive stellar cores and are supported against gravitational collapse by the pressure of degenerate neutrons. NSs typically have masses between 1 and 3 M_\odot and radii of the order of 10 km, hence the matter inside NSs reaches extremely high densities, up to 3-4 times the nuclear saturation density $\rho_0 \sim 2.7 \times 10^{14} \text{ g/cm}^3$. Therefore, neutron stars offer a unique tool to study the equation of state of supranuclear-dense matter, considering that such density conditions cannot be reproduced in laboratory experiments. Until a few years ago, the study of NSs was limited to electromagnetic observations, but gravitational waves now offer a new channel to investigate these objects. Up to now, two events generated by the coalescence of BNS systems have been detected: GW170817 [72] and GW190425 [18]. GW170817 was a very loud event and allowed already to place some constraints on the equation of state [73, 74]. In this section, we first introduce how NSs are described in GR and the equation of state that describes their matter. We then turn to BNS systems, focusing on the properties that can be measured from GW signals. Finally, we discuss the importance of the postmerger phase and we introduce the concept of quasi-universal relations.

Equation of state

The gravitational field of isolated, non-rotating NSs is described by a static, spherically-symmetric metric. Their matter can be modeled as a perfect fluid, described by the energy-momentum tensor

$$T^{\mu\nu} = (\rho + P)u^\mu u^\nu + Pg^{\mu\nu}, \quad (1.81)$$

where ρ is the total energy density, P the pressure, and u^μ the four-velocity $u^\mu = dx^\mu/d\tau$.

From the EFEs one can derive the hydrostatic equilibrium equations for a perfect fluid, which describe the structure of NSs: the Tolman-Oppenheimer-Volkov (TOV) equations [75, 76]

$$\frac{dm(r)}{dr} = 4\pi r^2 \rho(r) \quad (1.82a)$$

$$\frac{dP}{dr} = -\frac{Gm(r)\rho(r)}{r^2} \left(1 + \frac{P}{c^2\rho(r)}\right) \left(1 + \frac{4\pi r^3 P}{m(r)c^2}\right) \left(1 - \frac{2Gm(r)}{c^2 r}\right)^{-1}, \quad (1.82b)$$

with r being the coordinate radius. In Eq. 1.82b, the first term represents the Newtonian equation for hydrostatic equilibrium, while the other ones are relativistic corrections generated by the metric.

In order to solve these equations and find the functions $\rho(r)$, $P(r)$ and $m(r)$, we need some information about the matter inside NSs. Such information is encoded in the *equation of state* (EOS) $P(\rho)$. With an EOS and some boundary conditions, usually chosen as $P(R) = 0$ and $P(0) = p_c$, with p_c being the central pressure and $r = R$ corresponding to the NS's surface, one can solve the TOV equations, obtaining the functions $m(r, \rho_c)$ and $P(r, \rho_c)$, which depend parametrically on the central density ρ_c and determine all the macroscopic properties of the NS, such as its mass and radius. Finding the “true” EOS describing the extremely dense matter inside NSs remains one of the most important open questions in physics. During the inspiral phase of a BNS coalescence we can assume NSs’ matter to be “cold”, i.e., with a temperature $T = 0$, because the thermal effects are negligible for the structure, composition, and pressure of the NSs. For cold NSs, in principle, all we need to construct the EOS is the density of baryons in the core. However, deriving the EOS is not an easy

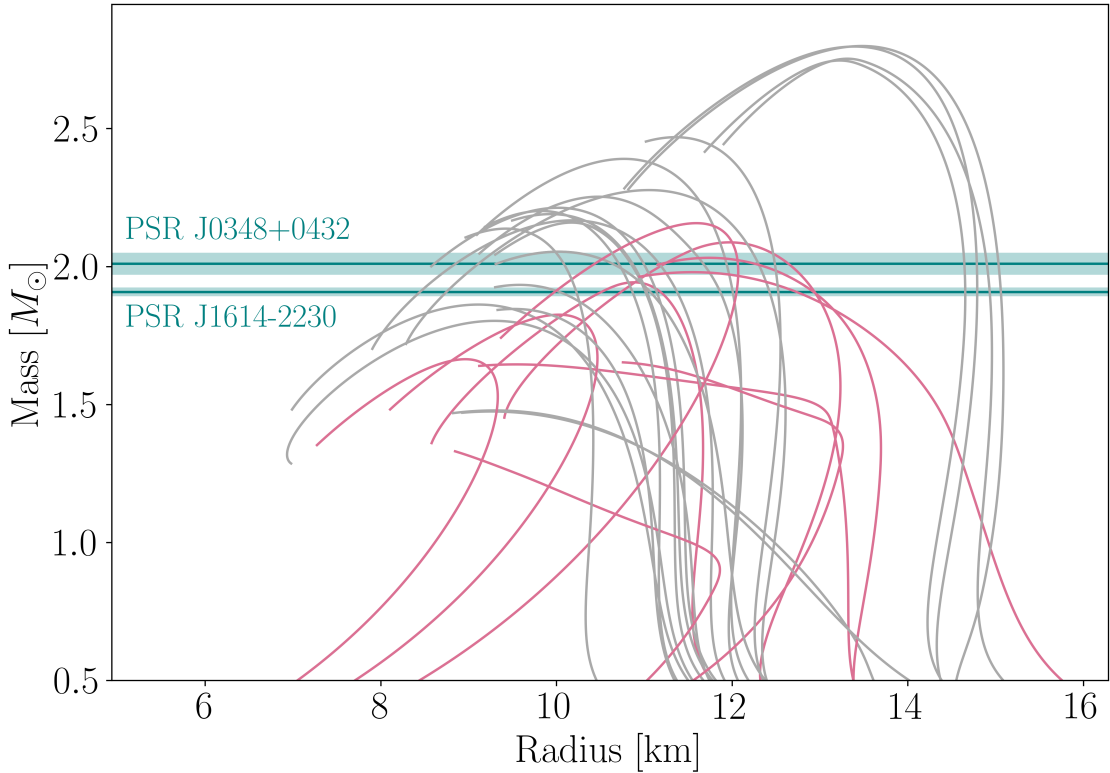


Figure 1.3: Mass-radius profiles for different EOSs included in the LIGO Algorithms Library (LAL) software suite [77]. The pink lines represent EOS with *not* pure nucleonic matter, for example including mesons, hyperons or quark matter. The green horizontal lines show the mass of the two heaviest pulsars observed so far, PSR J0348 + 0432 [78] and PSR J1614 – 2230 [79], together with their $1-\sigma$ uncertainty.

task, since one needs to take into account many-body effects, and nucleon-nucleon interactions must be described with the strong interaction, which is still not completely understood. The different ways in which one can deal with these two aspects lead to different predictions for the EOS. Moreover, the possible presence of phase transitions and hyperons, quarks or strange matter adds a further level of uncertainty. The various EOSs translate into different mass-radius profiles for the NSs, as shown in Fig. 1.3, and therefore constraining these parameters through GW signals helps constraining the EOS. Finally, the EOS determines also what is the maximum mass that can be supported by the TOV equations,⁴ M_{TOV} . Therefore, also the precise mass measurements for pulsars contribute to constraining the EOS, by providing a lower limit for the maximum mass that a physically-meaningful EOS must reach.

⁴The maximum TOV mass corresponds to the point where, in the mass-radius function, the stable, rising branch starts decreasing, hence becoming unstable.

Tidal deformability

The coalescence of a BNS system happens very similarly to a BBH one. The key difference is the presence of matter. During a BNS coalescence, the matter of one NS is deformed by the tidal field produced by the other one. Such effect is described with a quadrupole moment Q_{ij} , which, switching for simplicity to geometric units, i.e., setting $c = G = 1$, is written as

$$Q_{ij} = -\lambda \mathcal{E}_{ij} = -\Lambda m^5 \mathcal{E}_{ij}, \quad (1.83)$$

where m is the NS mass, \mathcal{E}_{ij} the tidal field experienced by the NS, and Λ is called *tidal deformability*. The tidal deformability parameter is defined by the NS's properties as

$$\Lambda = \frac{2}{3} k_2 \left(\frac{R}{m} \right)^5, \quad (1.84)$$

where k_2 is the tidal Love number and R the NS's radius, thus Λ depends on the EOS. In geometric units, Λ is a dimensionless quantity.

The macroscopic properties, determined by the EOS, of the NSs in a binary system leave an imprint in the GW signal emitted during the coalescence. Therefore, studying these GW signals unravels information about the EOS of NSs' matter. The mass and tidal deformability parameters influence the gravitational waveform already during the inspiral, and therefore we can try to estimate them. However, while the chirp mass can be recovered with a high precision, the effect of Λ is less strong and enters the waveform only around a few hundreds Hz, making it more complicated to obtain precise measurements for this parameter. For GW170817, the measured properties of the progenitor system ruled out large values of the tidal deformability parameter [73], hence showing evidence disfavoring the stiffest EOSs. In the future, the increased detectors sensitivity will allow us to place tighter and tighter constraints on the m - Λ relation and, consequently, on the EOS.

Postmerger

After the merger, the fate of the BNS system is determined by its mass and EOS, depending on which the binary can:

- Promptly collapse to a BH.
- Form a *hyper-massive NS*, which, thanks to differential rotation, can have mass larger than M_{TOV} , and survives for a few ms before collapsing to a BH.
- Form a *supra-massive NS* that can survive up to a roughly an hour before collapsing to a BH, if the baryonic mass is less than the limit supported by a rigid rotating NS.
- Produce a stable NS.

In the case of formation of a NS remnant, a GW signal is emitted also during the postmerger phase, carrying a wealth of information about the EOS. While, during the inspiral, NSs' matter could

be described by a cold EOS, in the postmerger temperatures up to 50-100 MeV ⁵ can be reached, and therefore one needs to take into account the non-zero temperature corrections to the EOS. The postmerger GW signal usually includes a main emission peak, commonly denoted as f_2 or f_{peak} , related to quadrupole oscillations in the matter fluid, plus multiple subdominant peaks produced by various processes [80–82]. The complicated spectra of the postmerger GW emission are strongly influenced by the EOS, therefore analyzing these signals helps gathering information about the EOS in a different density and temperature regime with respect to the inspiral. In addition, the even higher densities reached in this phase can lead to phase transitions, which might also leave an imprint in the GW signal.

Quasi-universal relations

Modeling NSs and their emission is complicated by the fact that NS properties depend on the EOS, which we do not know, and different EOS models lead to very different properties and predictions. However, *quasi-universal* relations have been found between different NS parameters or features of the emitted GW spectrum, which approximately do not depend on the EOS, and can therefore be used for a more general description and analysis, also if the EOS is not known. These quasi-universal relations are usually calibrated to numerical relativity waveforms (see Sec. 2.1.1). One of the first examples of such relations is the “I-Love-Q” relation [83] between the NSs’ moment of inertia, their Love numbers and the spin-induced quadrupole moment. Various relations have been discovered between different NSs’ properties [84–89] and in relation to the emitted GW spectrum [90–94].

Quasi-universal relations are widely employed also in the study of postmerger signals [80,82,95–105] to link the features in the emitted GW spectrum, such as the frequency of the dominant peak, to some parameters of the binary system.

1.4 Detection

In this section we focus on GWs detection, discussing the basics of laser interferometers, the main sources of noise affecting the measurement, and how we model them. We review how GW signals are extracted from noise and we finally provide an overview of existing and planned detectors.

1.4.1 Interferometers

We saw in Sec. 1.2.2 that the effect of GWs is to periodically stretch and compress space in perpendicular directions. A well-suited instrument to measure such effect is a Michelson interferometer, with two orthogonal arms. The basic layout is shown in Fig. 1.4: a laser is shone into a beam splitter, which reflects 50% of the laser beam into one arm and transmits 50% into the other one. The beams are then reflected back by two mirrors placed at the end of each arm and recombine at the beam splitter. Part of the recombined laser goes to the output photodiode, while part is fed back to the system. In the system at rest, i.e., in absence of GWs, the two beams, when they recombine at the beam splitter,

⁵Temperature can be expressed in units of energy by conversion through the Boltzmann constant k_B , so that $1\text{K} = \simeq 8.62 \times 10^{-5}\text{eV}$ and $1\text{MeV} \simeq 1.16 \times 10^{10}\text{K}$.

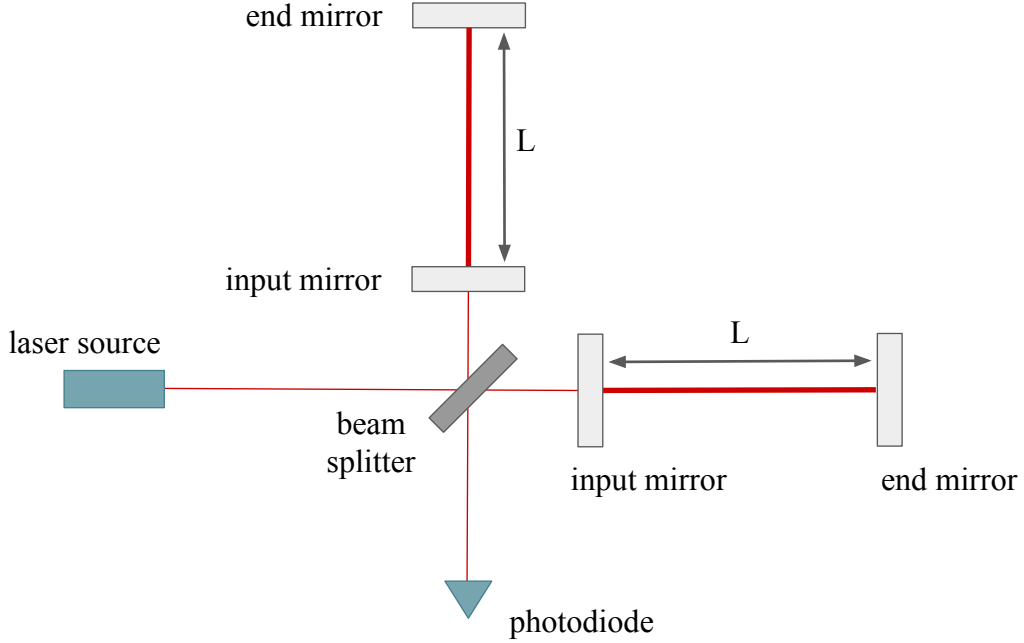


Figure 1.4: Schematic representation of a laser interferometer used to detect GWs.

interfere destructively. A GW will cause a change in the interferometer's arm length, hence producing a variation in the interference at the output. More specifically, if we write the electric field of the input laser as

$$E_{\text{laser}} = E_0 e^{-i\omega_L t - i\mathbf{k}_L \cdot \mathbf{x}}, \quad (1.85)$$

with ω_L and \mathbf{k}_L being the laser frequency and wavenumber, respectively, the total electric field after recombination at the beam splitter is [106]

$$E_{\text{out}} = -iE_0 e^{-i\omega_L t + ik_L(L_1 + L_2)} \sin[k_L(L_1 - L_2)], \quad (1.86)$$

where L_1 and L_2 are the lengths of the two arms, and the power measured at the output is proportional to

$$|E_{\text{out}}|^2 = E_0^2 \sin^2[k_L(L_1 - L_2)]. \quad (1.87)$$

Therefore, a change in arm length induced by a GW causes a variation in the detector output power.

In general, an interferometer is sensitive to the *gravitational-wave strain*, defined as

$$h(t) = \frac{\delta L}{L}, \quad (1.88)$$

with L the arm length in absence of GWs.

The strain $h(t)$ is the effect of GWs as seen by the interferometer, and we need to trace it back to the actual metric perturbations that we want to measure. The strain depends on the geometry of the detector and is related to the metric perturbations arriving at the interferometer h_{ij}^{det} through the *detector tensor* D^{ij}

$$h(t) = D^{ij} h_{ij}^{\text{det}}(t). \quad (1.89)$$

In most of the derivations reported up to now, we assumed that GWs are traveling in the \hat{z} direction. However, in general, they can propagate along any arbitrary direction, and the signal arriving at the detector h_{ij}^{det} does not usually correspond to h_+ , h_\times . In order to write the general strain in terms of h_+ and h_\times , we consider a new coordinate system (x', y', z') in which the GW propagates along \hat{z}' . With respect to the (x, y, z) frame, the direction of the z' -axis is given by two polar angles (θ, ϕ) . Moreover, once we have the direction of the z' -axis, we need to fix the (x', y') coordinate system in which the h_{ij} components correspond to h_+ and h_\times ; this is done by choosing a specific rotation angle ψ on the plane perpendicular to \hat{z}' , called *polarization angle*. The transformation from (x, y, z) to (x', y', z') can be described by the rotation matrix \mathcal{R}_{ik} , such that

$$h_{ij}^{\text{det}} = \mathcal{R}_{ik}\mathcal{R}_{jl}h_{kl}, \quad (1.90)$$

where h_{kl} is computed for the direction of propagation along \hat{z} .

Finally, the strain can be written in terms of the cross and plus polarizations as

$$h(t) = D^{ij}\mathcal{R}_{ik}\mathcal{R}_{jl}h_{kl} = h_+(t)F_+(\theta, \phi, \psi) + h_\times(t)F_\times(\theta, \phi, \psi), \quad (1.91)$$

where $F_+(\theta, \phi, \psi)$ and $F_\times(\theta, \phi, \psi)$ are called *antenna* or *beam pattern functions*. These functions include all the angular information about the signal and they depend on the detector geometry. Their value essentially contains information about how sensitive a given detector is to a GW coming from a direction (θ, ϕ) and with a polarization angle ψ . Every detector has blind spots, i.e., sky locations from where GWs cannot be detected. For example, a GW arriving from a direction perpendicular to the bisector of the detector will stretch and compress the two arms by the same amount, therefore the strain h will be zero. Therefore, one of the advantages of building a network of detectors with different orientations is that one detector can cover the blind spots of another one.

In reality, GW detectors are not simple Michelson interferometers. They must be sensitive to a strain $h \sim 10^{-21}$ or smaller, therefore more sophisticated instruments are needed. For example, as appears from Eq. 1.88, to reduce the strain h to which the detector is sensitive, one can increase the interferometer's arm length. Current detectors have an arm length of 3-4 km, but the effective arm length is increased to hundreds of km by implementing a Fabri-Perot cavity along the arms, between the “input” and “end” mirrors in Fig. 1.4. A review of GW interferometers instrumentation and techniques can be found in Ref. [107].

1.4.2 Noise characterization

The signal measured by a GW detector is not the “pure” strain $h(t)$, but it is contaminated by different kinds of noise. In general, the output signal of a detector is a time series $s(t)$ and can be written as

$$s(t) = h(t) + n(t), \quad (1.92)$$

where $n(t)$ represents the combined noise from all the various sources. Different kinds of noise affect GW interferometers, for example:

- *Gravity gradient noise*: gravitational coupling of the mirrors with moving massive bodies near the detector and mass density fluctuations of the air or earth surrounding it. Since the gravitational force cannot be shielded, gravity gradient creates a “wall” of noise that prevents current detectors from measuring anything below 10 Hz [108, 109].
- *Seismic noise*: mechanical vibrations, both of anthropogenic and natural origin, which cause a displacement of the mirrors; a system of attenuators is employed to reduce this kind of noise.
- *Thermal noise*: vibrations of mirrors or suspensions induced by the thermal movement of particles.
- *Quantum noise*: related to the wave-particle nature of light, it involves two effects; *quantum shot noise*, caused by the uncertainty in the number of photons measured as output, and *radiation pressure noise*, i.e., the mirror displacement generated by the fluctuating pressure of the momentum carried by photons. Increasing the laser power would help reducing the shot noise contribution, but at the same time radiation pressure noise is reduced by employing a low-power laser. Current detectors try to find a balance between these two conditions, slightly favoring the low-frequency part of the spectrum, where CBC signals spend more time in band.

Various technological solutions allow us to reduce the different kinds of noise. Moreover, if we know how to model it, noise caused by specific effects can be directly subtracted from the data. More details about the noise in GW detectors and related solutions can be found in Ref. [110–112].

Understanding the properties of the interferometers’ noise is crucial in order to detect and analyze GW data. The noise in GW detectors $n(t)$ is modeled as a stochastic Gaussian and stationary process:⁶ the noise generated by the system of the detector at different times produces different *noise realizations*, whose probability can be described by a Gaussian function, and time shifts do not change the noise statistical properties. Stationary Gaussian processes are described only by their average value $\langle n(t) \rangle$, which can be set to zero without loss of generality, and by their autocorrelation function

$$C(\tau) \equiv \langle n(t + \tau) n(t) \rangle, \quad (1.93)$$

which describes the correlation of noise realizations separated by a time interval τ .

In frequency domain, stationarity implies that the noise Fourier components are uncorrelated

$$\langle \tilde{n}^*(f) \tilde{n}(f') \rangle = \delta(f - f') S_n^{(2)}(f). \quad (1.94)$$

In Eq. 1.94, $S_n^{(2)}(f)$ is the *power spectral density*, which can be defined as the Fourier transform of the correlation function

$$S_n^{(2)}(f) \equiv \int_{-\infty}^{+\infty} C(\tau) e^{i 2\pi f \tau} d\tau. \quad (1.95)$$

⁶Noise modeling algorithms like the one introduced in Ref. [113] take into account also possible non-stationary features of the noise. Moreover, a considerable effort is invested into the characterization and subtraction of *glitches*, bursts of excess noise caused by different instrumental artifacts, which can mimic GW signals or overlap with them, complicating their detection and analysis [114–118].

More specifically, Eq. 1.95 defines the *two-sided power spectral density*; however, invariance under time translation implies that $C(-\tau) = \langle n(t - \tau)n(t) \rangle = \langle n(t)n(t + \tau) \rangle = C(\tau)$, and consequently $S_n(-f) = S_n(f)$. Therefore, the integral over all frequencies can be substituted by an integral over positive frequencies only and we can define the *one-sided power spectral density* (PSD)

$$\frac{1}{2}S_n(f) = S_n^{(2)}(f), \quad (1.96)$$

which is usually employed in GW science, since the use of positive frequencies only is physically justified. From a physics point of view, Eq. 1.94 means that, in frequency domain, the noise in different frequency bins is uncorrelated and in each bin $\tilde{n}(f)$ follows a Gaussian distribution with amplitude $\sqrt{S_n^{(2)}(f)}$.

The PSD has units of $1/\text{Hz}$, and detector sensitivities are typically characterized by its square root, the amplitude spectral density (ASD), with units of $1/\sqrt{\text{Hz}}$. As an example, the pink, blue and orange lines in Fig. 1.5 show the Advanced LIGO and Advanced Virgo sensitivities during O3.

1.4.3 Extracting signals from noise

In order to detect a GW signal, we need to somehow extract $h(t)$ in Eq. 1.92 from the detector output $s(t)$ that includes noise. As we saw in the previous section, different noise sources influence the detectors' output, and usually the strain induced by GWs is smaller than the noise contribution. However, if we have a model for $h(t)$, we can multiply it by the data $s(t)$ and take the time average over the observation time T

$$\frac{1}{T} \int_0^T dt s(t)h(t) = \frac{1}{T} \int_0^T dt h^2(t) + \frac{1}{T} \int_0^T dt n(t)h(t). \quad (1.97)$$

In Eq. 1.97, the first term is definite-positive, while the second one represents a random walk process. Hence, they can be approximated as

$$\frac{1}{T} \int_0^T dt h^2(t) + \frac{1}{T} \int_0^T dt n(t)h(t) \sim h_0^2 + \left(\frac{\tau_0}{T}\right)^{1/2} n_0 h_0, \quad (1.98)$$

with h_0 and n_0 the characteristic amplitude of the signal and noise respectively, and τ_0 the variation timescale of $h(t)$. Ideally, Eq. 1.98 implies that for $T \rightarrow \infty$ the noise contribution can be completely filtered out. In reality, our observation time, and the GW signals themselves, have a finite duration. However, Eq. 1.98 shows that, in general, with this *matched filtering* technique, we do not need $h_0 > n_0$ to detect a signal, but just

$$h_0 > \sqrt{\frac{\tau_0}{T}} n_0. \quad (1.99)$$

The factor $\sqrt{\tau_0/T}$ can be of the order $\mathcal{O}(10^{-2})$ for typical BBH signals, but also $\mathcal{O}(10^{-5})$ for continuous ones.

Matched filtering searches are improved by applying a filter $K(t)$ to the data

$$\hat{s} \equiv \int_{-\infty}^{\infty} dt s(t)K(t) = \int_{-\infty}^{\infty} df \tilde{s}(f)\tilde{K}^*(f), \quad (1.100)$$

with $\tilde{s}(f)$ the Fourier transform of $s(t)$, and $*$ denoting the complex conjugate. We can then define the *signal-to-noise ratio* (SNR) as the ratio between the mean value $\langle \hat{s} \rangle$ when a signal $h(t)$ is present and

the root mean square $\langle \hat{s}^2 \rangle^{1/2}$ when there is no GW signal in the data. Writing these two quantities explicitly in the Fourier domain, one finds that the signal-to-noise ratio ρ reads [106]

$$\rho = \frac{\langle h|\hat{K} \rangle}{\sqrt{\langle \hat{K}|\hat{K} \rangle}}, \quad (1.101)$$

where $\hat{K}(f) \equiv \frac{1}{2}S_n(f)\tilde{K}(f)$ and the noise-weighted inner product $\langle a|b \rangle$ is defined as

$$\langle a|b \rangle \equiv 4\Re \int_{f_{\text{low}}}^{f_{\text{high}}} \frac{\tilde{a}^*(f)\tilde{b}(f)}{S_n(f)} df, \quad (1.102)$$

with $S_n(f)$ being the noise spectral density. The optimal filter, for which ρ is maximum when a GW signal is present and minimum where the data consist of noise only, is

$$\tilde{K}(f) \propto \frac{\tilde{h}(f)}{S_n(f)}, \quad (1.103)$$

which gives the *optimal signal-to-noise ratio*

$$\rho_{\text{opt}} = \sqrt{\langle h|h \rangle}. \quad (1.104)$$

A GW signal is usually observed by multiple detectors, each one with a SNR determined by its antenna pattern. The information coming from multiple detectors can be combined, and, in general, the significance of an event is given by the *network signal to noise ratio*

$$\rho_{\text{net}} = \sqrt{\sum_{i=1}^N \rho_i^2}, \quad (1.105)$$

with ρ_i being the SNR of the single detector and N the total number of detectors.

Although very powerful, this approach requires a model for the GW signal $h(t)$, which strongly depends on the parameters of the sources. Therefore, matched-filter searches need *template banks* of many GW waveforms for possible different sources. The LVK collaboration relies on multiple pipelines for this kind of searches: PyCBC [119], MBTA [120], and GstLAL [121].

Without going into details, we mention here that also model-independent search methods have been developed, for example the cWB pipeline [122, 123]. These searches typically require only coherent response between the detectors: GW signals are expected to show, with a given time delay, in all the operating detectors, while spurious signals, like glitches, usually happen in a single detector with no correlation with the other ones. One of the main advantages of model-independent searches is that they do not rely on template banks, which are highly computationally expensive to build, especially for CBC signals generated by low-mass binaries. Moreover, if different factors are taken into account, like precession or eccentricity, the number of required templates increases. One must also consider the possibility of signals for which we do not have yet good models, like bursts from supernovae explosions, and which therefore cannot be detected with the approach described above.

Identification of events

The SNR of a candidate event basically tells us how strong the signal is compared to noise, therefore the higher the SNR, the larger the probability that we are dealing with a GW event. A SNR above a minimum value, usually between 4 and 8, means that the data are likely to contain a GW signal. However, also noise fluctuations, due to instrumental or environmental sources, might cause high SNR values, even though a GW signal is not present. Therefore, in order to assess the significance of a candidate event, the SNR distribution of the noise must be evaluated first. This is accomplished by computing a background distribution of the noise SNR, considering segments of detector data where we are sure that no GW signal is present. Since a passing GW is expected to be seen in all the detectors, unless its sky location corresponds to a blind spot of one of them, while noise artifacts should not be correlated between detectors, one condition to claim the presence of a GW signal is usually to have a detection in more than one instrument, with a time difference compatible with the travel time of the GW. To estimate the background SNR distribution, time segments in different detectors, with different artificial time shifts, are usually employed. The triggers from the background noise are then ranked according to their SNR.⁷ Once we have this background distribution, for each candidate event, we compute the false alarm rate probability, i.e., the probability of obtaining a SNR equal or larger than the one of the candidate event just from the background fluctuations. Dividing the false alarm probability by the total time of observation used to compute the background distribution, we obtain the false alarm rate (FAR), which defines the significance of a detection. Choosing a threshold on the FAR means deciding how many “errors”, intended as detections that in reality are just noise artifacts, we consider acceptable. For example, in GWTC-3, the threshold on FAR to consider an event significant was set to 2.0 yr^{-1} [14]. Setting a threshold on the FAR corresponds to set a threshold on the ranking statistics used to compute it. For example, during O3, public alerts for potential CBC events were released for events with $\text{FAR} > 1/(2 \text{ months})$, roughly corresponding to a SNR of 8.5 [124].

1.4.4 Existing and planned detectors

Currently, there exist four operating ground-based interferometers:⁸ two Advanced LIGO [111] instruments (both in the United States, one in Hanford and one in Livingston), Advanced Virgo [112] in Italy, and KAGRA [125–127] in Japan. Another LIGO detector is being built in India [128] and is supposed to become operational in a few years.

From the first observing run O1, various technological improvements have been implemented in the Advanced LIGO and Advanced Virgo detectors; the increased sensitivity is clearly proven by the rise in the number of detections, which went from the 11 detections of O1 and O2 together to the 74 of O3. However, the sensitivity can be further increased, but some of the required technological

⁷Here we are assuming that the optimal combined SNR is used as ranking statistics. Although this might be a good choice for purely Gaussian and stationary noise, real detectors’ noise is affected by glitches and transients of different nature. Therefore, in reality, search pipelines usually employ more sophisticated ranking statistics. An overview of how the different pipelines find candidate triggers and identify events can be found in Appendix D of Ref. [14].

⁸There exist another ground-based interferometer in Germany, GEO600, with a 600 m arm length, which is however used only to develop and test new technologies.

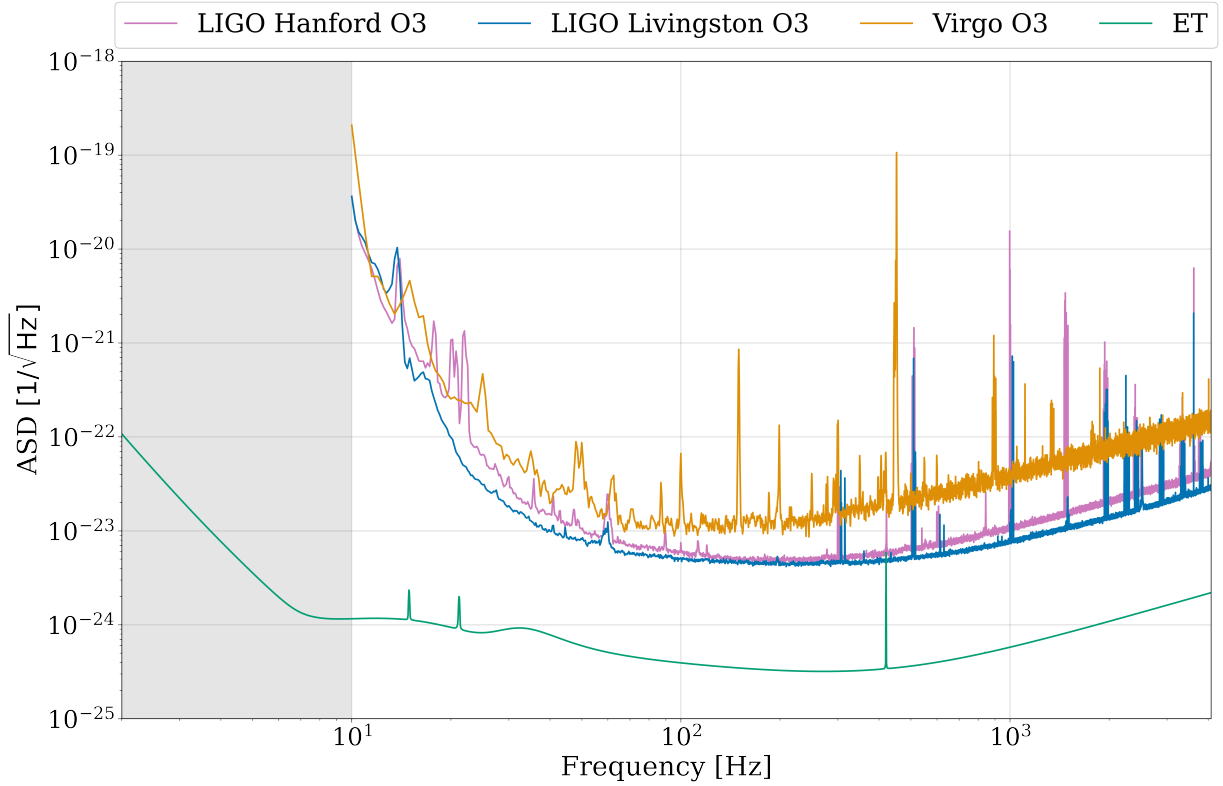


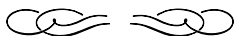
Figure 1.5: Example of ASD curves for different detectors. The pink, blue and orange lines show, respectively, the average sensitivity of LIGO Hanford, LIGO Livingston and Virgo during O3, while the green line represents the expected ASD for ET. The gray area indicates the frequency band dominated by gravity gradient noise for current detectors. The construction of ET underground will reduce this source of noise, thus allowing to gain sensitivity down to a few Hz.

improvements necessitate the construction of new detector sites. For the upcoming years, a new generation of detectors is planned [129]. Up to now, two of such *third-generation* (3G) detectors have been proposed: the Einstein Telescope (ET) [130–135] in Europe and the Cosmic Explorer (CE) [136–139] in the United States. One key improvement in both cases will be the increased arm length. While CE is currently planned to include one or two L-shaped interferometers, with 20 and 40 km arm length, for ET also a different design has been proposed: a triangular detector effectively composed of three interferometers, each one with an opening angle of 60 degrees between the arms. Specific studies have been performed in order to understand how the different proposed designs could affect various science cases [140].

One of the key improvements for ET is going to be an increased sensitivity below 10 Hz, which will be achieved by placing the detector underground, thus reducing the gravity gradient noise (see Fig. 1.5). Moreover, ET is expected to include a xylophone configuration [133], essential to reduce the contributions of quantum noise over the whole frequency band: each detector will be actually composed by two interferometers, one operating a high-power laser, which will increase sensitivity at high frequencies, and one with a low-power laser, and potentially operating at cryogenic temperatures, which improves sensitivity at low frequencies.

Finally, the construction of another detector has been proposed, built specifically to obtain a high sensitivity in the kilohertz band, where the merger and postmerger part of the GW signal emitted by BNS systems usually lies. This detector, called Neutron Star Extreme Matter Observatory [141], or NEMO, would be built in Australia as an L-shaped interferometer with 4 km arm length. Although its construction has not been approved yet, it is expected to have a large impact on the study of BNS systems.

Chapter 2



Data analysis tools

This chapter provides an overview of the models, the statistical and computational tools employed in gravitational-wave data analysis. The first section concerns the waveform templates used both in matched-filtering searches and in the subsequent analyses of the event. We then review Bayesian inference, focusing on its application to parameter estimation analyses, and finally we introduce the main sampling algorithms employed. Moreover, since GW analyses are computationally expensive, we need to find ways to reduce their computational cost: in the last part of this chapter, we discuss two of such techniques, relative binning and reduced order quadratures.

2.1 Waveforms

Accurate predictions of the gravitational waveforms emitted by CBC systems play a crucial role not only in the signal detection, as we saw in Sec. 1.4.3 regarding matched filtering, but also for the follow-up analyses that aim to recover the parameters and properties of the sources. In order to find the exact waveform of the gravitational signal, one needs to solve the Einstein field equations in Eq. 1.13, which, unfortunately, cannot be accomplished analytically. Different methods have been developed to compute theoretical models of the gravitational signal emitted during the different phases of the binary system coalescence (see Fig. 2.1): the inspiral part can be modeled through the post-Newtonian or the effective-one-body approximations; during the late inspiral and merger, when the strong-field effects become important, the full EFEs must be solved numerically, by means of *numerical relativity* (NR) simulations; after the merger, the ringdown phase of BBH systems is described via *black hole perturbation theory*, while the postmerger phase of BNS systems again requires full NR solutions. The different approximations and methods employed to compute the waveform lead to the construction of multiple families of waveform approximants. This section provides an overview of how the different waveform models are built, focusing on two models that will constitute the starting point for part of the work presented in this thesis, `IMRPhenomXPHM` and `IMRPhenomD_NRTidalv2`. At the end of the section, Table 2.1 provides a summary of the approximant families discussed.

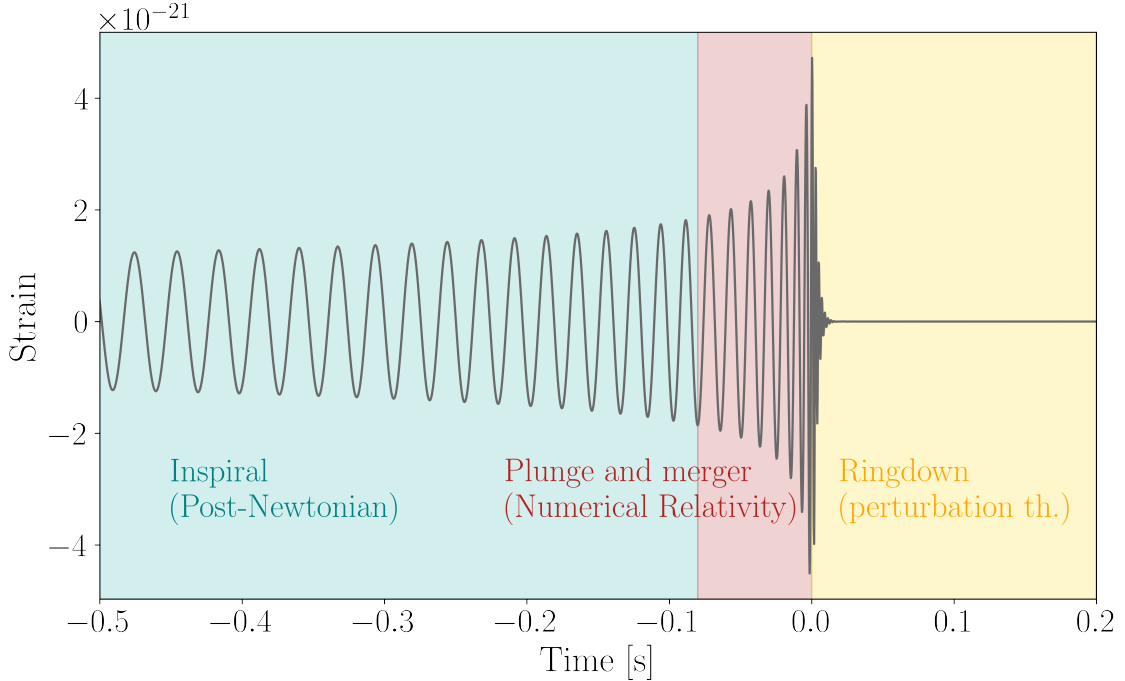


Figure 2.1: Example of a gravitational waveform emitted by a non-spinning binary black hole system with $m_1 = 20 M_\odot$, $m_2 = 18 M_\odot$, and at a distance of 100 Mpc, zoomed around the merger. The colors show approximately the different regimes, in which different techniques are needed to compute the waveform.

2.1.1 Numerical Relativity

Since it is not possible to find analytical solutions of the Einstein Field equations

$$R_{\alpha\beta} - \frac{1}{2}Rg_{\alpha\beta} = \frac{8\pi G}{c^4}T_{\alpha\beta}, \quad (2.1)$$

they must be solved numerically. Building numerical codes to evolve the spacetime around coalescing binary systems represented a great challenge for many years, until some breakthrough studies [142–144] allowed to develop techniques to successfully simulate the coalescence of compact binaries (see, e.g., Ref. [145] for a review). In order to perform the required numerical integrations, spacetime coordinates are quantized into a grid. Additionally, the “3 + 1” formulation allows to separate the time and space evolution of the equations by foliating the spacetime into a sequence of space-like surfaces at a constant time. Today, different codes to perform NR simulations are available, for both BBH and BNS systems: BAM [146–149], THC [150], LazEv [151], the Spectral Einstein Code (SpEC) [152], Whisky [153], and SACRA [154]. NR techniques are employed to simulate the gravitational signal emitted by merging binary systems, but also accretion to BHs, the electromagnetic signal emitted by BNSs, core-collapse supernovae, and a variety of astrophysical processes in which strong-field gravity is involved [155]. NR simulations can take into account different physics and microphysics processes, and, thanks to the accurate predictions of gravitational waveforms, they provide the data against which all the developed waveform approximants are calibrated. Ideally, one would want the full gravitational waveform being generated by a NR simulation, but they are computationally extremely expensive

and cannot be used directly to analyze GW data. Although, usually, simulations are performed on supercomputers, only the last orbits of the inspiral can be simulated: for BBH systems, the number of inspiral orbits ranges from just a few up to roughly 100, depending on the system's parameters and the code's features, with an average of approximately 20 in the most recent SXS catalog [156]; for BNSs, instead, NR simulations generally include the last 10-15 orbits [157, 158]. Therefore, to obtain the full inspiral signal, different methods need to be employed: the post-Newtonian and the effective-one-body approximations. Nonetheless, there exists a family of gravitational waveform models, known as *surrogate models* [159, 160], which are directly interpolated on a set of pre-computed NR waveforms. These models are extremely accurate and yield the most similarity compared to NR simulations. However, they are slow to generate, and they can be built only for systems with a rather high total mass, given the computational cost of the NR simulations needed, which increases for lower values of masses. The most recent waveform model in this family is the time-domain approximant `NRSur7dq4` [161].

2.1.2 Post-Newtonian expansion

In Sec. 1.3.1, we computed h_+ and h_\times from the quadrupole formula and, in Sec. 1.3.2, we found their expression taking into account the backreaction of the emitted GWs in an adiabatic, Newtonian, and quadrupolar approximation. We also saw, in Sec. 1.2.3, that in reality GWs are not generated only by the quadrupole moment, but have a multipolar structure that effectively represents an expansion in $\mathcal{O}(v/c)$. All these derivations assumed GWs propagating on a flat spacetime far from the source, where we took into account at most the second order corrections due to the energy carried by GWs. However, when we deal with CBCs, the GWs' source is gravitationally bound, and we cannot ignore the spacetime curvature induced by the source itself. More specifically, for a two-body gravitationally bound system, we can write its kinetic and potential energy in terms of the reduced mass μ and the total mass M_{tot} , and the virial theorem reads

$$\frac{1}{2}\mu v^2 = \frac{G\mu M_{\text{tot}}}{2r}, \quad (2.2)$$

with r being the orbital separation. Since GM_{tot}/rc^2 represents the gravitational interaction potential near the source, Eq. 2.2 shows that taking into account the source's gravity translates into an expansion in $\mathcal{O}(v^2/c^2)$, and hence it cannot be treated independently from the expansion we introduced previously (see Sec. 1.2.3). For semi-relativistic ($v^2/c^2 \ll 1$)¹ and weakly gravitating ($GM_{\text{tot}}/rc^2 \ll 1$) sources, these curvature corrections are expressed through the *post-Newtonian (PN) expansion* in (v/c) [162], in which the n -th order corresponds to the $\mathcal{O}(v^{2n}/c^{2n})$ term.

The effects produced by the spacetime curvature induce corrections at different orders both in the metric and in the stress-energy tensor, leading to modified equations of motion, from which one computes the radiated energy and energy flux up to the needed order in (v/c) . Working in the adiabatic approximation, the GW luminosity originates from the change in the binary's orbital energy averaged over one period

$$\mathcal{F} = -\frac{dE}{dt}. \quad (2.3)$$

¹During the final phase of the inspiral, the two objects can reach velocities up to $\sim c/2$, therefore high orders in $\mathcal{O}(v/c)$ must be taken into account to obtain an accurate approximation.

The *energy balance equation* Eq. 2.3 provides an easy way to write evolution equations for all the binary parameters,² for example $\dot{v} = dE/dt$ $dv/dE = -\mathcal{F}/(dE/dv)$.

To simplify notation, in the following we will switch to geometrical units, i.e., $c = G = 1$. In particular, the expansion is carried out in terms of the characteristic velocity of the binary, a dimensionless parameter defined as $v = (\pi M_{\text{tot}} f_{\text{gw}})^{1/3}$. Writing the energy and flux in terms of the velocity v , and using Kepler's third law, we find two ordinary differential equations to describe the evolution of the orbital phase, and, consequently, of the gravitational one³ [164, 165]

$$\frac{d\Phi_{\text{orb}}}{dt} - \frac{v^3}{M_{\text{tot}}} = 0 \quad (2.4a)$$

$$\frac{dv}{dt} + \frac{\mathcal{F}(v)}{\mathcal{E}'(v)} = 0, \quad (2.4b)$$

or

$$t(v) = t_{\text{ref}} + \int_v^{v_{\text{ref}}} dv \frac{\mathcal{E}'(v)}{\mathcal{F}(v)} \quad (2.5a)$$

$$\Phi_{\text{orb}}(v) = \phi_{\text{orb,ref}} + \int_v^{v_{\text{ref}}} dv v^3 \frac{\mathcal{E}'(v)}{M_{\text{tot}} \mathcal{F}(v)}. \quad (2.5b)$$

In the equations above, \mathcal{E}' is the derivative with respect to v of the binding energy per unit mass $\mathcal{E} = E/M_{\text{tot}}$, while we can arbitrary choose the values of the reference quantities v_{ref} , t_{ref} and $\phi_{\text{orb,ref}}$, with the latter two being integration constants.

Currently, the energy and flux are known to the 4 and 4.5 PN order respectively [166–173]:

$$\begin{aligned} \mathcal{E}_4(v) = & -\frac{1}{2}\eta v^2 \left\{ 1 - \left(\frac{3}{4} + \frac{1}{12}\eta \right) v^2 - \left(\frac{27}{8} - \frac{19}{8}\eta + \frac{1}{24}\eta^2 \right) v^4 \right. \\ & + \left[-\frac{675}{64} + \left(\frac{34445}{576} - \frac{205}{96}\pi^2 \right) \eta - \frac{155}{96}\eta^2 - \frac{35}{5184}\eta^3 \right] v^6 \\ & + \left[-\frac{3969}{128} + \left(-\frac{123671}{5760} + \frac{9037}{1536}\pi^2 + \frac{896}{15}\gamma_E + \frac{448}{15}\ln(16v^2) \right) \eta \right. \\ & \left. \left. + \left(-\frac{498449}{3456} + \frac{3157}{576}\pi^2 \right) \eta^2 + \frac{301}{1728}\eta^3 + \frac{77}{31104}\eta^4 \right] v^8 + \mathcal{O}(v^{10}) \right\} \end{aligned} \quad (2.6)$$

²In principle, one should take into account also the angular momentum balance equation. However, this is not needed if we consider circular orbits and no eccentricity, which in this scenario is justified because the GWs backreaction is expected to circularize the binary's orbit, so that when the emitted GW signal enters in the sensitive band of current detectors, the orbits can be effectively assumed circular in most cases [163].

³We saw in Sec. 1.3.1 that, for the fundamental GW mode, the frequency of the emitted GWs is twice the orbital one, $\omega_{\text{gw}} = 2\omega_{\text{orb}}$. Since the phase is related to the frequency by $d\phi(t)/dt = \omega$, it follows that the orbital and GW phase are related by $\phi_{\text{gw}} = 2\phi_{\text{orb}}$. In reality, as discussed in Sec. 1.2.4, GWs include also subdominant harmonics, with frequencies $\sim k\omega_{\text{orb}}$, where k is an integer number. Here, we discuss only the leading-order term, and therefore we have $\phi_{\text{gw}} = 2\phi_{\text{orb}}$.

and

$$\begin{aligned} \mathcal{F}_{4.5}(v) = & \frac{32}{5} \eta^2 v^{10} \left\{ 1 - \left(\frac{1247}{336} + \frac{35}{12} \eta \right) v^2 + 4\pi v^3 \right. \\ & - \left(\frac{44711}{9072} - \frac{9271}{504} \eta - \frac{65}{18} \eta^2 \right) v^4 - \left(\frac{8191}{672} + \frac{583}{24} \eta \right) \pi v^5 \\ & + \left[\frac{6643739519}{69854400} + \frac{16}{3} \pi^2 - \frac{1712}{105} \gamma_E + \left(\frac{41}{48} \pi^2 - \frac{134543}{7776} \right) \eta - \frac{94403}{3024} \eta^2 - \frac{775}{324} \eta^3 \right. \\ & - \frac{856}{105} \ln(16v^2) \Big] v^6 - \left(\frac{16285}{504} - \frac{214745}{1728} \eta - \frac{193385}{3024} \eta^2 \right) \pi v^7 \\ & + \left[-\frac{323105549467}{3178375200} + \frac{232597}{4410} \gamma_E - \frac{1369}{126} \pi^2 + \frac{39931}{294} \ln 2 - \frac{47385}{1568} \ln 3 + \frac{232597}{8820} \ln(v^2) \right. \\ & + \left(-\frac{1452202403629}{1466942400} + \frac{41478}{245} \gamma_E - \frac{267127}{4608} \pi^2 + \frac{479062}{2205} \ln 2 + \frac{47385}{392} \ln 3 + \frac{20739}{245} \ln(v^2) \right) \eta \\ & + \left(\frac{1607125}{6804} - \frac{3157}{384} \pi^2 \right) \eta^2 + \frac{6875}{504} \eta^3 + \frac{5}{6} \eta^4 \Big] v^8 \\ & + \left[\frac{265978667519}{745113600} - \frac{6848}{105} \gamma_E - \frac{3424}{105} \ln(16v^2) + \left(\frac{2062241}{22176} + \frac{41}{12} \pi^2 \right) \eta \right. \\ & \left. \left. - \frac{133112905}{290304} \eta^2 - \frac{3719141}{38016} \eta^3 \right] \pi v^9 + \mathcal{O}(v^{10}) \right\}, \end{aligned} \quad (2.7)$$

where $\eta = \frac{m_1 m_2}{(m_1 + m_2)^2}$ is the symmetric mass ratio, with $m_{1,2}$ being the component masses, and $\gamma = 0.577216\dots$ the Euler-Mascheroni constant. Inserting the expansions in Eqs. 2.6-2.7 into Eqs. 2.4a-2.4b yields an expression for the time evolution of the GW phase. Different ways of expanding and working with the quantity $\mathcal{E}'(v)/\mathcal{F}(v)$ in the integrals in Eqs. 2.5a-2.5b lead to different expressions for the GW phase evolution and therefore to different waveform approximants. The models computed directly from the PN expansion belong to the so-called **Taylor** family (see, e.g., Ref. [165] for an overview of the various models in this family). For example, for the **TaylorT2** model, the quantity $\mathcal{E}'(v)/\mathcal{F}(v)$ is expanded at a consistent PN order, then integrated as in Eqs. 2.5b-2.5a to obtain $\phi_{\text{orb}}(v)$ and $t(v)$, which are solved numerically to find $\phi(t)$. However, GW searches and data analysis are usually performed in frequency domain, therefore one needs Fourier domain models, such as **TaylorF2**. The Fourier transform is commonly obtained through the *stationary phase approximation* (SPA), which we briefly describe below.

From Eqs. 1.77a-1.77b, the time domain plus and cross polarizations can be written as

$$h_+(t) = B(t) (1 + \cos^2(\iota)) \cos(2\Phi_{\text{orb}}) \quad (2.8a)$$

$$h_\times(t) = B(t) 2 \cos(\iota) \sin(2\Phi_{\text{orb}}), \quad (2.8b)$$

with $B(t)$ representing the overall pre-factor. Since, from Eq. 1.91, $h(t) = F_+ h_+ + F_\times h_\times$, the time domain gravitational waveform reads

$$\begin{aligned} h(t) &= B(t) \sqrt{F_+^2 (1 + \cos^2(\iota))^2 + F_\times^2 4 \cos^2(\iota)} \cos(\Phi_{\text{gw}}(t) + \phi_0) \\ &= A(t) \cos(\Phi_{\text{gw}}(t) + \phi_0), \end{aligned} \quad (2.9)$$

where we used the fact that the GW phase is $\Phi_{\text{gw}} = 2\Phi_{\text{orb}}$,⁴ and with

$$\phi_0 = \arctan \left(\frac{-F_x 2 \cos \iota}{F_+ (1 + \cos^2 \iota)} \right). \quad (2.10)$$

Thus, its Fourier transform will be

$$\begin{aligned} \tilde{h}(f) &= \int_{-\infty}^{+\infty} dt A(t) \cos(\Phi_{\text{gw}}(t)) e^{2\pi i f t} \\ &= \frac{1}{2} \int_{-\infty}^{+\infty} dt A(t) \left[e^{i2\pi f t + i\Phi_{\text{gw}}(t)} + e^{i2\pi f t - i\Phi_{\text{gw}}(t)} \right]. \end{aligned} \quad (2.11)$$

In the first term of this integral, $\exp[i2\pi f t + i\Phi_{\text{gw}}(t)]$ has an argument that increases monotonically with time and is rapidly oscillating, therefore its contribution approximately averages to zero. The argument of the second term is also rapidly oscillating, but the largest contribution to the integral comes from the point t^* where the argument $[i2\pi f t - i2\Phi_{\text{orb}}(t)]$ is maximum, also called *saddle point*. The SPA approximation consists in expanding the exponential of the second term around this saddle point. More specifically, the condition for the maximum reads

$$\frac{d}{dt} [2\pi f t - \Phi_{\text{gw}}(t)] \Big|_{t=t^*} = 0, \quad (2.12)$$

resulting in

$$\pi f = \frac{1}{2} \dot{\Phi}_{\text{gw}}(t^*). \quad (2.13)$$

Writing the Taylor expansion of the second term's argument around t^* and up to the quadratic term,⁵ and assuming that the amplitude $A(t)$ varies only slowly near t^* , we find

$$\tilde{h}^{\text{SPA}}(f) = \frac{1}{2} A(t^*) e^{i(2\pi f t^* - \Phi_{\text{gw}}(t^*))} \int_{-\infty}^{+\infty} dt e^{-\frac{\ddot{\Phi}_{\text{gw}}}{2}(t-t^*)^2}. \quad (2.14)$$

Changing the integration variable and using

$$\int_{-\infty}^{+\infty} dx e^{-ix^2} = \sqrt{\pi} e^{-i\frac{\pi}{4}}, \quad (2.15)$$

we finally obtain

$$\tilde{h}^{\text{SPA}}(f) = \frac{1}{2} A(t^*) \sqrt{\frac{2\pi}{\ddot{\Phi}_{\text{gw}}}} e^{i[2\pi f t^* - \frac{\pi}{4} - \Phi_{\text{gw}}(t^*)]}. \quad (2.16)$$

The `TaylorF2` approximant is then calculated by inserting in Eq. 2.16 the parameteric equations $\Phi_{\text{orb}}(v)$ and $t(v)$ that are found for the `TaylorT2` model.

The final expression for the frequency-domain waveform in `TaylorF2` reads

$$\tilde{h}^{(F2)}(f) = A^{(F2)}(f) e^{-i\Phi^{(F2)}(f)}, \quad (2.17)$$

⁴We remind that this holds because here we are interested only in the dominant mode $(\ell, m) = (2, 2)$.

⁵The linear term in $(t - t^*)$ cancels out due to the condition in Eq. 2.12.

with the (quadrupolar) amplitude

$$A^{(F2)}(f) = \frac{\sqrt{F_+^2 (1 + \cos^2(\iota))^2 + F_\times^2 4 \cos^2(\iota)}}{2r} \sqrt{\frac{5\pi}{96}} \mathcal{M}_c^{5/6} (\pi f)^{-7/6} \quad (2.18)$$

and phase, implemented up to the 3.5 PN order,⁶

$$\Phi^{F2}(f) = 2\pi f t_{\text{ref}} + \Phi_{\text{ref}} + \frac{\pi}{4} + \frac{3}{128\eta} v^{-5} \left[\sum_{k=0}^7 \phi_k v^k + \sum_{k=5}^6 \phi_k^l \ln(v) v^k \right]. \quad (2.19)$$

In Eq. 2.19, Φ_{ref} represents some reference phase, while ϕ_k and ϕ_k^l are the *PN coefficients*, whose explicit expressions can be found in Appendix B of Ref. [174]. TaylorF2 comes with the advantage of a completely analytical expression in frequency domain, which makes it very fast to evaluate, a crucial feature in analyses like parameter estimation, as we will see later. However, it describes only the inspiral part of the waveform, missing all the information from the merger and after. Moreover, for high-mass systems, differences between the various models appear at high PN orders [165], due to the different methods with which they are computed, the adiabatic approximation starts to break down, and the merger and ringdown contribution to the emitted GW signal becomes larger and larger. Therefore, it is important to build full inspiral-merger-ringdown (IMR) models that describe the gravitational waveform emitted during the full coalescence.

2.1.3 Effective one body

A different approximation consists in mapping the two-body dynamics of the compact binary, up to the highest PN order available, into an *effective-one-body* (EOB) description of the motion of a particle with mass $\mu = m_1 m_2 / (m_1 + m_2)$ in an effective background metric $g_{\mu\nu}^{\text{eff}}$ [175, 176]. With this effective external metric, the line element takes the form

$$ds_{\text{eff}}^2 \equiv g_{\mu\nu}^{\text{eff}} dx^\mu dx^\nu = -A(r)c^2 dt^2 + \frac{D(r)}{A(r)} dr^2 + r^2(d\theta^2 + \sin^2 \theta d\phi^2), \quad (2.20)$$

where $A(r)$ and $D(r)$ can be Taylor-approximated as

$$A(r) = \sum_{i=0}^4 \frac{a_i(\eta)}{r^i}, \quad (2.21a)$$

$$D(r) = \sum_{i=0}^3 \frac{d_i(\eta)}{r^i}, \quad (2.21b)$$

with the $a_i(\eta)$ and $d_i(\eta)$ coefficients known up to the 3PN order [177]. The waveform up to the 3.5 PN order is computed by including the radiation-reaction contribution to the GW flux [178, 179]. Moreover, in order to improve the agreement with NR data in the last stages of the merger, i.e., at high frequencies, a pseudo-4PN coefficient $a_5(\eta)$ is added to $A(r)$ [176].

⁶The calculation of the 4 and 4.5 PN order of energy and flux, respectively, was provided only very recently. Therefore, it will take some time to update the waveform models, and the models presented here and in the following include PN information only up to the 3.5 PN order.

Motion in this effective metric is described by an effective Hamiltonian H_{eff} , from which one can obtain the real Hamiltonian as

$$H_{\text{real}} = M_{\text{tot}} \sqrt{1 + 2\eta \left(\frac{H_{\text{eff}} - \mu}{\mu} \right)} - M_{\text{tot}}. \quad (2.22)$$

If spin is not included, the binary is constrained to move on a plane, and hence we can use polar coordinates (r, ϕ, p_r, p_ϕ) , with p_r and p_ϕ the conjugate momenta. Finally, the EOB gravitational waveforms can be computed by solving the following system of equations [176]:

$$\frac{dr}{d\hat{t}} = \frac{\partial \hat{H}_{\text{real}}}{\partial p_r}(r, p_r, p_\phi), \quad (2.23a)$$

$$\frac{d\phi}{d\hat{t}} = \frac{\partial \hat{H}_{\text{real}}}{\partial p_\phi}(r, p_r, p_\phi), \quad (2.23b)$$

$$\frac{dp_r}{d\hat{t}} = -\frac{\partial \hat{H}_{\text{real}}}{\partial r}(r, p_r, p_\phi), \quad (2.23c)$$

$$\frac{dp_\phi}{d\hat{t}} = \hat{F}_\phi(r, p_r, p_\phi), \quad (2.23d)$$

where $\hat{H}_{\text{real}} = H_{\text{real}}/\mu$, $\hat{t} = t/M_{\text{tot}}$, and \hat{F}_ϕ represents the ϕ -component of the radiation-reaction force.

A full IMR waveform can then be created by adding a merger-ringdown model, obtained as a superimposition of quasi-normal modes [176]. Moreover, the accuracy of EOB models is further improved by introducing higher-order pseudo-PN terms and calibrating them against NR data [180–183]. Spin effects can also be taken into account in the EOB formalism [184], by considering the effective Hamiltonian of a particle of mass μ and effective spin S^* moving in the deformed spacetime of a BH with mass $M = m_1 + m_2$ and spin $S = S_1 + S_2$, where $S_{1,2}$ are the components' spins. The region of validity in the parameter space of the EOB waveforms can be extended with calibration against NR waveforms [185]; recent models include also precession [186].

Among the state-of-the-art EOB approximants we find **SEOBNRv4PHM**, which features precession and higher-order modes [187], and the models in the new **SEOBNRv5** family [188–191], developed in preparation for the O4 observing run.

2.1.4 Phenomenological models

The EOB approach, together with calibration to NR simulations, provides very accurate IMR waveform models. However, these models are built in time domain, and a system of differential equations needs to be solved in order to compute them, therefore they are rather slow to generate. Considering the huge amount of waveform generations, $\mathcal{O}(10^6 - 10^7)$, required in GW analyses like parameter estimation (see Sec. 2.2.2), the computational cost can become a major bottleneck. On one side, one can find strategies to reduce the computational cost, for example by constructing reduced order models [192] (more details are given in Sec. 2.3.3). However, there exist also different and faster approaches to the construction of gravitational waveform approximants.

An example are the phenomenological models, constructed with analytical ansätze that are calibrated against NR waveforms, where different ansätze are built for the inspiral, intermediate, and

merger-ringdown regions. These models comprise an approximant family known as **Phenom**. In the following, we discuss the **IMRPhenomD** model [174, 193], which represents the starting point for more complete approximants currently employed in GW data analysis.

IMRPhenomD includes information only for the dominant $(\ell, m) = (2, 2)$ mode, thus in frequency domain the waveform reads

$$\tilde{h}_{22}(f; \Xi) = A(f; \Xi)e^{i\phi(f; \Xi)}, \quad (2.24)$$

where $\Xi = (M, \eta, \chi_1, \chi_2)$ are the physical parameters for the binary, with $\chi_{1,2}$ the dimensionless component spins. This waveform model employs a piecewise analytical expression for $A(f; \Xi)$ and $\phi(f; \Xi)$, distinguishing three different frequency regions: inspiral, intermediate, and merger-ringdown.

Phase

The model of the signal emitted during inspiral is built starting from the **TaylorF2** phase $\Phi^{F2}(f)$ in Eq. 2.19, which describes the non-spinning, point-particle part of the phase, ψ_{PP} . However, as we saw in Sec. 1.3.3, binary systems, especially BBHs, can have spin, which interacts with the orbital angular momentum and with the spin itself; moreover, for BNS systems, the tidal deformability also affects the phase. Therefore, in general, the GW phase can be expressed as

$$\psi = \psi_{\text{PP}} + \psi_{\text{SO}} + \psi_{\text{SS}} + \psi_{\text{T}}, \quad (2.25)$$

where ψ_{SO} and ψ_{SS} are the spin-orbit and spin-spin contributions, respectively, and ψ_{T} the tidal one. In **IMRPhenomD**, spin-spin corrections are taken into account up to 2PN order [194–196] and spin-orbit ones up to 3.5 PN order [197]. Since the waveform intends to describe BBH systems coalescences, we do not need to include the tidal term for now. EOB approximants achieve a higher accuracy than PN ones towards the end of the inspiral thanks to higher terms in $\mathcal{O}(v/c)$ that cannot be modeled by the PN formalism. In the inspiral phase of **IMRPhenomD**, these higher order terms are included by adding the next higher-order PN terms through some coefficients σ_i , yielding

$$\Phi_{\text{Ins}} = \Phi_{\text{spin}}^{F2}(f; \Xi) + \frac{1}{\eta} \left(\sigma_0 + \sigma_1 f + \frac{3}{4} \sigma_2 f^{4/3} + \frac{3}{5} \sigma_3 f^{5/3} + \frac{1}{2} \sigma_4 f^2 \right), \quad (2.26)$$

where $\Phi_{\text{spin}}^{F2}(f; \Xi)$ is the **TaylorF2** phase including spin contributions.

In the intermediate region, which connects the inspiral and the merger-ringdown regimes, the phase ansatz reads

$$\Phi_{\text{Int}} = \frac{1}{\eta} \left(\beta_0 + \beta_1 f + \beta_2 \ln(f) - \frac{\beta_3}{3} f^{-3} \right). \quad (2.27)$$

Finally, the merger-ringdown phase is modeled with

$$\Phi_{\text{MR}} = \frac{1}{\eta} \left[\alpha_0 + \alpha_1 f - \alpha_2 f^{-1} + \frac{4}{3} \alpha_3 f^{3/4} + \alpha_4 \tan^{-1} \left(\frac{f - \alpha_5 f_{\text{RD}}}{f_{\text{damp}}} \right) \right], \quad (2.28)$$

with f_{RD} the ringdown frequency of the final BH, and f_{damp} the ringdown damping frequency.

The model coefficients σ_i , β_i and α_i are calibrated against hybrid waveforms, created by adding a late-inspiral and merger-ringdown description from NR simulations to an early-inspiral signal obtained from the **SEOv2** model.⁷ For the intermediate and merger-ringdown regime, however, all the information comes from NR simulations.

The full IMR waveform is built requiring $C(1)$ continuity between the different regions, which are joint via the step functions

$$\theta(f - f_0) = \begin{cases} -1, & f < f_0, \\ 1, & f \geq f_0 \end{cases}, \quad (2.29)$$

and

$$\theta_{f_0}^{\pm} = \frac{1}{2} [1 \pm \theta(f - f_0)]. \quad (2.30)$$

The complete IMR phase is given by

$$\Phi_{\text{IMR}}(f) = \Phi_{\text{Ins}}(f)\theta_{f_1}^- + \theta_{f_1}^+ \Phi_{\text{Int}}\theta_{f_2}^- + \theta_{f_2}^+ \Phi_{\text{MR}}(f), \quad (2.31)$$

with the transition frequencies being $M_{\text{tot}}f_1 = 0.018$ and $f_2 = 0.5f_{\text{RD}}$.⁸ The final waveform phase is determined up to an arbitrary phase and time shift, which are absorbed by the (σ_0, σ_1) coefficients. (α_0, α_1) and (β_0, β_1) are determined by the $C(1)$ conditions, while all the other coefficients are found via calibration against the hybrid waveforms.

Amplitude

The inspiral amplitude is derived from a re-expanded SPA amplitude as

$$A_{\text{Ins}} = A_0 \sum_{i=0}^6 \mathcal{A}_i (\pi f)^{i/3} + A_0 \sum_{i=1}^3 \rho_i f^{(6+i)/3}, \quad (2.32)$$

where the expansion coefficients \mathcal{A}_i are given in Ref. [193], and the normalization factor A_0 is obtained by factoring out the PN leading contribution proportional to $f^{-7/6}$,

$$A_0 \equiv \sqrt{\frac{2\eta}{3\pi^{1/3}}} f^{-7/6}. \quad (2.33)$$

The ρ_i fitting coefficients are arbitrarily set to three in order to ensure a better performance at high frequencies while maintaining a quite simple form.

The merger-ringdown amplitude, instead, is modeled as a Lorentzian around the main ringdown frequency,⁹ multiplied by an exponential to render the decay at the end of the full IMR waveform

$$\frac{A_{\text{MR}}}{A_0} = \gamma_1 \frac{\gamma_3 f_{\text{damp}}}{(f - f_{\text{RD}})^2 + (\gamma_3 f_{\text{damp}})^2} \times \exp \left[-\frac{\gamma_2}{(\gamma_3 f_{\text{damp}})} (f - f_{\text{RD}}) \right]. \quad (2.34)$$

⁷ **SEOv2** labels the uncalibrated version of the **SEOBNRv2** approximant [185]. The adjustments obtained via calibration to NR waveforms are set to zero in order to avoid possible biases caused by the different parameters space of the NR simulations considered for **SEOv2NR** compared to the ones employed for the calibration of **IMRPhenomD**.

⁸ The fits performed to calibrate the various coefficients, however, are carried out on wider frequency regions, in order to avoid boundary effects.

⁹ The ringdown signal in time is described as a damped sinusoid, hence its Fourier transform is a Lorentzian.

In Eq. 2.34, the γ_i coefficients are calibrated against NR data, while f_{RD} and f_{damp} are computed from the final mass and spin fits on NR waveforms. The effect of the exponential term is to move the amplitude peak from the Lorentzian peak value f_{RD} to

$$f_{\text{peak}} = \left| f_{\text{RD}} + \frac{\gamma_3 f_{\text{damp}} (\sqrt{1 - \gamma_2^2} - 1)}{\gamma_2} \right|. \quad (2.35)$$

For the intermediate region, the amplitude is modeled as a fourth-degree polynomial

$$A_{\text{Int}} = A_0(\delta_0 + \delta_1 f + \delta_2 f^2 + \delta_3 f^3 + \delta_4 f^4). \quad (2.36)$$

The δ_i coefficients are determined by the continuity conditions with the other regions at the transition frequencies $M_{\text{tot}} f_1 = 0.014$ and $f_2 = f_{\text{peak}}$, and by matching the amplitude value $A_{\text{NR}}(f_{\text{int}})$ at the intermediate frequency $f_{\text{int}} = (f_1 + f_2)/2$ with values obtained from NR simulations.

The complete IMR amplitude is then

$$A_{\text{IMR}}(f) = A_{\text{Ins}}(f)\theta_{f_1}^- + \theta_{f_1}^+ A_{\text{Int}}(f)\theta_{f_2}^- + \theta_{f_2}^+ A_{\text{MR}}(f), \quad (2.37)$$

with the θ -functions defined as in Eqs. 2.29-2.30.

Therefore, in total, the waveform is described by 17 phenomenological coefficients

$$\Lambda^j = \{\rho_i, A_{\text{NR}}(f_{\text{int}}), \gamma_i, \sigma_i, \beta_i, \alpha_i\}. \quad (2.38)$$

These coefficients are mapped onto the space of the binary's physical parameters [67, 68, 198] through

$$\Lambda^j = \sum_{m=0}^3 \sum_{n=0}^2 (\chi_{\text{PN}} - 1)^m (\lambda_{nm}^j \eta^n), \quad (2.39)$$

where η is again the symmetric mass ratio, and χ_{PN} is defined as

$$\chi_{\text{PN}} = \frac{m_1 \chi_1 - m_2 \chi_2}{M} - \frac{38\eta}{113} (\chi_1 + \chi_2). \quad (2.40)$$

The fitting coefficients λ_{mn}^j are given in Ref. [174].

We now turn to the description to two state-of-the-art phenomenological models, which will be employed for some of the work presented in this thesis: **IMRPhenomXPHM**, for precessing BBH systems including higher-order modes, and **IMRPhenomD_NRTidalv2** for BNSs.

IMRPhenomXPHM

An improved version of the **IMRPhenomD** model, **IMRPhenomXAS**, was developed in Ref. [199], where, among others, a more refined phenomenological ansatz was employed, and the calibration was performed on a wider set of NR waveforms. Nonetheless, **IMRPhenomXAS** still describes signals solely from

binaries with aligned spins and includes the contribution of the $(\ell, m) = (2, 2)$ fundamental mode only. However, we know that compact binary systems can be precessing, and for high-mass-ratio and high-mass systems the subdominant modes become non-negligible. Therefore, a waveform model that does not take into account these two effects might lead to significant biases in the analyses. Moreover, detecting the contribution of higher-order modes in the signal is expected to break the degeneracy between distance and inclination angle [16]. Consequently, state-of-the art waveforms include both these effects.

`IMRPhenomXHM` [200] is a phenomenological approximant constructed as `IMRPhenomXAS`, but including different models for the subdominant modes $(\ell, |m|) = (2, 1), (3, 3), (3, 2), (4, 4)$, each one calibrated to NR data. As introduced in Sec.1.2.4, the multipolar expansion of the GW strain can be decomposed in terms of the spherical harmonic modes $h_{\ell m}$ as

$$h(t, \iota, \phi; \Xi) = \sum_{\ell=2}^{\infty} \sum_{m=-\ell}^{\ell} h_{\ell m}(t, \Xi) Y_{\ell m}^{-2}(\iota, \phi). \quad (2.41)$$

The waveform model provides a description only for the $|m|$ modes, because, in absence of precession, the *equatorial symmetry*, i.e., the fact that the geometry of the system is symmetric with respect to the orbital plane, which remains constant over time, implies

$$h(t, \iota, \phi; \Xi) = h^*(t, \pi - \iota, \phi; \Xi), \quad (2.42)$$

and, for the individual modes,

$$h_{\ell m}(t, \Xi) = (-1)^{\ell} h_{\ell, -m}^*(t, \Xi). \quad (2.43)$$

In the Fourier domain, each mode is described by

$$\tilde{h}_{\ell m}(f) = A_{\ell m}(f) e^{-i\Phi_{\ell m}(f)} \quad (2.44)$$

and gives a contribution to the GW polarizations

$$\tilde{h}_+^{\ell m}(f) = \frac{1}{2} \left(Y_{\ell m} + (-1)^{\ell} Y_{\ell m}^* \right) \tilde{h}_{\ell m}(f), \quad (2.45a)$$

$$\tilde{h}_x^{\ell m}(f) = \frac{i}{2} \left(Y_{\ell m} - (-1)^{\ell} Y_{\ell m}^* \right) \tilde{h}_{\ell m}(f). \quad (2.45b)$$

`IMRPhenomXHM` is built in the frequency domain from closed-form expressions for the amplitude and phase of each mode in a piecewise way, with different expressions for the inspiral, intermediate and merger-ringdown regions.

The ringdown signal is modeled through the quasi-normal modes emission of a perturbed Kerr black hole [201] as

$$h(t, \iota, \phi) \approx \sum_{\ell mn} a_{\ell mn} e^{i(\omega_{\ell mn} t) + \Phi_{\ell mn}} {}_{-2}\mathcal{Y}_{\ell m}(\iota, \phi), \quad (2.46)$$

where ${}_{-2}\mathcal{Y}_{\ell m}(\iota, \phi)$ are the -2 spin-weighted spheroidal harmonics [202, 203], $\omega_{\ell mn}$ the ringdown frequencies, which depend only on the final BH's mass and spin, $a_{\ell mn}$ the amplitude parameters, and

$\Phi_{\ell mn}$ some phase offsets. The difference between the spherical harmonics structure used to extract the NR gravitational waveforms and the spheroidal harmonics employed to describe the ringdown signal can lead to an effect known as *mode-mixing* [204], when multiple spheroidal components get mixed into one spherical harmonic. As a consequence, for some modes, amplitude and phase do not vary smoothly in the region after the merger, creating a behaviour difficult to model analytically. **IMRPhenomXHM** includes a mode-mixing description for the (3, 2) mode.

The inspiral model is based on the SPA and retains the same expression for each (ℓ, m) mode. The amplitude description is based on a PN expansion together with some higher-order pseudo-PN coefficients, calibrated against NR simulations, to model the high-frequency part of the signal for which PN expressions are not available yet. The phase ansatz is based on the fact that, at low frequencies, the equatorial symmetry implies

$$\Phi_{\ell m} \sim \frac{m}{2} \Phi_{22}. \quad (2.47)$$

The approximation errors entailed by this assumption are negligible until the system reaches the minimal energy circular orbit [204], where the inspiral part for the phase ansatz is ended. In the intermediate region, the amplitude is modeled as an inverse fifth-order polynomial, whose coefficients are determined by ensuring continuity with the inspiral and ringdown regions and by requiring that the amplitude values at specific collocation points recover the values fitted from NR waveforms. A similar procedure is employed to determine the coefficients for the phase ansatz. However, in this case, the ansatz for the (3, 2) mode includes one extra degree of freedom to account for mode-mixing effects. Finally, the ringdown amplitude is modeled similarly to **IMRPhenomD**, with the core structure represented by a Lorentzian and an exponential factor, where the coefficients are again determined by continuity conditions and by calibration with NR data. Considering that the strongest mode-mixing effects appear in the ringdown region, for the (3, 2) mode the NR waveforms to which the ansatz is calibrated are first translated into a spheroidal-harmonic basis. Similarly, the model for the ringdown phase takes a different form for the (3, 2) mode, for which it is expressed in spheroidal harmonics.

Finally, the precessing approximant **IMRPhenomXPHM** [205] is obtained from **IMRPhenomXHM** through the so-called *twisting-up* procedure [69, 206, 207]. Two different coordinate systems are considered: the inertial *J*-frame, where the $\hat{\mathbf{z}}_J$ axis is aligned with the total angular momentum \mathbf{J} , and the co-precessing *L*-frame, where the $\hat{\mathbf{z}}_L$ axis is aligned with the orbital angular momentum \mathbf{L} . *Twisting-up* means building an approximate mapping between the aligned-spin waveform modes in the co-precessing frame and the precessing waveform modes in the inertial frame.

The underlying idea is that the waveform model describing the signal emitted from a precessing binary can be approximated with an aligned-spin model in the frame that follows the motion of the orbital angular momentum. Therefore, the gravitational waveform is modeled with **IMRPhenomXHM** in the non-inertial *L*-frame and then everything is rotated into the inertial *J*-frame. The exact form of this rotation is derived from the system dynamics, described by the Euler angles α, β, γ . The GW

modes in the two frames are related via the following transformations

$$h_{\ell m}^J = \sum_{m'=-\ell}^{\ell} \mathcal{D}_{mm'}^{\ell*}(\alpha, \beta, \gamma) h_{\ell m'}^L \quad (2.48a)$$

$$h_{\ell m'}^L = \sum_{m=-\ell}^{\ell} \mathcal{D}_{mm'}^{\ell}(\alpha, \beta, \gamma) h_{\ell m}^J. \quad (2.48b)$$

In Eq. 2.48a-2.48b, $\mathcal{D}_{mm'}^{\ell}$ are the Wigner D-matrices [208]

$$\mathcal{D}_{mm'}^{\ell}(\alpha, \beta, \gamma) = e^{im\alpha} e^{im'\gamma} d_{mm'}^{\ell}(\beta), \quad (2.49)$$

with $d_{mm'}^{\ell}(\beta)$ the real-valued Wigner d-matrices, which are polynomials in $\cos(\beta/2)$ and $\sin(\beta/2)$.

Therefore, the frequency-domain GW polarizations in the inertial frame, as a function of the modes in the co-precessing L -frame, read¹⁰

$$\tilde{h}_+^J(f > 0) = \frac{1}{2} \sum_{\ell \geq 2} \sum_{m' > 0}^{\ell} \tilde{h}_{\ell-m'}^L(f) e^{im'\gamma} \sum_{m=-\ell}^{\ell} \left[A_{m-m'}^{\ell} + (-1)^{\ell} A_{mm'}^{\ell*} \right], \quad (2.50a)$$

$$\tilde{h}_{\times}^J(f > 0) = \frac{i}{2} \sum_{\ell \geq 2} \sum_{m' > 0}^{\ell} \tilde{h}_{\ell-m'}^L(f) e^{im'\gamma} \sum_{m=-\ell}^{\ell} \left[A_{m-m'}^{\ell} - (-1)^{\ell} A_{mm'}^{\ell*} \right], \quad (2.50b)$$

where the mode-by-mode transfer functions are defined as

$$A_{mm'}^{\ell} = e^{im\alpha} d_{mm'}^{\ell}(\beta) {}_{-2}Y_{\ell m}. \quad (2.51)$$

IMRPhenomXPHM represents a computationally efficient, state-of-the art model for the GW signal emitted during BBH coalescences. It includes both precession and higher-order modes, hence it was one of the models employed in the LVK analyses of O3 data [14, 38].

IMRPhenomD_NRTidalv2

In BNS systems, the effects of matter leave an imprint in the GW signal emitted during coalescence. Measuring such signatures represents one of the main goals of GW data analysis, because it allows us to constrain the EOS describing NSs' matter.

In frequency domain, the gravitational waveform reads

$$\tilde{h}(f) = \tilde{A}(f) e^{-i\psi(f)}, \quad (2.52)$$

where the phase can be divided into the explicit contributions

$$\psi(\hat{\omega}) = \psi_{\text{PP}}(\hat{\omega}) + \psi_{\text{SO}}(\hat{\omega}) + \psi_{\text{ss}}(\hat{\omega}) + \psi_{\text{T}}(\hat{\omega}) + \dots \quad (2.53)$$

¹⁰Since $\tilde{h}_{+, \times}^J(f)$ is the Fourier transform of the real function $h_{+, \times}^J(t)$, the following property holds: $\tilde{h}_{+, \times}^J(f) = \tilde{h}_{+, \times}^{J*}(-f)$. Therefore, one can equivalently consider only the positive or negative frequency regime. In this case, positive frequencies are chosen for consistency with other GW data-analysis tools.

with $\hat{\omega} = M_{\text{tot}}\omega_{\text{gw}}$ the dimensionless GW frequency. The tidal term ψ_{T} enters at the 5PN order and in the PN approximation is computed as [209–211]

$$\begin{aligned}\psi_{\text{T}}(v) = & \frac{3}{128\eta}v^{-5} \sum_{i=1}^2 \Lambda_i X_i^4 \left[-24(12 - 11X_i)v^{10} \right. \\ & + \frac{5}{28}(3179 - 919X_i - 2286X_i^2 + 260X_i^3)v^{12} + 24\pi(12 - 11X_i)v^{13} \\ & - 24 \left(\frac{39927845}{508032} - \frac{480043345}{9144576}X_i + \frac{9860575}{127008}X_i^2 - \frac{421821905}{2286144}X_i^3 \right. \\ & \left. + \frac{4359700}{35721}X_i^4 - \frac{10578445}{285768}X_i^5 \right) v^{14} \\ & \left. + \frac{\pi}{28}(27719 - 22127X_i + 7022X_i^2 - 10232X_i^3)v^{15} \right],\end{aligned}\quad (2.54)$$

where $i = \{1, 2\}$ is the index labeling the two NSs in the binary, $X_i = \frac{m_i}{M_{\text{tot}}}$, $\Lambda_i = \frac{2}{3}k_2 \left(\frac{R_i}{m_i} \right)^5$ is the tidal deformability parameter introduced in Eq. 1.84, with R_i and m_i being the radius and mass of the component NSs, respectively, and $\eta = m_1m_2/M_{\text{tot}}^2$ as usual.

The **NRTidal** approach introduced in Ref. [158] provides a closed-form approximation for the phase tidal contribution in Eq. 2.54, calibrating it against NR simulations obtained with different EOSs. This model can be added to all the existing waveform approximants for BBH systems, creating a BNS waveform model. In its improved version **NRTidalv2** [212], the frequency-domain tidal phase contribution is obtained via the SPA and approximated as

$$\psi_{\text{T}}(x) = -\kappa_{\text{eff}}^{\text{T}} \frac{39}{16\eta} x^{5/2} \tilde{P}_{\text{NRTidalv2}}(x), \quad (2.55)$$

with $x = (\hat{\omega})^{2/3}$. In the above Eq. 2.55, $\kappa_{\text{eff}}^{\text{T}}$ is the *effective tidal coupling*, defined as

$$\kappa_{\text{eff}}^{\text{T}} = \frac{2}{13} \left[\left(1 + 12 \frac{X_2}{X_1} \right) \left(\frac{X_1}{C_1} \right)^5 k_2^1 + (1 \leftrightarrow 2) \right], \quad (2.56)$$

where $\{1, 2\}$ represents the NS label, $C_{1,2} \equiv m_{1,2}/R_{1,2}$ the NS compactness, with $R_{1,2}$ the NS radius, and $k_2^{1,2}$ the static quadrupolar tidal Love numbers [213–216]. The Padé approximant $\tilde{P}_{\text{NRTidalv2}}(x)$ is parameterized as

$$\tilde{P}_{\text{NRTidalv2}}(x) = \frac{1 + \tilde{n}_1 x + \tilde{n}_{3/2} x^{3/2} + \tilde{n}_2 x^2 + \tilde{n}_{5/2} x^{5/2} + \tilde{n}_3 x^3}{1 + \tilde{d}_1 x + \tilde{d}_{3/2} x^{3/2} + \tilde{d}_2 x^2}, \quad (2.57)$$

where \tilde{n}_1 , $\tilde{n}_{3/2}$, \tilde{n}_2 , and $\tilde{d}_{3/2}$ are fixed by requiring agreement with the PN expression in Eq. 2.54, while the other coefficients are fitted against NR waveforms. Due to the lack of a large set of high-quality NR simulations for asymmetric BNS systems, the **NRTidalv2** model is constructed for equal-mass binaries only. Adding the **NRTidalv2** model for the tidal phasing to the **IMRPhenomD** approximant results in the BNS waveform model **IMRPhenomD_NRTidalv2**.

The GW phase tidal contribution depends on two combinations of the NS's tidal deformabilities

Model family	Built from	Advantages	Disadvantages	Examples
Taylor	Directly from PN expansion	Fully analytical, fast	Inspiral only, not very accurate	TaylorF2: for the inspiral of non-spinning BH coalescences
EOB	Mapping two-body dynamics into an EOB description, calibration to NR waveforms	Accurate, full IMR models possible	Computational cost	SEOBNRv4PHM: IMR model for precessing BBHs, including higher-order modes
NR surrogates	Interpolation of NR waveforms	Very accurate, models also for the ringdown regime of validity	Computational cost of the NR simulations required, with consequent reduced regime of validity	NRSur7dq4: IMR model for precessing BBHs with the full mode content; valid for $q \leq 1/6$ and $M_{\text{tot}} \gtrsim 66 M_{\odot}$
Phenom	Phenomenological expressions calibrated to NR and EOB waveforms	Very fast, complete IMR models possible	Less accurate	IMRPhenomD: IMR model for aligned-spin BBHs, fundamental mode only IMRPhenomXPHM: IMR model for precessing BBHs, including higher-order modes IMRPhenomD_NRTidalv2: inspiral and merger model for aligned-spin BNSs

Table 2.1: Main features of the waveform model families described in Sec. 2.1, including how they are built, their principal advantages and disadvantages, and examples of specific models discussed or used in this thesis.

Λ_1 and Λ_2 , the mass-weighted tidal deformability [217, 218]

$$\begin{aligned}\tilde{\Lambda} &= \frac{8}{13} \left[(1 + 7\eta - 31\eta^2) (\Lambda_1 + \Lambda_2) + \sqrt{1 - 4\eta} (1 + 9\eta - 11\eta^2) (\Lambda_1 - \Lambda_2) \right] \\ &= \frac{16}{3} \frac{(m_1 + 12m_2)m_1^4\Lambda_1 + (m_2 + 12m_1)m_2^4\Lambda_2}{(m_1 + m_2)^5}\end{aligned}\quad (2.58)$$

and

$$\begin{aligned}\Delta\tilde{\Lambda} &= \frac{1}{2} \left[\sqrt{1 - 4\eta} \left(1 - \frac{13272}{1319}\eta + \frac{8944}{1319}\eta^2 \right) (\Lambda_1 + \Lambda_2) \right. \\ &\quad \left. + \left(1 - \frac{15910}{1319}\eta + \frac{32850}{1319}\eta^2 + \frac{3380}{1319}\eta^3 \right) (\Lambda_1 - \Lambda_2) \right],\end{aligned}\quad (2.59)$$

where we assumed $m_1 > m_2$.

$\tilde{\Lambda}$ and $\Delta\tilde{\Lambda}$ determine the tidal phase contribution to the 5PN and 6PN order, respectively, therefore their effect appears in the high-frequency part of the GW signal, starting from a hundred Hz. Being the leading order, $\tilde{\Lambda}$ is usually much better constrained than $\Delta\tilde{\Lambda}$. In principle, both $\tilde{\Lambda}$ and $\Delta\tilde{\Lambda}$ are needed in order to determine the tidal deformabilities $\Lambda_{1,2}$ of both NSs, but in the `NRTidal` (as well as in the `NRTidalv2`) model the system is assumed to have equal masses and hence, assuming the same EOS for both NS, the same tidal deformability, $\Lambda_1 = \Lambda_2$. The analysis of GW170817 data with the `IMRPhenomD_NRTidalv2` model already allowed us to place some constraints on the measurement of $\tilde{\Lambda}$ and, consequently, on the EOS [73].

2.2 Bayesian inference

Once a GW signal is detected, a lot of information can be extracted from it. For example, we want to determine which kind of source emitted the signal and recover its parameters, or check whether the signal is consistent with the predictions of general relativity. Different analyses have been developed to investigate multiple aspects of the GWs signals and sources, usually in the framework of Bayesian inference, which is the topic of this section.

2.2.1 Probabilities and Bayes theorem

The probability of a proposition or event A , defined as a subset of the set of all outcomes of an experiment, tells us how likely A is to be true or to happen, and takes values between 0, corresponding to impossible, to 1, corresponding to certain. The sum of probabilities of all possible outcomes is 1 by definition. Two events are defined to be *mutually exclusive* when their joint probability is $P(A \cap B) \equiv P(A, B) = 0$ and *independent* when $P(A \cap B) \equiv P(A, B) = P(A)P(B)$. Finally, for two mutually exclusive events, the probability of event A or event B to happen is simply $P(A \cup B) = P(A) + P(B)$.

From these “rules” we can define the conditional probability of an event A occurring given another event B as¹¹

$$P(A|B) = \frac{P(A \cap B)}{P(B)}. \quad (2.60)$$

¹¹Since probabilities are not absolute, but related to the context in which they are measured, every probability is conditioned to whatever background information I is available at the moment of performing the experiment. Therefore, in principle, each probability should be expressed as $p(A|I)$, $p(B|I)$, $p(A|B, I)$, and so on, but here we drop the I -conditioning to simplify notation.

There exist two different approaches to statistics: *Bayesian* and *frequentist*. In Bayesian statistics, probabilities μ are random variables with a probability distribution $p(\mu)$. Based on some prior knowledge, we might have some degree of belief in $p(\mu)$ before the experiment, and we use the data to update our knowledge about $p(\mu)$. On the other hand, frequentist statistics considers probabilities as fixed values and does not incorporate any prior knowledge. The probability μ is determined through the experiment, as the frequency of specific outcomes; with more and more repetitions of the experiment, the collected data sample gets closer and closer to the true population distribution. Although both approaches are employed in different branches of physics, the frequentist one assumes that we have access to multiple realizations of the same experiment, which allows us to “count” the different outcomes. This is not possible in GW physics, where we have access to data only from single events. Therefore, in GW data analysis usually a Bayesian approach is adopted.

Bayesian statistics is based on *Bayes theorem*, which can be derived from Eq. 2.60

$$P(A|B) = \frac{P(B|A)P(A)}{P(B)}. \quad (2.61)$$

Essentially, Bayes theorem shows how our prior knowledge about something, in this case about the event A , is updated thanks to the data B , resulting in the posterior knowledge $P(A|B)$.

Given a set of mutually exclusive and exhausting events B_i , where the latter condition simply means that $\sum_i P(B_i) = 1$, the *marginalization rule* states

$$P(A) = \sum_i P(A, B_i). \quad (2.62)$$

Probability distributions can be discrete, when we assign a probability value to each outcome, or continuous, when we evaluate them for a continuum of values in a given range. A continuous probability for a variable x is described by a *probability density function* $pdf(x)$, defined as

$$P(x \in [a, b]) = \int_a^b pdf(x) dx. \quad (2.63)$$

In this case, the marginalization rule becomes

$$pdf(x) = \int pdf(x, y) dy. \quad (2.64)$$

2.2.2 Parameter estimation

In the context of GW data analysis, Bayes theorem can be employed to find the probability of specific values for the source’s parameters, given the observed detector data d and under the hypothesis \mathcal{H} . \mathcal{H} represents a hypothesis regarding the signal in the data, for example if it was generated from a BNS or BBH system; in parameter estimation (PE) analyses, usually \mathcal{H} corresponds to the waveform model employed to analyze the data.

Equation. 2.61 can be formulated as:

$$p(\vec{\theta}|\mathcal{H}, d) = \frac{p(d|\mathcal{H}, \vec{\theta})p(\vec{\theta}|\mathcal{H})}{p(d|\mathcal{H})}, \quad (2.65)$$

where $\vec{\theta}$ denotes the set of parameters. The posterior probability $p(\vec{\theta}|\mathcal{H}, d)$ represents the probability density function of a specific set of parameters values $\vec{\theta}$, given the data d and the hypothesis \mathcal{H} . The *prior* probability density $p(\vec{\theta}|\mathcal{H})$ encodes our prior knowledge about the source or the model: for example, if our hypothesis is that the signal was produced by a BNS system, we know that the component masses will be in the range $[1 - 3] M_\odot$, not larger. The *evidence*, or *marginal likelihood*, $p(d|\mathcal{H})$ describes the probability of observing the data d given the model \mathcal{H} , independently of the specific choice of parameters $\vec{\theta}$; for PE purposes, it just serves as a normalization factor. It is determined by the requirement that probability must be normalized

$$\int d^N \theta p(\vec{\theta}|d, \mathcal{H}) = 1, \quad (2.66)$$

with N being the total number of parameters, and is given by

$$p(d|\mathcal{H}) = \int d\vec{\theta} p(d|\mathcal{H}, \vec{\theta}) p(\vec{\theta}|\mathcal{H}), \quad (2.67)$$

where the integral is performed over the whole parameter space. The *evidence*, however, constitutes the key ingredient in model selection and hypothesis ranking, as we shall see in Sec. 2.2.4. Finally, the likelihood $p(d|\mathcal{H}, \vec{\theta})$ represents the probability of observing the data d with the specific set of parameters $\vec{\theta}$ and model \mathcal{H} . Assuming that the data consists of Gaussian noise $n(t)$ and a GW signal $h(t, \vec{\theta})$, cf. Eq. 1.92, where now the detector output is denoted by d , in the frequency domain the likelihood takes the form [219]

$$p(d|\mathcal{H}, \vec{\theta}) \propto \exp \left[-\frac{1}{2} \langle d - h(\vec{\theta}) | d - h(\vec{\theta}) \rangle \right], \quad (2.68)$$

with the GW signal $h(\vec{\theta})$ depending on the source parameters. In Eq. 2.68, $\langle a|b \rangle$ indicates the noise-weighted inner product defined in Eq. 1.102 as

$$\langle a|b \rangle \equiv 4\Re \int_{f_{\text{low}}}^{f_{\text{high}}} \frac{\tilde{a}^*(f) \tilde{b}(f)}{S_n(f)} df, \quad (2.69)$$

with $S_n(f)$ the noise spectral density, $\tilde{a}(f)$ the Fourier transform of $a(t)$, and $*$ denoting the complex conjugate.

2.2.3 Characterizing and combining posteriors

The posterior probability density $p(\vec{\theta}|\mathcal{H}, d)$ contains information about all the N parameters in $\vec{\theta}$. Therefore, once obtained $p(\vec{\theta}|\mathcal{H}, d)$, we need to extract information about the single parameters θ_i . This is accomplished through the marginalization rule in Eq. 2.64 as

$$p(\theta_i|\mathcal{H}, d) = \int d\vec{\lambda} p(\vec{\theta}|d, \mathcal{H}) \quad \text{for } \vec{\lambda} = \vec{\theta} \setminus \theta_i. \quad (2.70)$$

Equation 2.70 allows us to get the one-dimensional posterior distribution for each of the parameters in the set $\vec{\theta}$. From such distribution, one can compute point estimates, i.e., significant values providing the best estimate of the parameter given its posterior, like the *mean* value

$$\theta_i^{\text{mean}} = \int_{\theta_i^{\text{min}}}^{\theta_i^{\text{max}}} d\theta_i p(\theta_i|d, \mathcal{H}), \quad (2.71)$$

or the *median* value θ^{median} , defined through

$$\frac{1}{2} = \int_{\theta_i^{\min}}^{\theta_i^{\text{median}}} d\theta_i p(\theta_i|d, \mathcal{H}). \quad (2.72)$$

The width of the posterior distribution indicates how well the parameter is constrained and provides the uncertainty on the point estimate values. We can define a γ -*credible interval* as the interval $[\theta_i^{\text{low}}, \theta_i^{\text{high}}]$ in which a parameter θ_i falls with probability γ :

$$\gamma = \int_{\theta_i^{\text{low}}}^{\theta_i^{\text{high}}} d\theta_i p(\theta_i|d, \mathcal{H}), \quad (2.73)$$

where θ_i^{low} and θ_i^{high} are defined as

$$\frac{1}{2}(1 - \gamma) = \int_{-\infty}^{\theta_i^{\text{low}}} d\theta_i p(\theta_i|d, \mathcal{H}) \quad \text{and} \quad \frac{1}{2}(1 - \gamma) = \int_{\theta_i^{\text{high}}}^{+\infty} d\theta_i p(\theta_i|d, \mathcal{H}). \quad (2.74)$$

The most commonly used credible intervals are 90%, 68% or 95%, with the last two corresponding, respectively, to the 1- σ and 2- σ standard deviation intervals for a Gaussian probability distribution.

It has been shown [220] that, under the correct prior assumptions, these credible intervals actually represent the confidence we have in the recovered parameters, and therefore are consistent with the frequentist confidence intervals. In frequentist analysis, the γ -confidence interval represents the range in which we expect the outcome to be γ times out of the total number of realizations.

If we have data from N independent events d_1, d_2, \dots, d_N with measurements of the same set of parameters $\vec{\theta}$, we can combine their information to obtain tighter constraints on $\vec{\theta}$ by computing the *combined posterior*

$$p(\vec{\theta}|d_1, d_2, \dots, d_N, \mathcal{H}) = \frac{p(d_1, d_2, \dots, d_N|\vec{\theta}, \mathcal{H})p(\theta|\mathcal{H})}{p(d_1, d_2, \dots, d_N|\mathcal{H})}. \quad (2.75)$$

Since the N measurements are independent, their joint probabilities are

$$p(d_1, d_2, \dots, d_N|\vec{\theta}, \mathcal{H}) = \prod_{i=1}^N p(d_i|\vec{\theta}, \mathcal{H}), \quad (2.76)$$

$$p(d_1, d_2, \dots, d_N|\mathcal{H}) = \prod_{i=1}^N p(d_i|\mathcal{H}) \quad (2.77)$$

and the combined posterior can be written as

$$\begin{aligned} p(\vec{\theta}|d_1, d_2, \dots, d_N, \mathcal{H}) &= p(\vec{\theta}, \mathcal{H}) \prod_{i=1}^N \frac{p(d_i|\vec{\theta}, \mathcal{H})}{p(d_i|\mathcal{H})} \\ &= p(\vec{\theta}, \mathcal{H})^{1-N} \prod_{i=1}^N p(\vec{\theta}|d_i, \mathcal{H}). \end{aligned} \quad (2.78)$$

2.2.4 Hypothesis ranking and model selection

One of the main applications of Bayesian analysis is comparing different hypotheses to investigate which one explains the data better. Let us consider two different hypotheses, \mathcal{H}_A and \mathcal{H}_B ; for example, one might represent a signal consistent with GR and the other one a signal with deviations from GR. For each one of them, the data yield a posterior distribution, which from Bayes theorem reads

$$p(\mathcal{H}_A|d) = \frac{p(\mathcal{H}_A)p(d|\mathcal{H}_A)}{p(d)}, \quad (2.79)$$

and same for hypothesis \mathcal{H}_B . In Eq. 2.79, $p(\mathcal{H}_A)$ denotes the prior associated with hypothesis \mathcal{H}_A and $p(d|\mathcal{H}_A)$ is the marginal likelihood, or evidence, of hypothesis \mathcal{H}_A , i.e., the denominator in Eq. 2.65. Model comparison is performed by considering the ratio between the posterior probabilities for the different hypotheses, also called *odds ratio*

$$\mathcal{O}_A^B = \frac{p(\mathcal{H}_B|d)}{p(\mathcal{H}_A|d)} = \frac{p(d|\mathcal{H}_B)p(\mathcal{H}_B)}{p(d|\mathcal{H}_A)p(\mathcal{H}_A)} = \mathcal{B}_A^B \pi_A^B. \quad (2.80)$$

The *prior odds* $\pi_A^B = p(\mathcal{H}_B)/p(\mathcal{H}_A)$ represents our prior degree of belief in the different hypothesis. If, before looking at the data, we have no reason to prefer one of the models, the prior odds is usually set to $\pi_A^B = 1$. The *Bayes factor* \mathcal{B}_A^B , on the other hand, is obtained from the evidence ratio, and, using Eq. 2.67, reads

$$\mathcal{B}_A^B = \frac{p(d|\mathcal{H}_B)}{p(d|\mathcal{H}_A)} = \frac{\int d\vec{\theta}_B p(d|\vec{\theta}_B, \mathcal{H}_B)p(\vec{\theta}_B|\mathcal{H}_B)}{\int d\vec{\theta}_A p(d|\vec{\theta}_A, \mathcal{H}_A)p(\vec{\theta}_A|\mathcal{H}_A)}. \quad (2.81)$$

In particular, we have distinguished between the set of parameters $\vec{\theta}_A$ for hypothesis \mathcal{H}_A and $\vec{\theta}_B$ for \mathcal{H}_B , because different models can have different sets of parameters. This leads us to the advantage of comparing models through *odds ratios* or *Bayes factors*:¹² it naturally embeds Occam's razor, the principle according to which, if two theories explain the data equally well, the simplest one is to be preferred. For example, if we compare one model, \mathcal{H}_1 , with one free parameter, and another model, \mathcal{H}_2 , with two free parameters, the second model will likely describe the data better, thanks to its additional degree of freedom. This will result in a higher likelihood for this model $p(d|\vec{\theta}_2, \mathcal{H}_2)$, which is however not "physical", i.e., due to the fact that \mathcal{H}_2 actually is the best theory for the data, but just a spurious effect of the additional degree of freedom. The Bayes factor, however, is computed as the ratio of the integrals over the parameters space of the likelihood times the parameters prior; therefore, a model with more parameters will have a larger parameter space and a "penalizing" prior that compensates the effect of the larger likelihood.

Also in this case, if we have a set of N independent observations d_1, d_2, \dots, d_N , we can combine Bayes factors, and consequently odds ratios, to obtain more stringent constraints

$$\mathcal{B}_A^{B(\text{comb})} = \frac{p(d_1, d_2, \dots, d_N|\mathcal{H}_B)}{p(d_1, d_2, \dots, d_N|\mathcal{H}_A)} = \frac{\prod_{k=1}^N p(d_k|\mathcal{H}_B)}{\prod_{k=1}^N p(d_k|\mathcal{H}_A)} = \sum_k \mathcal{B}_{A,k}^B, \quad (2.82)$$

where $\mathcal{B}_{A,k}^B$ denotes the Bayes factor from the k -th observation.

¹²If we have no initial preference for one of the models compared, and therefore $\pi_A^B = 1$, the Bayes factor is equivalent to the odds ratio, $\mathcal{O}_A^B = \mathcal{B}_A^B$. If, instead, one of the hypotheses is preferred due to our prior knowledge, we set $\pi_A^B = p(\mathcal{H}_B)/p(\mathcal{H}_A) = \alpha$. However, it just gives an overall scaling factor to the odds ratio.

2.3 Computational methods

Estimating posterior probability densities or evidences to perform Bayesian analyses as explained in the previous section can prove to be a very challenging task from the computational point of view. Likelihood or evidence evaluations require multidimensional integrals over the space of parameters $\vec{\theta}$: when dealing with CBCs, the GW signal depends on both the intrinsic parameters of the binary, e.g., masses and spins, and extrinsic ones, such as distance, inclination, and so on. For BBH systems, we are speaking of a total of 15 parameters, which become 17 for BNSs, since in this case we need to include also the NSs' tidal deformabilities. In addition, some analyses extend the existing models to allow for additional effects, for instance due to GR violations, hence further increasing the number of free parameters.

Approximation methods exist to predict the accuracy of measurements from GW data, like the Fisher matrix formalism, which we briefly describe below. Let us consider a signal h with a high SNR and generated from a source with parameters $\hat{\theta}^k$ in $\vec{\theta}$: if the priors are chosen constant over some parameter ranges, the posterior probability density will depend only on the likelihood. Assuming Gaussian and stationary noise, the likelihood can be approximated as a multivariate Gaussian centered on the true parameters' values $\hat{\theta}^k$

$$p(\vec{\theta}|d, \mathcal{H}) \propto p(d|\mathcal{H}, \vec{\theta}) \propto e^{-\frac{1}{2} \sum_{ij} \Gamma_{ij} \delta\theta^i \delta\theta^j}. \quad (2.83)$$

In Eq. 2.83, $\delta\theta^k = \theta^k - \hat{\theta}^k \simeq \theta^k - \theta_{\text{ML}}^k$, because, given the high SNR, the *maximum likelihood* (ML) values θ_{ML}^k , i.e., the parameter values at which the likelihood peaks, are assumed to correspond to the true parameter values. The Fisher matrix elements Γ_{ij} are computed as

$$\Gamma_{ij} = \left\langle \frac{\partial h}{\partial \theta^i} \left| \frac{\partial h}{\partial \theta^j} \right. \right\rangle_{\text{ML}}, \quad (2.84)$$

estimated at the maximum likelihood values $\vec{\theta}_{\text{ML}}$, and provide an estimate of the accuracy with which a parameter can be estimated. In this high-SNR scenario, the parameters distribution is approximated with a Gaussian centered at θ_{ML}^k and with standard deviation $\Delta\theta^k = \sqrt{\Sigma_{kk}}$, with Σ_{ij} being the variance-covariance matrix and Σ_{kk} the diagonal element corresponding the parameter k , with no summation implied. The inverse of the Fisher matrix yields the covariance matrix, $\Sigma_{ij} \equiv (\Gamma_{ij})^{-1}$, and thus the estimate of the uncertainty on the parameters recovery.

Although the Fisher matrix formalism supplies a very efficient way to evaluate measurement accuracy, it relies on the assumption that the signal has a very high SNR and, therefore, that the posterior distribution for $\vec{\theta}$ peaks at the maximum likelihood value $\vec{\theta}_{\text{ML}}$. However, in reality, we do not always deal with high-SNR signals, and the presence of noise in real interferometer data will cause a shift of $\vec{\theta}_{\text{ML}}$ with respect to the true parameters' values. Furthermore, we are not interested only in the estimated error for parameters measurements, but we want to recover realistic posterior distributions and compute the evidence. For this purpose, different techniques have been developed to extract information from the GW data. The direct computation of posteriors and evidences is usually not possible due to the high dimensionality of the parameter space, therefore sampling methods are employed, meaning

that the population's features are estimated from samples that form a subset of the population. In this section, we introduce two stochastic sampling methods, i.e., algorithms based on repeated random sampling, which are widely used in GW data analysis: nested sampling and Markov chain Monte Carlo (MCMC) sampling. Despite their efficiency, the computational cost of these algorithms becomes higher and higher with the increasing number of events, their SNR, and their duration, making it a crucial point to develop techniques to reduce the computational cost. Two of these methods, relative binning and reduced order quadratures, are introduced at the end of this section.

2.3.1 Nested sampling

The nested sampling algorithm, introduced by Skilling in 2006 [221], computes the evidence in Eq. 2.67

$$p(d|\mathcal{H}) = \int d\vec{\theta} p(d|\mathcal{H}, \vec{\theta}) p(\vec{\theta}|\mathcal{H}) \quad (2.85)$$

by evaluating the contributions of nested shells in the prior space volume and supplies posterior distributions as a byproduct. To simplify notation, following Ref. [221], we call the evidence Z , the likelihood function $p(d|\mathcal{H}, \vec{\theta}) = L = L(\vec{\theta})$, and the prior $p(\vec{\theta}|\mathcal{H}) = \pi(\vec{\theta})$; thus, Eq. 2.85 can be rewritten as

$$Z = \int L(\vec{\theta}) \pi(\vec{\theta}) d\vec{\theta}. \quad (2.86)$$

This multi-dimensional integral is substituted with a one-dimensional one by defining the prior mass

$$X(\lambda) = \int_{\vec{\theta}: L(\vec{\theta}) > \lambda} \pi(\vec{\theta}) d\vec{\theta} \quad (2.87)$$

as the integral over the prior volume of all parameter points $\vec{\theta}$ whose likelihood $L(\vec{\theta})$ is greater than a value λ . Since the prior $\pi(\vec{\theta})$ is normalized, $X(\lambda) \in [0, 1]$, where $X = 1$ represents the mass enclosed in the hypersurface where all points have likelihood greater than λ , i.e., λ corresponds to the minimum likelihood value $\lambda = L_{\min}$, while $X = 0$ corresponds to the situation where no point with a larger likelihood can be found, i.e., to $\lambda = L_{\max}$. This allows us to approximate Eq. 2.86 as

$$Z = \int_0^1 L(X) dX, \quad (2.88)$$

where $L(X)$ is the inverse of Eq. 2.87 and is a positive-valued, monotonically decreasing function of X . For a prior mass X within the prior parameter space enclosing all the points with likelihood smaller than λ , $L(X)$ is the likelihood of the points on the hypersurface that bounds the prior mass X .

Nested sampling finds, in the parameter space defined by the prior, points $\vec{\theta}_k$ with increasing values of likelihood L_k and decreasing prior mass X_k . From these samples, the evidence is computed by approximating the integral in Eq. 2.88 with a Riemann sum

$$Z \sim \hat{Z} = \sum_{k=0}^N f(L_k) \Delta X_k \equiv \sum_{k=0}^N \hat{w}_k, \quad (2.89)$$

where $\Delta X_k = X_{k-1} - X_k$ is the difference in prior mass, and the exact expression for the function $f(L_k)$ depends on the integration rule applied. For example, one can employ a trapezoidal integration

scheme with $f(L_k) = 1/2(L_{k-1} + L_k)$.

According to Bayes theorem, the parameters' posterior distribution, with the new notation, reads

$$p(\vec{\theta}|d, \mathcal{H}) = \frac{L(\vec{\theta})\pi(\vec{\theta})}{Z}. \quad (2.90)$$

Therefore, using the discrete approximation above, we can find the posterior distribution by assigning to each sample point $\vec{\theta}_k$ an *importance weight*

$$p(\vec{\theta}_k|d, \mathcal{H}) \equiv p_k \simeq \hat{p}_k = \frac{\hat{w}_k}{\sum_{k=0}^N \hat{w}_k} = \frac{\hat{w}_k}{Z}. \quad (2.91)$$

Basically, the posterior probability of a given set of parameters $\vec{\theta}_k$ corresponds to its relative contribution to the total evidence.

The nested sampling algorithm works as follows:

1. First, N_{live} *live points* $\{\vec{\theta}_1, \vec{\theta}_2, \dots, \vec{\theta}_{N_{\text{live}}}\}$ are randomly sampled from the prior and their likelihood computed.
2. The sample with the lowest likelihood, which we label as $\vec{\theta}_k$, is removed from the live points, i.e., it becomes a *dead point*, and its prior mass X_k is estimated statistically, then saved together with the point's likelihood L_k as (L_k, X_k) .
3. The evidence is increased by $Z_k = f(L_k)\Delta X_k$.
4. We randomly draw a new sample $\vec{\theta}_j$ from the prior, with the condition that $L(\vec{\theta}_j) > L_k$; in this way, we have again N_{live} live points.
5. We repeat the previous steps, finding a series of (L_k, X_k) values, with increasing values of likelihood L_k and decreasing values of prior mass X_k . The algorithm stops when a given termination condition is reached; an example of a possible termination condition will be provided later.

From the sequence of (L_k, X_k) values provided by the nested sampling algorithm, we can compute the evidence and the posterior distributions with Eq. 2.89 and Eq. 2.91.

Two main technical difficulties arise when implementing this algorithm. First, in step (2.) one needs to compute the prior mass. Calculating it explicitly turns out to be very challenging in the high-dimensional parameter space we are investigating. Therefore, the value of X_k at each step is estimated statistically. The underlying idea is that, since the sampled points are all drawn from the prior distribution, according to the *probability integral transform*,¹³ the prior mass, which technically is the cumulative distribution function of samples drawn from the prior with likelihood values $L > L_k$, follows a uniform distribution, $p(X) = U[0, 1]$. At the first iteration we set $X_0 = 1$, meaning that we are considering the maximum prior mass possible, enclosed by the hypersurface comprised by points

¹³The *probability integral transform* states that, if we draw random samples from a continuous (probability) distribution, their cumulative distribution function will follow a uniform distribution.

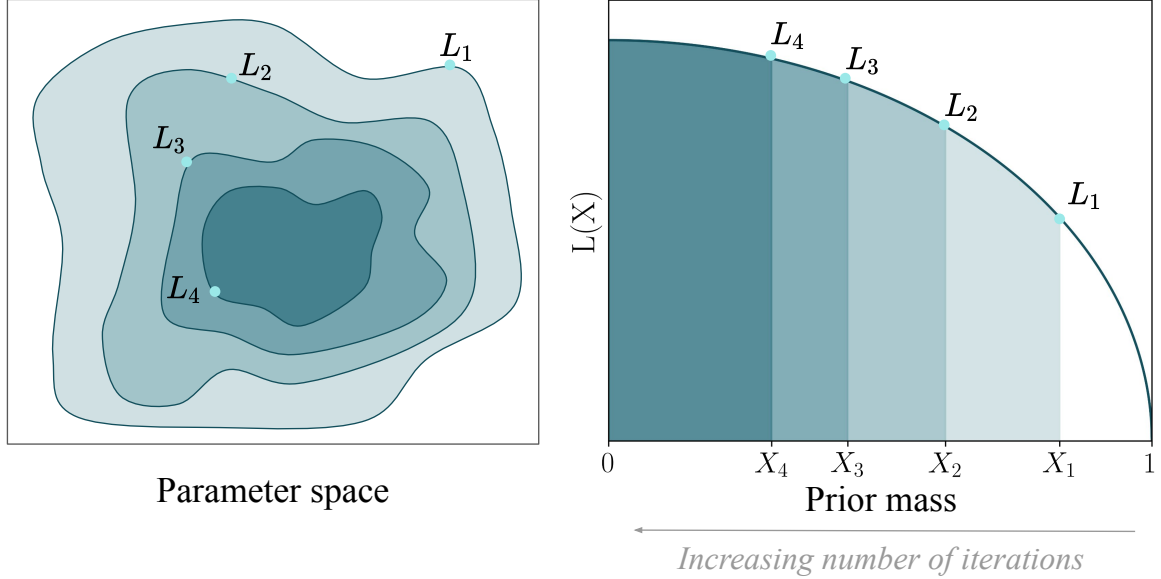


Figure 2.2: *Left:* Representation of likelihood hypersurfaces for different sampled points assuming one live point and a two-dimensional parameter space. *Right:* evolution of the likelihood as function of the prior mass $L(X)$, as introduced in Eq. 2.88; at each iteration of the algorithm, i.e., for subsequent dead points, the likelihood increases and the prior mass shrinks.

with the minimum likelihood. However, as we proceed, the points we remove from the live points will have increasing likelihood and decreasing corresponding prior masses, as shown in Fig. 2.2. Therefore, at each iteration, instead of computing the prior mass of the specific point $\vec{\theta}_i$, we pick a value of prior mass in $U[0, X_k]$, whith $k = i - 1$, since we know that the new prior mass must be $X_i < X_k$. In particular, if we have a set of N_{live} points, each one with prior mass X_i , the probability of having prior mass not larger than a value χ corresponds to the probability of having all prior masses $\{X_i\}$ smaller or equal to χ . Assuming the samples are independent, we can write

$$P(\{X_i\} \leq \chi) = \prod_{i=1}^{N_{\text{live}}} P(X_i \leq \chi). \quad (2.92)$$

Since the prior mass distribution, as we saw before, is uniform in $[0, 1]$, and for a uniform distribution the cumulative distribution function is

$$F(y) = \int_0^y dy' = y, \quad (2.93)$$

we have

$$\begin{aligned} P(\{X_i\} \leq \chi) &= \prod_{i=0}^{N_{\text{live}}} \int_0^\chi dX_i \\ &= \prod_{i=1}^{N_{\text{live}}} \chi = \chi^{N_{\text{live}}}. \end{aligned} \quad (2.94)$$

Finally, the probability density for the prior mass maximum value χ is given by

$$p(\chi) = \frac{d}{d\chi} P(\{X_i\} \leq \chi) = N_{\text{live}} \chi^{N_{\text{live}} - 1}. \quad (2.95)$$

Therefore, at each iteration, instead of computing the prior mass of the given point, we pick a value from the $p(\chi)$ distribution. Mathematically, from Eq. 2.95 we see that χ follows a beta distribution

$$p(\chi) = \text{Beta}(\chi; N_{\text{live}}, 1), \quad (2.96)$$

which represents the probability distribution of the maximum value of prior mass. Nested sampling implies that at each iteration we find a prior mass smaller than the previous one. Therefore, we set $X_0 = 1$, but for the following points the upper bound of the prior mass is determined by the prior mass of the last dead point, so $X_i \in [0, X_{i-1}]$. We define the *shrinkage ratio* $t = X_k/X_{k-1}$, which follows the same distribution

$$p(t) = \text{Beta}(t; N_{\text{live}}, 1). \quad (2.97)$$

In practical terms, at each iteration k we generate a beta distribution depending on the number of live points N_{live} , from which we randomly draw a value of the shrinkage ratio t_k , and we compute the prior mass as $X_k = t_k X_{k-1}$.

This shrinking effect of the prior mass leads us to the second technical difficulty of this algorithm: drawing random and independent samples from the prior mass gets more and more difficult as X_k gets smaller. In principle, a brute force method would be to just pick a point, compute its likelihood and reject it if it does not satisfy the constraint $L(\vec{\theta}_k) > L(\vec{\theta}_{k-1})$. However, one can easily see how this becomes more and more inefficient as L_k increases and X_k decreases. Different nested sampling algorithms employ different techniques to overcome this issue, for example by “guessing” the distribution of parameters in a likelihood shell from the distributions in the previous ones [219, 222–224].

The statistical approach to the evaluation of X_k through random draws of t_k from a beta distribution generates uncertainties on the estimated values. Nonetheless, the mean and standard deviation on the shrinkage ratio, considering large values of N_{live} , read

$$\langle t \rangle = \frac{N}{N+1} \approx 1 - \frac{1}{N} \approx e^{-1/N} \quad (2.98)$$

$$\sigma_t^2 = \frac{N}{(N+1)^2(N+2)} \approx \frac{1}{N^2}. \quad (2.99)$$

Therefore, the uncertainty on t decreases with increasing N_{live} and, if we choose a sufficiently large number of live points, typically of the order $\mathcal{O}(10^3)$, it becomes negligible. This justifies the statistical evaluation of t , but in the end we are interested in the parameters’ posterior and in the Bayes factors, whose statistical error generally does not become negligible even by increasing the number of live points (cf. Fig. 4 in Ref. [219]).

The final missing piece is the algorithm termination criterion. At each iteration, the remaining evidence is approximated with

$$\Delta \hat{\mathcal{Z}}_k \approx L_{\max,k} X_k, \quad (2.100)$$

where $L_{\max,k}$ is the likelihood of the point with the maximum likelihood among the remaining live points. The idea is to stop when the evidence is estimated with the desired accuracy, which is translated into a threshold on the log-ratio between the estimated and the remaining evidence

$$\epsilon < \Delta \ln \hat{Z}_k \equiv \ln \left(\frac{\hat{\mathcal{Z}}_k + \Delta \hat{\mathcal{Z}}_k}{\hat{\mathcal{Z}}_k} \right). \quad (2.101)$$

The value $\epsilon \ll 1$ is chosen arbitrarily. This criterion essentially means that we stop the algorithm when we think that the maximum contribution that could come by adding sample points is negligible, i.e., a fraction ϵ , compared to the evidence accumulated up to that point.

2.3.2 Markov chain Monte Carlo

With a different approach, the MCMC method samples directly the posterior distribution, without need to compute the evidence first. Markov chain processes define a sequence of states of a system, in which each state X_i depends on the previous one X_{i-1} and *only* on the previous one, meaning that all the earlier states $X_{i-2}, X_{i-3} \dots$ play no role in determining X_i . Markov chains are usually characterized by a *transition matrix* M , a square matrix that describes the probability of transition from one state to another, and a *stationary distribution* ξ , i.e., a probability distribution that does not change over time: $\xi = \xi M$. The existence of a stationary distribution for a transition matrix M relies on the *detailed balance* condition¹⁴In general, “detailed balance” refers to systems that can be decomposed into elementary processes and indicates that, at equilibrium, every process is in equilibrium with its reverse. which requires that the transformation matrix M satisfies the reversibility condition

$$\xi_i M_{ij} = \xi_j M_{ji} \quad \forall i, j. \quad (2.102)$$

This condition is necessary to ensure that

$$\{\xi M\}_j = \sum_i \xi_i M_{ij} = \sum_i \xi_j M_{ji} = \xi_j, \quad (2.103)$$

where in the last step we used the fact that the sum of transition probabilities from one state to all possible states is normalized to 1, i.e., $\sum_j M_{ij} = 1$, and therefore that $\xi M = \xi$. If, for a given Markov chain, a unique stationary distribution is guaranteed to exist, the process is called “ergodic”. In GW data analysis, the stationary distribution is the posterior distribution we want to estimate. In particular, MCMC techniques employed in GW data analysis usually are Metropolis-Hastings MCMC algorithms [225, 226], whose basic workflow is outlined in the following.

The algorithm begins by choosing a random point $\vec{\theta}$ in the prior $\pi(\vec{\theta})$. Then, the next point is generated from the *proposal distribution* $Q(\vec{\theta}'|\vec{\theta})$, which provides the conditioned probability of the new point $\vec{\theta}'$ given the current point $\vec{\theta}$.¹⁵ We compare the posterior probability of the new and the

¹⁴,

¹⁵For example, in a basic Metropolis algorithm, the proposal function is a simple Gaussian; however, the proposal function represents the key component in MCMC sampling and determines the algorithm’s efficiency, therefore more sophisticated distributions are usually employed.

starting point by assessing their ratio

$$r_{\text{acc}} = \frac{p(\vec{\theta}'|\mathcal{H}, d)}{p(\vec{\theta}|\mathcal{H}, d)} = \frac{L(\vec{\theta}')\pi(\vec{\theta}')}{Z} \frac{Z}{L(\vec{\theta})\pi(\vec{\theta})} = \frac{L(\vec{\theta}')\pi(\vec{\theta}')}{L(\vec{\theta})\pi(\vec{\theta})}. \quad (2.104)$$

Equation 2.104 shows clearly why Metropolis-Hastings MCMC algorithms do not need evidence calculations. We either accept the new point $\vec{\theta}'$, and thus append it to the list of samples, or reject it, in which case we append $\vec{\theta}$ to the samples list. In both cases, we repeat the procedure, using as starting point the one added to the set of samples.

In order to find a criterion to decide whether or not to accept the new point $\vec{\theta}'$, let us consider again the detailed balance equation, which can be written as

$$p(\vec{\theta}|\mathcal{H}, d)M_{\theta\theta'} = p(\vec{\theta}'|\mathcal{H}, d)M_{\theta'\theta}. \quad (2.105)$$

The probability to transition from state $\vec{\theta}$ to $\vec{\theta}'$, denoted by $M_{\theta\theta'}$, is divided into the two steps that we just mentioned: i) make a proposal for $\vec{\theta}'$, and ii) accept $\vec{\theta}'$ with an *acceptance probability* α . Therefore, the detailed balance condition can be decomposed as

$$\xi_i q_{ij} a_{ij} = \xi_j q_{ji} a_{ji}, \quad (2.106)$$

where q_{ij} is the proposal transition matrix, which, in our case, corresponds to the proposal distribution $Q(\vec{\theta}'|\vec{\theta})$, and a_{ij} represents the acceptance probability. In Ref. [226], Hastings proposed to choose

$$a_{ij} = \begin{cases} 1 & \text{if } \frac{\xi_j q_{ji}}{\xi_i q_{ij}} \geq 1 \\ \frac{\xi_j q_{ji}}{\xi_i q_{ij}} & \text{if } \frac{\xi_j q_{ji}}{\xi_i q_{ij}} \leq 1 \end{cases}, \quad (2.107)$$

which, in the algorithms applied to GW signals, means that the new point $\vec{\theta}'$ is accepted according to an *acceptance probability* defined as

$$\alpha = \min \left\{ 1, \frac{L(\vec{\theta}')\pi(\vec{\theta}')Q(\vec{\theta}'|\vec{\theta})}{L(\vec{\theta})\pi(\vec{\theta})Q(\vec{\theta}|\vec{\theta}')} \right\} = \min \left\{ 1, r_{\text{acc}} \frac{Q(\vec{\theta}'|\vec{\theta})}{Q(\vec{\theta}|\vec{\theta}')} \right\}. \quad (2.108)$$

Practically, if the probability of the new point $\vec{\theta}'$ is larger than the probability of $\vec{\theta}$, the point is accepted, otherwise we randomly decide whether to accept it or not. This decision is made by drawing a random number from a uniform distribution $u \in [0, 1]$: if $\alpha \geq u$ the point is accepted, otherwise rejected.

Introducing temperature

The procedure known as *parallel tempering* [227, 228] allows us to deal with multimodal probability distributions and to compute the evidence Z . Choosing an efficient proposal function $Q(\vec{\theta}'|\vec{\theta})$ becomes complicated when dealing with multimodal distributions, where large-likelihood regions are separated by low-probability ones, and moving from one to another is not straightforward for the sampler. The idea of parallel tempering is to run MCMC with different chains, typically 10 or 20, each chain with a different “temperature” T that modifies the likelihood and, consequently, the posterior as

$$p(\vec{\theta}|d, \mathcal{H})_T = L(\vec{\theta})^{1/T} \pi(\vec{\theta}), \quad (2.109)$$

with $T \in [1, T_{\max}]$. The chain with $T = 1$ samples the “true” posterior distribution, while for the other ones the effect of the $1/T$ factor is to smoothen the likelihood profile: a flatter likelihood is easier to explore, also if multiple peaks are present in the “original” one. The chains communicate between themselves by periodically proposing swaps of their location in the parameter space with the location of adjacent chains. In this way, the regions with high support found by the high-temperature chains, which in general are able to explore a wider region, can be investigated in more detail by the low-temperature chains. This swapping happens with an acceptance rate

$$r_s = \min \left(1, \left(\frac{L(\vec{\theta}_j)}{L(\vec{\theta}_i)} \right)^{\frac{1}{T_i} - \frac{1}{T_j}} \right), \quad (2.110)$$

with $T_i < T_j$.

MCMC algorithms do not directly compute the evidence as the nested sampling ones, but parallel tempering allows us to estimate its logarithm via *thermodynamic integration* [229–231]. Introducing the parameter $\beta = 1/T$, with $0 \leq \beta \leq 1$, where $\beta = 1$ corresponds to the “true” posterior and $\beta = 0$ to the prior distribution, the evidence is expressed as a function of temperature as

$$p(d|\mathcal{H}, \beta) = \int d\vec{\theta} p(d|\mathcal{H}, \vec{\theta})^\beta p(\vec{\theta}|\mathcal{H}). \quad (2.111)$$

Differentiating the logarithm of the evidence with respect to β , we recover the expectation value of $\ln(Z)$ for the chain with temperature $1/\beta$ from

$$\frac{d}{d\beta} \ln p(d|\mathcal{H}, \beta) = \langle \ln p(d|\mathcal{H}, \vec{\theta}) \rangle_\beta. \quad (2.112)$$

Therefore, the evidence logarithm can be obtained by integrating

$$\ln Z = \int_0^1 d\beta \langle \ln p(d|\mathcal{H}, \vec{\theta}) \rangle_\beta \simeq \sum_{\beta=1/T_{\max}}^{\beta=1} \Delta\beta \langle \ln p(d|\mathcal{H}, \vec{\theta}) \rangle_\beta, \quad (2.113)$$

which is quite straightforward to compute since $\langle \ln p(d|\mathcal{H}, \vec{\theta}) \rangle_\beta$ is simply calculated as the sample average for the chain with temperature $1/\beta$.

Thinning and burn-in

Adjacent samples collected with MCMC sampling are correlated, since each new sample is computed from the previous one, and this correlation can hinder the calculation of the statistical properties of the final probability distributions. In order to avoid such correlation, one typically keeps only one sample every τ steps, where τ is the *integrated autocorrelation time* of the chain and can be computed by various existing codes, e.g., Refs. [232, 233]. If N_s is the total number of accumulated samples, this *thinning process* leaves us with N_s/τ independent, i.e., not correlated, *effective samples*.

The stationary distribution of a Markov chain process does not depend on the sampling starting point. However, it takes a few iterations for the algorithm to achieve the stationary distribution, hence

the first samples accumulated are not guaranteed to be representative of the posterior distribution we want to sample. This “adjustment” phase is called *burn-in*, and the samples collected during this stage must be removed in order to avoid biases in the posterior distribution.

Termination condition and variable number of parameters

While in nested sampling we can define a clear, although to a certain extent arbitrary, termination condition, in MCMC we stop the simulation when the algorithm has sufficiently converged towards the posterior distribution. Different diagnostic methods have been developed in order to test convergence, both analytical and empirical (see for example Ref. [234] for a review). One of the most popular methods is the Gelman-Rubin statistic [235]: the underlying idea is that, if the sampler converged to the true distribution, all chains should be similar, since they should all resemble the stationary distribution, and one should find only small variations within the single chains, i.e., the chains should be almost stationary. This is evaluated by computing a coefficient R , with $R = 1$ meaning that the chain reproduces exactly the stationary distribution. In practice, this will never be the case, because it would require an infinite number of samples. Typically, the sampling algorithm is considered converged when R is close to 1, with the specific value depending on the context.

Finally, without going into details, we mention that there exists an extension of the MCMC algorithm, the Reversible Jump Markov chain Monte Carlo (RJMCMC) [236], which allows sampling over a parameter space with variable dimension, by jumping between subspaces. Its application is particularly useful in Bayesian model comparison, when, depending on the model, the parameters vector $\vec{\theta}$ has a non-fixed size. In GW data analysis, an example would be comparing a BBH model with a BNS model, since the latter includes also the tidal deformability parameters.

2.3.3 Reducing the computational cost

Stochastic sampling methods allow us to estimate both the parameters’ posterior probability density and the evidence needed for Bayesian hypothesis ranking. Nested and MCMC sampling resort to different solutions to overcome the computational challenge that a direct calculation of these quantities would imply. However, running this kind of analyses on GW data takes from days to months, depending on the features of the signal. The main computational bottleneck is the likelihood term, which in frequency domain is given by Eq. 2.68

$$\mathcal{L}(d|\mathcal{H}, \vec{\theta}) = p(d|\mathcal{H}, \vec{\theta}) \propto \exp \left[-\frac{1}{2} \langle d - h(\vec{\theta}) | d - h(\vec{\theta}) \rangle \right], \quad (2.114)$$

with the overlap integral $\langle \cdot | \cdot \rangle$ defined in Eq. 2.69

$$\langle a | b \rangle \equiv 4\Re \int_{f_{\text{low}}}^{f_{\text{high}}} \frac{\tilde{a}^*(f)\tilde{b}(f)}{S_n(f)} df. \quad (2.115)$$

Computing the likelihood integral requires many evaluations of the waveform, on a dense and uniform frequency grid in the range $[f_{\text{low}}, f_{\text{high}}]$, where the step df is the inverse of the signal duration and typically takes values between $df = 0.25$ Hz, for heavy BBHs, and $df \simeq 0.04$ Hz, for BNSs. Despite the ongoing effort to develop faster waveform approximants, the number of evaluations required,

$\mathcal{O}(10^6 - 10^7)$, and the size of the frequency grid still make these analyses computationally expensive. This issue will exacerbate with future detectors, whose improved sensitivity will lead to more, louder, and longer signals. The latter does not only include a larger number of BNSs detections: in the 3G detectors era, ET is expected to gain sensitivity down to 10 Hz and even lower. This will increase the range of the frequency grid over which the likelihood integral is computed, but it also implies that significantly more inspiral cycles will be in band, also for BBHs signals, increasing the duration of the detected GW signals; consequently, both the density and size of the grid will increase. Therefore, computational costs represent one of the primary challenges for GW data analysis with future detectors. In this section, we present two techniques that have been developed in order to reduce the computational cost of parameter estimation analyses, *relative binning* and *reduced order quadratures* (ROQs). Although with different procedures, the core idea of both these methods is to approximate the likelihood instead of calculating it explicitly.

Relative binning

The relative binning technique [237–239] relies on the assumption that the sets of parameters with a non-negligible posterior probability produce similar waveforms $h(f)$, whose ratio, therefore, varies smoothly in the frequency domain. If we choose a *reference* or *fiducial* waveform $h_0(f)$ that describes sufficiently well the data, and if we divide the frequency range $[f_{\text{low}}, f_{\text{high}}]$ in small bins, within each frequency bin $b = [f_{\text{min}}(b), f_{\text{max}}(b)]$ the ratio between the sampled (non-negligible) waveforms $h(f)$ and the fiducial one can be approximated by a linear function in frequency

$$r(f) = \frac{h(f)}{h_0(f)} = r_0(h, b) + r_1(h, b)(f - f_m(b)) + \dots, \quad (2.116)$$

with $f_m(b)$ being the central frequency of the bin b .

Considering a discrete frequency grid f_k , the overlap integral $\langle a|b \rangle$ in Eq. 2.69 can be approximated with the discrete form

$$\langle a|b \rangle \approx 4\Re\Delta f \sum_k \frac{\tilde{a}^*(f_k)\tilde{b}(f_k)}{S_n(f_k)}, \quad (2.117)$$

with $\Delta f = 1/T$, where T is the observation time, i.e., in this case, the signal duration.

The logarithm of the likelihood in Eq. 2.114 can be written as

$$\ln \mathcal{L}(d|\mathcal{H}, \vec{\theta}) = \frac{1}{2} \left[2\langle d|h(\vec{\theta}) \rangle - \langle h(\vec{\theta})|h(\vec{\theta}) \rangle - \langle d|d \rangle \right]. \quad (2.118)$$

Equation 2.118 includes two terms which require waveform evaluations, $\langle d|h(\vec{\theta}) \rangle$ and $\langle h(\vec{\theta})|h(\vec{\theta}) \rangle$. For frequency-domain waveforms, relative binning approximates these discrete overlap integrals as

$$\langle d(f)|h(f) \rangle \approx \sum_b (A_0(b)r_0^*(h, b) + A_1(b)r_1^*(h, b)), \quad (2.119a)$$

$$\langle h(f)|h(f) \rangle \approx \sum_b (B_0(b)|r_0(h, b)|^2 + 2B_1(b)\Re[r_0(h, b)r_1^*(h, b)]), \quad (2.119b)$$

where $A_0(b)$, $A_1(b)$, $B_0(b)$, and $B_1(b)$ are called *summary data* and are given by

$$A_0(b) = 4 \sum_{f \in b} \frac{d(f) h_0^*(f)}{S_n(f)/T}, \quad (2.120a)$$

$$A_1(b) = 4 \sum_{f \in b} \frac{d(f) h_0^*(f)}{S_n(f)/T} (f - f_m(b)), \quad (2.120b)$$

$$B_0(b) = 4 \sum_{f \in b} \frac{|h_0(f)|^2}{S_n(f)/T}, \quad (2.120c)$$

$$B_1(b) = 4 \sum_{f \in b} \frac{|h_0(f)|^2}{S_n(f)/T} (f - f_m(b)). \quad (2.120d)$$

The summary data are computed on the frequency grid with maximum resolution Δf , but only for the reference waveform $h_0(f)$. The overlaps for all the sampled waveforms $h(f)$ are then obtained from Eqs. 2.119a-2.119b and need only the calculation of the coefficients $r_0(h, b)$ and $r_1(h, b)$. One needs to compute these coefficients for each sampled waveform, but they can be determined from the values of $r(f)$ in Eq. 2.116 computed only at the edges of the frequency bin b . Therefore, relative binning allows to greatly reduce the number of waveform evaluations required for the analysis.

Binning scheme The next question is, how do we decide the binning of the frequency grid. The choice of the bins in which the waveform will be evaluated plays a crucial role and is dictated by the requirement that the differential phase change in each bin must be smaller than some threshold δ_ϕ :

$$|\delta\Psi_{\max}(f_{\max}(b)) - \delta\Psi_{\max}(f_{\min}(b))| < \delta_\phi, \quad (2.121)$$

with $\delta\Psi_{\max}(f)$ being the maximum phase change at a given frequency f . This condition ensures that the parameters obtained as perturbations of the fiducial waveform ones still yield a significant contribution to the likelihood. In Ref. [237], the binning is determined by expressing the GW signal phase as

$$\Psi(f) = \sum_i \alpha_i f^{\gamma_i}, \quad (2.122)$$

where, based on the PN approximation, each term i , characterized by a coefficient α_i and a frequency power γ_i , represents the effect of one or more parameters.¹⁶ To ensure small variations in the phase, the absolute value change of the α_i coefficient of each term in Eq. 2.122 can be at maximum

$$\delta\alpha_i^{\max} \approx 2\pi\chi/(f_{*,i})^{\gamma_i}, \quad (2.123)$$

with χ being a tunable factor, $f_{*,i} = f_{\max}$ for $\gamma_i > 0$ and $f_{*,i} = f_{\min}$ for $\gamma_i < 0$. Thus, from Eq. 2.122, the maximum phase difference at a given frequency is computed as

$$\delta\Psi_{\max}(f) = 2\pi\chi \sum_i (f/f_{*,i})^{\gamma_i} \text{sgn}(\gamma_i), \quad (2.124)$$

¹⁶In principle, the PN expression for the GW phase includes also logarithmic terms in frequency. However, Eq. 2.122 does not aim at reproducing the PN phase formula, but it just exploits the idea, derived from the PN theory, that different source's parameters yield a contribution to the phase proportional to different powers of frequency.

where the factor $\text{sgn}(\gamma_i)$ is introduced to take into account the case in which the signs combination of the α_i coefficients produce the maximum possible differential phase change. Although the phase expression in Eq. 2.122 originates from PN theory, we stress that this choice is made simply to obtain an analytical expression for $\delta\Psi_{\max}$, i.e., Eq. 2.124, which can be easily implemented in the relative binning algorithms. In the work presented in this thesis, we will use the relative binning technique also to analyze GW signals in regimes where the PN formalism is not valid. However, we will show in Sec. 5.3.5 that, as long as the frequency bins are chosen small enough to ensure a differential phase change below the desired threshold, it does not matter how the bins are computed, and the relative binning method can be employed.

Reduced order models and quadratures

The overlap integrals $\langle d|h(\vec{\theta}) \rangle$ and $\langle h(\vec{\theta})|h(\vec{\theta}) \rangle$ in Eq. 2.118, in their discrete form given in Eq. 2.117, include the sum over a frequency grid with a large number L of points, with $L \sim \text{int}([\text{f}_{\text{high}} - \text{f}_{\text{low}}]\text{T})$. Large values of L cause computational issues, not only in the calculation of the sum, but also because the waveform needs to be evaluated L times. The basic idea of a reduced-order model approach is to find a representation of the data with fewer degrees of freedom; well-known examples are the spectral value decomposition or the principal components analysis. A highly computationally efficient method, developed specifically for parameterized problems, is the *reduced basis* approach [240]. When applied to gravitational waveforms, a reduced basis denotes a representation of the waveform space for a given set of parameters, whose span can accurately reproduce all the waveforms in that space. In the frequency domain, a waveform $h(\vec{\theta}, f)$ can be approximated as

$$h(\vec{\theta}, f) \approx \mathcal{P}_{\mathcal{E}_m}[h(\vec{\theta}; f)] \equiv \sum_{i=1}^m \langle e_i | h(\vec{\theta}) \rangle e_i, \quad (2.125)$$

where the vectors in the reduced basis $\mathcal{E}_m = \{e_i\}_{i=1}^m$ are orthonormal with respect to the inner product, \mathcal{P} is a projection operator, and $\langle e_i | h(\vec{\theta}) \rangle$ the projection coefficients, identified through minimization of the error [241]

$$\left\| h(f; \vec{\theta}) - \sum_{i=1}^m \langle e_i | h(\vec{\theta}) \rangle e_i(f) \right\|^2. \quad (2.126)$$

Without going into details, since this technique will not be employed in the work presented in this thesis, we mention that a *reduced order quadrature* rule is obtained by identifying a suitable reduced-order-model model and inserting it into the equation for the overlap integral. For GW waveforms, one way to build ROQs [241–245] is with a combination of the *reduced basis* and *empirical interpolation* methods [246]. The speed-up obtained through ROQs can reach $\mathcal{O}(100)$ for the analysis of BNS signals.

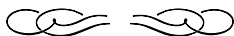
Relative binning and ROQs provide two different methods to approximate the likelihood and therefore accelerate its computation. The main caveat for ROQs resides in the need of computing beforehand the set of basis, which implies a computational cost. Moreover, since building a basis for the whole

parameter space results difficult, ROQs are usually built separately for different regions of the parameter space. These regions are identified with different chunks in chirp-mass values, which offer the great advantage of investigating regions of the template space where waveforms have a similar duration. However, this further division of the waveform space means an increased computational cost to find the reduced basis. On the other hand, ROQs produce very reliable results and ensure a great accuracy for the waveform representation. In addition, we do not need any information about the signal to analyze, apart from a crude estimate of the chirp mass, which is however usually provided by low-latency analyses, needed to decide which basis to employ, .

On the other hand, relative binning offers a fast tool to speed-up parameter estimation analyses, without the need to pre-compute anything. However, this approach requires a fiducial waveform that describes well the data and that can be difficult to infer when analyzing real events: although one can employ the parameters estimated in low-latency analyses to build the fiducial waveform, the signal might still involve “unpredicted” features which are not well described by the available models.

Both methods provide valid ways to reduce the computational cost of GW data analysis, especially for parameter estimation. Which one to employ strongly depends on the context: if we need to analyze a few simulated events, relative binning is the best choice, since we can easily find a fiducial waveform and the computational cost of building ROQs would not be compensated by the gain in the analysis of a few events. If, on the other hand, we want to analyze many events, especially real ones, and maybe repeat the analysis with different configuration settings, ROQs are to be preferred, considering their accuracy and the variety of signals, or settings, that we want to investigate.

Chapter 3



Testing general relativity using higher-order modes of gravitational waves from binary black holes

In Sec. 1.3.3, we discussed how the detection of GW signals allows us to perform various tests of GR in the strong-field regime. Among them, parameterized tests employ suitable parametrizations to look for deviations of GR related to specific effects, but not to specific alternative theories of gravity. For example, there exist tests that parametrize possible deviations from the coefficients in the PN expansion of the phase of the emitted GW signal; these parameters are introduced in the waveform model used for the analysis and estimated with a Bayesian inference [209, 247].

In this chapter, we present a new parametrized test of GR, designed to look for deviations of the amplitude of the subdominant modes in the GW signal from the values predicted by GR. The content of this chapter is based on the work in Ref. [248].

3.1 Introduction

As we discussed in Sec. 1.2.4, according to GR, the GW signal emitted by a coalescing binary system includes not only the fundamental quadrupolar mode, but also higher-order modes [27], whose contribution to the signal becomes non-negligible for high-mass and high-mass-ratio systems. During O3, strong evidence was obtained for the presence of higher-order modes in the gravitational wave signals GW190412 and GW190814 [16, 19, 249], which were emitted by coalescing binary compact objects with significantly different component masses. Measuring these subdominant harmonics of the basic signal enables more precise measurements of the source parameters, and can allow for stronger constraints on certain deviations from GR [32, 33].

Several tests of GR that directly probe the harmonic structure for binary black hole coalescences¹

¹Given the low mass of the lighter component of GW190814 ($\simeq 2.6 M_{\odot}$), there is a possibility that it was a signal from

were proposed in Refs. [252–255]. These fall into two categories. In the first case, one tests the phase evolution, e.g., by testing for deviations in the way parameters like the chirp mass and symmetric mass ratio enter into the expressions for the different harmonics [252]. This kind of test has already been applied to GW190412 and GW190814 in Ref. [256]. A second test looks for anomalies in the amplitudes of the subdominant modes [253]; the latter test is the focus of our work.

Specifically, defining $h(t) \equiv h_+(t) - i h_\times(t)$ with h_+ , h_\times the two polarizations, we saw in Sec. 1.2.4 that the GW signal from a coalescing binary can be written as

$$h(t; \iota, \phi_0, \vec{\lambda}) = \sum_{\ell=2}^{\infty} \sum_{m=-\ell}^{\ell} Y_{-2}^{\ell m}(\iota, \phi_0) h_{\ell m}(t; \vec{\lambda}), \quad (3.1)$$

where the $Y_{-2}^{\ell m}$ are spin-weighted spherical harmonics of weight -2 , (ι, ϕ_0) indicate the direction of the radiation in the source frame, and $\vec{\lambda}$ collects all other parameters in the problem. The latter are the total mass $M \equiv m_1 + m_2$ (with m_1, m_2 the component masses), the mass ratio $q \equiv m_1/m_2$ (where we assume $m_1 \geq m_2$), the dimensionless spin vectors \mathbf{S}_1 and \mathbf{S}_2 at some reference time t_{ref} , a reference phase φ_{ref} , and the luminosity distance D_L . The $h_{\ell m}$ will be referred to as the “modes” of the gravitational-wave signal. Taking the contribution with $\ell = 2$, $m = \pm 2$ to constitute the fundamental mode, the test of GR considered here follows Ref. [253] to allow for deviations in the amplitudes of the higher-order modes:

$$\begin{aligned} h(t; \iota, \phi_0, \vec{\lambda}) &= \sum_{m=\pm 2} Y_{-2}^{2m}(\iota, \phi_0) h_{2m}(t; \vec{\lambda}) \\ &+ \sum_{\substack{\text{HOM} \\ \ell}} \sum_{m=-\ell}^{\ell} (1 + c_{\ell m}) Y_{-2}^{\ell m}(\iota, \phi_0) h_{\ell m}(t; \vec{\lambda}), \end{aligned} \quad (3.2)$$

where HOM stands for the ℓ labels of the higher-order modes. The $c_{\ell m}$ are free parameters, to be measured together with all the other parameters in the problem; the case where GR is valid corresponds to $c_{\ell m} = 0$. Although for precessing signals one does not have the symmetry $h_{\ell-m} = (-1)^\ell h_{\ell m}^*$ [257], for definiteness we set $c_{\ell-m} = c_{\ell m}$. Here we will perform parameterized tests where the $c_{\ell|m|}$ are allowed to vary one by one, as in the phase-based tests performed in [21, 22, 258–260], and we will focus on modes that will usually be the strongest, namely the ones with $(\ell, |m|) = (3, 3)$ and $(\ell, |m|) = (2, 1)$. We will not only perform parameter estimation, as was done in Ref. [253], but also model selection; as we shall see, the latter will be of particular importance here.

To leading order, the observed strengths of the higher harmonics are set by the total mass M , the inclination angle ι , and the relative mass difference $\Delta \equiv (m_1 - m_2)/M$ [27, 162]. One aim of the work presented here is to investigate to what extent deviations in amplitudes of the harmonics can be determined depending on the values of these parameters, in terms of both parameter estimation and

a neutron star-black hole rather than a binary black hole coalescence [19], but studies based on the known properties of neutron stars make a BBH origin much more likely [250, 251]. For the purposes of this chapter we will assume that GW190814 came from a BBH coalescence.

model selection. Secondly, when performing tests that allow for non-zero $c_{\ell m}$, there will be correlations between these and the angular parameters, notably ι , which will affect both the measurability of the deviations from GR and the shapes of the posterior distributions. We will map out this interplay, which is necessary to interpret the results of our tests. Finally, for the first time we apply this test to GW190412 and GW190814.

3.2 Properties of higher harmonics and waveform model

Let us start by recalling some properties of the harmonics $h_{\ell m}$ in Eq. (3.1), which we will need to interpret the results in subsequent sections. In doing so we limit ourselves to qualitative statements, mostly referring to the inspiral regime; for explicit dependences on the parameters in the problem we refer to Refs. [27, 162]. The salient features relevant to us here are:

- (i) At zeroth post-Newtonian order (0PN) in amplitude there is the harmonic with $\ell = |m| = 2$, which is the most dominant of all multipole modes.
- (ii) At 0.5PN order in amplitude, harmonics with $(\ell, |m|) = (2, 1), (3, 3), (3, 1)$ appear. In the work presented here, we will be the most interested in the $(2, 1)$ and $(3, 3)$ harmonics, since the $(3, 1)$ harmonic is suppressed with respect to the others due to its small overall numerical prefactor. For purposes of testing GR we will also not consider harmonics that only appear at higher PN orders.
- (iii) The $(2, 1)$ and $(3, 3)$ modes are proportional to the relative mass difference $\Delta = (m_1 - m_2)/M$, so that they are more prominent for systems with a higher value of $q = m_1/m_2$.
- (iv) The fact that the harmonics enter the polarizations through the spin-weighted spherical harmonics $Y_{-2}^{\ell m}(\iota, \phi_0)$ causes their prominence to depend sensitively on the inclination angle ι , as illustrated in Fig. 3.1. For systems that are “face-on” ($\iota = 0$) or “face-off” ($\iota = 180^\circ$), only the fundamental harmonic is visible. The subdominant harmonics on which we will focus on are strongest around $\iota \simeq 50^\circ$ and $\iota \simeq 130^\circ$. In the figure we also indicate the peak likelihood values of ι for GW190412 and GW190814.
- (v) Finally, the observed power in the subdominant modes relative to that in the $(2, 2)$ mode increases with the total mass. During inspiral, at a given frequency f the ratios of the subdominant mode amplitudes to that of the dominant one grow with M through powers of $(Mf)^{1/3}$, though also the merger part of the signal and the shape of the noise power spectral density $S_n(f)$ will have an effect.

To make the latter point more concrete, let us define the quantities

$$\alpha_{\ell m} \equiv \frac{\int_{f_{\text{low}}}^{f_{\text{high}}} \frac{|\tilde{h}_{\ell m}(f; \vec{\lambda})|^2}{S_n(f)} df}{\int_{f_{\text{low}}}^{f_{\text{high}}} \frac{|\tilde{h}_{22}(f; \vec{\lambda})|^2}{S_n(f)} df}, \quad (3.3)$$

where $\tilde{h}_{\ell m}(f; \vec{\lambda})$ is the (ℓ, m) mode in the frequency domain, and $S_n(f)$ denotes the one-sided detector noise power spectral density, which we take to be the one for Advanced LIGO at design sensitivity

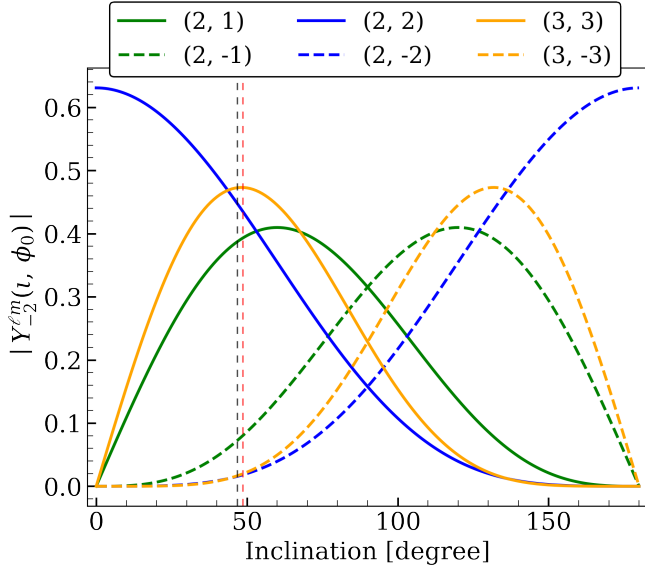


Figure 3.1: The absolute values of spin-weighted spherical harmonics of weight -2 as function of the inclination angle ι . The vertical lines indicate the peak likelihood values of ι for GW190412 (black dashed) and GW190814 (red dashed), located at $\simeq 47^\circ$ and $\simeq 49^\circ$, respectively [16, 19].

[111]. The integrals are evaluated from a lower cut-off frequency $f_{\text{low}} = 20\text{ Hz}$ to an upper cut-off frequency $f_{\text{high}} = 2048\text{ Hz}$, which amply suffices for the kinds of signals considered in this work. The waveform model is taken to be the most up-to-date phenomenological inspiral-merger-ringdown model **IMRPhenomXPHM** [205, 261], described in Sec. 2.1.4, which incorporates harmonics with $(\ell, |m|) = (2, 2), (2, 1), (3, 3), (3, 2), (4, 4)$ modes, as well as effects of spin-induced precession. Figure 3.2 shows the dependence of the $\alpha_{\ell m}$ on total mass M and mass ratio q , for $(\ell, m) = (2, 1), (3, 3)$, where, for simplicity, we have focused on binaries composed of non-spinning black holes. Note that $q = 3, 6, 9$ correspond to $\Delta \simeq 0.5, 0.71, 0.8$, respectively, which explains why the curves with $q = 6, 9$ are closer to each other than to the ones for $q = 3$.

3.3 Analysis framework and setup of simulations

We now explain our data analysis methodology for measuring source parameters and to rank hypotheses based on the available detector data. Next we will detail the choices made for simulations that were performed to understand the response of the analysis framework to possible violations of GR in the amplitudes of different harmonics.

3.3.1 Analysis framework

As discussed in Sec. 2.2, in a Bayesian setting the posterior probability density $p(\theta_k|d, \mathcal{H})$ for a particular parameter θ_k in the set of parameters $\vec{\theta}$ is obtained by integrating out all the other parameters $\vec{\xi}$ in $\vec{\theta} = (\theta_k, \vec{\xi})$:

$$p(\theta_k|d, \mathcal{H}) = \int d\vec{\xi} p(\theta_k, \vec{\xi}|d, \mathcal{H}). \quad (3.4)$$

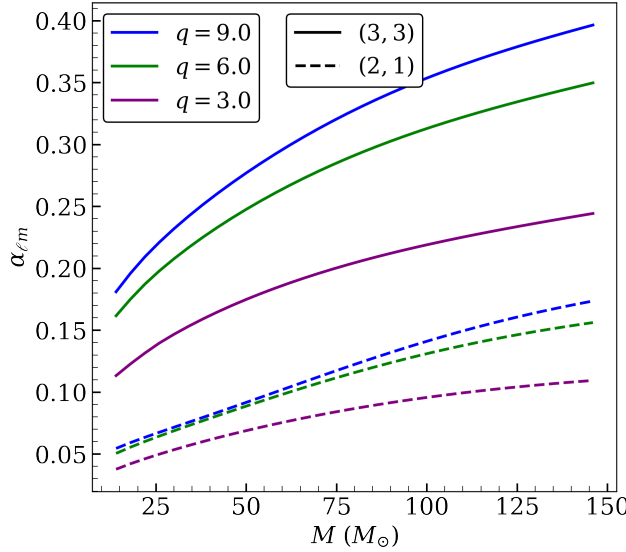


Figure 3.2: The relative signal power in the real part of $h_{\ell m}$ for some of the higher-order modes with respect to the dominant $(2, 2)$ mode, as a function of the total mass M of the binary, for three different values of the mass ratio q and assuming Advanced LIGO at design sensitivity.

Additionally, we will want to rank hypotheses: the GR hypothesis \mathcal{H}_{GR} versus hypotheses $\mathcal{H}_{\text{NonGR}}$, which allow one of the $c_{\ell m}$ to be non-zero. To this end we calculate Bayes factors, or ratios of evidences,

$$\mathcal{B}_{\text{GR}}^{\text{NonGR}} \equiv \frac{p(d|\mathcal{H}_{\text{NonGR}})}{p(d|\mathcal{H}_{\text{GR}})}, \quad (3.5)$$

where $p(d|\mathcal{H}_{\text{NonGR}})$ and $p(d|\mathcal{H}_{\text{GR}})$ are obtained using Eq. 2.67, taking \mathcal{H} to be $\mathcal{H}_{\text{NonGR}}$ or \mathcal{H}_{GR} , respectively. In practice it is usually convenient to focus on the logarithm of the Bayes factor, $\ln \mathcal{B}_{\text{GR}}^{\text{NonGR}}$, as will also be done here. To interpret the size of (log) Bayes factors, one could make use of the Jeffreys scale [262], in which $\mathcal{B}_{\text{GR}}^{\text{NonGR}} > 10^2$ (or $\ln \mathcal{B}_{\text{GR}}^{\text{NonGR}} \gtrsim 4.6$) would be deemed a “decisive” grade of evidence. Alternatively, one could construct a background distribution for $\ln \mathcal{B}_{\text{GR}}^{\text{NonGR}}$ from a large number of injections that are in accordance to GR (see e.g. [263]), though this is computationally costly. Here we mainly want to show trends; a more extensive treatment of (log) Bayes factors is left for future work.

It will also be important to consider the loudness of a signal as it appears in a detector. The optimal signal-to-noise ratio is defined as $\rho \equiv \langle h(\vec{\theta}) | h(\vec{\theta}) \rangle^{1/2}$, as introduced in Sec. 1.4.3. For a network of detectors, the combined optimal SNR is obtained by summing in quadrature the SNRs in the individual detectors.

Finally, for estimating the evidence integrals as in Eq. 2.67, and obtaining samples for posterior density distributions $p(\vec{\theta}|d, \mathcal{H})$, we used nested sampling [219, 221] as implemented in the LALINFERENCE package [220] of the LIGO Algorithms Library (LAL) software suite [77]. Both for simulated signals and for template waveforms we use **IMRPhenomXPHM**, with testing parameters $c_{\ell m}$ added as in Eq. (3.2) in the case of non-GR waveforms. For the purpose of our analyses, the free parameters are then the usual ones that enter a binary black hole signal, together with one of the $c_{\ell m}$ in the case of a non-GR hypothesis. The posterior density distribution for a $c_{\ell m}$ by itself is obtained from the joint posterior distribution by integrating out all other parameters, as in Eq. 3.4.

3.3.2 Setup of the simulations

To understand the response of our analysis pipeline to GR violations in mode amplitudes with various strengths, we add simulated signals, or injections, to synthetic stationary, Gaussian noise for a network of Advanced LIGO and Advanced Virgo detectors following the predicted noise spectral densities at design sensitivity [111, 112]. Since higher-order modes are more prominent for larger total masses, we will start by considering heavier BBH systems. However, later we will also analyze the real GW events GW190412 and GW190814 to look for GR violations. To this end, we also perform injections for lower-mass systems whose source parameter values and SNRs are set to the maximum-likelihood values obtained from analyses on these events that assumed GR to be correct. Specifically:

- We will inject signals with $M = 65 M_{\odot}$ and $M = 120 M_{\odot}$, for mass ratios $q = 3, 6, 9$. Here the inclination angle is fixed to be $\iota = 45^\circ$, and the network SNR to 25. For simplicity, in these injections we set the spins to zero, although, in general, the analyses presented here allow for non-zero, precessing spins.
- For GW190412-like injections, $M = 46.6 M_{\odot}$, $q = 4.2$, $\iota = 47^\circ$. Spin-related and other parameters are set to their maximum-likelihood values for the real event [16], so that, in particular, these injections have precessing spins. The network SNR is 19.8.
- For GW190814-like injections, $M = 27.6 M_{\odot}$, $q = 9.3$, $\iota = 49^\circ$; here too all parameters are set to the maximum-likelihood ones [19]. The network SNR is 25.

We also need to choose values for the deviation parameters c_{33} and c_{21} in the injections. Since the (3,3) mode will tend to be the strongest (see Fig. 3.2), we can expect smaller values of c_{33} to lead to detectable GR violations than for c_{21} , where ‘‘detectable’’ indicates that the 90% credible region of the posterior density function has support that excludes zero. We found that, at least for the higher masses listed above, the following choices provide examples ranging from non-detectability to easy detectability of the GR violations:

- $c_{33} = 0.5, 1.5, 3$.
- $c_{21} = 1, 3, 6$.

Hence these are the values for which we will show results in the next section.

3.4 Results of simulations, and analyses of GW190412 and GW190814

We now describe the results for our simulations, as well as for the real events GW190412 and GW190814, in terms of parameter estimation and hypothesis ranking. In doing so, it will be useful to make a distinction between the more massive BBHs ($M = 65, 120 M_{\odot}$), the injections with parameters similar to those of the real events, and the real events themselves.

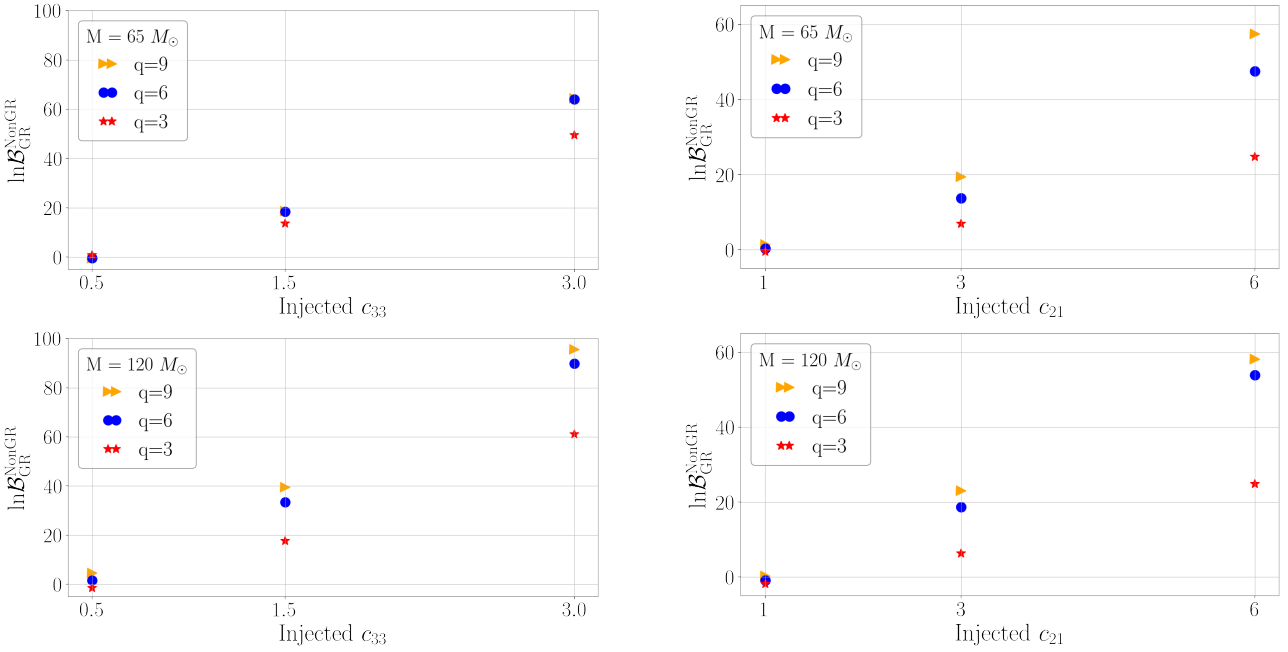


Figure 3.3: $\ln \mathcal{B}_{\text{GR}}^{\text{NonGR}}$ for $M = 65 M_{\odot}$ (top row) and $M = 120 M_{\odot}$ (bottom row), for different mass ratios q indicated by the differently shaped markers. The horizontal axes show the injected values of c_{33} (left column) and c_{21} (right column). In each case, the non-GR hypothesis has the corresponding $c_{\ell m}$ as free parameter.

3.4.1 More massive binary black holes

Let us first look at results for injections with $M = 65 M_{\odot}$ and $M = 120 M_{\odot}$. To have an easier overview it is convenient to first look at the behavior of log Bayes factors, $\ln \mathcal{B}_{\text{GR}}^{\text{NonGR}}$, which we do in Fig. 3.3. The trends are as follows:

1. As expected, for a larger injected $c_{\ell m}$, the log Bayes factor is larger. The cases $c_{33} = 0.5$ and $c_{21} = 1$ lead to $\ln \mathcal{B}_{\text{GR}}^{\text{NonGR}}$ that tend to be consistent with zero, meaning that the data are not sufficiently informative to clearly distinguish between hypotheses. However, starting from $c_{33} = 1.5$ or $c_{21} = 3$, the $\ln \mathcal{B}_{\text{GR}}^{\text{NonGR}}$ are significantly away from zero, and, as will be seen in terms of parameter estimation below, here the GR deviations tend to be detectable.
2. Higher values of M lead to higher $\ln \mathcal{B}_{\text{GR}}^{\text{NonGR}}$, consistent with there being more power in the higher-order modes relative to the $(2, 2)$ mode; see Fig. 3.2.
3. Again as expected, on the whole a larger mass ratio q tends to lead to a higher $\ln \mathcal{B}_{\text{GR}}^{\text{NonGR}}$, consistent with there being more power in the higher-order modes. We do see that the $\ln \mathcal{B}_{\text{GR}}^{\text{NonGR}}$ tend to differ less between $q = 6$ and $q = 9$ than between $q = 3$ and $q = 6$; in fact, for $M = 65 M_{\odot}$ and c_{33} , the log Bayes factors for the higher two values of q are nearly equal. Again pointing to Fig. 3.2, we note that the cases $q = 6$ and $q = 9$ are closer to each other than to $q = 3$ in terms of the power present in higher-order modes.

Figure 3.4 shows posterior probability densities for the corresponding injections. The trends show broad consistency with what we saw for the log Bayes factors. In particular, for the injected values

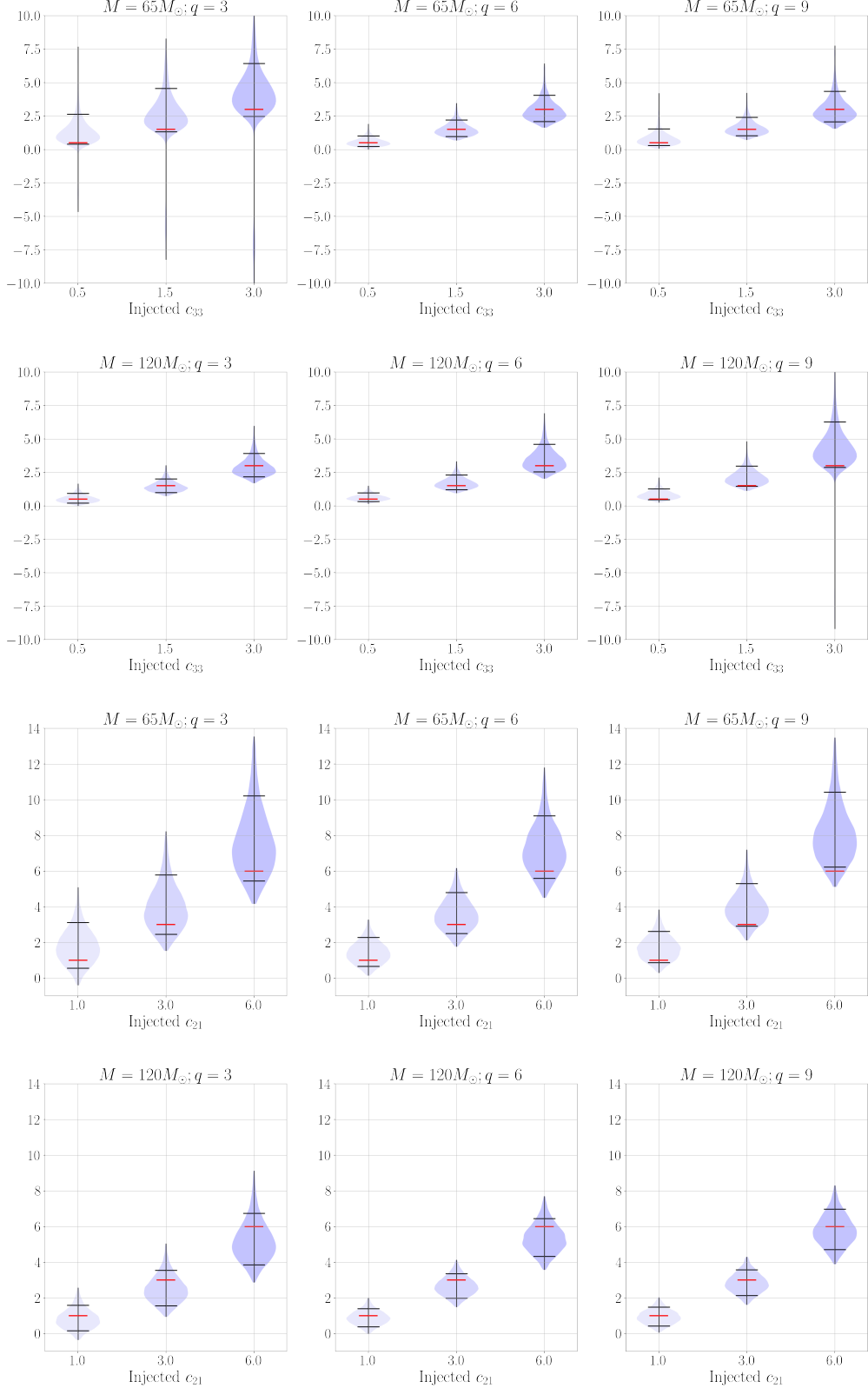


Figure 3.4: Violin plots for the posterior density distributions of c_{33} (top two rows) and c_{21} (bottom two rows), for $M = 65, 120 M_\odot$, and $q = 3$ (left column), $q = 6$ (middle column), and $q = 9$ (right column). In each case the black horizontal bars indicate 90% confidence intervals, and the red horizontal bar the injected value; the black vertical line shows the support of the posterior.

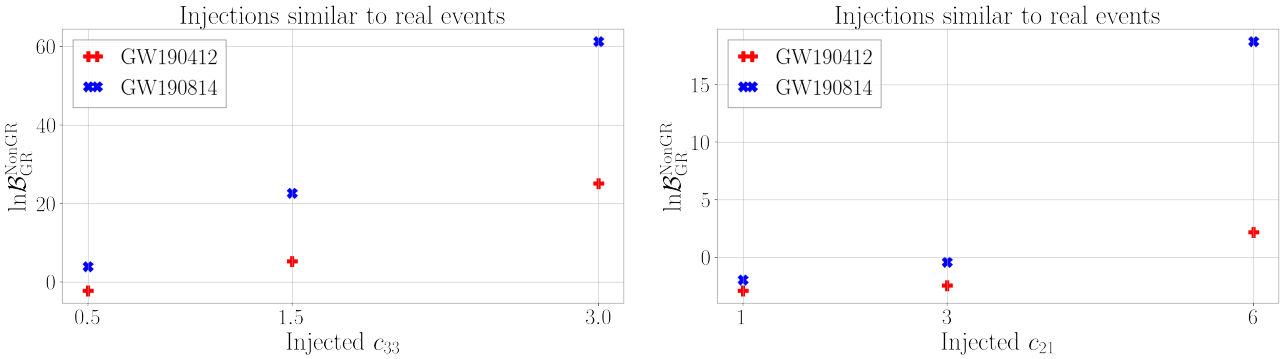


Figure 3.5: $\ln \mathcal{B}_{\text{GR}}^{\text{NonGR}}$ for injections with GR parameters similar to those of GW190412 and GW190814.

$c_{33} = 0.5$ and $c_{21} = 1$, posterior densities either include the GR value of zero, or extend to quite close to it, while, for higher injected values, the GR value tends to be outside the support of the distribution. Also, the 90% confidence intervals tend to be tighter for higher total mass and for higher mass ratio, again consistent with the behavior of the $\ln \mathcal{B}_{\text{GR}}^{\text{NonGR}}$ in Fig. 3.3, and indeed with Fig. 3.2.

3.4.2 Injections with parameters similar to those of GW190412 and GW190814

Next we turn to injections with GR parameters close to those of the real events GW190412 and GW190814. Figure 3.5 shows results for $\ln \mathcal{B}_{\text{GR}}^{\text{NonGR}}$. Here too the trends are as expected: the log Bayes factor increases with increasing injected values for c_{33} and c_{21} . Note that although GW190412 had a higher mass than GW190814 ($M = 46.6 M_{\odot}$ versus $M = 27.6 M_{\odot}$), the mass ratio of GW190412 was considerably smaller than that of GW190814 ($q = 4.2$ versus $q = 9.3$). The log Bayes factors are higher for the latter event, consistent with Fig. 3.2. We see that for GW190412 one has $\ln \mathcal{B}_{\text{GR}}^{\text{NonGR}} < 0$ for $c_{33} = 0.5$, and the same is true for both injections in the cases $c_{21} = 1$ and $c_{21} = 3$, presumably due to the lower mass ratios. We note that uncertainties on log Bayes factors can be expected to be of $\mathcal{O}(\text{few})$ [219]. Hence the small negative values can be interpreted as being consistent with zero, and the $\ln \mathcal{B}_{\text{GR}}^{\text{NonGR}}$ are uninformative in these cases.

Figure 3.6 shows posterior probability distributions for the same injections. In all cases, the injected value for c_{33} and c_{21} lies within the support of the posterior. For c_{21} the results look like what one might expect, but for c_{33} the posteriors are bimodal, with the true value not always lying in the strongest mode. As will be clarified in the next section, this behavior results from a partial degeneracy between c_{33} and the inclination angle ι .

3.4.3 Results for GW190412 and GW190814

Finally, we turn to the real events GW190412 and GW190814. Table 3.1 shows the results for $\ln \mathcal{B}_{\text{GR}}^{\text{NonGR}}$ when comparing the hypothesis of a non-zero c_{33} or c_{21} with the GR hypothesis. All the log Bayes factors are negative, so that we have no reason to suspect a violation of GR in the amplitudes of subdominant modes.

More interesting are the posterior distributions for c_{21} and especially c_{33} , which are shown in Figs. 3.7 and 3.8. For both events, the posterior for c_{21} is unimodal and consistent with the GR value

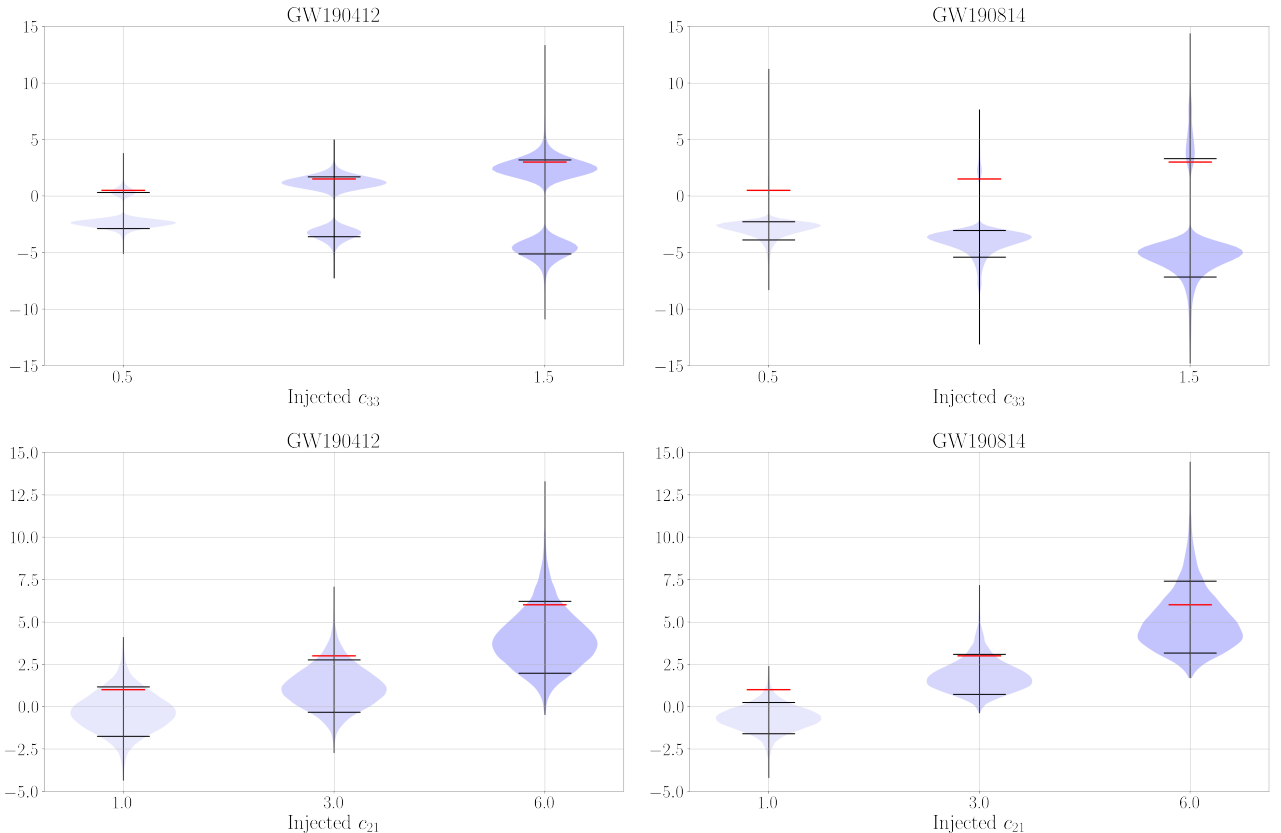


Figure 3.6: Violin plots for the posterior density distributions of c_{33} (top row) and c_{21} (bottom row), for injections similar to GW190412 (left column) and GW190814 (right column). In each case the black horizontal bars indicate 90% confidence intervals, and the red horizontal bar the injected value; the black vertical line shows the support of the posterior.

Event	GW190412	GW190814
c_{33}	-1.25	-3.96
c_{21}	-2.48	-1.77

Table 3.1: Values of $\ln \mathcal{B}_{\text{GR}}^{\text{NonGR}}$ for analyses of the real events GW190412 and GW190814.

of zero. However, just like in the simulations of the previous section, the posterior for c_{33} is bimodal, also for both events.

As it turns out, this bimodality results from a degeneracy between c_{33} and the inclination angle ι . The lower panels of Figs. 3.7 and 3.8 show *mismatches* between (a) a reference waveform $\tilde{h}_{\text{ref}}(f)$, which is a GR waveform with maximum-likelihood parameters for the respective signals, and (b) a waveform $\tilde{h}(c_{\ell m}, \iota; f)$ in which $c_{\ell m}$ and ι can take on arbitrary values, but all other parameters are the maximum-likelihood ones from the GR analysis. Specifically, we compute the mismatch

$$\text{MM} = 1 - \max_{t_0, \varphi_0} \frac{\langle h_{\text{ref}} | h(c_{\ell m}, \iota) \rangle}{\sqrt{\langle h_{\text{ref}} | h_{\text{ref}} \rangle} \sqrt{\langle h(c_{\ell m}, \iota) | h(c_{\ell m}, \iota) \rangle}}, \quad (3.6)$$

where the maximization is over a rigid time shift and overall phase.

In the bottom panels of Figs. 3.7 and 3.8, these mismatches are indicated with color coding, with dark colors signifying small mismatch. Overlaid are dashed lines indicating the peak-likelihood values in the (bimodal) posterior distribution for ι obtained when analyzing the events with either c_{21} or c_{33} as additional free parameters. Focusing first on the case of c_{33} and GW190412 in Fig. 3.7, we see that there are two regions in the (c_{33}, ι) plane where mismatches are low: one region that contains the GR value $c_{33} = 0$ and is consistent with the lower value of ι , and another region consistent with the higher ι value and $c_{33} \neq 0$. In either region, waveforms $h(c_{33}, \iota)$ are consistent with the reference waveform h_{ref} , which explains the bimodality in the posterior for c_{33} . By contrast, based on the analogous plot for (c_{21}, ι) , no such bimodality is to be expected, and, indeed, the posterior for c_{21} is unimodal. The corresponding Fig. 3.8 for GW190814 leads to similar conclusions.

3.5 Summary and conclusions

We have set up a Bayesian analysis framework to test GR by looking at the amplitudes of subdominant modes in GW signals from BBH coalescences, employing a state-of-the-art waveform model. Specifically, we allow for modifications in the amplitudes of the (3,3) and (2,1) modes, which tend to be the strongest among the subdominant modes. Apart from performing parameter estimation on the associated testing parameters c_{33} and c_{21} , this allows for hypothesis ranking between the presence and absence of such anomalies in the modes.

Results from simulations involving injected waveforms in stationary, Gaussian noise largely follow the trends one would expect based on the dependence of mode amplitudes on total mass and mass ratio: for similar SNRs, heavier and more asymmetric systems make it easier to find violations of GR of the type studied here.

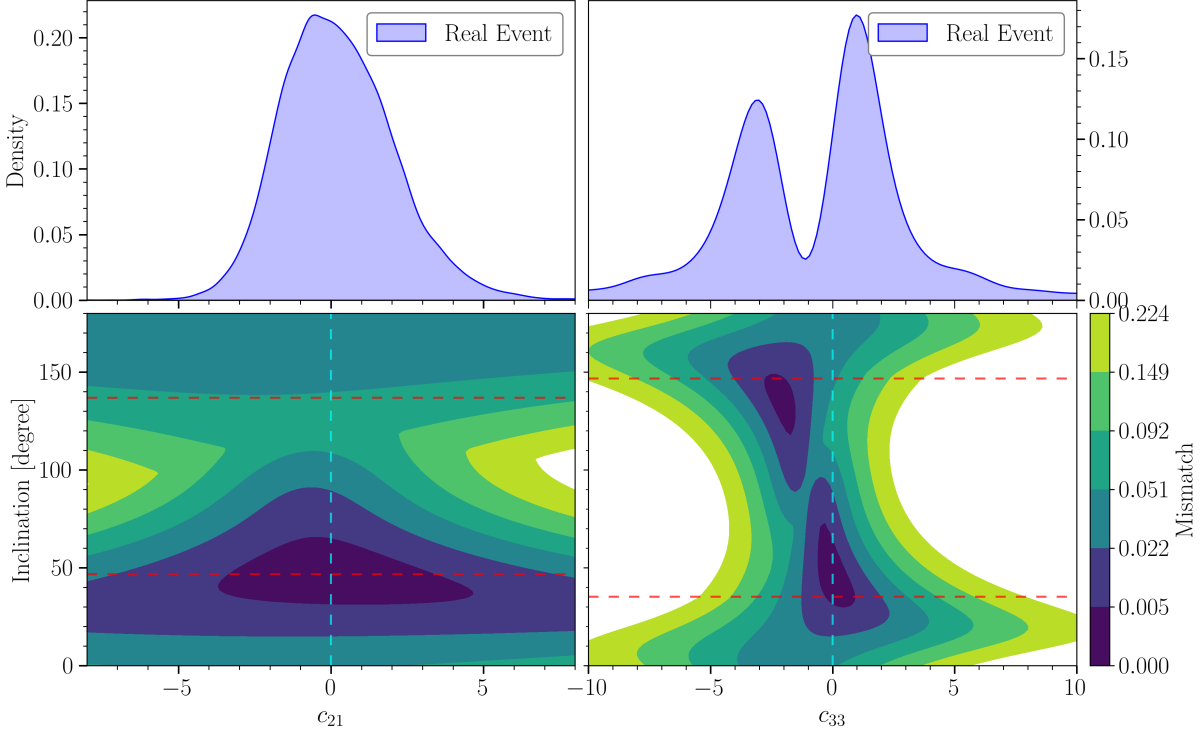


Figure 3.7: *Top panels:* Posterior density functions for c_{21} (left) and c_{33} (right) for GW190412. *Bottom panels:* Contours of constant mismatch between the maximum-likelihood GR waveform, and a waveform in which ι and c_{21} (left) or c_{33} (right) are varied while keeping all other parameters the same. The dashed vertical lines indicate the GR values $c_{21} = 0$ and $c_{33} = 0$, respectively, and the dashed horizontal lines indicate the peak-likelihood values for ι obtained from the analyses of GW190412 with respectively c_{21} and c_{33} as free parameters.

We then performed the first analysis of this kind on the real events GW190412 and GW190814, which were associated with significantly unequal component masses, and in which strong evidence for subdominant mode content had been found [16, 19, 249]. Log Bayes factors indicated no evidence for a GR violation in either the (2, 1) or (3, 3) mode. In the case where the (3, 3) mode was being investigated, the posterior density function for c_{33} , while being consistent with the GR value $c_{33} = 0$, did exhibit bimodality, but this was shown to result from correlations between c_{33} and the inclination angle ι . Since the bimodality was also present in c_{33} posterior densities for injections with parameters similar to the ones of GW190412 and GW190814 and $c_{33} \neq 0$, some caution is called for in interpreting such posteriors, at least for BBHs with total mass $M \lesssim 50 M_\odot$. However, our results show that log Bayes factors $\ln \mathcal{B}_{\text{GR}}^{\text{NonGR}}$, which were not considered in previous work in this context [253], are robust indicators for or against the presence of a violation of GR.

Even in systems with significantly asymmetric masses and high total mass, with second-generation detectors, GR violations have to be sizeable ($c_{33} \gtrsim 1.5$ and $c_{21} \gtrsim 3$) in order to be confidently detected. It will be of interest to see how the sensitivity of our method will improve going towards Einstein Telescope, Cosmic Explorer, and the space-based LISA [264], but this is left for future work.

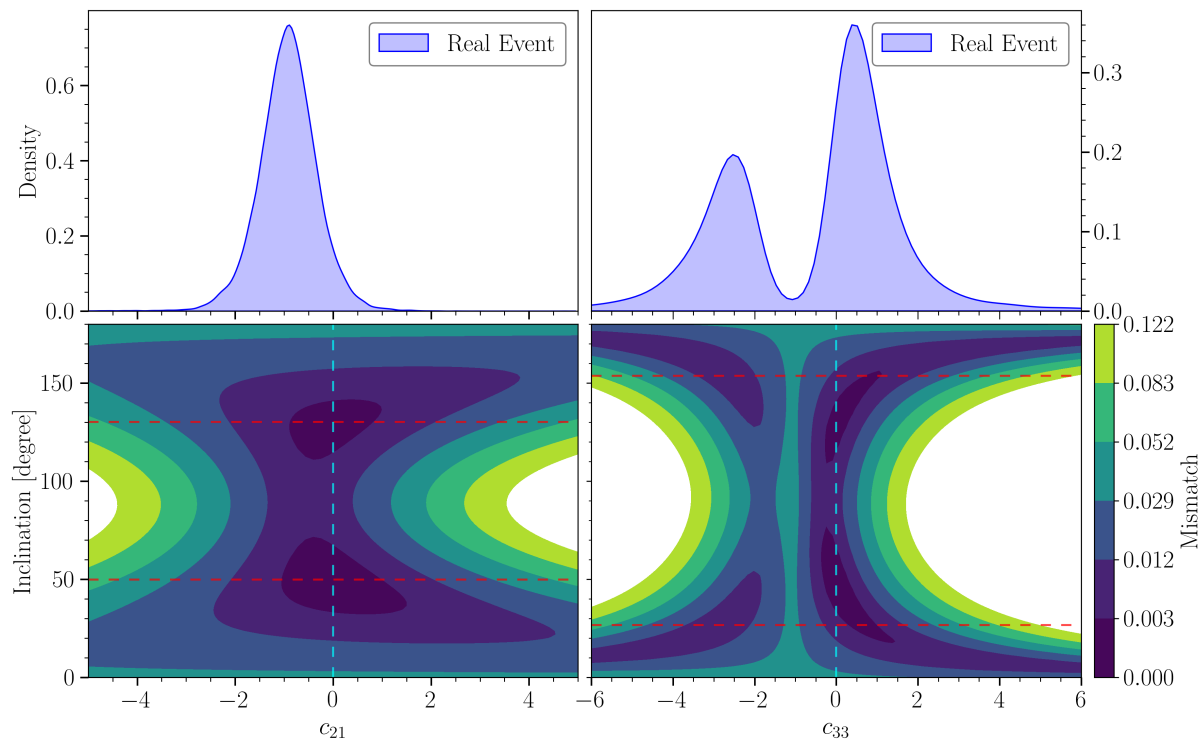
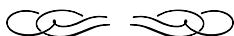


Figure 3.8: The same as in Fig. 3.7 but for GW190814.

Chapter 4



Comparing gravitational waveform models for binary black hole mergers through a hypermodels approach

Waveform models constitute a key ingredient not only in template-based searches, but also in GW analyses like parameter estimation. As described in Sec. 2.1, different approximation methods exist to derive waveform models. The increasing sensitivity and the consequent larger number of detections in future observing runs, and especially with future-generation detectors, will start showing potential systematics induced by different waveform models. A study of this possible systematic bias is therefore important not only to interpret upcoming results, but also to highlight a possible avenue for future waveform model development. In this chapter, based on Ref. [265], we employ a *hypermodels* approach to sample directly on four state-of-the-art binary black hole waveform models from different families, in order to quantify possible preferences between the models from the 13 heaviest GW sources with moderate to high signal-to-noise ratios in GWTC-3.

4.1 Introduction

With close to 90 significant observations of binary black hole mergers [14], hyperparameters characterizing population models [40] as well as more stringent bounds on strong-field gravity parameters from combining multiple events [20] have been estimated. Ongoing and future observing runs of the LVK collaboration will operate at higher sensitivities and enable us to see many more events. However, as the statistical biases reduce through improved detector sensitivities and by combining multiple events, the systematic effects from the GW models employed to analyze our data will start dominating. Several studies have been made to expose this problem with future-generation detectors, e.g., Ref. [266].

Typically, GWs' source properties are inferred by analyzing the data with multiple waveform

models where the estimates broadly agree. This serves as a consistency test between different models developed employing different techniques. Separate analyses are therefore performed on a single event to obtain estimates of the same. However, while individual sources may be consistent, combining the data may expose a bias or preference for one model over another. In this work, we infer the parameter properties of the 13 heaviest significant BBH observations by Advanced LIGO and Advanced Virgo in GWTC-3 and quantify the preference for one waveform model over another from the combined GW data. The choice of events is determined by the fact that, for one of the models employed, the region of validity covers only high values of the binary’s total mass; moreover, the shorter duration of signals produced by high-mass systems reduces the computational cost of the analysis. Reference [267] has looked at a very similar problem from a technical point of view, performing a joint Bayesian analysis with three different models on a large set of simulated events, showing consistent results with the ones obtained via a Bayesian model averaging method and with a significant gain in terms of computational cost. However, the analyzed signals were all simulations apart from one real GW event, GW200129_065458, also included in our suite of events. The focus of our work is instead on real events, with the goal to investigate possible systematic biases caused by the different waveform approximants. We employ four waveform models: `NRSur7dq4` [161], `IMRPhenomXPHM` [205], `IMRPhenomTPHM` [268], and `SEOBNRv4PHM` [187]. In Ref. [269], all the events in GWTC-3 are analyzed with the `NRSur7dq4` model, finding, in some cases, different results with respect to the ones obtained with the `IMRPhenomXPHM` and `SEOBNRv4PHM` models in the LVK analyses.

For our study, we focus on the method introduced in Ref. [270], henceforth referred to as *hypermodels*. The purpose of our study is to obtain a quantitative measure of selection, in this case by using the *odds ratio*, between one waveform and another from a combination of GW events.

4.2 Methods

In this section, we introduce the waveform models and the Bayesian framework, in particular the *hypermodels* method, employed in this study.

4.2.1 Waveform models

For our analysis, we consider four state-of-the-art BBH waveforms, all including precession and higher-order modes. The construction of the precessing approximant is usually based on a non-precessing one. The specific subdominant modes $(\ell, |m|)$ included, and listed below, are the ones provided by the aligned-spin model: when constructing the precessing one, it will include all the higher-order modes corresponding to a given ℓ , although their description might be incomplete based on the mode content of the aligned-spin approximant. The employed models are briefly described below. More details regarding how the different approximants are built are given in Sec. 2.1.

`NRSur7dq4`

`NRSur7dq4` [161] is a time-domain surrogate model that extends the previous `NRSur7dq2` [271] to higher values of mass ratio. Surrogate models [159, 160] are constructed by interpolating over a set of precomputed waveforms, in this case numerical-relativity waveforms built over the parameter space

for precessing BBH systems. This approach produces very accurate waveforms, since it does not rely on any approximation, except for the numerical discretization in the simulations. However, due to the computational cost of NR simulations, only a limited parameter space region can be covered. In particular, the `NRSur7dq4` model is valid for mass ratio values up to $1/q \leq 6$, where now we assume $q = m_2/m_1$ with $m_1 > m_2$, and for total mass values $M \gtrsim 66M_\odot$ (cf. Fig. 9 in Ref. [161] for the precise range of validity as a function of the system’s mass ratio). `NRSur7dq4` includes, in the co-precessing frame, all the subdominant modes up to $\ell \leq 4$.

`SEOBNRv4PHM`

`SEOBNRv4PHM` [187] is a time-domain, effective-one-body precessing waveform built from the aligned-spin model in Ref. [272]. The EOB formalism maps the dynamics of two bodies into the dynamic of a reduced-mass body moving in a deformed metric. The gravitational waveforms computed with this approach are accurate but slow to generate. For `SEOBNRv4PHM`, the precessing sector is not calibrated to NR simulations. In the co-precessing frame, it includes the subdominant harmonics $(\ell, |m|) = (2, 1), (3, 3), (4, 4), (5, 5)$, and it is valid for mass ratio values in the range $1 \leq 1/q \leq 50$.

`IMRPhenomXPHM`

`IMRPhenomXPHM` [205] is a phenomenological, frequency-domain approximant based on the non-precessing `IMRPhenomXHM` model and constructed via the so-called “twisting-up” procedure (see Sec. 2.1.4), which allows us to map non-precessing systems to precessing ones. IMR phenomenological models are built from piecewise closed-form expressions, which make them computationally cheap. `IMRPhenomXHM` is constructed separately for the three different inspiral, intermediate, and ringdown regions. The intermediate region is fully calibrated to NR simulations, while the inspiral and ringdown ones also include information from the post-Newtonian expansion or black hole perturbation theory, respectively. In the co-precessing frame, this approximant includes the subdominant modes $(\ell, |m|) = (2, 1), (3, 3), (3, 2), (4, 4)$, which are calibrated to NR waveforms individually. The model is valid for spin magnitude values up to 0.99 and $1/q < 1000$.

`IMRPhenomTPHM`

This approximant also belongs to the family of phenomenological models, but it is built in the time domain. Although working in the frequency domain offers an additional speed-up when computing the noise-weighted inner products, a time-domain model allows a direct description of the system’s dynamics. `IMRPhenomTPHM` [268] is built from the non-precessing model `IMRPhenomTHM` [273] via the “twisting-up” procedure, which is however different to the procedure applied in the frequency domain. In the co-precessing frame, this model includes the subdominant harmonics $(\ell, |m|) = (2, 1), (3, 3), (4, 4), (5, 5)$. The parameter range of validity is defined by: $m_2 \geq 0.5M_\odot$, with m_2 being the secondary mass, and spin magnitude $|\chi_{1,2}| \leq 0.99$ for $1/q \leq 20$.

4.2.2 Bayesian framework

Analyzing GW signals in a Bayesian framework, as described in Sec. 2.2, allows both inference of the source parameters and a comparison between different possible models describing the gravitational waveform. The source parameters $\vec{\theta}$ can be recovered from the detector data d evaluating the posterior $p(\vec{\theta}|d, \Omega)$, where Ω is the waveform model. We employed the same default priors used in the parameter estimation analysis for these events in the LVK catalog papers [14, 38], adjusting them as follows in order to respect the region of validity of all the four approximants considered: $1/q \leq 6$, $\chi_{1,2} \leq 0.99$, $m_2 \geq 0.5 M_\odot$. For some events, we also adjust the prior on chirp mass to ensure $\mathcal{M}_c \geq 26 M_\odot$, to allow for the validity of `NRSur7dq4` in the entire region of the prior volume. As discussed in Sec. 2.2.4, the evidence enables us to compare different models, say Ω_A and Ω_B , computing the *odds ratio*

$$\mathcal{O}_B^A = \frac{p(\Omega_A|d)}{p(\Omega_B|d)}. \quad (4.1)$$

The posterior probability density and the evidence can be estimated with stochastic sampling methods. In particular, here we employ the *hypermodels* approach introduced in Ref. [270], with a Metropolis-Hastings MCMC algorithm, based on the implementation of the BILBY-MCMC sampler [274].

4.2.3 Hypermodels

If n is the number of models we want to study, the waveform model Ω employed during the sampling is substituted with a hypermodel $\Omega = \{\Omega_0, \Omega_1, \dots, \Omega_{n-1}\}$. The parameter space investigated by the sampler, therefore, becomes $\{\vec{\theta}, \omega\}$, where $\vec{\theta}$ are the usual source parameters, while ω is a categorical parameter $\omega \in [0, 1, \dots, n - 1]$ representing the waveform approximant. We define a mapping between the value of the parameter ω and a specific waveform approximant, so that at each iteration the sampler picks a value of $\{\vec{\theta}, \omega\}$ and generates the waveform with parameters $\vec{\theta}$ and the approximant corresponding to ω . We employ an uninformative prior $\pi(\omega) = 1/n$, which translates into a prior odds $\pi_B^A = 1$ for all the combinations of models considered. Among the final N posterior samples, we can distinguish the samples for each waveform ℓ from the value of the ω parameter. If n_ℓ is the number of samples for the ℓ -th approximant, its probability with respect to the other waveforms is given by $p_\ell = n_\ell/N$. The odds ratio between two models $\omega = A$ and $\omega = B$ is computed as

$$\mathcal{O}_B^A = \frac{p_A}{p_B} = \frac{n_A}{n_B}. \quad (4.2)$$

The error on $p_{A,B}$ is given by the variance of a Poisson process, yielding $\sigma_{p_{A,B}}^2 = p_{A,B}/N$; thus, propagating the uncertainty, and ignoring any correlation, the variance for the odds ratio \mathcal{O}_B^A is given by

$$\sigma_{\mathcal{O}_B^A}^2 \approx \frac{(\mathcal{O}_B^A)^2}{N} \left(\frac{1}{p_A} + \frac{1}{p_B} \right). \quad (4.3)$$

Event	$\mathcal{M}_c [M_\odot]$				q					
	NRSur	SEOBB	IMRX	IMRT	Combined	NRSur	SEOBB	IMRX	IMRT	Combined
GW150914	31.0 $^{+1.1}_{-1.2}$	30.6 $^{+1.6}_{-1.5}$	30.6 $^{+1.3}_{-1.6}$	31.1 $^{+1.2}_{-1.2}$	30.9 $^{+1.3}_{-1.5}$	0.9 $^{+0.1}_{-0.2}$	0.9 $^{+0.1}_{-0.2}$	0.9 $^{+0.1}_{-0.2}$	0.9 $^{+0.1}_{-0.2}$	0.9 $^{+0.1}_{-0.2}$
GW190519_153544	66.4 $^{+6.7}_{-11.6}$	66.2 $^{+8.1}_{-12.0}$	64.6 $^{+7.8}_{-10.6}$	67.5 $^{+7.4}_{-12.5}$	65.7 $^{+7.8}_{-11.4}$	0.6 $^{+0.3}_{-0.2}$	0.6 $^{+0.2}_{-0.2}$	0.6 $^{+0.3}_{-0.2}$	0.6 $^{+0.2}_{-0.2}$	0.6 $^{+0.3}_{-0.2}$
GW190521_074359	40.4 $^{+2.0}_{-3.2}$	40.7 $^{+2.8}_{-2.7}$	39.4 $^{+2.3}_{-2.4}$	40.8 $^{+1.9}_{-3.0}$	40.4 $^{+2.5}_{-2.9}$	0.8 $^{+0.2}_{-0.2}$	0.8 $^{+0.2}_{-0.2}$	0.8 $^{+0.2}_{-0.2}$	0.8 $^{+0.2}_{-0.2}$	0.8 $^{+0.2}_{-0.2}$
GW190620_030421	58.6 $^{+7.2}_{-10.9}$	60.3 $^{+9.8}_{-10.3}$	58.9 $^{+9.2}_{-12.9}$	60.1 $^{+6.6}_{-11.0}$	59.5 $^{+8.2}_{-11.3}$	0.7 $^{+0.3}_{-0.3}$	0.7 $^{+0.3}_{-0.3}$	0.6 $^{+0.3}_{-0.3}$	0.7 $^{+0.3}_{-0.3}$	0.7 $^{+0.3}_{-0.3}$
GW190630_185205	29.5 $^{+1.5}_{-1.8}$	29.3 $^{+1.9}_{-1.9}$	29.4 $^{+1.7}_{-1.6}$	29.6 $^{+1.6}_{-1.8}$	29.5 $^{+1.6}_{-1.8}$	0.7 $^{+0.3}_{-0.2}$	0.6 $^{+0.3}_{-0.2}$	0.7 $^{+0.3}_{-0.2}$	0.7 $^{+0.3}_{-0.2}$	0.7 $^{+0.3}_{-0.2}$
GW190910_112807	43.3 $^{+3.6}_{-3.7}$	43.3 $^{+3.9}_{-3.7}$	43.2 $^{+4.1}_{-4.2}$	43.5 $^{+3.9}_{-3.5}$	43.3 $^{+3.9}_{-3.8}$	0.8 $^{+0.2}_{-0.2}$	0.8 $^{+0.2}_{-0.2}$	0.8 $^{+0.2}_{-0.2}$	0.8 $^{+0.2}_{-0.2}$	0.8 $^{+0.2}_{-0.2}$
GW191222_033537	52.6 $^{+5.4}_{-6.2}$	51.6 $^{+7.3}_{-6.6}$	51.0 $^{+6.6}_{-7.0}$	52.8 $^{+5.6}_{-5.9}$	52.2 $^{+6.1}_{-6.6}$	0.8 $^{+0.2}_{-0.3}$	0.8 $^{+0.2}_{-0.3}$	0.8 $^{+0.2}_{-0.3}$	0.8 $^{+0.2}_{-0.3}$	0.8 $^{+0.2}_{-0.3}$
GW200112_155838	33.8 $^{+2.5}_{-1.9}$	34.1 $^{+3.4}_{-2.5}$	33.8 $^{+2.6}_{-2.3}$	34.0 $^{+2.7}_{-2.0}$	33.9 $^{+2.8}_{-2.1}$	0.8 $^{+0.2}_{-0.2}$	0.8 $^{+0.2}_{-0.3}$	0.8 $^{+0.2}_{-0.3}$	0.8 $^{+0.2}_{-0.2}$	0.8 $^{+0.2}_{-0.2}$
GW200224_222234	40.3 $^{+3.9}_{-3.8}$	40.7 $^{+3.7}_{-3.8}$	40.6 $^{+3.1}_{-3.7}$	40.3 $^{+4.4}_{-3.8}$	40.5 $^{+3.6}_{-3.8}$	0.8 $^{+0.2}_{-0.3}$	0.8 $^{+0.2}_{-0.2}$	0.8 $^{+0.2}_{-0.2}$	0.8 $^{+0.2}_{-0.3}$	0.8 $^{+0.2}_{-0.3}$
GW200311_115853	32.7 $^{+2.6}_{-2.9}$	32.6 $^{+2.8}_{-2.6}$	32.4 $^{+2.6}_{-2.7}$	33.1 $^{+2.9}_{-3.2}$	32.6 $^{+2.8}_{-2.8}$	0.8 $^{+0.2}_{-0.3}$	0.8 $^{+0.2}_{-0.3}$	0.8 $^{+0.2}_{-0.3}$	0.8 $^{+0.2}_{-0.3}$	0.8 $^{+0.2}_{-0.3}$
GW190521	112.8 $^{+12.1}_{-13.2}$	119.3 $^{+18.9}_{-16.9}$	104.5 $^{+16.9}_{-14.4}$	114.5 $^{+18.7}_{-14.8}$	114.5 $^{+18.9}_{-15.4}$	0.8 $^{+0.1}_{-0.3}$	0.7 $^{+0.2}_{-0.2}$	0.7 $^{+0.3}_{-0.1}$	0.8 $^{+0.2}_{-0.2}$	0.8 $^{+0.2}_{-0.2}$
GW191109_010717	60.3 $^{+5.6}_{-9.4}$	62.2 $^{+9.1}_{-7.5}$	59.4 $^{+13.5}_{-8.4}$	66.3 $^{+6.8}_{-8.4}$	62.9 $^{+9.0}_{-8.2}$	0.7 $^{+0.2}_{-0.3}$	0.7 $^{+0.2}_{-0.2}$	0.8 $^{+0.2}_{-0.2}$	0.8 $^{+0.2}_{-0.2}$	0.7 $^{+0.2}_{-0.3}$
GW200129_065458	29.9 $^{+2.5}_{-1.5}$	31.6 $^{+0.8}_{-1.3}$	31.7 $^{+2.3}_{-3.1}$	31.4 $^{+1.8}_{-1.8}$	30.9 $^{+2.8}_{-2.4}$	0.5 $^{+0.4}_{-0.1}$	0.8 $^{+0.2}_{-0.4}$	0.7 $^{+0.3}_{-0.3}$	0.8 $^{+0.1}_{-0.2}$	0.6 $^{+0.4}_{-0.2}$

Table 4.1: Median values and their 5% and 95% quantiles from the probability density functions of mass parameters, chirp mass \mathcal{M}_c and mass ratio q , for the different models' posteriors and for the combined one.

	χ_{eff}					χ_{p}				
Event	NRSur	SEOBB	IMRX	IMRT	Combined	NRSur	SEOBB	IMRX	IMRT	Combined
GW150914	-0.02 $^{+0.09}_{-0.11}$	-0.03 $^{+0.11}_{-0.12}$	-0.04 $^{+0.10}_{-0.14}$	-0.01 $^{+0.09}_{-0.10}$	-0.02 $^{+0.10}_{-0.12}$	0.35 $^{+0.44}_{-0.27}$	0.33 $^{+0.43}_{-0.25}$	0.50 $^{+0.39}_{-0.39}$	0.39 $^{+0.42}_{-0.31}$	0.39 $^{+0.44}_{-0.31}$
GW190519_153544	0.31 $^{+0.20}_{-0.23}$	0.34 $^{+0.21}_{-0.26}$	0.33 $^{+0.19}_{-0.26}$	0.31 $^{+0.21}_{-0.26}$	0.33 $^{+0.20}_{-0.25}$	0.50 $^{+0.33}_{-0.32}$	0.45 $^{+0.35}_{-0.27}$	0.47 $^{+0.36}_{-0.29}$	0.52 $^{+0.34}_{-0.34}$	0.48 $^{+0.35}_{-0.30}$
GW190521_074359	0.12 $^{+0.11}_{-0.13}$	0.15 $^{+0.11}_{-0.12}$	0.08 $^{+0.12}_{-0.11}$	0.16 $^{+0.10}_{-0.14}$	0.14 $^{+0.11}_{-0.14}$	0.44 $^{+0.34}_{-0.31}$	0.43 $^{+0.37}_{-0.29}$	0.32 $^{+0.39}_{-0.25}$	0.45 $^{+0.36}_{-0.31}$	0.42 $^{+0.37}_{-0.30}$
GW190620_030421	0.32 $^{+0.22}_{-0.25}$	0.39 $^{+0.20}_{-0.22}$	0.35 $^{+0.20}_{-0.28}$	0.37 $^{+0.19}_{-0.23}$	0.35 $^{+0.21}_{-0.25}$	0.51 $^{+0.35}_{-0.33}$	0.46 $^{+0.35}_{-0.30}$	0.54 $^{+0.35}_{-0.36}$	0.46 $^{+0.33}_{-0.29}$	0.49 $^{+0.35}_{-0.32}$
GW190630_185205	0.10 $^{+0.13}_{-0.14}$	0.10 $^{+0.14}_{-0.14}$	0.09 $^{+0.13}_{-0.13}$	0.11 $^{+0.14}_{-0.15}$	0.10 $^{+0.13}_{-0.14}$	0.34 $^{+0.40}_{-0.25}$	0.30 $^{+0.35}_{-0.22}$	0.30 $^{+0.38}_{-0.23}$	0.31 $^{+0.34}_{-0.23}$	0.31 $^{+0.37}_{-0.23}$
GW190910_112807	-0.02 $^{+0.17}_{-0.18}$	0.00 $^{+0.16}_{-0.20}$	-0.01 $^{+0.17}_{-0.20}$	0.00 $^{+0.18}_{-0.18}$	-0.01 $^{+0.17}_{-0.19}$	0.43 $^{+0.42}_{-0.34}$	0.39 $^{+0.39}_{-0.32}$	0.39 $^{+0.45}_{-0.31}$	0.40 $^{+0.42}_{-0.32}$	0.41 $^{+0.42}_{-0.32}$
GW191222_033537	-0.03 $^{+0.19}_{-0.22}$	-0.01 $^{+0.20}_{-0.25}$	-0.05 $^{+0.19}_{-0.24}$	-0.02 $^{+0.19}_{-0.20}$	-0.02 $^{+0.19}_{-0.23}$	0.41 $^{+0.44}_{-0.32}$	0.41 $^{+0.43}_{-0.32}$	0.40 $^{+0.42}_{-0.30}$	0.42 $^{+0.43}_{-0.33}$	0.41 $^{+0.44}_{-0.32}$
GW200112_155838	0.04 $^{+0.15}_{-0.13}$	0.07 $^{+0.17}_{-0.15}$	0.05 $^{+0.14}_{-0.15}$	0.06 $^{+0.16}_{-0.13}$	0.06 $^{+0.16}_{-0.14}$	0.36 $^{+0.42}_{-0.28}$	0.35 $^{+0.41}_{-0.28}$	0.39 $^{+0.45}_{-0.30}$	0.36 $^{+0.41}_{-0.28}$	0.36 $^{+0.43}_{-0.28}$
GW200224_222234	0.09 $^{+0.17}_{-0.15}$	0.11 $^{+0.14}_{-0.16}$	0.10 $^{+0.14}_{-0.16}$	0.11 $^{+0.17}_{-0.16}$	0.10 $^{+0.15}_{-0.16}$	0.43 $^{+0.41}_{-0.34}$	0.39 $^{+0.42}_{-0.30}$	0.48 $^{+0.39}_{-0.35}$	0.38 $^{+0.41}_{-0.30}$	0.44 $^{+0.41}_{-0.33}$
GW200311_115853	-0.02 $^{+0.16}_{-0.19}$	-0.01 $^{+0.15}_{-0.19}$	-0.04 $^{+0.16}_{-0.19}$	0.01 $^{+0.17}_{-0.21}$	-0.02 $^{+0.16}_{-0.19}$	0.44 $^{+0.39}_{-0.34}$	0.40 $^{+0.43}_{-0.31}$	0.49 $^{+0.39}_{-0.37}$	0.48 $^{+0.40}_{-0.37}$	0.46 $^{+0.41}_{-0.35}$
GW190521	-0.14 $^{+0.35}_{-0.37}$	0.07 $^{+0.32}_{-0.38}$	-0.08 $^{+0.35}_{-0.46}$	-0.17 $^{+0.38}_{-0.31}$	-0.10 $^{+0.39}_{-0.38}$	0.75 $^{+0.20}_{-0.35}$	0.71 $^{+0.24}_{-0.37}$	0.49 $^{+0.35}_{-0.34}$	0.76 $^{+0.19}_{-0.33}$	0.73 $^{+0.22}_{-0.37}$
GW191109_010717	-0.42 $^{+0.29}_{-0.27}$	-0.32 $^{+0.38}_{-0.26}$	-0.33 $^{+0.59}_{-0.33}$	-0.24 $^{+0.25}_{-0.28}$	-0.31 $^{+0.36}_{-0.28}$	0.60 $^{+0.29}_{-0.26}$	0.74 $^{+0.22}_{-0.36}$	0.60 $^{+0.31}_{-0.35}$	0.85 $^{+0.12}_{-0.33}$	0.75 $^{+0.21}_{-0.37}$
GW200129_065458	-0.01 $^{+0.14}_{-0.11}$	0.07 $^{+0.09}_{-0.04}$	0.10 $^{+0.15}_{-0.18}$	0.07 $^{+0.13}_{-0.13}$	0.04 $^{+0.18}_{-0.16}$	0.86 $^{+0.12}_{-0.35}$	0.28 $^{+0.52}_{-0.13}$	0.82 $^{+0.15}_{-0.39}$	0.48 $^{+0.38}_{-0.34}$	0.83 $^{+0.14}_{-0.41}$

 Table 4.2: Median values and their 5% and 95% quantiles from the probability density functions of spin parameters, effective inspiral spin χ_{eff} and effective precessing spin χ_{p} , for the different models' posteriors and for the combined one.

4.3 Results

We analyze 13 events of GWTC-3, focusing on the ones with the highest total mass ($M > 59.4 M_{\odot}$), and with moderate to high SNRs. In particular, we consider events with a network SNR $\rho_{\text{net}} \geq \sqrt{D \times 8^2}$, where D is the number of interferometers detecting the event, corresponding to at least a signal-to-noise ratio 8 per detector, without, however, constraints on the single detector SNR.¹

The waveform models employed include higher-order modes, and we restricted to the modes that are available for all models: $(\ell, m) = (2, 2), (2, 1), (3, 3), (4, 4), (2, -2), (2, -1), (3, -3), (4, -4)$. We remark that this implies that the models are not used at their full capabilities, since we could not include their full mode content. For `SEOBNRv4PHM`, the sampling rate must ensure that the Nyquist frequency is larger than the ringdown frequency. For most events, this means that the required sampling rate was higher than the one used for the LVK catalog papers [14, 38]; therefore we estimated the events' power spectral densities in the needed frequency range, using `BayesLine` [113] and the same settings as in Refs. [14, 38]. The new PSDs are released together with the obtained samples in Ref. [275].

The detector frame masses and spins estimated with the various models are reported in Table 4.1 and Table 4.2, respectively, while Table 4.3 shows the median value, along with its 90% confidence interval, of the distribution of the log-likelihood, $\ln \mathcal{L}$. For each model, it corresponds to the distribution of the log-likelihood values (see Sec. 2.2.2) for all the samples with parameters $\{\vec{\theta}, \omega\}$ for which ω corresponds to the specific model. The logarithm is used simply because, as shown in Eq. 2.68, in the frequency domain the likelihood takes an exponential form, and therefore it is easier for the samplers to compute its logarithm. In general, we expect that higher values of $\ln \mathcal{L}$ correspond to a higher probability for a given model. However, Table 4.3 reports the median of the recovered $\ln \mathcal{L}$ distribution, therefore, since the shape of the distribution will affect the median value, in some cases the model with the largest $\ln \mathcal{L}$ value might not correspond to the model with the largest probability.

Regarding the spins, information is reported through two parameters (cf. Sec. 1.3.3), the *effective inspiral spin*

$$\chi_{\text{eff}} = \frac{(m_1 \chi_{1,\parallel} + m_2 \chi_{2,\parallel})}{m_1 + m_2}, \quad (4.4)$$

with $\chi_{1,\parallel}, \chi_{2,\parallel}$ being the spin components parallel to the angular momentum, and the *effective precessing spin*

$$\chi_p = \max \left\{ \chi_{1,\perp}, \frac{q(4q+3)}{4+3q} \chi_{2,\perp} \right\}, \quad (4.5)$$

where $\chi_{1,\perp}, \chi_{2,\perp}$ are the spin components perpendicular to the angular momentum. Figure 4.1 shows the posterior probability density of \mathcal{M}_c , q , χ_{eff} , and χ_p for all the events, comparing the posteriors recovered with the different waveform models.

We can usually place only weak constraints on χ_p . Thus, its posterior distribution is heavily affected by the prior one, which in turn is determined by the source parameters χ_1, χ_2 , and q , and peaks at non-zero values of χ_p also in the absence of precession. Therefore, recovering a non-zero value of χ_p does not constitute sufficient evidence of precession, but we need to check if the posterior

¹This is a conservative choice, since usually a network SNR of roughly 8 is already enough to consider a detection significant. However, it ensures a signal loud enough to obtain significant results in parameter estimation analyses.

Event	$\ln \mathcal{L}$				
	NRSur	SEOBI	IMRX	IMRT	Combined
GW150914	$322.2^{+2.7}_{-4.3}$	$321.6^{+2.5}_{-4.1}$	$322.2^{+2.8}_{-4.0}$	$322.4^{+2.6}_{-4.4}$	$322.2^{+2.7}_{-4.3}$
GW190519_153544	$114.6^{+3.7}_{-4.9}$	$115.4^{+3.7}_{-5.3}$	$115.1^{+3.3}_{-5.1}$	$114.6^{+3.2}_{-5.2}$	$115.0^{+3.5}_{-5.1}$
GW190521_074359	$320.0^{+3.5}_{-4.8}$	$321.3^{+3.2}_{-5.1}$	$319.7^{+3.1}_{-4.4}$	$320.6^{+3.4}_{-4.6}$	$320.6^{+3.5}_{-4.8}$
GW190620_030421	$64.1^{+3.9}_{-5.3}$	$64.0^{+4.1}_{-5.6}$	$63.7^{+3.6}_{-5.4}$	$64.2^{+3.8}_{-5.6}$	$64.0^{+3.9}_{-5.5}$
GW190630_185205	$117.7^{+3.1}_{-5.1}$	$116.8^{+3.2}_{-5.1}$	$116.9^{+3.1}_{-4.9}$	$117.7^{+3.1}_{-5.0}$	$117.4^{+3.2}_{-5.1}$
GW190910_112807	$90.5^{+3.3}_{-4.6}$	$90.8^{+3.9}_{-4.6}$	$90.4^{+3.1}_{-4.5}$	$90.4^{+3.7}_{-4.5}$	$90.5^{+3.5}_{-4.6}$
GW191222_033537	$70.0^{+2.5}_{-4.1}$	$69.5^{+2.5}_{-4.0}$	$69.3^{+2.5}_{-4.0}$	$70.1^{+2.5}_{-4.1}$	$69.8^{+2.6}_{-4.1}$
GW200112_155838	$166.2^{+2.9}_{-4.4}$	$165.5^{+2.8}_{-4.6}$	$165.6^{+2.7}_{-4.4}$	$166.4^{+2.9}_{-4.4}$	$166.0^{+2.9}_{-4.5}$
GW200224_222234	$188.1^{+3.6}_{-4.5}$	$188.0^{+2.7}_{-4.4}$	$188.6^{+3.3}_{-4.6}$	$187.4^{+2.7}_{-4.5}$	$188.1^{+3.3}_{-4.5}$
GW200311_115853	$145.4^{+2.7}_{-4.2}$	$146.0^{+2.6}_{-4.2}$	$146.2^{+2.5}_{-4.3}$	$145.6^{+2.8}_{-4.2}$	$145.9^{+2.7}_{-4.3}$
GW190521	$88.0^{+4.2}_{-5.6}$	$87.4^{+4.2}_{-5.4}$	$83.6^{+4.3}_{-4.3}$	$88.4^{+3.6}_{-5.5}$	$87.8^{+4.1}_{-5.8}$
GW191109_010717	$133.3^{+3.9}_{-6.2}$	$136.4^{+5.6}_{-6.9}$	$132.2^{+6.9}_{-6.6}$	$135.9^{+5.4}_{-6.7}$	$135.8^{+5.9}_{-6.9}$
GW200129_065458	$347.2^{+4.4}_{-7.1}$	$341.0^{+2.6}_{-3.8}$	$345.3^{+4.7}_{-6.4}$	$341.1^{+5.3}_{-4.6}$	$346.1^{+4.8}_{-7.0}$

Table 4.3: Median values and their 5% and 95% quantiles from the probability density functions of the recovered $\ln \mathcal{L}$ with the different models and for the combined results. For each event, the highest value of $\ln \mathcal{L}$ is marked in bold.

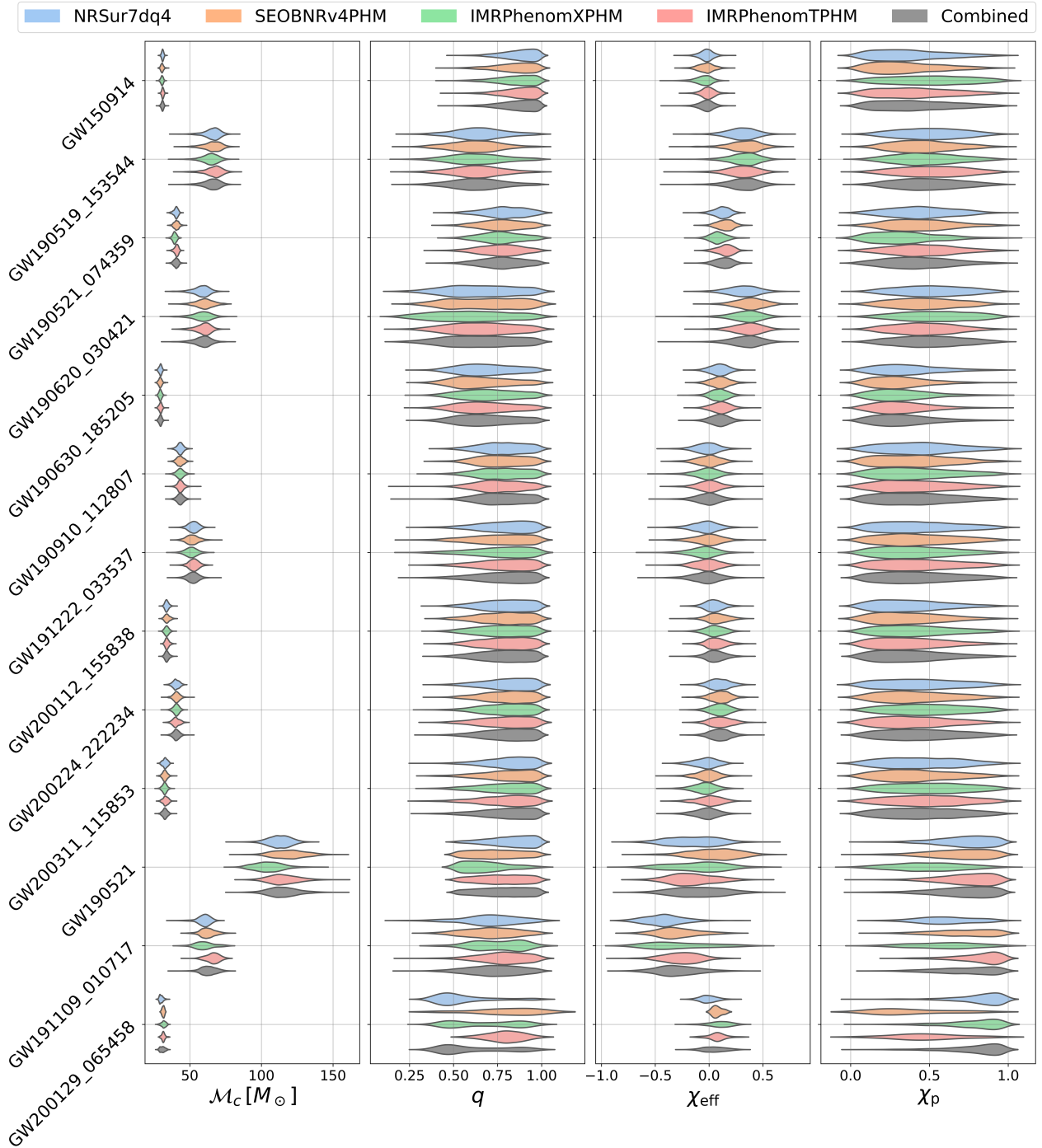


Figure 4.1: Posterior probability densities for \mathcal{M}_c , q , χ_{eff} , and χ_p as recovered with the different waveform approximants and for the combined posterior, for all the events analyzed.

Event	NRSur	SEOBI	IMRX	IMRT	Combined
GW150914	0.008	0.010	0.050	0.017	0.015
GW190519_153544	0.010	0.017	0.010	0.011	0.011
GW190521_074359	0.037	0.029	0.027	0.029	0.029
GW190620_030421	0.010	0.006	0.016	0.012	0.006
GW190630_185205	0.030	0.067	0.049	0.065	0.050
GW190910_112807	0.023	0.012	0.009	0.014	0.014
GW191222_033537	0.012	0.011	0.014	0.012	0.011
GW200112_155838	0.012	0.015	0.011	0.014	0.012
GW200224_222234	0.008	0.011	0.024	0.010	0.010
GW200311_115853	0.026	0.018	0.041	0.038	0.031
<i>GW190521</i>	<i>0.243</i>	<i>0.158</i>	<i>0.007</i>	<i>0.264</i>	<i>0.202</i>
<i>GW191109_010717</i>	<i>0.095</i>	<i>0.227</i>	<i>0.070</i>	<i>0.422</i>	<i>0.243</i>
<i>GW200129_065458</i>	<i>0.459</i>	<i>0.005</i>	<i>0.330</i>	<i>0.051</i>	<i>0.378</i>

Table 4.4: $D_{JS}^{\chi_p, \text{prior}}$ values in bit computed between the posterior of χ_p obtained with our analysis and the prior distribution conditioned to χ_{eff} , for the posteriors recovered with the different waveforms and the combined one. Events for which we find values of χ_p significantly different from the prior are marked in italic.

distribution is significantly different from the prior one. This is evaluated through the Jensen-Shannon (JS) divergence [276], which estimates the difference between two probability distributions p_1 and p_2 as

$$D_{\text{JS}}(p_1(x)||p_2(x)) = \frac{1}{2} \left[\sum_x p_1(x) \ln \left(\frac{p_1(x)}{m(x)} \right) + \sum_x p_2(x) \ln \left(\frac{p_2(x)}{m(x)} \right) \right], \quad (4.6)$$

with $m(x) = 0.5(p_1(x) + p_2(x))$. The JS divergence derives from the Kullback-Leibler (KL) divergence [277], or relative entropy,

$$D_{\text{KL}}(p_1(x)||p_2(x)) = \sum_x p_1(x) \ln \left(\frac{p_1(x)}{p_2(x)} \right), \quad (4.7)$$

which basically quantifies the information lost when we use $p_2(x)$ to model the “true” distribution $p_1(x)$. The KL divergence is not symmetric, i.e., $D_{\text{KL}}(p_1(x)||p_2(x)) \neq D_{\text{KL}}(p_2(x)||p_1(x))$. In order to get a symmetric quantity, instead of directly computing the KL divergence between $p_1(x)$ and $p_2(x)$, one considers the average distribution $m(x) = 0.5(p_1(x) + p_2(x))$ and computes the average of the KL divergence of both $p_1(x)$ and $p_2(x)$ with respect to $m(x)$, obtaining the JS divergence as

$$D_{\text{JS}}(p_1(x)||p_2(x)) = \frac{1}{2} [D_{\text{KL}}(p_1(x)||m(x)) + D_{\text{KL}}(p_2(x)||m(x))]. \quad (4.8)$$

Table 4.4 shows the JS divergence values for χ_p posteriors with respect to their prior distribution, $D_{\text{JS}}^{\chi_p, \text{prior}}$. We also compare our results with the ones from LVK analyses in Table 4.5, where the difference between the posterior distributions is again evaluated as a JS divergence. Furthermore, the probability percentages for each model for the different events, with their associated errors, are given in Table 4.6 for each event.

4.3.1 Single events

In this section, we comment on the individual event recoveries with the different waveform models.

GW150914

For this event, the parameters and the log-likelihoods recovered are consistent for all four models. The recovered values for the source parameters can be found in Tables 4.1-4.2, and are consistent with the LVK results [36, 38], as shown in Table 4.5. The probabilities for each approximant are reported in Table 4.6, where we see a slight preference for the `IMRPhenomTPHM` model.

GW190519 _ 153544

In this case, data show a preference for `IMRPhenomXPHM` (see Table 4.6), although parameter estimates and log-likelihood values are consistent for all the models. As shown in Table 4.2, we find support for positive, non-zero values of χ_{eff} . This is consistent with the results reported in Ref. [38].

GW190521

GW190521 is the most massive event detected so far, and one among the ones with the strongest signature of higher-order modes in the signal [17, 41]. The consequently high values needed for the prior on chirp mass, combined with the employed prior on mass ratio, cause potential issues within the

Event	IMRPhenomXPHM				SEOBNRv4PHM			
	$D_{JS}^{\chi_p}$	$D_{JS}^{\chi_{\text{eff}}}$	$D_{JS}^{\mathcal{M}_c}$	D_{JS}^q	$D_{JS}^{\chi_p}$	$D_{JS}^{\chi_{\text{eff}}}$	$D_{JS}^{\mathcal{M}_c}$	D_{JS}^q
GW150914	0.006	0.001	0.007	0.005	0.005	0.076	0.032	0.052
GW190519_153544	0.002	0.001	0.001	0.001	0.011	0.002	0.014	0.007
GW190521_074359	0.007	0.004	0.005	0.001	0.024	0.033	0.005	0.007
GW190620_030421	0.005	0.001	0.007	0.001	0.001	0.001	0.006	0.001
GW190630_185205	0.002	0.001	0.004	0.002	0.010	0.022	0.025	0.015
GW190910_112807	0.002	0.000	0.002	0.001	0.007	0.002	0.015	0.009
GW200112_155838	0.002	0.007	0.004	0.003	0.009	0.018	0.014	0.026
GW200224_222234	0.001	0.003	0.006	0.001	0.004	0.016	0.018	0.006
GW200311_115853	0.002	0.001	0.001	0.001	0.006	0.006	0.015	0.014
GW190521	0.019	0.003	0.066	0.075	0.020	0.003	0.018	0.035
GW191109_010717	0.024	0.006	0.012	0.006	0.029	0.011	0.016	0.007
GW200129_065458	0.003	0.010	0.005	0.008	0.139	0.046	0.137	0.141

Table 4.5: Values of Jensen-Shannon divergence for χ_p , χ_{eff} , \mathcal{M}_c , and q , computed between the posteriors recovered by our analysis and the LVK ones [14, 38] for the available waveforms, IMRPhenomXPHM and SEOBNRv4PHM.

`IMRPhenomTPHM` model since the computed peak frequency for the $(\ell, m) = (2, 2)$ mode might be below the 20 Hz low-frequency cutoff used for the analysis. To avoid this issue, for this event we adjust the prior on mass ratio such that $1/q \leq 2$. The recovered values for mass and spin parameters are reported in Table 4.1 and Table 4.2, respectively. They are consistent with the results in Ref. [38], where, however, only the `IMRPhenomXPHM` and `SEOBNRv4PHM` approximants were used,², and with the `NRSur7dq4` results first shown in the discovery paper [17]. We find evidence of precession for the `NRSur7dq4`, `SEOBNRv4PHM`, and `IMRPhenomTPHM` models, cf. Table 4.4. The probabilities for the different approximants are shown in Table 4.6: the `IMRPhenomTPHM` model is slightly favored over the other ones, while `IMRPhenomXPHM` is strongly disfavored. Interestingly, these findings are consistent with the fact that the `IMRPhenomXPHM` model provides a less accurate description of precession in the ringdown phase: being a frequency-domain model, it is not straightforward to compute a specific closed-form ansatz for the Euler angles during the ringdown, and therefore the same prescription for the inspiral is employed; moreover, the stationary phase approximation (see Sec. 2.1.2) is used in the whole waveform, although it is not adequate for the merger and ringdown. These limitations become more evident in the case of signals where the merger and ringdown phase prevail, like GW190521. Nevertheless, the extremely short duration of this event and the lack of the inspiral part of the signal³ make it difficult to draw clear conclusions. Many works investigated this event from different perspectives and explored the possible processes that lead to the formation of such a system. One of the most investigated hypotheses is the presence of eccentricity [278–280], which could mimic precession [281, 282]. Multiple alternative scenarios that could lead to the emission of this signal have been proposed, like dynamical capture in hyperbolic orbits [283], a primordial BH merger [284], and a high-mass BH-disk system [285]. In Ref. [286], an analysis of this event with a population-based prior led to the conclusion that neither of the component masses lies in the pair-instability supernova mass gap. In Ref. [287], the use of a high-mass prior showed the possibility of GW190521 being an intermediate-mass-ratio BBH merger. However, a further investigation carried out in Ref. [288], where different precession prescriptions and higher-order-modes contents were investigated with the `IMRPhenomXPHM` and `IMRPhenomTPHM` models, showed that, despite the presence of a multimodal likelihood for the mass ratio parameter, the peaks are characterized by very different probabilities. The parameters recovered by our analysis are consistent with both the `IMRPhenomXPHM` and `IMRPhenomTPHM` results in Ref. [288], when using models with the same settings.

GW190521_074359

This event shows a preference for the `SEOBNRv4PHM` approximant, although the recovered parameters and log-likelihood values are similar for all four models. Also in this case, our results are consistent with the ones in the LVK papers [38], and we find no evidence of precession.

²In Ref. [38] further analyses computed the precession SNR to be too small to claim the presence of strong evidence for precession.

³As discussed in Sec. 1.3.2, the GW signal emitted by heavier binaries spends less time in band, and the GWs emitted during their inspiral involve lower frequencies. In addition, the ISCO frequency at which commonly we consider the inspiral ended is also inversely proportional to the total mass of the binary. Therefore, for GW190521, due to its high total mass, the signal entered in band only during the merger-ringdown phase of the coalescence.

GW190620_030421

The LVK studies report this source as a BBH binary with high effective spin χ_{eff} . In our re-analysis, we find all the waveform families to perform comparably and return consistent estimates of parameters as well as the values of log-likelihood. Moreover, the existing LVK analyses on this event with `IMRPhenomXPHM` and `SEOBNRv4PHM` return consistent results with ours. We also find support for positive values of χ_{eff} , as shown in Table 4.2. The estimates of intrinsic parameters from different models are consistent with each other; however, from the values of posterior probability (see Table 4.6), `NRSur7dq4` seems to be the most favored.

GW190630_185205

We find consistent estimates of parameters and log-likelihoods among all models compared, and no evidence for spin. Among the four models considered, `NRSur7dq4` and `IMRPhenomTPHM` seem to be most preferred by the data, with almost the same probability.

GW190910_112807

This event again returns very consistent estimates of log-likelihood and intrinsic parameters among the different models. In particular, we find no evidence for spins. From the values of posterior probabilities supported by all waveforms, we also note that the data have an almost equal preference for all models.

GW191109_010717

We find `SEOBNRv4PHM` to be the most favored model, as reported in Table 4.6. We also recover a high probability for `IMRPhenomTPHM`, while `NRSur7dq4` and `IMRPhenomXPHM` are strongly disfavored. We find evidence of non-zero χ_p with both `SEOBNRv4PHM` and `IMRPhenomTPHM`, but not for the other two models, as shown in Tables 4.2 and 4.4. For all models, we find significant support for negative values of χ_{eff} , confirming the results in Refs. [14, 289]. In the latter, the possibility of formation by dynamical capture for the binary generating this event is discussed. However, `GW191109_010717` was among the O3 events that required data mitigation due to the presence of glitches. In particular, `GW191109_010717` was affected by a glitch in both the detectors online at the time of the event, in the frequency range 25-45 Hz for Hanford and 20-32 Hz for Livingston. As shown in Ref. [118], different deglitching procedures influence the posteriors obtained for both χ_{eff} and χ_p . In particular, if the Livingston data are analyzed only for frequencies larger than 40 Hz, the support for negative χ_{eff} disappears. However, this result is not sufficient to label the negative support of χ_{eff} as a noise artifact, since most of the spin information comes from low frequencies, and, being `GW191109_010717` already a signal with a short inspiral, removing the low-frequency part discards most of the information, yielding non-informative results. The presence of glitches overlapping a significant part of the inspiral for both the detectors is also regarded as the most likely cause for deviations from general relativity found for this event by some LVK testing-GR analyses [20].

Event	NRSur	SEOBNRv4	IMRPhenomTPHM	IMRPhenomXPHM
GW150914	27.55 ± 0.7	16.22 ± 0.8	23.34 ± 0.7	32.88 ± 0.7
GW190519_153544	20.82 ± 0.6	20.95 ± 0.6	40.87 ± 0.5	17.35 ± 0.6
GW190521_074359	14.76 ± 1.2	40.50 ± 1.0	17.53 ± 1.2	27.22 ± 1.1
GW190620_030421	32.98 ± 0.6	19.48 ± 0.6	20.22 ± 0.6	27.32 ± 0.6
GW190630_185205	33.79 ± 0.6	15.36 ± 0.6	18.90 ± 0.6	31.95 ± 0.6
GW190910_112807	22.86 ± 0.6	25.92 ± 0.6	27.85 ± 0.6	23.37 ± 0.6
GW191222_033537	28.11 ± 0.5	20.58 ± 0.6	18.78 ± 0.6	32.53 ± 0.5
GW200112_155838	30.56 ± 0.6	15.61 ± 0.6	19.82 ± 0.6	34.01 ± 0.5
GW200224_222234	21.82 ± 0.6	23.39 ± 0.6	40.43 ± 0.5	14.36 ± 0.7
GW200311_115853	15.68 ± 0.6	27.70 ± 0.6	35.69 ± 0.6	20.93 ± 0.6
<i>GW190521</i>	31.78 ± 0.6	26.39 ± 0.6	4.60 ± 0.7	37.23 ± 0.5
<i>GW191109_010717</i>	7.54 ± 1.6	62.29 ± 1.0	5.06 ± 1.7	25.11 ± 1.5
<i>GW200129_065458</i>	46.94 ± 1.4	$0.66^{+1.9}_{-0.66}$	51.14 ± 1.3	$1.25^{+1.9}_{-1.25}$

Table 4.6: Probability percentages recovered for the different models for each event, including errors. Events that strongly favor or disfavor some of the models are marked in italic.

GW191222_033537

Although the returned parameter estimates, as well as log-likelihood values, are quite similar, IMRPhenomTPHM seems to be the most favored model (see Table 4.6), while the least favored model is IMRPhenomXPHM. We find no evidence for spins.

GW200112_155838

We recover similar probabilities for all the approximants, with SEOBNRv4PHM slightly disfavored and IMRPhenomTPHM slightly favored, as shown in Table 4.6. Consistently, we find no significant difference between the recovered parameters and log-likelihoods for the different waveforms. The IMRPhenomXPHM and SEOBNRv4PHM posteriors estimated by our study are consistent with the LVK ones.

GW200129_065458

We find a strong preference for `NRSur7dq4` and `IMRPhenomXPHM`, while the probability for `SEOBNRv4PHM` and `IMRPhenomTPHM` is close to zero. This discrepancy is reflected in the posteriors of χ_p , with `NRSur7dq4` and `IMRPhenomXPHM` finding strong evidence for high χ_p values, cf. Table 4.4, while for the other two models results are dominated by the prior. This is consistent with what was found in the LVK GWTC-3 analysis, where `IMRPhenomXPHM` recovers χ_p and `SEOBNRv4PHM` does not. In Ref. [290], strong evidence for precession was found when analyzing this event with the `NRSur7dq4` model. For this event, precession was measured also in Ref. [291], where the recoil velocity was also estimated. The main difference between these two works and the LVK analysis, which did not find conclusive evidence of precession, is that in the latter data were analyzed only with the `IMRPhenomXPHM` and `SEOBNRv4PHM` approximants. In Refs. [290] and [291], the `NRSur7dq4` model was used, because, being generated from NR simulations, it is expected to be more accurate, as shown by the mismatch computation in Ref. [290]. However, in our study, we do not find an overall preference for `NRSur7dq4`. `GW200129_065458` data were affected by a glitch overlapping the event in the Livingston detector [118], therefore, in our analysis, we used the deglitched data, as was done in Ref. [14]. Reference [292] explores the influence of data quality issues for this event, finding that the evidence for precession comes exclusively from the Livingston strain of data between 20-50 Hz, where such issues are present.

GW200224_222234

For this event the recovered parameters and log-likelihood values are consistent for the different waveforms. We find a slight preference for `IMRPhenomXPHM`, cf. Table 4.6. Our results for both `IMRPhenomXPHM` and `SEOBNRv4PHM` are consistent with the LVK analysis. We do not find support for precession.

GW200311_115853

Specific to this event, we find no evidence of spin and consistent source parameters and log-likelihood estimates among all models. However, `IMRPhenomXPHM` seems to be the most favored approximant by the event (cf. Table 4.6).

4.3.2 Combined events

Figure 4.2 shows the cumulative joint odds ratio as a function of the number of events, while Table 4.7 reports the odds ratio values obtained by combining information from all the sources analyzed. We do not find a specific approximant being preferred or disfavored consistently for all the events. Combining results for all the 13 sources, the `NRSur7dq4` model results favored with respect to `SEOBNRv4PHM`, with an odds ratio of 29.43. However, this value is dominated by the results for `GW200129_065458`, and without this event the odds ratio becomes 0.46. This is unexpected, because `NRSur7dq4`, being fully informed by NR simulations, is assumed to be the most accurate model and therefore to describe the data best. Table 4.7 shows also how odds ratios change with the three events with a strong preference for one of the models: while `GW200129_065458` is responsible for `NRSur7dq4` being favored over

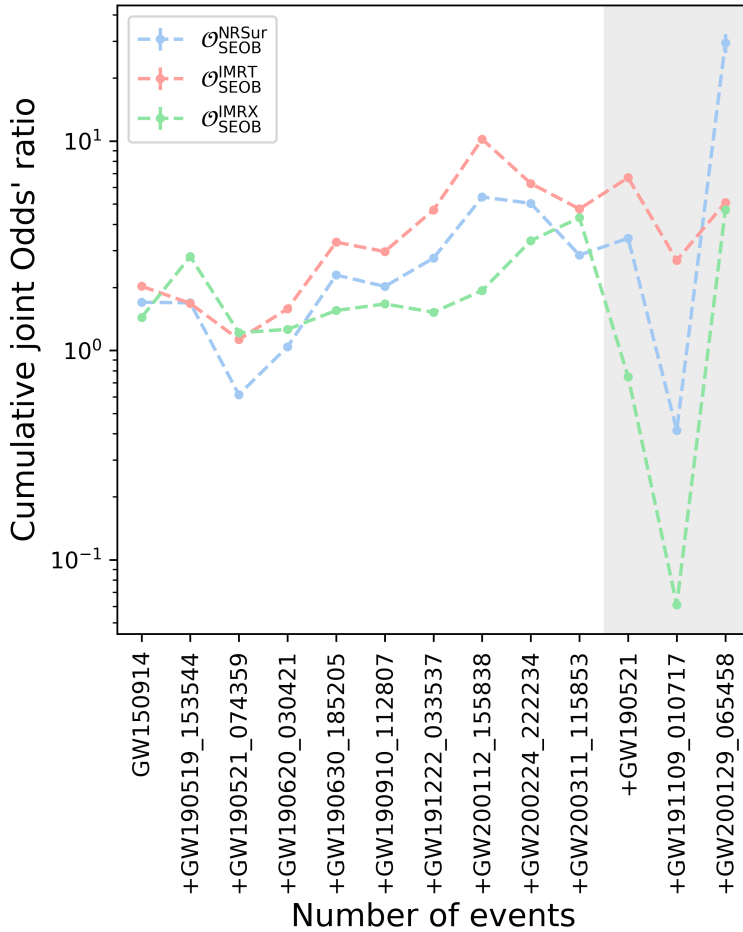


Figure 4.2: Evolution of the joint odds ratio for each approximant with respect to SEOBNRv4PHM as events are added; for any one event shown on the x-axis, the joint odds ratio is calculated from all the events occurring to the left of that event. The events in the gray-shaded area are affected by possible data quality issues. Note that the symmetric error bars 1σ are included in the data points but too small to be discernible.

SEOBNRv4PHM, GW191109_010717, which instead finds a significant preference for SEOBNRv4PHM and IMRPhenomTPHM, balances this result; if we do not take GW191109_010717 into account, NRSur7dq4 and IMRPhenomXPHM are strongly favored over SEOBNRv4PHM, with an odds ratio $\mathcal{O}_{\text{SEOB}}^{\text{NRSur}} = 243.31$ and $\mathcal{O}_{\text{SEOB}}^{\text{IMRX}} = 57.84$, respectively. In addition, without this event, $\mathcal{O}_{\text{SEOB}}^{\text{IMRT}} = 12.62$, and $\mathcal{O}_{\text{IMRT}}^{\text{NRSur}} = 19.27$. Similarly, the results from GW190521 heavily influence the final odds ratio for IMRPhenomXPHM: if we do not include this event, we obtain $\mathcal{O}_{\text{SEOB}}^{\text{IMRX}} = 26.99$. Without these three sources, we find no significant preference for any of the models.

We look for possible trends for the preference of given approximants with respect to the binary parameters, which would point to the waveforms with the best description for specific regions of the parameter space. Figure 4.3 shows the probabilities recovered for the different models as a function of the sources' mass and spin parameters, and the optimized network matched-filter SNR, as computed by the parameter estimation analyses in the catalog papers [14, 38]. We do not find any trends with respect to the binary parameters or the signal SNR.

Interestingly, we find that for all the events that show a strong preference for one of the models,

	$\mathcal{O}_{\text{NRSur}}^{\text{SEO}}$	$\mathcal{O}_{\text{SEOB}}^{\text{IMRX}}$	$\mathcal{O}_{\text{SEOB}}^{\text{IMRT}}$	$\mathcal{O}_{\text{IMRX}}^{\text{NRSur}}$	$\mathcal{O}_{\text{IMRT}}^{\text{NRSur}}$	$\mathcal{O}_{\text{IMRT}}^{\text{IMRX}}$
All events	29.43 ± 1.11	4.70 ± 0.07	5.09 ± 0.08	6.26 ± 0.11	5.78 ± 0.10	0.92 ± 0.01
No GW200129_065458	0.42 ± 0.00	0.06 ± 0.00	2.69 ± 0.03	6.82 ± 0.12	0.15 ± 0.00	0.02 ± 0.00
No GW190521	24.44 ± 0.84	26.99 ± 0.97	3.61 ± 0.05	0.91 ± 0.01	6.77 ± 0.12	7.48 ± 0.14
No GW191109_010717	243.31 ± 26.35	57.84 ± 3.05	12.62 ± 0.31	4.21 ± 0.06	19.27 ± 0.59	4.58 ± 0.07
Without all three	2.85 ± 0.03	4.30 ± 0.06	4.74 ± 0.07	0.66 ± 0.00	0.60 ± 0.00	0.91 ± 0.01

Table 4.7: Joint odds ratios including errors. We report results for all the events combined and results without the events that show a strong preference for some models.

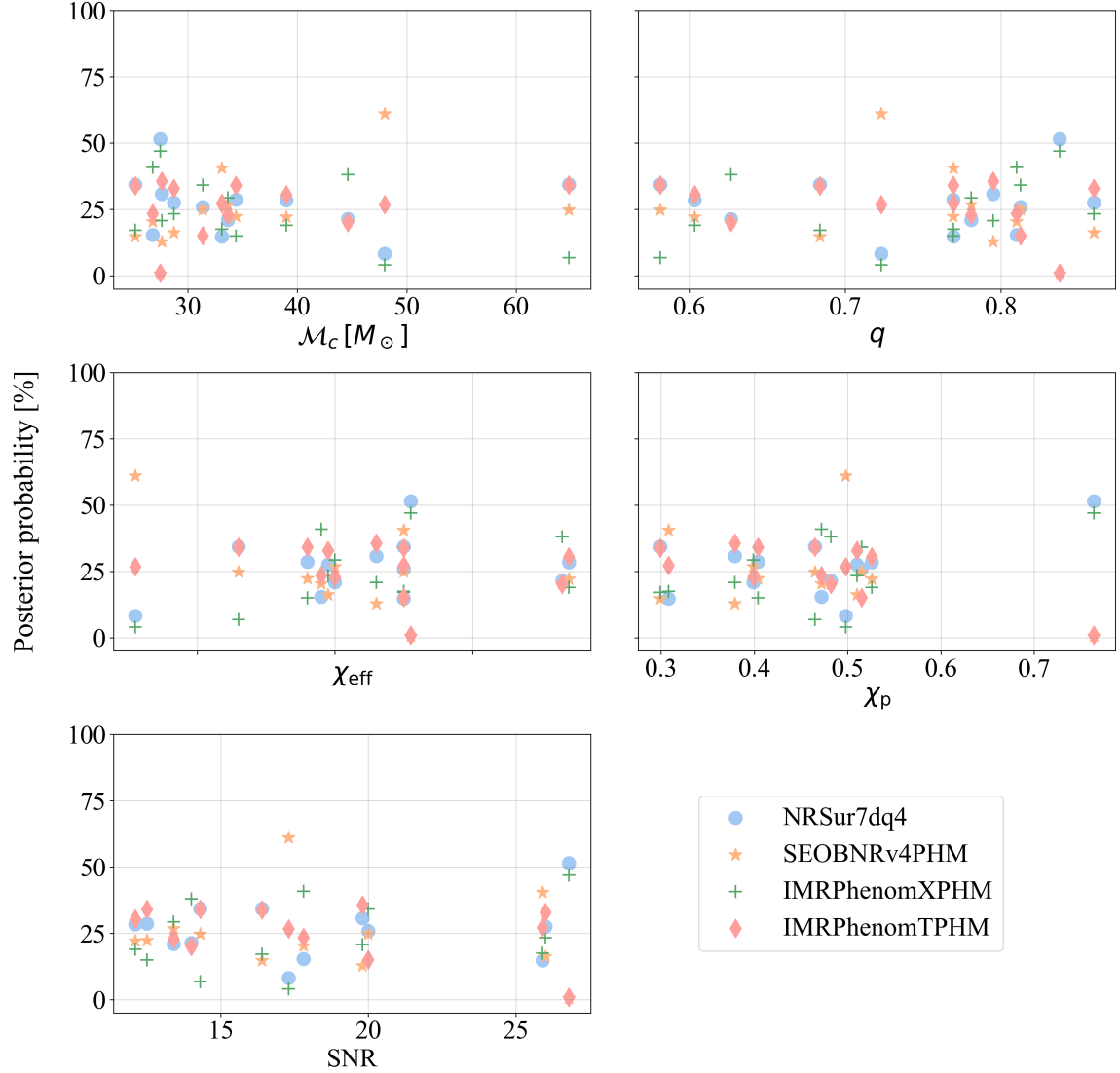


Figure 4.3: Posterior probability for the different approximants as a function of the LVK estimated values of \mathcal{M}_c (top left panel), q (top right), χ_{eff} (middle left), χ_p (middle right), and SNR (bottom left panel).

i.e., GW190521, GW191109_010717, and GW200129_065458, the preferred models are not the same, but in each case are the ones that recover precession. This is particularly evident in the case of GW190521, where `IMRPhenomXPHM` does not recover evidence of precession and has a probability only of roughly 4%, while the other models, which show evidence supporting non-zero values of χ_p , all have a probability roughly 30%. Although, as mentioned, the results for these events might be biased by their short duration or potential data quality issues, the fact that a given model recovers precession better than another one systematically implies a higher probability. Evidence for this behavior is supported by the fact that the preferred models are different for the three events, leaving the recovery of precession as the only element systematically connected to higher probability values.

4.4 Injection runs

In addition to the analysis of real GW events, we want to corroborate in the following the validity of the method through an injection study. For this purpose, we perform a hypermodels analysis with the same waveform approximants and settings previously described, to analyze simulated signals in zero noise.

	Model	\mathcal{M}_c [M_\odot]	q	a_1	θ_1 [rad]	a_2	θ_2 [rad]	D_L [Mpc]
Injection 1	<code>IMRPhenomTPHM</code>	108.79	0.92	0.97	2.59	0.93	1.66	2751.72
Injection 2	<code>SEOBNRv4PHM</code>	71.32	0.54	0.99	1.12	0.81	1.96	3488.44
Injection 3	<code>IMRPhenomXPHM</code>	28.94	0.42	0.88	1.55	0.73	1.95	1358.51
Injection 4	<code>NRSur7dq4</code>	28.94	0.42	0.88	1.55	0.73	1.95	1358.51
Injection 5	<code>IMRPhenomXPHM</code>	65.72	0.63	0.81	1.74	0.68	1.72	2000.0
Injection 6	<code>NRSur7dq4</code>	65.72	0.63	0.81	1.74	0.68	1.72	2000.0
Injection 7	<code>IMRPhenomXPHM</code>	65.72	0.63	0.64	0.0	0.58	0.0	2000.0
Injection 8	<code>NRSur7dq4</code>	65.72	0.63	0.64	0.0	0.58	0.0	2000.0

Table 4.8: Approximant model and parameters used for injections; $a_{1,2}$ and $\theta_{1,2}$ represent the magnitude and tilt angle of the components' spins, while D_L is the luminosity distance.

The details of the injections are given in Table 4.8. Injection 1 and 2 are produced using the maximum-likelihood parameters and approximants recovered from the analyses of GW190521 and GW191109_010717, respectively. Injection 3 and 4 are generated with the maximum-likelihood parameters of GW200129_065458 using `IMRPhenomXPHM` and `NRSur7dq4`, which are the models with the highest recovered probability and likelihood, respectively. For the other injections we employed the maximum-likelihood mass values recovered for GW190519_153544, a fixed luminosity distance, and

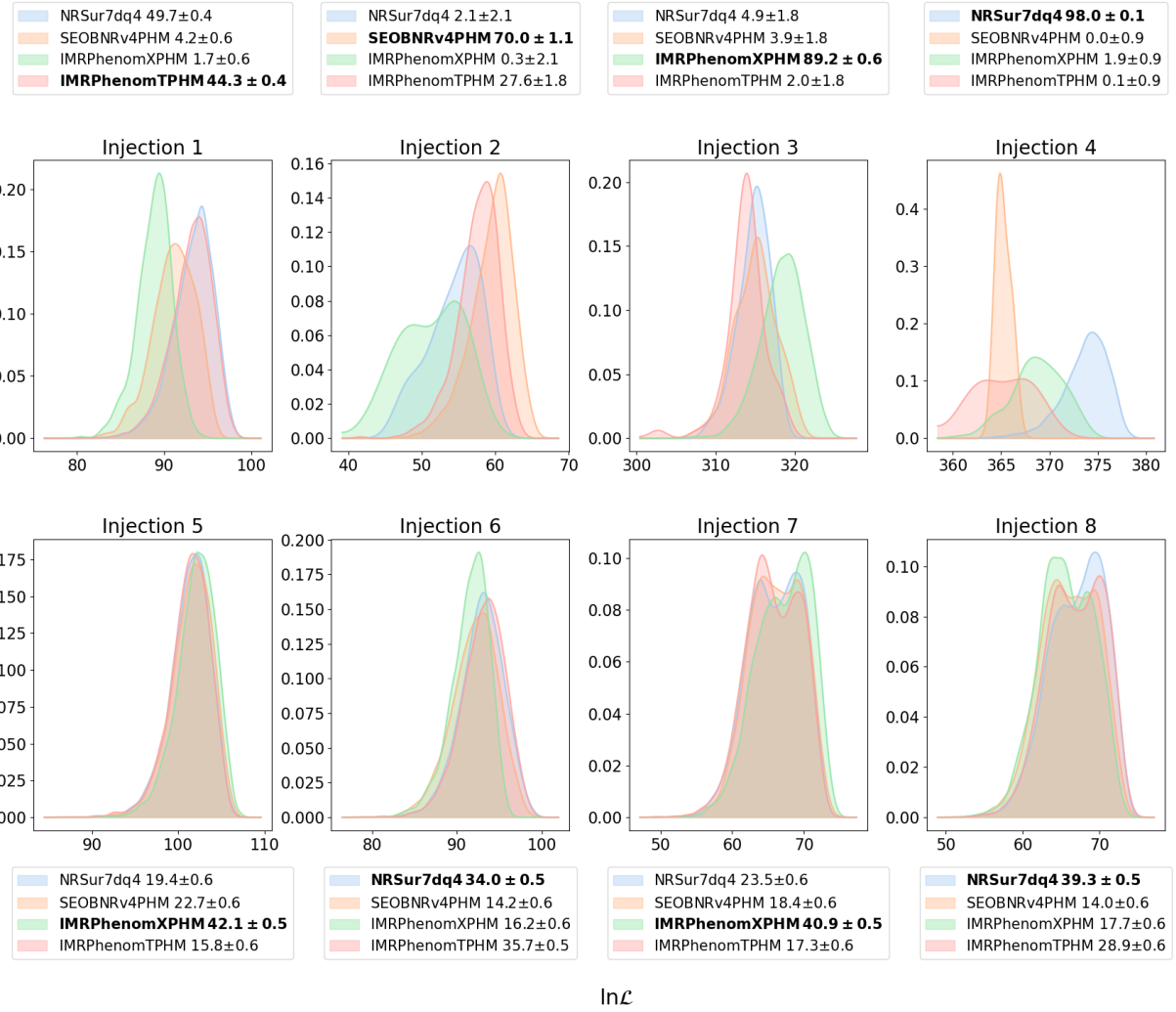


Figure 4.4: Probability density distributions for $\ln \mathcal{L}$ for the different models considered in the analysis. The legend reports the recovered probability percentages, including errors; the model marked in bold is the one used for the injection.

two different values of spin magnitudes and inclinations, considering injections both with `IMRPhenomXPHM` and `NRSur7dq4`. Figure 4.4 shows the probability density distributions of the recovered log-likelihoods for the different models, together with their percentage probabilities, including errors. In most cases we clearly recover the highest probability for the injected model. When the most favored model is not the injected one, however, the probability of the injected model is very close to the highest one. This is likely due to the fact that the two waveform descriptions are very similar, and the injected model is guaranteed to provide the best fit only at the injection point. To further understand why the injected model in some cases is not the most favored one, a detailed analysis of different ingredients for all employed waveform models would be required, which is however outside the scope of this paper. From the statistical point of view, the injection study indicates that our uncertainty on the odds might not measure the full uncertainty. A validation of the uncertainty estimates would need multiple runs on the same data set.

We also note that, in order to validate the method, we performed these analyses in zero noise: in real-events analysis, the presence of noise and noise fluctuations will affect the differences between the evidences.

4.5 Summary

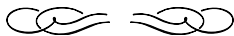
We analyzed the 13 events with the highest mass and moderate to high SNR among the ones detected so far by Advanced LIGO and Advanced Virgo, using the “hypermodels” technique developed in Ref. [270]. This method allows us to sample directly over different waveform approximants, in order to determine which one is favored by the data. We analyzed data with four different approximants, all including precession and higher-order modes: `NRSur7dq4`, `SEOBNRv4PHM`, `IMRPhenomXPHM`, and `IMRPhenomTPHM`. For each event, we recover the source parameters, finding both mass and spin parameters to be in agreement with the LVK results, cf. Table 4.5. For three events, `GW191109_010717`, `GW200129_065458`, and `GW190521`, we recover non-zero values for the effective precession spin parameter, with a distribution significantly different from the prior one. These events are also the ones for which we find a strong preference for some models over the other ones, although the preferred approximants are different. `GW191109_010717` shows a strong preference for `SEOBNRv4PHM`, with `NRSur7dq4` and `IMRPhenomXPHM` being disfavored. On the other hand, for `GW200129_065458` `NRSur7dq4` and `IMRPhenomXPHM` are strongly favored, and the probability for `SEOBNRv4PHM` and `IMRPhenomTPHM` is close to zero. Finally, `GW190521` recovers a very low probability, roughly 4%, for `IMRPhenomXPHM`, while the other models do not show significant differences among them. However, `GW191109_010717` and `GW200129_065458` data were affected by glitches [118], and the short duration of `GW190521` implies that we could not see its inspiral phase; therefore, we cannot draw clear conclusions about these events. Nonetheless, we systematically find that the models recovering evidence for non-zero values of χ_p are the ones with the higher probabilities. For all the other events, we recover only slight preferences for a given approximant, with the recovered parameters’ posteriors and log-likelihoods being similar.

We also performed some zero-noise injection runs to validate our method, showing that in most cases we recover the highest probability for the injected model, although an extensive injection study

would be needed in order to fully validate the uncertainty estimates.

Overall, we do not find one model to be consistently preferred over the others. This is unexpected, considering that we included `NRSur7dq4` in the analysis, which is predicted to be the most accurate model for high-mass signals, being interpolated from NR simulations. However, we also remark that the models are not used at their full capabilities since, in order to compare them, we consider only the subdominant modes present in all of them. The odds ratios combined over all the sources show `NRSur7dq4` being favored over `SEOBNRv4PHM`, with $\mathcal{O}_{\text{SEO}}^{\text{NRSur}} = 29.43$, while for `IMRPhenomXPHM` and `IMRPhenomTPHM` we find $\mathcal{O}_{\text{SEO}}^{\text{IMRX}} = 4.70$ and $\mathcal{O}_{\text{SEO}}^{\text{IMRT}} = 5.09$ respectively. However, this result is mostly determined by `GW200129_065458`, for which `SEOBNRv4PHM` and `IMRPhenomTPHM` probabilities are close to zero. If we remove this event from the combined odds ratio calculation, we obtain $\mathcal{O}_{\text{SEO}}^{\text{NRSur}} = 0.42$. Finally, if we do not take into account the three sources favoring one of the approximants, we find no significant preference for any of the models.

Chapter 5



Unraveling information about supranuclear-dense matter from the complete binary neutron star coalescence process using future gravitational-wave detector networks

Binary neutron star mergers offer a unique tool to study the EOS of supranuclear-dense matter, which can be constrained through measurements of the NSs' macroscopic properties. We saw in Sec. 1.3.4 that the EOS determines not only the signal emitted during inspiral, but also the possible postmerger one, which contains a wealth of information but proves very difficult to detect and analyze. In this chapter, based on Ref. [293], we build a waveform model to describe the GW signal emitted during the full coalescence of a BNS system, and we employ it in parameter estimation analyses with future detectors, with the goal to extract information about the EOS.

5.1 Introduction

In addition to a more detailed analysis of the inspiral, third-generation GW detectors such as the Einstein Telescope and the Cosmic Explorer are also expected to detect GWs from the postmerger phase of the BNS coalescence [294–298]. This is of special interest, since the postmerger probes a different, even higher density and temperature regime than the inspiral. During the inspiral only densities up to the central density of the individual stars are probed, which corresponds to about 3 to 4 times the nuclear saturation density, while the postmerger phase probes densities even beyond five times the nuclear saturation density; cf. Fig. 1 of Ref. [299]. In addition, also temperatures of about 50 MeV are reached during the postmerger phase, which is large enough that the effect of different transport coefficients will start to impact the data [300–302].

Unfortunately, postmerger studies pose numerous challenges. First, the amplitude of the post-

merger part of the observed GW signal is expected to be weaker than the inspiral one [80, 99, 100, 103, 303]. Second, at higher frequencies, the detectors' sensitivity drops due to quantum shot noise. For these reasons, it is not surprising that the dedicated searches for GWs emitted by a possible remnant of GW170817 [304, 305] found no evidence of such a signal and showed that with the sensitivity of Advanced LIGO and Advanced Virgo the source distance should have been at least one order of magnitude less for the postmerger signal to be detectable. Finally, postmerger physics includes thermal effects, magnetohydrodynamical instabilities, neutrino emission, dissipative processes, and possible phase transitions [306–312], which make the postmerger particularly difficult to model, but, on the other hand, allow us to investigate a variety of interesting physical processes. Because of the complexity of the evolution, the study of the postmerger relies heavily on numerical-relativity simulations, which, however, are also limited due to their high computational cost and the fact that it is currently not possible to take into account all the physical processes that influence the postmerger.

Nonetheless, previous studies based on NR simulations showed some common key features of the postmerger GW spectrum, finding in some cases universal relations with the NS properties [80, 82, 95–105], and some efforts have been made also to construct full inspiral, merger, and postmerger models for BNS coalescences. Also morphology-independent analyses of the postmerger GW signal have been proposed in Refs. [81, 97, 104], while in Ref. [313] a hierarchical model to generate postmerger spectra was developed. With a different approach, Refs. [314–316] construct analytical models for the postmerger signal, based on features found in NR simulated waveforms. Breschi *et al.* in Ref. [317] proposed a frequency-domain model for the postmerger, built with a combination of complex Gaussian wavelets, and showed in Ref. [318] how this model performs using a 3G detector network. Wijngaarden *et al.* [319] built a hybrid model, using analytical templates for the premerger phase and a morphology-independent analysis, based on sine-Gaussian wavelets, for the postmerger one.

Following similar ideas, we construct a phenomenological frequency-domain model for the entire BNS coalescence consisting of the inspiral, merger, and postmerger phases. Our final aim is to employ the developed model for parameter estimation analyses. Moreover, we investigate the performance of different detector networks to determine the improvement that future detectors will bring to our analysis.

5.2 The waveform model

We construct a frequency-domain waveform model, `IMRPhenomD_NRTidalv2_Lorentzian`, to describe the full inspiral, merger, and postmerger of a BNS coalescence. To model the coalescence during the inspiral up to the merger, we rely on `IMRPhenomD_NRTidalv2` [212], described in Sec. 2.1.4. The postmerger phase is modelled with a three-parameter Lorentzian describing the main emission peak of its spectrum, following Tsang *et al.* [320]. For the Lorentzian, we use two different approaches: in one case, we compute the parameters from quasi-universal relations, describing them as a function of the BNS's properties; in the other one, we treat them as free parameters. Both versions can be directly employed by existing parameter estimation pipelines; see, e.g., Refs. [321, 322].

In this section, we describe how we model the postmerger part of the signal and how we connect it to the inspiral-merger model to obtain the full waveform. As we explained in Sec. 2.1, waveform approximants are commonly calibrated against NR data, which are employed also to check the accuracy of the models. In particular, for this work we employ the NR postmerger data and the complete inspiral-merger-postmerger hybrid waveforms in the CoRe [323, 324] and SACRA [157] databases.

5.2.1 Inspiral-merger-postmerger model construction

Multiple studies have shown that the postmerger GW spectrum includes various strong peaks [80, 82, 95, 98–103, 325]. For simplicity, we limit ourselves to the main emission peak at a frequency f_2 , which corresponds to the dominant GW frequency; see, e.g., Ref. [95]. Following this approach, the postmerger can be described in time domain by a simple damped sinusoidal waveform [320], whose Fourier transform is a Lorentzian. Therefore, in frequency domain, we model the postmerger with a three-parameter Lorentzian

$$h_{22}(f) = \frac{c_0 c_2}{\sqrt{(f - c_1)^2 + c_2^2}} e^{-i \arctan\left(\frac{f - c_1}{c_2}\right)}, \quad (5.1)$$

where c_0 corresponds to the maximum amplitude value, c_1 to the dominant emission frequency f_2 , and c_2 to the inverse of the damping time, which sets the Lorentzian’s width.

We determine the coefficients c_i with two different approaches: (I) we treat them as free parameters, and try to measure c_0 , c_1 , and c_2 together with the other BNS’s properties; and (II) we compute the c_i coefficients from quasi-universal relations that describe them as functions of the system’s parameters.

Depending on its properties and EOS, a given BNS could undergo a prompt collapse to a black hole, hence without a postmerger emission. In this scenario, while in case (I) we expect that the values recovered for the free parameters reflect the absence of a postmerger signal, in (II) the quasi-universal relations employed might lead to a bias in the estimation of the binary’s intrinsic parameters. For this reason, we ideally want to use the Lorentzian model with quasi-universal relations only when we know that a postmerger emission is present. Since the threshold mass for a prompt collapse is EOS-dependent and still unknown, following Ref. [314] we assume that a BNS system undergoes prompt collapse if the tidal polarizability parameter κ_2^T is lower than a threshold value $\kappa_{\text{thr}} = 40$. The quantity κ_2^T is defined as

$$\kappa_2^T = 3 [\Lambda_2^1(X_1)^4 X_2 + \Lambda_2^2(X_2)^4 X_1], \quad (5.2)$$

where $\Lambda_2^j = \frac{2}{3} k_2 (R_j/m_j)^5$ with $j \in \{1, 2\}$ are the dimensionless tidal deformabilities, and $X_j = m_j/M$. Here k_2 is the dimensionless $\ell = 2$ Love number, R_j and m_j are the radius and gravitational mass of the individual stars, respectively, and $M = m_1 + m_2$ is the BNS’s total mass.¹

Quasi-universal relations for the Lorentzian parameters

For the approach introduced as method (II), we use quasi-universal relations, i.e., phenomenological relations that are independent of the EOS (see Sec. 1.3.4), to constrain the coefficients c_i in Eq. (5.1). This provides a direct connection between the Lorentzian coefficients and the BNS’s properties.

¹See also Ref. [326] for more updated relations which were not yet available when we started this work.

Since the postmerger Lorentzian model extends the waveform used for inspiral and merger beyond its merger frequency f_{merg} , a straightforward way to find the value of c_0 is by rescaling the amplitude of the `IMRPhenomD_NRTidalv2` waveform at merger $\mathcal{A}_{\text{NRTidalv2}}(f_{\text{merg}})$. Specifically, we use

$$c_0 = \sigma \times \mathcal{A}_0 \times \mathcal{A}_{\text{NRTidalv2}}(f_{\text{merg}}), \quad (5.3)$$

where \mathcal{A}_0 is the mass and distance scaling factor employed in `IMRPhenomD` [174]. The prefactor σ is added to obtain a better calibration to the NR waveforms, and we set $\sigma = 10.0$, which gives the lowest mismatch values (the definition of mismatch and details about its computation are provided in Sec. 5.2.2).

Since c_1 represents the dominant postmerger oscillation frequency f_2 , we resort to the fit in Eq. (8) of Ref. [320]

$$Mc_1(\zeta) = \beta \frac{1 + A\zeta}{1 + B\zeta}, \quad (5.4)$$

with $\beta = 3.4285 \times 10^{-2}$, $A = 2.0796 \times 10^{-3}$, and $B = 3.9588 \times 10^{-3}$. The parameter ζ is

$$\zeta = \kappa_{\text{eff}}^T - 131.7010 \frac{M}{M_{\text{TOV}}}. \quad (5.5)$$

In the last equation, $\kappa_{\text{eff}}^T = (3/18) \tilde{\Lambda}$, with $\tilde{\Lambda}$ being the binary's mass-weighted tidal deformability (cf. Eq. 2.58). Although ζ , and therefore c_1 , in Eq. (5.5) is a function of the maximum mass allowed for a non-rotating stable NS, M_{TOV} , which depends on the specific EOS, we fix $M_{\text{TOV}} = 2 M_{\odot}$ for the model version with quasi-universal relations in this work.² The median relative error introduced on ζ by this approximation is 0.31, for the hybrid waveforms in the SACRA and CoRe database. This error propagates to the c_1 parameter causing a median relative error of approximately 5%.

With this choice for c_0 and c_1 , a model for c_2 is built from a set of 48 non-spinning NR waveforms, from the CoRe database. For this, we first find the values of c_2 that minimize the mismatch of the Lorentzian waveform and the NR one between 0.75 c_1 and 8192 Hz using a flat noise power spectral density; see Sec. 5.2.2 for details. The flat PSD ensures that no high-frequency information is suppressed in the match computation. For each waveform, c_2 minimization is performed using the ‘L-BFGS-B’, ‘SLSQP’, ‘TNC’, and ‘Powell’ methods available in `SciPy` [329], and the value of c_2 with the least mismatch value is used. It was seen that c_2 showed a similar trend against $\kappa_{\text{eff}}^T q^{-2}$, where $q = m_2/m_1$, with $m_1 > m_2$, is the mass ratio, as c_1 does against ζ . Hence, NR data were fitted with an analogous ansatz. However, using obtained from performing a simple curve fit showed unphysical amplitude behaviour for a few of the NR waveforms. For further tuning, the mismatch was minimized for all the NR waveforms by varying the fit parameters, and the parameters that gave the least mismatch were then recorded and added to the model. The functional form of c_2 and the values obtained for the fit parameters in this manner are

$$c_2 = 2 + \gamma \frac{1 + C\kappa_{\text{eff}}^T q^{-2}}{1 + D\kappa_{\text{eff}}^T q^{-2}}, \quad (5.6)$$

²In principle, we could treat M_{TOV} as a free parameter, but this would impair the main benefit of this version of the model—namely to avoid additional parameters to sample over. However, in the future, given the increasing number of multi-messenger detections of binary neutron star mergers and the possibility to observe high-mass pulsars [78, 94, 327, 328], one can expect to have a significantly smaller uncertainty in M_{TOV} than today. The value of the maximum supported mass estimated from this new information will then provide the fixed value of M_{TOV} to employ in our model.

with $\gamma = 19.4579017$, $C = -9.63390738 \times 10^{-4}$, and $D = 6.45926154 \times 10^{-5}$. The median relative error for c_2 during minimization is 0.56.

The full waveform

To obtain a model describing the full coalescence, the previously derived postmerger model is connected to the waveform describing the inspiral and merger part of the signal, for which we use the phenomenological waveform `IMRPhenomD_NRTidalv2` [212].

Amplitude: To ensure a smooth transition³ between the two models, we apply a Planck-taper window $\alpha_{\text{Pl}}(f)$:

$$\alpha_{\text{Pl}}(f) = \begin{cases} 0 & \text{for } f < f_{\text{tr}}, \\ \exp\left[\frac{f_{\text{end}}-f_{\text{tr}}}{f-f_{\text{tr}}} + \frac{f_{\text{end}}-f_{\text{tr}}}{f-f_{\text{end}}} + 1\right]^{-1} & \text{for } f_{\text{tr}} < f < f_{\text{end}}, \\ 1 & \text{for } f > f_{\text{end}}. \end{cases} \quad (5.7)$$

The window is applied just before the frequency of the main postmerger peak f_2 , which corresponds to our model's parameter c_1 . The value of the window's starting frequency f_{tr} is chosen to ensure a good match with NR waveforms. In particular, in Ref. [320] one of the time-domain features identified in the postmerger signal morphology is the *first postmerger minimum*, which corresponds to a clear amplitude minimum present shortly after the merger, before the amplitude starts increasing again. By comparison with NR waveforms in the CoRe database, we found that this feature is best reproduced by our model when the Planck window is applied between $f_{\text{tr}} = 0.75 c_1$ and $f_{\text{end}} = 0.9 c_1$. Following Ref. [174], we add an exponential correction factor $\exp\left[-\frac{p(f-c_1)}{c_2}\right]$ to the Lorentzian amplitude, in order to smoothen possible kinks arising when going to the time domain. We set $p = 0.01$, which is enough to reduce the kink, but not so large that it significantly influences the merger amplitude.

Phase: To ensure that the waveform phase is C^1 continuous, we introduce two coefficients a and b , writing the phase as

$$\phi_{\text{IM}}(f) = \phi_{\text{Lor}}(f) + a + b f, \quad (5.8)$$

with ϕ_{IM} being the phase of `IMRPhenomD_NRTidalv2` waveform and $\phi_{\text{Lor}} = \arg(h_{22}(f))$ the Lorentzian one. The values of a and b are computed at the same transition frequency $f_{\text{tr}} = 0.75 c_1$ at which we start the Planck-taper window for the amplitude, such that

$$\left. \frac{d\phi_{\text{IM}}}{df} \right|_{f_{\text{tr}}} = \left. \frac{d\phi_{\text{Lor}}}{df} \right|_{f_{\text{tr}}} + b, \quad (5.9)$$

$$\phi_{\text{IM}}(f_{\text{tr}}) = \phi_{\text{Lor}}(f_{\text{tr}}) + b f_{\text{tr}} + a. \quad (5.10)$$

Finally, to reduce the Lorentzian contribution to the pre-merger and merger amplitude, we multiply the waveform by a factor $\exp[-i2\pi\Delta t f]$, which will induce a time shift of Δt in the time-domain waveform; Δt is computed as the time interval between the merger and the *first postmerger minimum*

³We note that the employed approach neglects any contribution of the postmerger signal towards frequencies below the merger frequency.

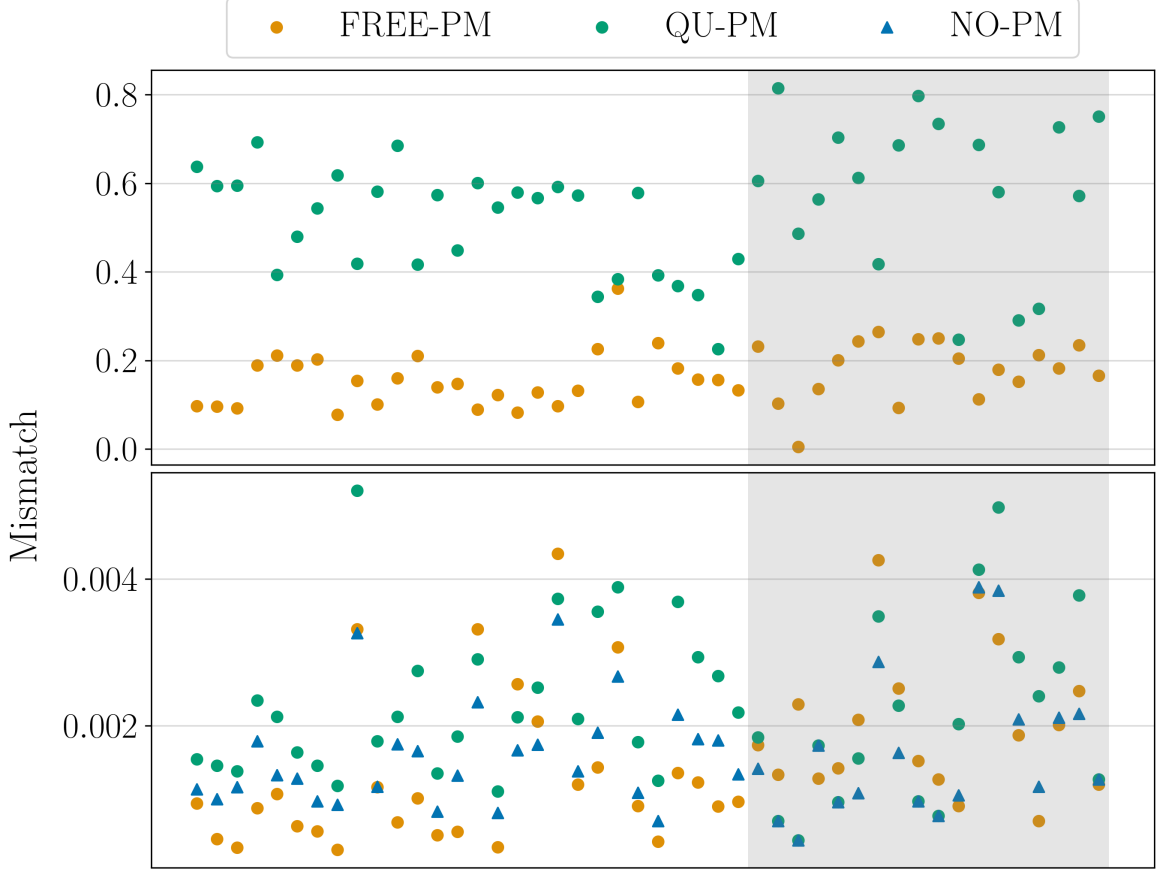


Figure 5.1: Mismatches between hybrid waveforms from the CoRe (in the gray-background band) and SACRA databases, and our postmerger model, for both the versions FREE-PM and QU-PM. The top panel shows mismatches in the postmerger frequency band (i.e., within $[1.1 f_{\text{merg}}, 4096]$ Hz), while the bottom panel shows mismatches for the whole waveform (within $[30, 4096]$ Hz). In the latter case, for comparison we show also mismatches computed between the hybrids and the NO-PM model.

described by Eq. (2) in Ref. [320].

The frequency-domain gravitational waveform can be written as

$$\tilde{h}(f) = \mathcal{A}(f)e^{i\phi(f)}, \quad (5.11)$$

with $\mathcal{A}(f)$ the amplitude and $\phi(f)$ the phase. Therefore, in our model the full waveform is given by:

$$\tilde{h}(f) = \begin{cases} \mathcal{A}_{\text{IM}}(f)e^{i\phi_{\text{IM}}} & \text{for } f < f_{\text{tr}}, \\ \left(\mathcal{A}_{\text{IM}}(f) + \alpha_{\text{Pl}}(f)\mathcal{A}_{\text{Lor}}(f)e^{-\frac{p(f-c_1)}{c_2}} \right) e^{i(\phi_{\text{Lor}}+bf+a)-i2\pi\Delta tf} & \text{for } f > f_{\text{tr}}, \end{cases} \quad (5.12)$$

where $\mathcal{A}_{\text{IM}}(f)$ and $\phi_{\text{IM}}(f)$ are the amplitude and phase, respectively, of the `IMRPhenomD_NRTidalv2` waveform, and $\mathcal{A}_{\text{Lor}} = |h_{22}(f)|$ the amplitude of the Lorentzian one.

In the following, we refer to the `IMRPhenomD_NRTidalv2_Lorentzian` postmerger model with quasi-universal relations as QU-PM, to the one with free Lorentzian parameters as FREE-PM, and to the model without postmerger, `IMRPhenomD_NRTidalv2`, as NO-PM.

5.2.2 Mismatch

The mismatch between two waveforms h_1 and h_2 is defined as

$$MM = 1 - \max_{\phi_c, t_c} \frac{\langle h_1(\phi_c, t_c) | h_2 \rangle}{\sqrt{\langle h_1 | h_1 \rangle \langle h_2 | h_2 \rangle}}, \quad (5.13)$$

where t_c and ϕ_c are an arbitrary time and phase shift, and $\langle \cdot | \cdot \rangle$ the noise-weighted inner product, as defined in Eq. 2.69. To validate the `IMRPhenomD_NRTidalv2_Lorentzian` model, we compute mismatches with the hybrid waveforms in the CoRe and SACRA databases. The mismatch is computed with PyCBC [330] functions and zero noise, i.e., with a flat PSD. For the FREE-PM model, to get the Lorentzian parameters that better describe each hybrid’s postmerger, we optimize the mismatch over c_1, c_2 ; we do not include the Lorentzian maximum value c_0 in the minimization, because, giving just an amplitude scaling factor, the mismatch is insensitive to it. The initial values for the optimization are found with a least-squares fit on the postmerger part of the hybrid waveform, for $f \geq 1.3 f_{\text{merg}}$. Fixing c_1 and c_2 to the optimal values, we then compute the optimal value for c_0 with a least-square fit on the hybrid’s postmerger signal. We use the optimal values for the c_i coefficients to generate the FREE-PM waveform, for which we compute the mismatch with the hybrid in different frequency ranges. For the QU-PM model, instead, the Lorentzian parameters are computed from the quasi-universal relations described in Sec. 5.2.1, using the values of the hybrid’s binary parameters. The top panel of Fig. 5.1 shows the mismatches in the frequency band $[1.1 f_{\text{merg}}, 4096]$ Hz: despite our simple description of the postmerger, for almost all hybrids mismatches lie below 0.3 when using the FREE-PM model. Mismatches values increase systematically by roughly a factor of 3 when computing them with respect to the QU-PM model, which is expected since in this case the Lorentzian parameters are not optimized to the hybrid waveform. When considering the whole waveform, in the frequency range $[30, 4096]$ Hz, the mismatch is always below 0.005, as shown in the bottom panel of Fig. 5.1. Also in this case, for most hybrids the FREE-PM model gives better matches compared to the QU-PM one. The fact that mismatches computed over the whole waveform do not follow the trend of the ones computed only in the high frequency region is due to the fact that different values of the Lorentzian parameters translate also into different tapering and continuity conditions, influencing the late inspiral-merger phase too. For comparison, we show also the mismatches computed in the same frequency range with the NO-PM waveform. The plot does not highlight a systematic improvement in the mismatches when using one of the models; the difference between the mismatch obtained with the NO-PM and FREE-PM models varies from 0.0019 to 8×10^{-6} , with an average variation of 0.0005 . In some cases, the NO-PM model gives lower mismatches than one of the models with postmerger. This occurs because the NO-PM waveform includes no signal after the merger, therefore computing the mismatch for frequencies higher than the merger one, in a region where the waveform is zero, does not contribute to the overall mismatch. Hence, the lack of the postmerger signal does not reduce the match computed up to the merger frequency. However, in more than 60% of cases, the mismatch is reduced when using the FREE-PM model, showing that our postmerger description with optimized parameters improves the signal characterization.

5.3 Methods and setup

In this section, we explain the framework used for data analysis, describing the employed detector networks, the analysis setup, and the BNS sources that we study to determine to what extent future detector networks will enable postmerger studies. We show an example of the performance of future detectors in general parameter estimation analyses, and we provide more details about the application in this specific context of the relative binning technique, employed to reduce the computational cost of the analyses.

5.3.1 Detector networks

Ground-based GW detectors have the best sensitivity around a few tens to hundreds of Hz, which makes the inspiral and merger signal of coalescing compact objects the perfect candidate for detections. In this work, however, we are interested in the postmerger part of the signal, which is usually weaker and involves higher frequencies. Current detectors are strongly limited at these high frequencies, but the improvements planned for the future detectors' upgrades and the next-generation detectors are expected to make postmerger measurements feasible. Therefore, one of the goals of this work is to assess how future detectors can improve the studies we present.

We include in our analysis the upgraded versions of existing detectors, Advanced LIGO+, Advanced Virgo+, and KAGRA, as well as new detectors whose construction has been planned for the next few years, LIGO-India and NEMO, and the next detector generation, the Einstein Telescope and the Cosmic Explorer. Advanced LIGO+ design [334] will improve the current 4 km arm-length detectors in Hanford (H) and Livingston (L) sites, including a frequency-dependent light squeezing and new test masses with improved coating. Advanced Virgo+ (V), similarly, is the planned upgrade for the current Advanced Virgo detector in Cascina, Italy [112]. This transition will happen in two separate phases and include upgrades like the introduction of signal recycling and a higher laser power. Advanced LIGO+ and Advanced Virgo+ are the planned designs for the O5 observing run, which is scheduled to start roughly in 2025, and during which their BNS detection range will reach approximately 330 Mpc and 150–260 Mpc, respectively [124]. KAGRA (K) [125–127] is a 3 km arm-length interferometer built underground in the Kamioka mine in Japan, which already employs innovative technologies like cryogenic mirrors. For O5, its sensitivity at the end of the observing run is predicted to allow a BNS range of at least 130 Mpc [124]. The LIGO network involves a third detector in India (I) [128], which is currently under construction and is expected to become operative approximately in 2025. Finally, the Neutron Star Extreme Matter Observatory, or NEMO (N), is an Australian proposal for a gravitational-wave detector with 4 km arm length, specifically designed to have a high sensitivity in the kilohertz band [141]. The possible location of NEMO has not been decided yet, therefore for this work we arbitrary place it at the location shown in Fig. 5.2. Although not officially approved yet, we include it in our analysis, since its high-frequency sensitivity is particularly interesting for postmerger studies.

3G detectors are expected to increase the sensitivity by a factor between 10 and 30 [124] with respect to current LIGO detectors, but they require the construction of new facilities and are expected to start observing in the mid 2030s. At the moment, the intended 3G detector network includes plans

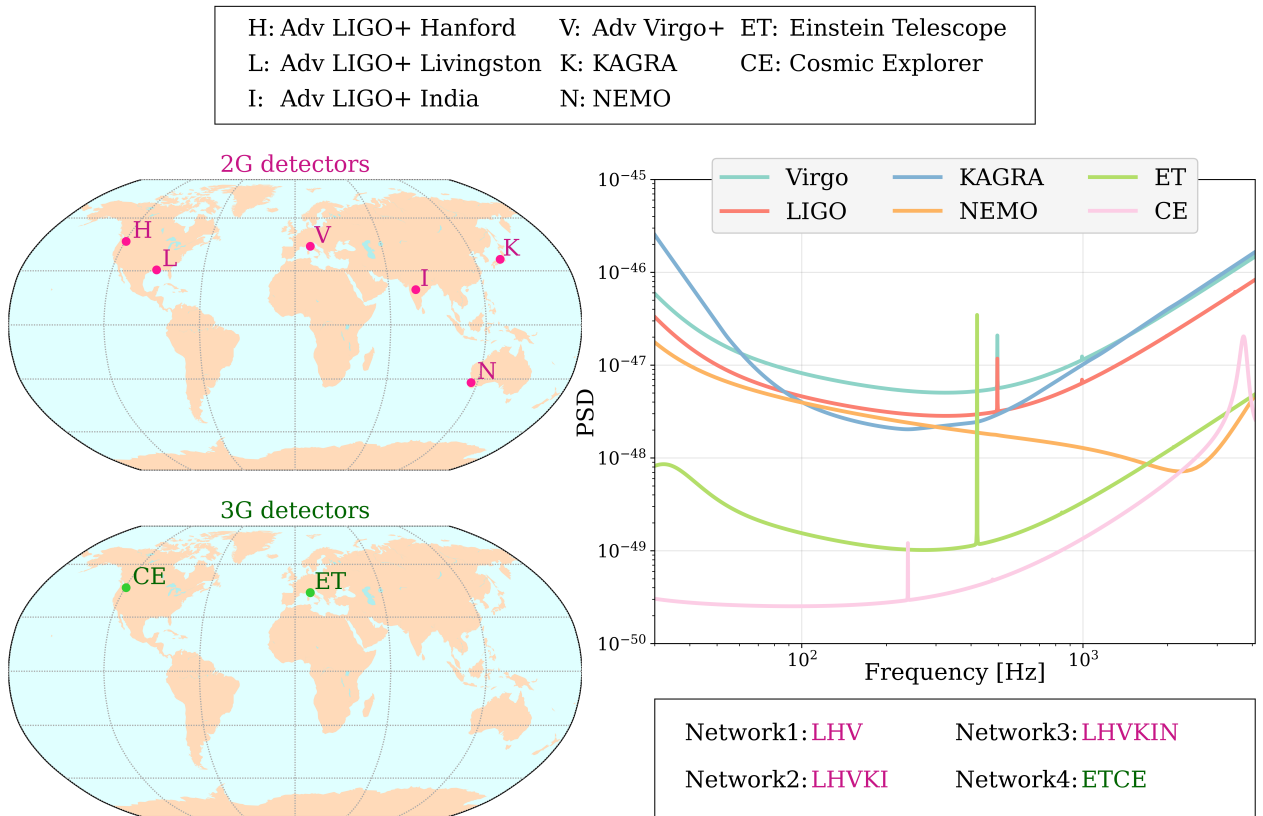


Figure 5.2: *Left:* location of the detectors used in this study, top panel for second generation (2G) detectors and bottom panel for third generation (3G) ones. *Right:* PSDs, in units of [1/Hz], for the different detectors. The Advanced LIGO+ PSD [331] is used for H, L, and I detectors. Since the official sensitivity curve for Advanced Virgo+ is not available yet, we computed its ASD curve by scaling the one of the LIGO detectors by a factor 4/3 to account for the different arm length. ET sensitivity is the one referred to as “ET-D” and provided in Ref. [134], while CE sensitivity is given in Ref. [332]; for KAGRA we employ the PSD labeled as “Combined” in Ref. [333].

for Cosmic Explorer in the United States and the Einstein Telescope in Europe. CE is planned as an L-shaped interferometer with 40 km arm length.⁴ For the purpose of this paper, we assume it placed at the current Hanford site. The ET design includes a so-called “xylophone” configuration, which guarantees an improved sensitivity at high and low frequencies at the same time [134]. The two candidates for the ET site are Sardinia, in Italy, and Limburg, at the border between the Netherlands, Germany, and Belgium.⁵ For this work, we assume ET is placed at the current Virgo site. Although the final design of ET is still under development, here we consider it as a triangular detector—i.e., composed of three V-shaped interferometers with a 60° opening angle and 10 km arms.

In this work, we study four different detector networks: HLV, HLVKI, HLVKIN, and ETCE. The detectors’ locations and sensitivities are shown in Fig. 5.2.

⁴Recently, also a configuration consisting of a 40 km and an additional 20 km detector has received attention and was considered as the reference concept for the recent Horizon study of Ref. [138]. In Ref. [139], also a tunable design for the CE detector was proposed, which would enhance sensitivity in the kilohertz band.

⁵In addition, recent interest arose for a third possible site located in the eastern part of Germany.

5.3.2 Parameter estimation

In the following, we employ a Bayesian framework to recover the source's parameters, as discussed in Sec. 2.2.2. To sample the likelihood function, we employ the nested sampling package `dynesty` [335, 336], which is included in the `bilby` library [321, 322].

The computational cost of parameter estimation analyses increases both with the duration of the signal and the maximum frequency employed. In our case, we set $f_{\max} = 4096$ Hz, since the postmerger GW signal is expected to lie within the few-kilohertz regime. Moreover, we study BNS systems, whose low masses imply a long signal duration. Although we set the starting frequency to $f_{\text{low}} = 30$ Hz, the typical duration of the signal in band is still roughly 200 s. To overcome the issue of the computational cost of the analyses needed for this work, we resort to the technique of relative binning, described in detail in Sec. 2.3.3. To use relative binning with `bilby` inference, we employ the code in Ref. [337]. More details about the application of relative binning method to our analysis are provided in Sec. 5.3.5.

5.3.3 Simulations

We test the performance of our model in parameter estimation analyses with simulated signals. We consider three different sources, and analyze them through `bilby` injections, i.e., using our own GW models, and through injecting NR hybrids with the same parameters; cf. Table 5.1. The employed hybrids have a postmerger signal duration of roughly 10 ms, and the postmerger contribution to their SNR for each detector network is shown in Tab. 5.2.

All simulated signals are injected with zero inclination ι and polarization angle ψ , and with sky location $(\alpha, \delta) = (0.76, -1.23)$ rad. The sky location has been chosen such that none of the employed detector networks is particularly preferred. Depending on the analysis, we performed injections at three different distances: 225 Mpc, 135 Mpc, and 68 Mpc, which, in a network with Advanced LIGO+ and Advanced Virgo+, correspond approximately to a signal-to-noise ratio of 30, 50, and 100, respectively. Table 5.3 reports the SNR for Source2_[QU-PM] injections in the different detector networks and at different distances. We use priors uniform in $[0.5, 1.0]$ for mass ratio q , and uniform in $[\mathcal{M}_{c,s} - 0.05 M_{\odot}, \mathcal{M}_{c,s} + 0.05 M_{\odot}]$ for chirp mass, where $\mathcal{M}_{c,s}$ is the chirp mass of the source and the prior width is given by the precision on chirp-mass measurements that we anticipate for future detectors. Regarding tidal deformability parameters, we sample over $\tilde{\Lambda}$ and $\Delta\tilde{\Lambda}$, with a prior uniform in $[0, 5000]$ and $[-5000, 5000]$, respectively, where $\Delta\tilde{\Lambda}$ is defined as in Eq. 2.59. Luminosity distance priors are uniform in comoving volume, with $D_L \in [1, 450]$ Mpc. Although all the sources considered are non-spinning, our baseline model `IMRPhenomD_NRTidalv2` allows for aligned spins; we choose a uniform prior on the spin magnitudes $|\chi_1|, |\chi_2| \in [0.0, 0.20]$. Finally, when using the postmerger model with free parameters for recovery, we choose uniform priors $c_1 \in [2000, 4096]$ Hz and $c_2 \in [10, 200]$ Hz, while for c_0 we employ a logarithmic uniform prior in $[5 \times 10^{-27}, 1 \times 10^{-22}]$ s.

5.3.4 Parameter estimation with future detectors

Our discussion will focus on the recovery of the $\tilde{\Lambda}$ parameter, or of the c_1 parameter in the case of the FREE-PM model, because these are the quantities that encode most of the information about the EOS. However, it is also interesting to look at the recovery of all the other parameters of the binary,

Name	$\mathcal{M}_c [M_\odot]$	q	$\tilde{\Lambda}$	Injection
Source1 _[NR-inj]	1.17524	0.8	604	NR: H_121_151_00155 [338]
Source1 _[QU-PM]	1.17524	0.8	604	Bilby: quasi-universal
Source1 _[FREE-PM]	1.17524	0.8	604	Bilby: free parameters
Source2 _[NR-inj]	1.08819	1.0	966	NR: H_125_125_0015 [339]
Source2 _[QU-PM]	1.08819	1.0	966	Bilby: quasi-universal
Source2 _[FREE-PM]	1.08819	1.0	966	Bilby: free parameters
Source3 _[NR-inj]	1.17524	1.0	607	NR: H_135_135_00155 [338]
Source3 _[QU-PM]	1.17524	1.0	607	Bilby: quasi-universal
Source3 _[FREE-PM]	1.17524	1.0	607	Bilby: free parameters

Table 5.1: Properties of the sources used for injections. The NR hybrids are taken from the SACRA database, where the employed EOSs of the NR data are simple two-piece polytropes as outlined in Ref. [157]. For the hybridization, we follow the procedure outlined in Sec. III C of Ref. [158]. The inspiral waveform model with which we hybridize is `SEOBNRv4T` [340]. For `bilby` injections, we used our `IMRPhenomD_NRTidalv2_Lorentzian` model, both with quasi-universal relations and with free Lorentzian parameters. In case of injections with the free parameters model, the injected c_0, c_1, c_2 values are obtained from the best fit of the correspondent NR hybrid.

to see how future detectors will help improving our knowledge of these systems. Figure 5.3 shows the comparison between the normalized posterior probability density for \mathcal{M}_c , q , $\tilde{\Lambda}$, χ_1 , χ_2 , α , δ , and luminosity distance D_L , obtained using different detector networks, for Source2_[QU-PM] injections at 68 Mpc and in zero noise. We find that 3G detectors will yield a strong improvement not only for what concerns $\tilde{\Lambda}$ recovery, but also in the estimation of \mathcal{M}_c , q , and D_L ; in particular, with the ETCE network we can estimate \mathcal{M}_c with a precision roughly 10 times better than the LHV one. We find only a slight improvement in the recovery of the spin magnitude values χ_1 and χ_2 . The best estimation of the sky location parameters (α, δ) comes from the LHV_{KIN} network, which is expected considering the larger number of detectors and their geographical distribution, as shown in Fig. 5.2.

We also note that the improvement obtained by adding NEMO to the network is roughly of a factor 1.9 and 1.6 for \mathcal{M}_c and q , respectively, when computed in comparison with the LHV_{KI} network, but it reaches a factor 4.4 for $\tilde{\Lambda}$ estimation. As we will discuss in Sec. 5.4.2, this is achieved thanks to the postmerger contribution to the signal, which for NEMO is significant as a result of its very high sensitivity in the kilohertz band.

Overall, future detectors will grant very precise constraints on the BNS parameters, allowing us to better understand the properties and populations of these objects. We also point out that, for computational reasons, our analyses are performed starting from a frequency $f_{\text{low}} = 30$ Hz, and hence, in reality, additional information will be available by analyzing signals starting from lower frequencies.

	Source1 _[NR-inj]		Source2 _[NR-inj]		Source3 _[NR-inj]	
	Total	PM	Total	PM	Total	PM
LHV	100	2.0	94	2.5	100	2.7
LHVKI	107	2.1	101	2.6	108	2.9
LHVKIN	126	6.8	119	8.8	126	9.9
ETCE	1267	10.2	1190	12.3	1268	13.3

Table 5.2: SNR of the NR waveforms employed in our analysis for the different detector networks (with acronyms as shown in Fig. 5.2), considering the source at a distance of 68 Mpc; we show both the SNR for the whole waveform (in the ‘Total’ column), computed starting at 30 Hz, and the SNR of the postmerger part of the signal (in the ‘PM’ column), computed starting from the merger frequency.

Network	Distance [Mpc]	SNR
ETCE	68	1239
	135	624
	225	355
LHVKIN	68	121
	135	61
	225	36
LHVKI	68	105
	135	53
	225	31
LHV	68	98
	135	49
	225	30

Table 5.3: SNR values for zero-noise Source2_[QU-PM] injections in the different networks (with acronyms as shown in Fig. 5.2) and for different distances.

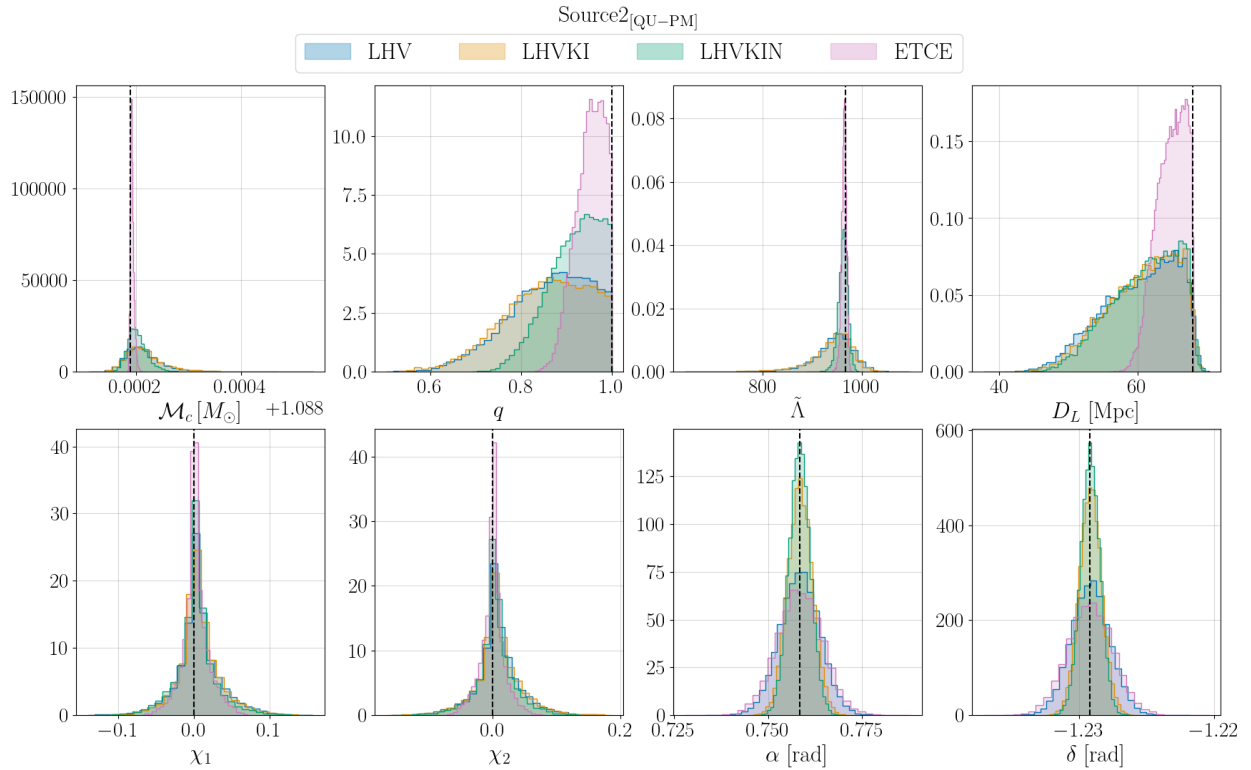


Figure 5.3: Normalized posterior probability density for the binary’s parameters recovered with the QU-PM model with the different detector networks, for Source2_[QU-PM] at 68Mpc; the dashed vertical lines show the injected values.

This will lead to a large improvement especially for the 3G detectors, because, for example, the xylophone configuration of ET, with the low-frequency interferometer possibly operating at cryogenic temperatures, will ensure a good sensitivity down to $f_{\text{low}} = 5 \text{ Hz}$. The additional information carried in the many inspiral cycles at low frequencies will further improve the constraints on the BNS parameters (see Sec. 6.3.3 for more details), resulting particularly beneficial for the spin parameters, considering that at low frequencies also spin-induced quadrupole moment effects become significant.

5.3.5 Relative binning settings and validity

The relative binning method allows us to greatly reduce the computational cost of our analysis. As explained in Sec. 2.3.3, a fundamental requirement to employ this technique is having a reference waveform that describes the data sufficiently well. Although with real data we do not know the exact parameters of the source a priori, we can use information from low-latency analyses and quasi-universal relations to find the values to use as the fiducial parameters. Since there might still be biases in the parameters determined in such a way, we checked the influence of the choice of fiducial parameters, performing some tests with different fiducial values for Λ_1 , Λ_2 , and we found consistency between results.

In Ref. [237], the authors show results obtained with this method for GW170817, which, despite being a loud event, has an SNR much lower to the ones we study in this work (cf. Table 5.3). The

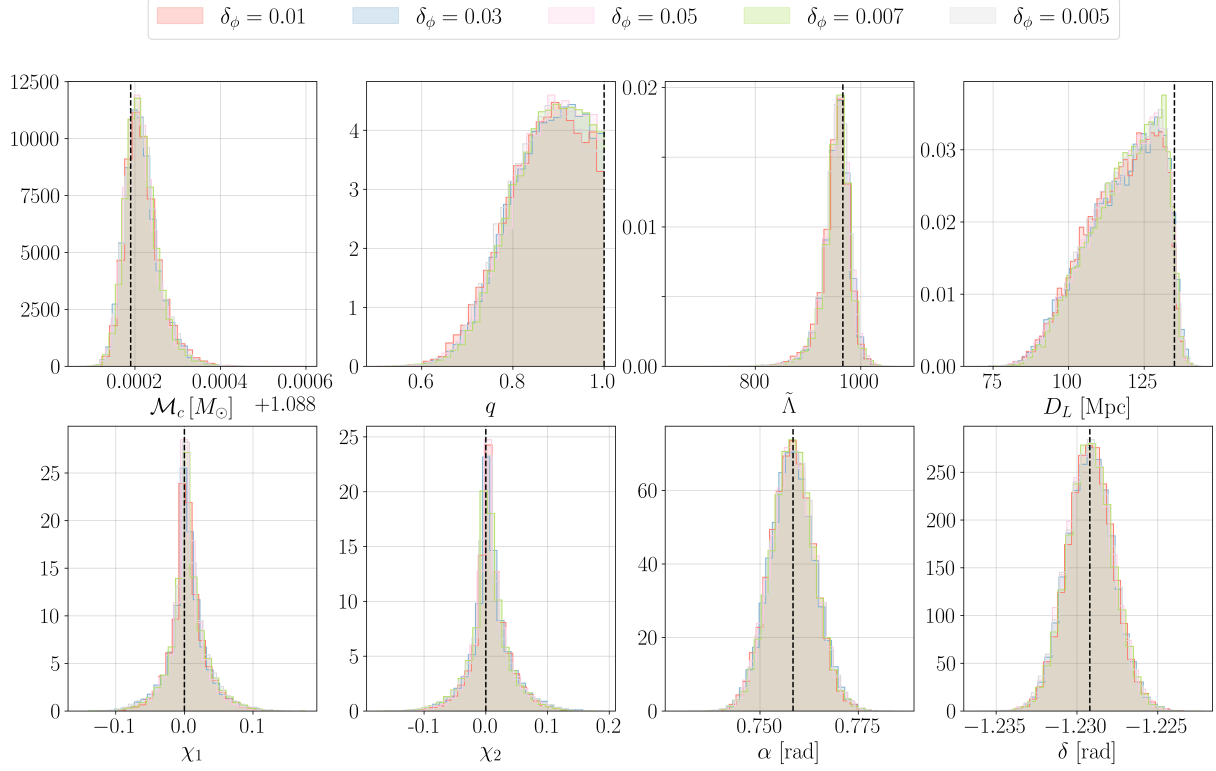


Figure 5.4: Comparison between the normalized posteriors for the binary’s parameters recovered with the QU-PM model, for Source2_[QU-PM] injections at 135 Mpc with the LHKIN network, using the relative binning technique with different precision requirements. The different colors show the posteriors for the analysis with different values of δ_ϕ , while the black dashed lines represent the injected values.

approximations used in relative binning are not expected to retain validity only in a given SNR range, but we tested the efficacy of this method applied to very loud signals by checking the consistency against results obtained with the nested sampling package LALINFERENCE [220] of the LAL software suite [77].

Finally, when using the relative binning method, the choice of frequency bins in which the waveform is evaluated plays a crucial role. Following Ref. [237], this choice is dictated by the requirement that the differential phase change in each bin is smaller than some threshold δ_ϕ . In Ref. [237], the phase change is computed assuming a post-Newtonian description of the signal, in which the effect of the different binary parameters enters the phase with different powers of frequency. In the merger and postmerger part of the signal, the PN approximation is not valid anymore. It is not easy to find a similar way to properly describe the phase in the postmerger, without having to evaluate the waveform and incurring in computationally expensive processes that would undermine the speed-up advantage of this method. On the other hand, the phase computed with the PN approximation is then interpolated with frequency, and the frequency bins are determined by evaluating this interpolant over a grid of phases determined by the required precision δ_ϕ . Therefore, if such a threshold is chosen small enough (for our analysis we set $\delta_\phi = 0.01$), we expect that the way in which the phase change is computed will play little role, and the dense frequency binning produced ensures that the bins’ width will be small enough to allow a linear interpolation of the ratio between the generated waveform and the fiducial

δ_ϕ	Total bins	PM bins
0.005	6285	2767
0.007	4489	1976
0.01	3143	1384
0.03	1049	462
0.05	630	277

Table 5.4: Number of frequency bins employed in the relative binning method for different values of δ_ϕ , both for the frequency range [30, 4096] Hz and in the postmerger region, starting at the merger frequency.

one anyway, as in Eq. 2.116. If this was not true, we would expect that changing the threshold δ_ϕ , and consequently the frequency bins over which the waveform is evaluated, would yield different results also if δ_ϕ was kept small. Figure 5.4 shows the posteriors recovered with the QU-PM model for the binary parameters of a Source2_[QU-PM] injection at 135Mpc, with the LHKIN network. We repeated the analysis multiple times, keeping the same settings but changing the frequency binning by using different values of δ_ϕ . We keep δ_ϕ small, but consider both larger and smaller values with respect to the $\delta_\phi = 0.01$ used throughout this work. As the plot shows, we find great consistency between the results obtained with all the different values of δ_ϕ . Consequently, despite the fact that the PN approximation does not hold in the postmerger phase, using it to determine the frequency bins for the relative binning method does not spoil the results, provided that the chosen δ_ϕ results in small bin widths.

Table 5.4 reports the number of frequency bins employed by the relative binning technique for different values of δ_ϕ , both in the whole frequency range considered for the analysis and for the postmerger region only. Choosing small values of δ_ϕ means increasing the number of bins over which we evaluate the waveform and therefore the computational cost of the analysis; nevertheless, performing the analysis using relative binning with these settings is still much faster than running “standard” parameter estimation analyses, which, for this kind of signals, are not computationally feasible. For standard parameter estimation, the waveform needs to be evaluated on a uniform grid that, with signals of the duration of roughly 200 s as the ones analysed here, includes approximately 8×10^4 points. Hence, considering that relative binning needs the evaluation of each sampled waveform only at the edges of the bins, this technique greatly reduces the number of required waveform evaluations.

5.4 Results

In the following, we present the results of our simulations, for what concerns both the performance of our model and the improvement we obtain with future detectors. When using the postmerger model with quasi-universal relations, we are mainly interested in studying how well we can recover the tidal deformability parameter $\tilde{\Lambda}$. Since the quasi-universal relations that we derived depend on $\tilde{\Lambda}$, we expect that the postmerger part of the signal, when detected, brings additional information about

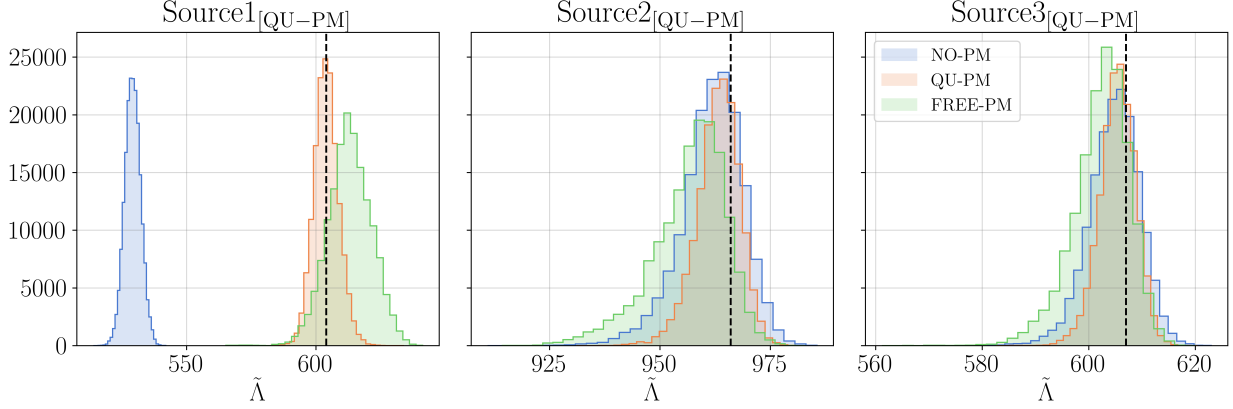


Figure 5.5: Posterior probability density for $\tilde{\Lambda}$ in the case of `bilby` injections with the QU-PM model, for sources at 68 Mpc and with the ETCE network, and recovery with the three different models NO-PM, QU-PM, and FREE-PM, in blue, orange, and green, respectively. The black dashed lines correspond to the injected values.

this parameter. This will likely lead to a narrower posterior with respect to what we can obtain using a model without postmerger. In the case of the postmerger model with free Lorentzian parameters, instead, we study how well the Lorentzian parameters c_0, c_1, c_2 can be recovered, and especially c_1 since it represents the frequency of the main postmerger emission peak.

5.4.1 Best-case scenario

We start by testing both versions of our model, FREE-PM and QU-PM, in the best-case scenario, i.e., for `bilby` injections in zero noise, for sources as described in Table 5.1, at a distance of 68 Mpc and with the ETCE network. Figure 5.5 shows the posterior probability density of $\tilde{\Lambda}$ for signals obtained with QU-PM injections and recovered with both our postmerger models, QU-PM and FREE-PM, and with the model without postmerger NO-PM. As expected, the $\tilde{\Lambda}$ posterior becomes tighter when going from the NO-PM to the QU-PM model, with the width of the 90% confidence interval reducing by about 30%, from 23.11 to 15.84 in the case of Source2_[QU-PM], and from 15.42 to 11.07 for Source3_[QU-PM]. In the FREE-PM recovery case, the posteriors become wider, with the width of the 90% confidence interval reaching 27.66 for Source2_[QU-PM]. We also note that when analyzing the data with this model, the median of $\tilde{\Lambda}$ is slightly underestimated with respect to the injected values. Both these features are predictable due to the higher number of parameters we have to sample over.

For Source1_[QU-PM], the injected value lies outside the NO-PM $\tilde{\Lambda}$ posterior distribution, but is well recovered with both the QU-PM and FREE-PM models. Given that the sampler converged to the maximum-likelihood values for the parameters, this shift is not caused by sampling issues, but is probably due to the fact that injections are performed with a signal including postmerger, and when we recover with a model without the postmerger description, the waveform tries to latch on to the signal after the merger, causing a bias in the parameter estimation. This is confirmed by the comparison, shown in Fig. 5.6, between the injected Source2_[QU-PM] waveform, the NO-PM waveform generated with the maximum-likelihood parameters recovered with the NO-PM model, and the one generated with the injected parameters. The maximum-likelihood NO-PM waveform tries to recover part of the injected

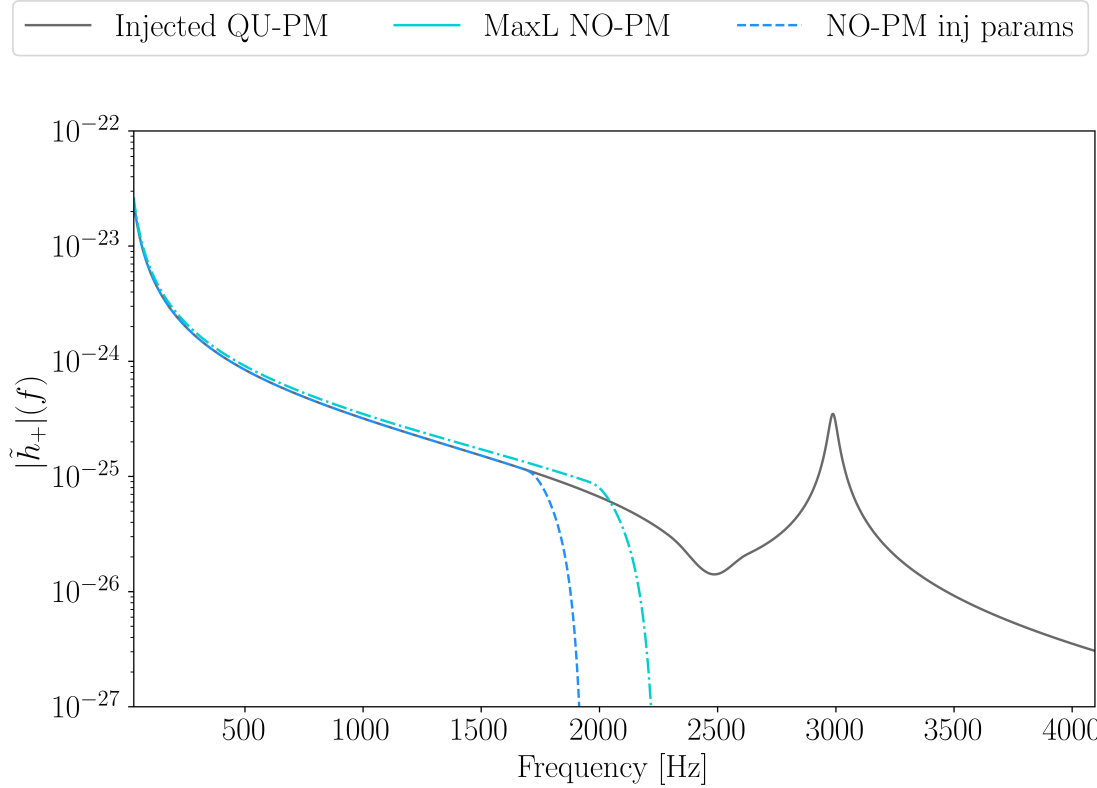


Figure 5.6: Injected signal for Source1_[QU-PM] (gray solid line), compared to the NO-PM waveform generated with the injected parameters (dashed blue line) and with the maximum-likelihood parameters recovered with the NO-PM model (dash-dotted cyan line).

postmerger signal, resulting in a deviation with respect to the NO-PM waveform obtained from the injection parameters, which explains the bias in the $\tilde{\Lambda}$ posterior.

Figure 5.7 shows the posteriors for the c_1 Lorentzian parameter in the case of injection and recovery with the FREE-PM model, for the three different sources. The injected values of c_0 , c_1 , and c_2 are the ones that yield the best fit on the NR hybrid with the same system's parameters of the source considered. The c_1 parameter, which corresponds to the frequency of the main postmerger emission peak, is well recovered in all cases. Although we are mainly interested in the recovery of c_1 , the FREE-PM model provides posteriors also for the c_0 and c_2 parameters, which are related to the maximum amplitude and width of the Lorentzian, respectively. Note that the c_0 and c_2 parameters, which are not shown in the figure, are not recovered as well as the c_1 parameter, but their injected values lie in the 90% confidence interval of the posterior in all cases, as reported in Table 5.5. While our model works for the main purpose of measuring the frequency of the dominant postmerger peak, the shifts that we see in the other parameters suggest that we can further improve the FREE-PM model; see, e.g., Refs. [317, 319] for recent developments including postmerger features beyond the main emission frequency.

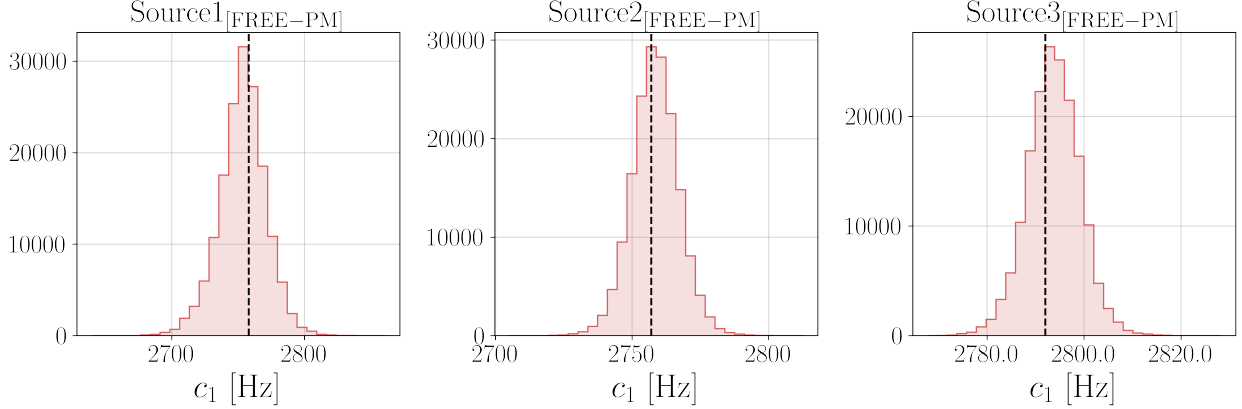


Figure 5.7: Posteriors of c_1 parameters for the three different sources, obtained when using the FREE-PM model both for injection and recovery. The black dashed lines show the injected values.

	$\log c_0$	$\log c_{0,\text{inj}}$	c_2	$c_{2,\text{inj}}$
Source1 _[FREE-PM]	$-56.79^{+0.29}_{-0.34}$	-56.65	$96.40^{+52.55}_{-36.90}$	74.0
Source2 _[FREE-PM]	$-56.18^{+0.21}_{-0.24}$	-56.15	$52.01^{+19.13}_{-14.19}$	48.0
Source3 _[FREE-PM]	$-55.89^{+0.19}_{-0.211}$	-55.90	$41.26^{+14.06}_{-9.52}$	39.0

Table 5.5: Median with 5% and 95% quantile values of the posterior probability density for the c_0 and c_2 parameters, together with their injected values, for each of the three sources analyzed, in the case of injection and recovery with the FREE-PM model.

5.4.2 Detector network performances in zero noise

We want to investigate how future detector networks will improve our postmerger analysis. For this purpose, we inject signals obtained from the QU-PM model in zero noise and recover both with the QU-PM and the NO-PM model. We analyze signals injected at three different distances (68 Mpc, 135 Mpc, and 225 Mpc), and we compare results for the four detector networks LHV, LHVKI, LHVKIN, and ETCE (as described in Sec. 5.3.1). Due to limited computational resources, we look only at two different sources, Source2_[QU-PM] and Source3_[QU-PM].

Figure 5.8 shows the Source2_[QU-PM] injected signal and the corresponding NR waveform: the signal injected with our QU-PM model describes well the main postmerger emission peak, but the NR waveform morphology includes also different subdominant emission peaks that our single Lorentzian cannot describe, and more structure in the frequency region right after the merger. Both these features should be addressed in future improvements of the model. In the same figure we show the maximum-likelihood waveforms recovered both with the QU-PM and the NO-PM model, for a zero-noise injection with the ETCE network. The recovered maximum-likelihood QU-PM signal overlaps with the injected one, showing how well 3G detectors will be able to recover this kind of signals. In the inspiral region,

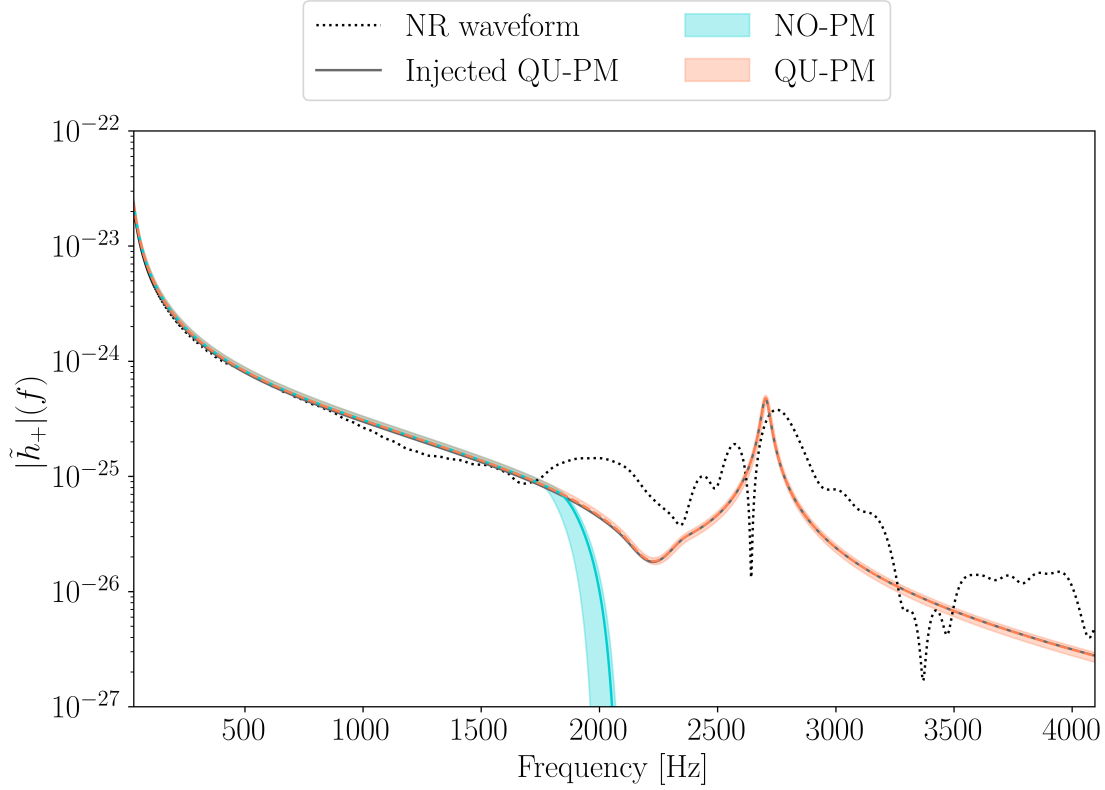


Figure 5.8: Frequency-domain waveform for Source2_[QU-PM], injected at a distance of 68 Mpc and using the QU-PM model (gray solid line), and the corresponding NR waveform (black dotted line). The dashed orange line and the cyan solid line show the maximum-likelihood waveforms recovered for a zero-noise injection in the ETCE network with the QU-PM and NO-PM model, respectively. The orange and cyan shaded regions show the 90% confidence interval on the recovered waveforms for the two models.

this applies also to the NO-PM maximum-likelihood waveform. The inspiral signal, which we see is well recovered also with the NO-PM model, already contains information about the $\tilde{\Lambda}$ parameter; therefore, for a ETCE network with such high SNR, we expect that little contribution to the $\tilde{\Lambda}$ measurement comes from the postmerger part of the signal, given that this parameter is already very well constrained from the inspiral.

Figure 5.9 shows the uncertainty $\tilde{\Lambda}_{90\text{conf}}$, computed as the width of the 90% confidence interval of the $\tilde{\Lambda}$ posterior probability density, as a function of the detector network employed for the analysis, comparing the different distances and recovery models. As expected, Fig. 5.9 shows that for all the detector networks considered, and for both models, the width of the 90% confidence interval decreases with decreasing distance. In particular, for the LHV network, we find an improvement of $\sim 50\%$ when going from 225 Mpc to 135 Mpc, and of $\sim 25\%$ (for Source2_[QU-PM] even 56%) when going from 135Mpc to 68 Mpc, for both models; for the ETCE network we find an improvement $\sim 45\%$ when going from 225Mpc to 135 Mpc, and $\sim 55\%$ when going from 135 Mpc to 68Mpc. Using the QU-PM model yields systematically tighter constraints on $\tilde{\Lambda}$, thanks to the additional information arising from the quasi-universal relations that describe the postmerger part of the signal. For both the sources,

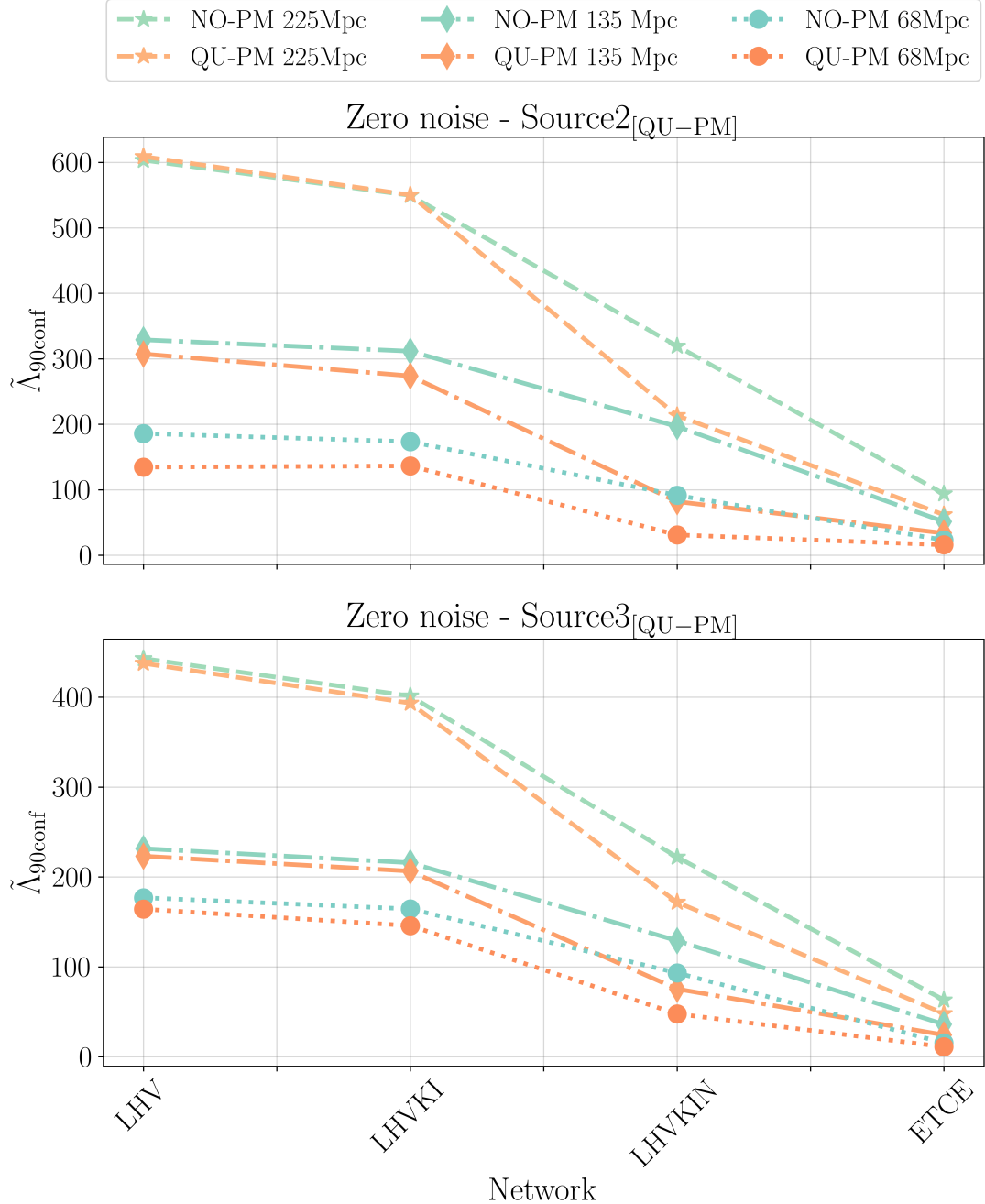


Figure 5.9: Width of the 90% confidence interval of $\tilde{\Lambda}$ posterior for Source2_[QU-PM] (top panel) and Source3_[QU-PM] (bottom panel), as functions of the different detector networks. Orange shades represent recovery with the QU-PM model, green shades with the NO-PM one.

in the case of injections at 225 Mpc and with the LHV or LHVKI network, we see no significant differences in $\tilde{\Lambda}_{90\text{conf}}$ in the case of recovery with the QU-PM or NO-PM model. Considering that such injections generate a SNR $\simeq 30$ in the case of the LHV network, this is consistent with the fact that in these situations we do not detect the postmerger signal.

Interestingly, the best improvement when using the QU-PM model comes in the case of the LHVKIN network. Going from the LHVKIN to the ETCE network, the constraint on $\tilde{\Lambda}$ improves of about $\sim 70\%$ for both models, while adding NEMO to the LHVKI network leads to an improvement in $\tilde{\Lambda}_{90\text{conf}}$ of $\sim 60\%$ for the QU-PM model, against the just $\sim 40\%$ for the NO-PM one. For both sources, we also see that for the LHVKIN network the constraint on $\tilde{\Lambda}$ obtained with the QU-PM model for injections at 135 Mpc is better than the one we retrieve with the NO-PM model for injections at 68 Mpc. 3G detectors are expected to have the best sensitivity over the whole frequency band, and indeed we see that for the ETCE network we get the smallest $\tilde{\Lambda}_{90\text{conf}}$ for both models. However, the high sensitivity at lower frequencies allows us to obtain precise measurements of $\tilde{\Lambda}$ from the inspiral part of the signal alone, therefore reducing the impact of the possible information gained from the postmerger phase. In the case of the LHVKIN network, instead, the constraint on $\tilde{\Lambda}$ from the inspiral is the one of second-generation detectors, but the high sensitivity of NEMO in the kilohertz band leads to a better detection of the postmerger, and therefore to significantly tighter constraints when using the QU-PM model. If its realization is approved, adding NEMO to the network of second-generation detectors will significantly help the detection of postmerger signals and related studies. We note that for this work we analyze signals with a lower frequency cutoff $f_{\text{low}} = 30$ Hz, missing many inspiral cycles; an additional improvement on $\tilde{\Lambda}$ measurements will be provided by the use of a lower f_{low} .

5.4.3 Detector network performances in non-zero noise

In the previous sections, we focused on model and network performances, using injections in zero noise. Now we want to investigate the influence of noise on our study. For this reason, we repeat the analysis using Gaussian noise. Due to limited computational resources, we restrict to only two sources, Source2_[QU-PM] and Source3_[QU-PM], and to one distance, 68 Mpc. We inject signals using the QU-PM model, and we recover them with both the QU-PM and NO-PM models, comparing results for the different detector networks LHV, LHVKI, LHVKIN, and ETCE. Figure 5.10 shows $\tilde{\Lambda}_{90\text{conf}}$ for the different detector networks. In order to assess the impact of noise fluctuations, we show results for two different noise realizations, which we call noise_A and noise_B . Due to the noise impact on the analysis, we do not see the clear trends that we found in the zero-noise runs, as described in the previous section Sec. 5.4.2. In the case of Source3_[QU-PM] (bottom panels in Fig. 5.10), with the noise_A realization the constraints obtained with the QU-PM model are even wider than the ones recovered with the NO-PM model. The most extreme fluctuation is found for Source3_[QU-PM], in the case of LHVKI network and QU-PM model, for which $\tilde{\Lambda}_{90\text{conf}} = 88.26$ in case of noise_A and $\tilde{\Lambda}_{90\text{conf}} = 4.84$ for noise_B . However, we see that in general $\tilde{\Lambda}_{90\text{conf}}$ decreases with more advanced detectors, with an improvement between 80% and 90% when going from the LHV to the ETCE network. In most cases the QU-PM model allows us to better determine $\tilde{\Lambda}$, although the quantitative improvement strongly depends on the source and especially on the noise realization. Moreover, noise fluctuations impact also the median of the

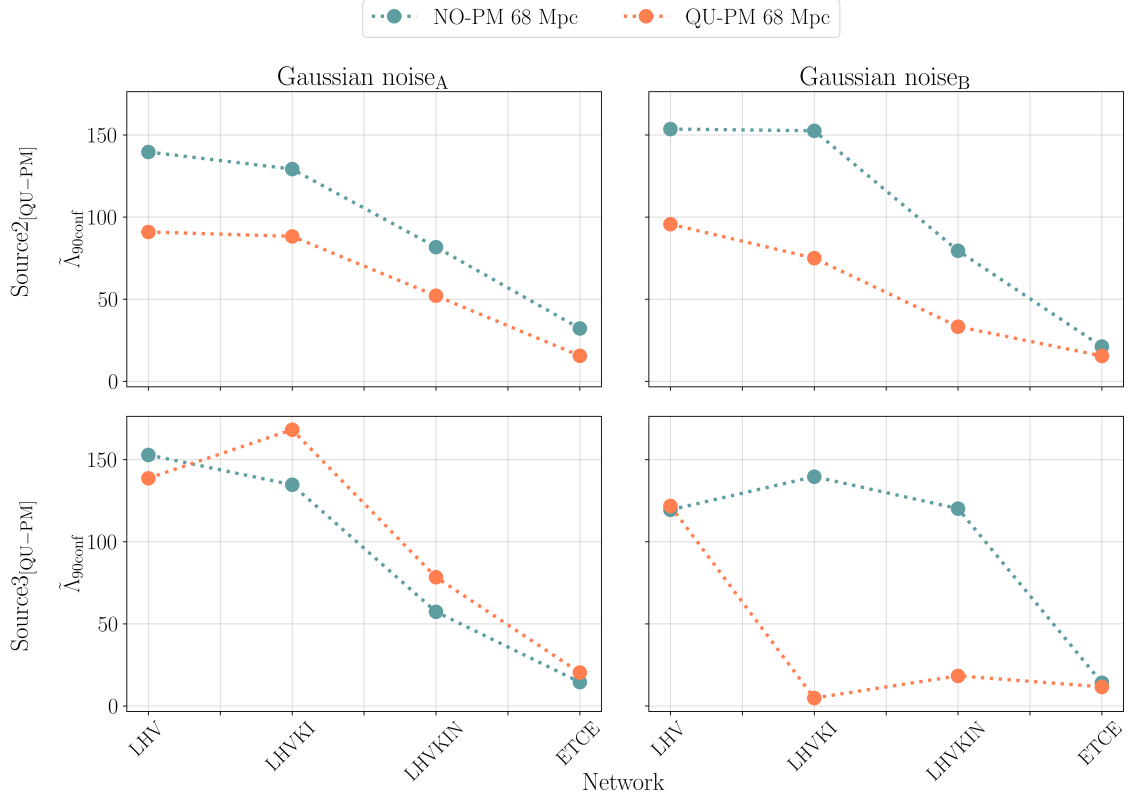


Figure 5.10: Width of the 90% confidence interval of $\tilde{\Lambda}$ posterior for $\text{Source2}_{[\text{QU-PM}]}$ (top row) and $\text{Source3}_{[\text{QU-PM}]}$ (bottom row), as a function of the different detector networks, obtained with two different noise realizations, noise_A for the left panels, and noise_B for the right ones.

$\tilde{\Lambda}$ posterior probability density, causing different shifts with respect to the injected values (see Table 5.6). Although such shifts appear to be small, they can cause the posterior's median to lie outside the 90% confidence interval, especially in the case of the ETCE network, where the $\tilde{\Lambda}_{90\text{conf}}$ is remarkably small.

5.4.4 Results for the free-parameter model

In the following, we show some results obtained with the postmerger model using free Lorentzian parameters. Performing parameter estimation analysis with the FREE-PM waveform requires sampling over three additional parameters, which implies even higher computational costs. For this reason, we could not run the same analyses with the FREE-PM model as we did for the QU-PM one. As shown in Sec. 5.4.1, with high-SNR and zero-noise injections we can recover c_1 accurately. In Fig. 5.11, we show how different detector networks can recover the c_1 parameter in the case of Gaussian noise injections, for simulated signals corresponding to $\text{Source3}_{[\text{FREE-PM}]}$ at 68 Mpc. In the case of second generation detectors, we basically recover the prior, although with a peak within [2500,3000] Hz, where also the injected value lies. Adding NEMO to the network leads to a strong improvement, resulting in a very sharp peak for the c_1 posterior. The recovered value of c_1 with the LHV+KIN network is slightly overestimated with respect to the injected value. However, this happens also for the ETCE network, where again the posterior is a sharp peak, and the injected value lies in its lower tail, outside of the

	Model	$\tilde{\Lambda}_m$ noise _A	$\tilde{\Lambda}_m$ noise _B	$\tilde{\Lambda}_{\text{inj}}$
Source2 _[QU-PM]	QU-PM	956.68 ^{+7.08} _{-8.37}	959.93 ^{+6.87} _{-8.71}	966
	NO-PM	966.35 ^{+9.35} _{-11.82}	953.10 ^{+13.11} _{-19.11}	966
Source3 _[QU-PM]	QU-PM	608.04 ^{+11.65} _{-6.27}	602.36 ^{+7.86} _{-12.49}	607
	NO-PM	611.76 ^{+6.68} _{-7.51}	604.35 ^{+6.84} _{-7.70}	607

Table 5.6: Median values with 90% confidence interval for the posterior probability density of $\tilde{\Lambda}$ in case of two different noise realizations, labeled as noise_A and noise_B, for injections at 68 Mpc in the ETCE network and for recovery with the two different models QU-PM and NO-PM; the last column reports the injected value of $\tilde{\Lambda}$.

90% confidence interval. In Sec. 5.4.1, we saw that, for the ETCE network, for the same simulated signal injected in zero noise, the value of c_1 is recovered very well. Therefore, we conclude that the shifts in the posterior peaks for the ETCE and LHVKIN networks for the injections in Gaussian noise are most likely due to noise fluctuations, which, as reported in Sec. 5.4.3, for this source affect also the $\tilde{\Lambda}$ measurements. Although the FREE-PM model still needs improvement for the analysis of real signals, the results in Fig. 5.11 are promising, and in particular they show that adding NEMO to a network of second-generation detectors will certainly make a difference for the study of BNS postmerger signals.

5.4.5 Numerical relativity injections

Finally, we analyze simulated signals obtained by injecting NR waveforms on top of Gaussian noise. Analyses performed with the FREE-PM model do not recover either of the Lorentzian parameters, mainly because of the complex structure of the postmerger signal, as we will explain later. Figure 5.12, instead, shows the posterior probability density of $\tilde{\Lambda}$ for injections at 68 Mpc in the ETCE network. For Source2_[NR-inj] the recovered posteriors of $\tilde{\Lambda}$ peak at the injected value, but for the other sources the posterior is shifted with respect to it. For Source1_[QU-PM], the $\tilde{\Lambda}$ injected value lies in the tail of the posteriors recovered with the QU-PM and FREE-PM model, and completely outside the posterior obtained with the NO-PM model; for Source3_[QU-PM], the posteriors recovered with all the models peak at values between 575 and 578, with the injected value $\tilde{\Lambda} = 607$ lying completely outside their distributions. These shifts are due to noise fluctuations, as we showed in Sec. 5.4.3, and possible limitations of our waveform models. The case analyzed here, using the ETCE network, generates a signal with a high SNR, and therefore a narrow posterior probability density for $\tilde{\Lambda}$; hence, the shifts induced by noise fluctuations can result in the injected value being situated outside the 90% confidence interval.

Using one of the postmerger models to analyze signals obtained with NR waveforms does not lead to a meaningful improvement in the $\tilde{\Lambda}$ constraints as the ones shown in Sec. 5.4.1. This is consistent with the fact that mismatches computed over the whole waveform (cf. lower panel of Fig. 5.1) do not show significant improvements when using one of the postmerger models, considering that the noise and the complicated morphology of the NR injection make it more difficult for our models to recover the postmerger part of the signal, and therefore almost all the $\tilde{\Lambda}$ information comes from the inspiral.

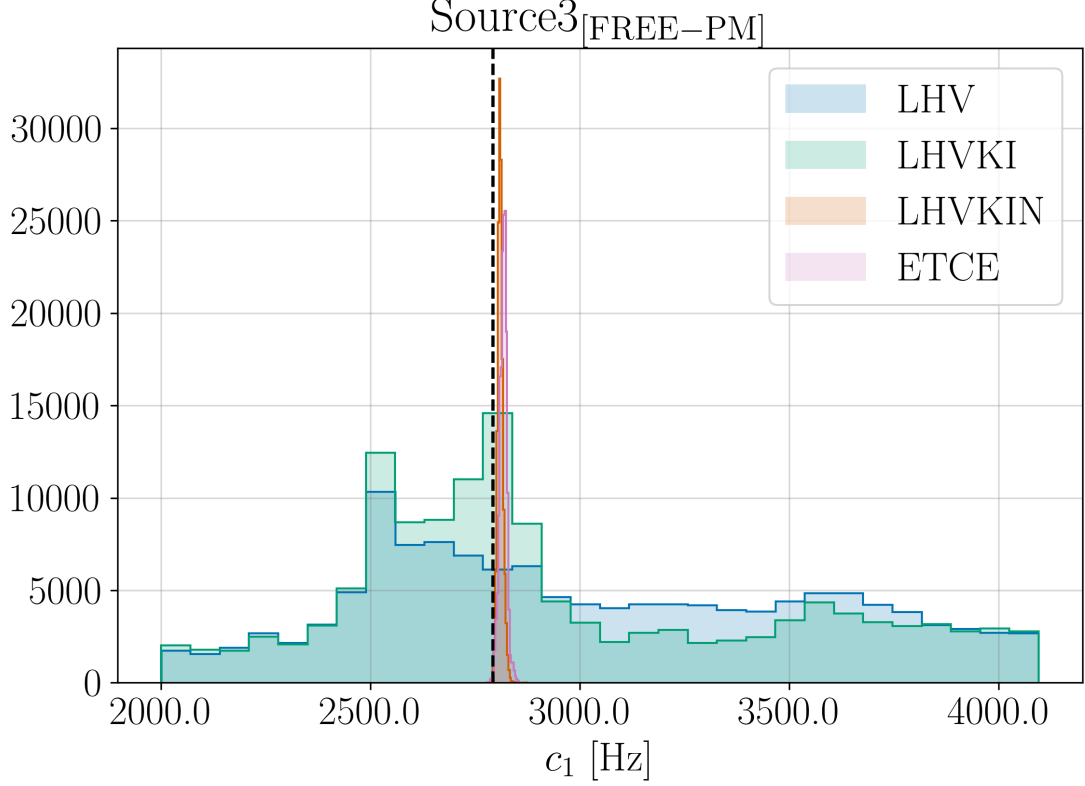


Figure 5.11: Posterior probability density for the c_1 Lorentzian parameter for the different detector networks, in the case of Gaussian-noise injections for Source3_[QU-PM] at 68 Mpc. The dashed vertical line indicates the injected value.

Nonetheless, when using the postmerger models, we see a modest improvement in the recovery of $\tilde{\Lambda}$ for Source2_[NR-inj], with respect to the NO-PM one, and a clear improvement for Source1_[NR-inj]. The latter is consistent with the results found in Sec. 5.4.1 for this source, where we concluded that, when using the NO-PM model, the presence of a postmerger signal, to which the NO-PM waveform tries to latch on, causes a bias in the $\tilde{\Lambda}$ parameter recovery.

In Sec. 5.4.3, we saw that noise fluctuations alone can impact the performance of our model, but in this case an additional issue is the fact that the NR simulations contain a more complex GW structure in the postmerger, which is not fully recovered with our simple Lorentzian model. This appears clearly in Fig. 5.13, which shows the injected NR waveform together with the maximum-likelihood ones recovered with the different models and their 90% confidence interval. The postmerger peak obtained with the QU-PM model is slightly shifted with respect to the main postmerger peak of the NR waveform; however, the same shift was present also in the Source2_[QU-PM] injected waveform in Fig. 5.8, and hence we conclude that it is due to the imperfection of the model, not to issues in the parameter estimation process. When optimizing the mismatches to compute the best values of the fit parameters for our quasi-universal relations, it is likely that the model tries to adapt to the whole morphology of the postmerger NR signal, thus shifting with respect to what would be the description of the main emission peak only. For the FREE-PM model maximum-likelihood waveform, the postmerger

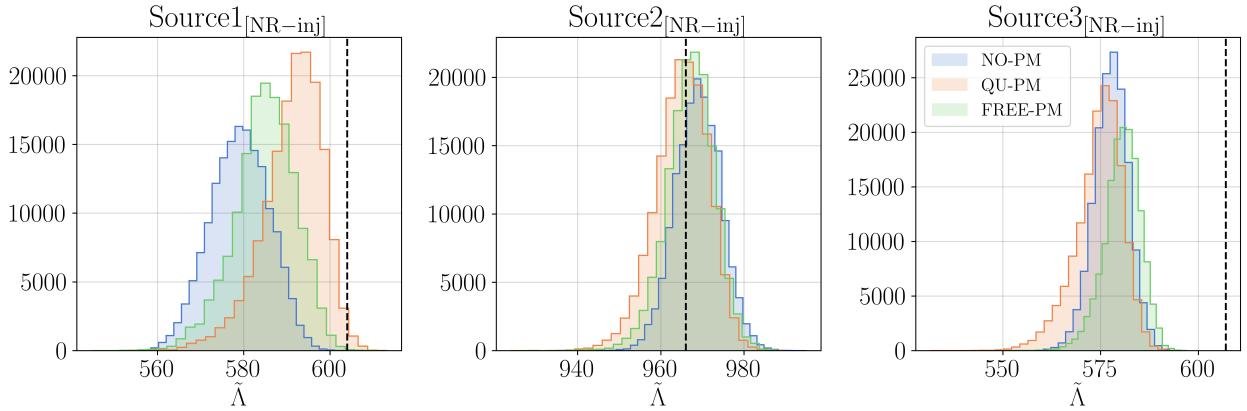


Figure 5.12: Posterior probability density for $\tilde{\Lambda}$ as recovered with the different models (NO-PM, QU-PM and FREE-PM) in the case of signals simulated by injecting NR waveforms in Gaussian noise at a distance of 68 Mpc, for the ETCE detector networks. The black dashed lines show the injected values.

peak lies at a higher frequency than the true one, is much wider and with a non-physical amplitude, though this does not affect the $\tilde{\Lambda}$ recovery (cf. Fig. 5.12). Given the large bias in c_0 , and the fact that the injected values vary in a small range, an improvement would probably be obtained already by restricting the prior range for this parameter. For comparison, in Fig. 5.13, we show also the waveform obtained from the FREE-PM model with the optimized parameters computed as explained in Sec. 5.2.2: the postmerger peak of the optimized FREE-PM waveform overlaps to the one of the NR waveform. Hence, the FREE-PM model can in principle describe the data well, but the additional information contained in the complex and more structured morphology of the postmerger in the NR signal makes it challenging for our simple model to recover all the parameters correctly. Therefore, both our QU-PM and FREE-PM models need to be improved towards more structured signals.

The fact that, with the FREE-PM model, the postmerger Lorentzian parameters cannot be recovered with a good precision causes the 90% confidence interval of the recovered waveform to be very broad. The spectra recovered with the QU-PM model, instead, lie in a narrower interval because their values are determined by the binary's parameters, which, with 3G detectors, are recovered with a very high accuracy, as shown in Sec. 5.3.4. We also note that the optimized FREE-PM model peak does not present the same shift as the QU-PM one, which is consistent with the fact that the mismatches in the high-frequency region shown in Fig. 5.1 are systematically lower for the FREE-PM model.

Moreover, hybridization of NR waveforms starts from the few last cycles of the inspiral, so that also the late-inspiral and merger waveform is based on NR simulations, and thus different from the model we employ. The difference between the hybrids and the waveform models in the late-inspiral region is visible also in Fig. 5.13 and can lead to biases, affecting the results obtained not only with our FREE-PM or QU-PM models, but also with the model without postmerger.

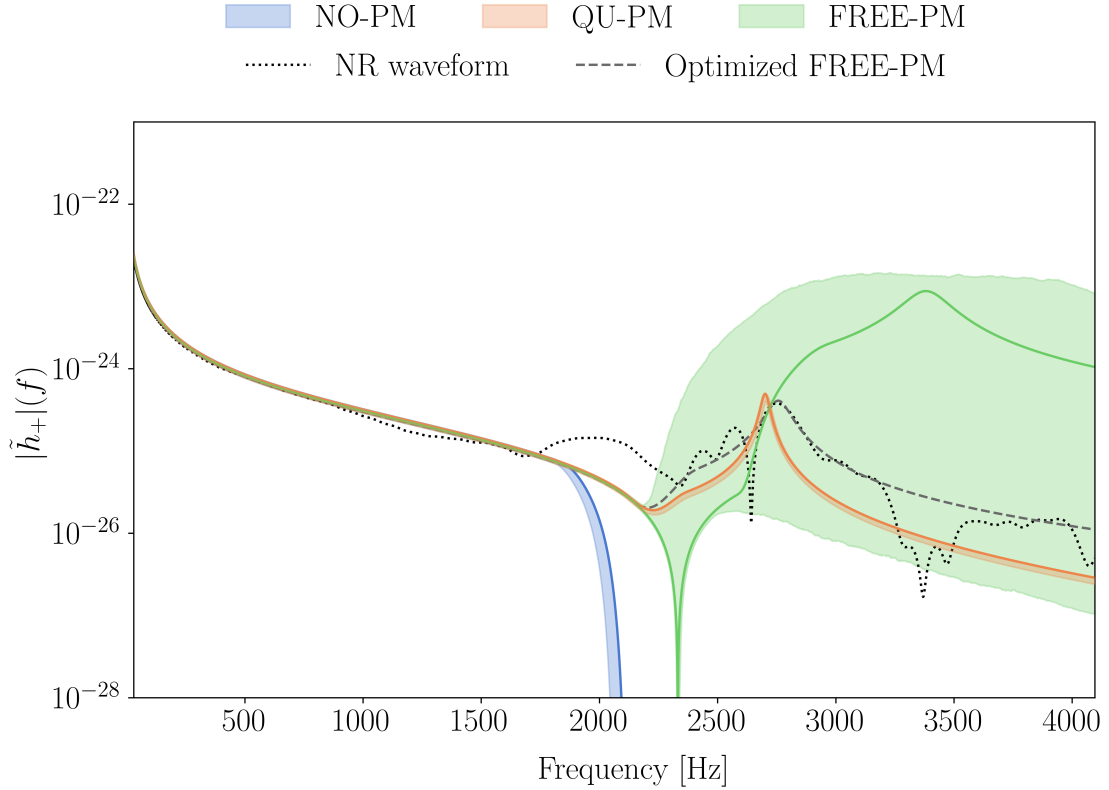


Figure 5.13: Frequency-domain waveform of the injected NR (black dotted line) waveform, compared to the waveforms generated from the maximum-likelihood parameters recovered for each model. The dashed gray line shows the FREE-PM waveform obtained by optimizing the Lorentzian parameters as explained in Sec. 5.2.2. The shaded regions represent the 90% confidence interval of the posterior of the recovered waveform with the different models.

5.5 Conclusions

We have developed an analytical, frequency-domain model to describe the GW emission during the inspiral, merger, and postmerger phases of a BNS coalescence. For the inspiral and merger, we employed the `IMRPhenomD_NRTidalv2` waveform. We incorporate the postmerger part through modeling the main emission peak with a Lorentzian, whose parameters, in the two versions of our model, are either free or determined by quasi-universal relations. Due to the computational cost of the analysis, our study was limited to a restricted number of BNS systems.

We have shown that in the best-case scenario of simulations with zero noise and high SNR – i.e., at a distance of 68 Mpc and with the ETCE network – the QU-PM model leads to better constraints on the $\tilde{\Lambda}$ posteriors compared to the ones obtained with the NO-PM model, and the FREE-PM model grants an accurate measurement of the frequency of the main postmerger emission peak. Within our study, we find that noise fluctuations can significantly impact the results; as shown in Sec. 5.4.3, they produce both large differences on the accuracy of $\tilde{\Lambda}$ measurements (quantified by the width of the 90% confidence interval of the recovered $\tilde{\Lambda}$ posterior, e.g., Fig. 5.10) and shifts in the median value of such posterior, cf. Table 5.6. In some cases, this overcomes the improvement on $\tilde{\Lambda}$ measurements yielded

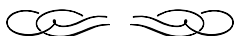
by the use of the QU-PM model and calls for caution in the interpretation of the results, to distinguish the effects of a different model from the ones of noise. It is important to note that the shifts in $\tilde{\Lambda}$ recovery caused by noise fluctuations, which are evident especially in high-SNR injections, given the narrowing of the posterior, also affect the results obtained with the model without postmerger. In general, including the postmerger during the analysis provides tighter constraints on the $\tilde{\Lambda}$ posterior than the original inspiral-only `IMRPhenomD_NRTidalv2` model.

Finally, we used our model to recover signals obtained by injecting NR waveforms. Although we still see improvements in some cases when using the postmerger models, they are not as significant as we found for the simulated signals. This is due to noise effects and the fact that NR waveforms include postmerger signals with a complex structure, which a simple Lorentzian model struggles to recover. Despite the promising results, we conclude that our model, in both its versions, still needs improvements in order to be employed in the analysis of real signals.

Another central point of our study was to assess the performance of different detector networks, and to understand how future detectors will improve the analysis of postmerger signals. In particular, we considered four different networks: (i) Advanced LIGO+ in Hanford and Livingston together with Advanced Virgo+; (ii) the same network as (i) extended by KAGRA and LIGO-India; (iii) the same network as (ii) extended with NEMO; (iv) a network consisting of a 40 km Cosmic Explorer and a 10 km, triangular Einstein Telescope. Although 3G detectors, as expected, will give the best constrains on $\tilde{\Lambda}$, we found that NEMO, thanks to its very high sensitivity in the kilohertz band, yields the biggest improvement when using the QU-PM model.

This study showed how, with future detector networks, GW observations from the postmerger phase of a BNS coalescence will allow us to unravel information about the fundamental physics describing supranuclear-dense matter.

Chapter 6



Measuring tidal effects with the Einstein Telescope: A design study

Originally, the Einstein Telescope’s design consisted of a triangular detector, with three V-shaped interferometers built a few hundred meters underground in order to reduce the seismic noise [130, 134]. However, the ET collaboration has recently been investigating also an alternative design, with two L-shaped interferometers. In the study presented in this chapter, based on Ref. [341], we investigate how the different designs impact the estimate of the source’s parameters, especially tidal deformability, for GW signals emitted from BNS systems.

6.1 Introduction

The observation of the first gravitational-wave signal from a BNS source, GW170817, thanks also to the simultaneous observation of electromagnetic radiation emitted as its counterpart [12, 13, 342], already allowed to place some constraints on the supranuclear-dense matter EOS.

As a detector with a much wider frequency band sensitive to GWs, the Einstein Telescope promises to observe BNS signals for many cycles, increasing the detected signals’ duration up to an hour. ET will certainly provide more constrained bounds on the neutron star EOS, even without an accompanying electromagnetic counterpart [343–349].

Unfortunately, it is very challenging to perform realistic studies exploiting the full capability of ET due to the wide frequency range it will cover and the large associated computational costs. However, significant progress has been made regarding GW searches for ET signals, e.g., Refs. [350, 351], and full parameter estimation studies, as discussed below. Reference [352] performed the first full Bayesian estimation analysis of GW signals from BNS sources observed by ET with a lower frequency cutoff f_{low} of 5 Hz. For this, they constructed reduced order quadratures to make their study computationally feasible. Here, we perform PE employing *relative binning* (see Sec. 2.3.3) to reduce the computational cost of our analysis. We use a lower frequency cutoff of $f_{\text{low}} = 6$ Hz, to provide realistic estimates of

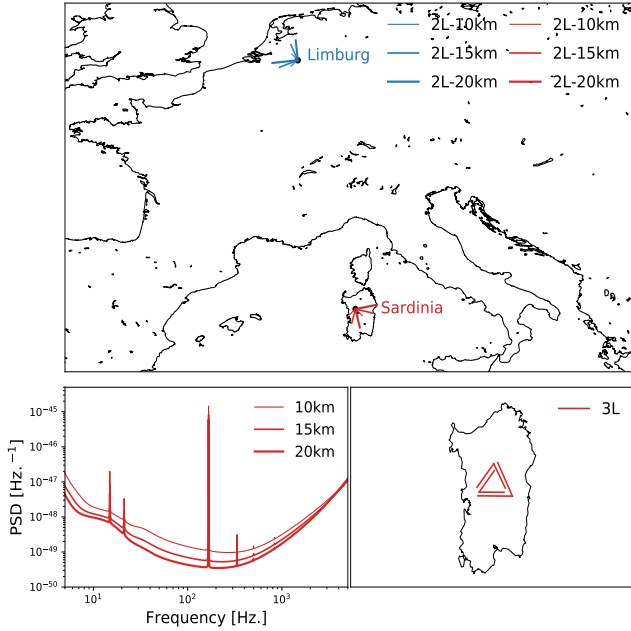


Figure 6.1: *Top panel:* Location of the ET detectors in case of two L-shaped interferometers, showing also the possible different arm lengths in misaligned orientations. *Bottom panel (left):* PSD curves for the xylophone configuration in cryogenic mode for different arm lengths. *Bottom panel (right):* Representation of the ET triangular configuration, located in Sardinia for the purpose of this work.

the source parameters, such as the chirp mass or the tidal deformability.

In the past, various PE studies have already been performed to estimate the Science returns to constrain tidal deformability from BNS observations in ET, including using ET in a network of detectors, e.g., Refs. [93, 131, 135, 293, 343–349, 352–364]. However, up to our knowledge, all of them have focused on the originally proposed triangular design with three interferometers, each having a 60° opening angle and arm length of 10 km, arranged in an equilateral triangle.

Recently, there has been an increasing interest in studying also different detector configurations and layouts. With this regard, Ref. [140] provided a detailed discussion with respect to numerous scientific cases and how they are affected by different proposed designs for ET, including different arm lengths and shapes. More explicitly, Ref. [140] considered the originally conceived triangular configuration, as well as two separate L-shaped detectors; for the latter, also different alignments, i.e., orientation between the detectors. In the study presented here, we compare these different designs, cf. Fig. 6.1, for recovery of tidal deformability and the other parameters of BNS systems via full PE analysis. In all the studied cases, we analyze BNS simulations and look at differing results from varying the detector setup, keeping the source properties of the BNS system and the settings of the PE analyses unchanged.

6.2 Methods

Following standard techniques, we perform a Bayesian analysis (see Sec. 2.2.2) to construct posterior probability density functions on the parameters of interest, i.e., those characterizing the gravitational

waveform describing a BNS merger. To sample the likelihood function, we employ the `bilby` library [321, 322] and specifically the `dynesty` [335, 336] algorithm. The waveform model used for both signal injection and recovery is `IMRPhenomD_NRTidalv2` [212].

As we use quite low values of f_{low} to make our estimates realistic with what is envisaged for the ET detector, our likelihood integral calculation is computationally expensive. For this reason, we resort to the technique of *relative binning*, introduced in Sec. 2.3.3. This approach reduces our computational costs noticeably and makes our runs computationally feasible. For our purposes, we followed the implementation outlined in Ref. [239]; however, we used a different waveform, `IMRPhenomD_NRTidalv2`, and we employed the above code in conjunction with the sampling library `bilby`, as implemented in the code in Ref. [337].

6.2.1 Sources and configurations

We consider three different sources (A,B,C) with parameters chosen following mainly the injection study performed by the LVK collaboration to mimic GW170817 [73]. The properties of the sources used for injections are listed in Table 6.1, where m_i , χ_i , and Λ_i , with $i \in \{1, 2\}$ are the mass, dimensionless spin, and dimensionless tidal deformability of the component neutron star, respectively, while \mathcal{M}_c is the chirp mass and $\tilde{\Lambda}$ the binary's mass-weighted tidal deformability, as defined in Eq. 2.58.

All the simulated signals are injected at a distance $D_L = 100$ Mpc with inclination $\iota = 0.4$ rad, zero polarization angle, and at a sky location $(\alpha, \delta) = (1.375, -1.211)$ rad. The priors used for the analysis are reported in Table 6.2, where $\delta\tilde{\Lambda}$ is defined in Eq. 2.59.

Name	$m_1, m_2 [M_\odot]$	$\mathcal{M}_c [M_\odot]$	Λ_1, Λ_2	$\tilde{\Lambda}$	χ_1, χ_2
Source A	1.68, 1.13	1.19479	77, 973	303	0, 0
Source B	1.38, 1.37	1.19700	275, 309	292	0.02, 0.03
Source C	1.38, 1.37	1.19700	1018, 1063	1040	0, 0

Table 6.1: Source properties used for injections.

Two different shapes have been proposed for ET in Ref. [140]: (i) a single detector with a triangular configuration, henceforth called Δ , (ii) two L-shaped detectors¹ in separate locations, with aligned or misaligned arms, henceforth called 2L-0° and 2L-45°, respectively. The Δ configuration consists of three V-shaped detectors, with each V having a 60° opening angle between the arms. For 2L-0°, the detectors have arms with the same orientation, while in the case of 2L-45° one detector has the arms rotated by 45° with respect to the other one.

The Δ detector may have an arm length of 10 km or 15 km, while the L-shaped ones may have an arm length of 15 km or 20 km. As of now, there are two main candidate sites for ET,² one in Sardinia

¹L-shaped detectors have a 90° opening angle between the arms, as the basic interferometer configuration described in Sec. 1.4.1. The two LIGO instruments and Virgo are all L-shaped.

²Recently, also a third location in Saxony, Germany, has been considered as a possible site option.

Parameter	Range
\mathcal{M}_c	$[\mathcal{M}_{c,s} \pm 0.05 [M_\odot]]$
q	$[0.5, 1]$
χ_1, χ_2	$[0.0, 0.15]$
D_L	$[1,500] \text{ Mpc}$
$\tilde{\Lambda}$	$[0,5000]$
$\delta\tilde{\Lambda}$	$[-5000, 5000]$

Table 6.2: Priors employed in the PE analysis, where $\mathcal{M}_{c,s}$ represents the chirp-mass injected value of the specific source analyzed. For the luminosity distance D_L , the prior is taken uniform in comoving volume; for all the other parameters, the prior is uniform in the indicated range.

Name	Shape	Relative orientation	Arm length
$\Delta 10\text{km}$	Triangular	-	10 km
2L-0° 15km	2 L-shaped	aligned	15 km
2L-45° 15km	2 L-shaped	misaligned	15 km
2L-0° 20km	2 L-shaped	aligned	20 km
2L-45° 20km	2 L-shaped	misaligned	20 km
$\Delta 15\text{km}$	Triangular	-	15 km
2L-0° 10km	2 L-shaped	aligned	10 km
2L-45° 10km	2 L-shaped	misaligned	10 km

Table 6.3: Names used throughout this work for the different detector configurations and arm lengths.

(Italy) and one in Limburg (at the border shared by Netherlands, Belgium and Germany) [140]. In this paper, the Δ detector is located in Sardinia, whereas in the case of two L-shaped detectors one is in Sardinia and the other one in Limburg. All detector configurations used in our work are listed in Table 6.3.

One of the main challenges to reach the sensitivity planned for ET is dealing with quantum noise, which includes shot noise at high frequencies and radiation pressure noise at low frequencies. A high laser power reduces shot noise, but a low laser power is instead required to reduce radiation pressure noise. To counter this problem, ET will in practice be composed of two interferometers working together in a xylophone configuration, one detector optimized for low frequencies and with a low laser power, and the other one optimized at high frequencies and with a high power. Low-frequency sensitivity is also affected by thermal noise, therefore a further improvement is expected if the low frequency detector operates at cryogenic temperatures [134].

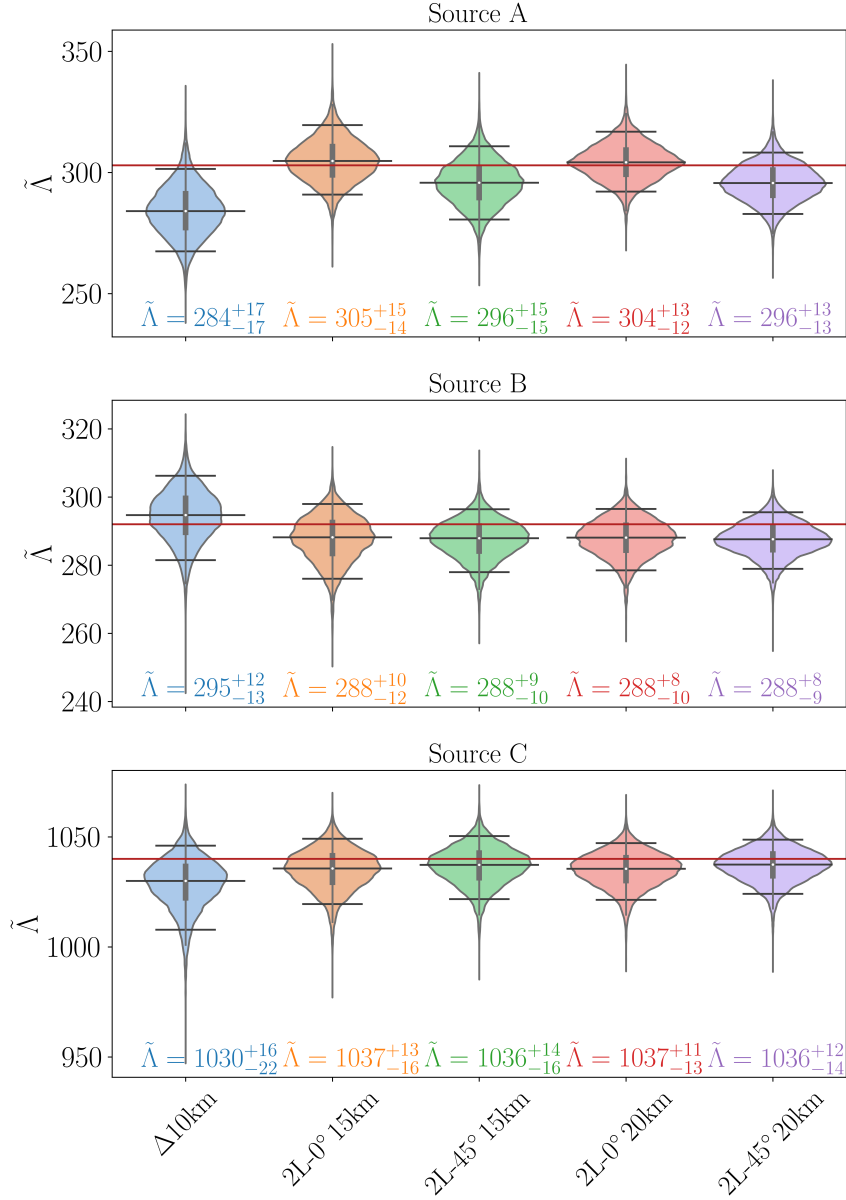


Figure 6.2: Violin plots for the posterior density distribution of $\tilde{\Lambda}$ for the five reference detector configurations and for all three sources in Table 6.1: Source A (*top panel*), Source B (*middle panel*), and Source C (*bottom panel*). The black horizontal bars indicate the median value and the 90% confidence interval, the black vertical lines mark the support of the posterior; the red horizontal line shows the injected value of $\tilde{\Lambda}$. For each posterior we also report the median, together with the 5% and 95% quantile values.

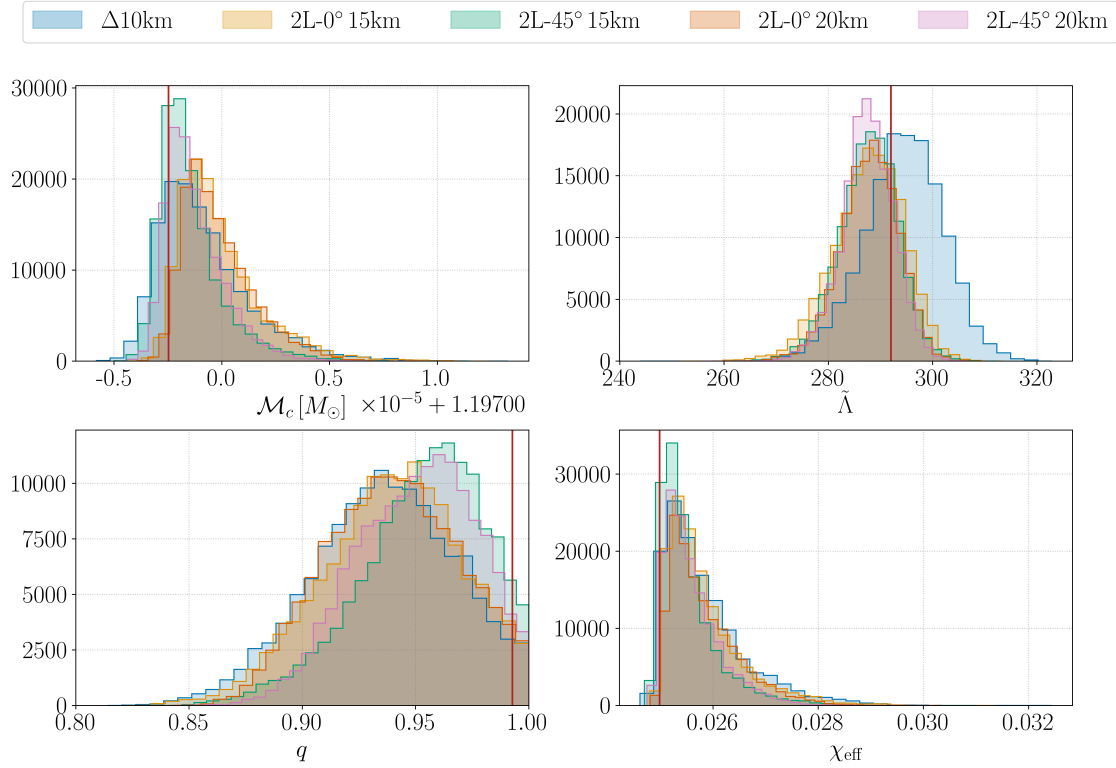


Figure 6.3: Posteriors for chirp mass \mathcal{M}_c (top left), tidal deformability $\tilde{\Lambda}$ (top right), mass ratio q (bottom left), and effective spin χ_{eff} (bottom right), for Source B (cf. Tab. 6.1). The different colors correspond to the various configurations considered, while the red line indicates the injected values.

6.3 Results

In this section, we present the results of PE runs, comparing the different detector configurations, arm lengths and laser power. We also look at the improvement we get when analyzing data starting at different frequencies.

6.3.1 Detector configuration comparison

First, we test how the different detector configurations (Δ , 2L- 0° or 2L- 45°) perform in PE analyses. We take into account only the five reference configurations [140]: Δ with 10 km arms, 2L- 0° and 2L- 45° , both with 15 km or 20 km arms. For this comparison, all the runs are performed with starting frequency $f_{\text{low}} = 10$ Hz, and using the PSD curve for the xylophone configuration with the low frequency detector operating at cryogenic temperatures, henceforth denoted as ‘‘LFHF’’. Figure 6.2 shows the posteriors for the tidal deformability parameter $\tilde{\Lambda}$ for the three different sources, reporting the median and 90% intervals for each configuration.

For Source B, in Fig. 6.3 we show also the posterior distributions for the other binary parameters: chirp mass \mathcal{M}_c , mass ratio $q = m_2/m_1$, with $m_1 > m_2$, and effective spin χ_{eff} , as defined in Eq. 1.79. From Fig. 6.3 and especially from Fig. 6.2 we see an improvement going from the Δ to the two L-shaped detectors, since, for example, the width of the 90% interval on $\tilde{\Lambda}$ reduces between 12% and

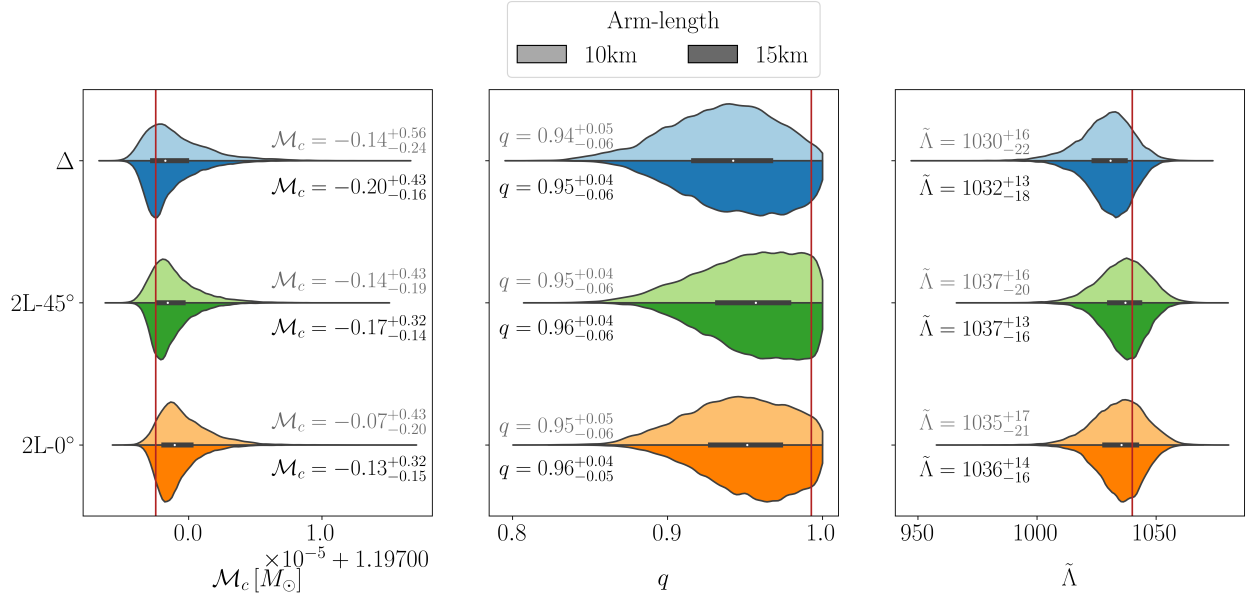


Figure 6.4: Comparison of \mathcal{M}_c , $\tilde{\Lambda}$, and q posteriors between Δ , $2L-0^\circ$, and $2L-45^\circ$ with same arm length, for Source C (cf. Table 6.1). The darker color shade refers to detectors with 15 km arm length, the lighter one to detectors with 10 km arm length. The red line indicates the parameter’s injected value. For each parameter and configuration, we also report the median and 5% and 95% quantile values; for \mathcal{M}_c , also the reported values have an offset $1 \times 10^{-5} + 1.19700 M_\odot$.

24% when going from the Δ 10km to the $2L-45^\circ$ configuration. However, we must take into account the fact that the Δ detector here is assumed to have a shorter arm length, which has a great influence on the PSD, cf. Fig. 6.1. For this reason, we also compare the Δ and 2L configurations assuming they have the same arm length. Figure 6.4 shows Source C posteriors for \mathcal{M}_c , q , and $\tilde{\Lambda}$, for the different configurations, but assuming the same arm length. In this case, we do not see a strong difference in the parameters recovery, as indicated by the 5% and 95% quantile values reported in the plot. This suggests that the specific configuration does not have a major impact on the precision of parameter estimation. However, if the configuration choice is bound to a certain arm length, e.g., due to limitations to the overall budget, one must take into account the improvements obtained with longer arms.

6.3.2 Effect of varying PSDs

As mentioned in the previous sections, the current plan for ET includes a “xylophone” configuration, in which each detector is effectively composed of two interferometers, operating a high- or low- power laser. The high-power laser is expected to improve sensitivity at high frequencies, the low-power one, on the other hand, improves sensitivity below 30 Hz [133,134]. We perform the same PE analysis using the PSD of the different interferometers and we compare results. In particular, we study the PSD for the detector optimized at high frequencies (HF-PSD), the one optimized at low frequencies (LF-PSD), and the xylophone combination (LFHF-PSD), with the low-frequency interferometer operating at cryogenic temperatures. Since we are interested only in the effect of the PSD, here we study just

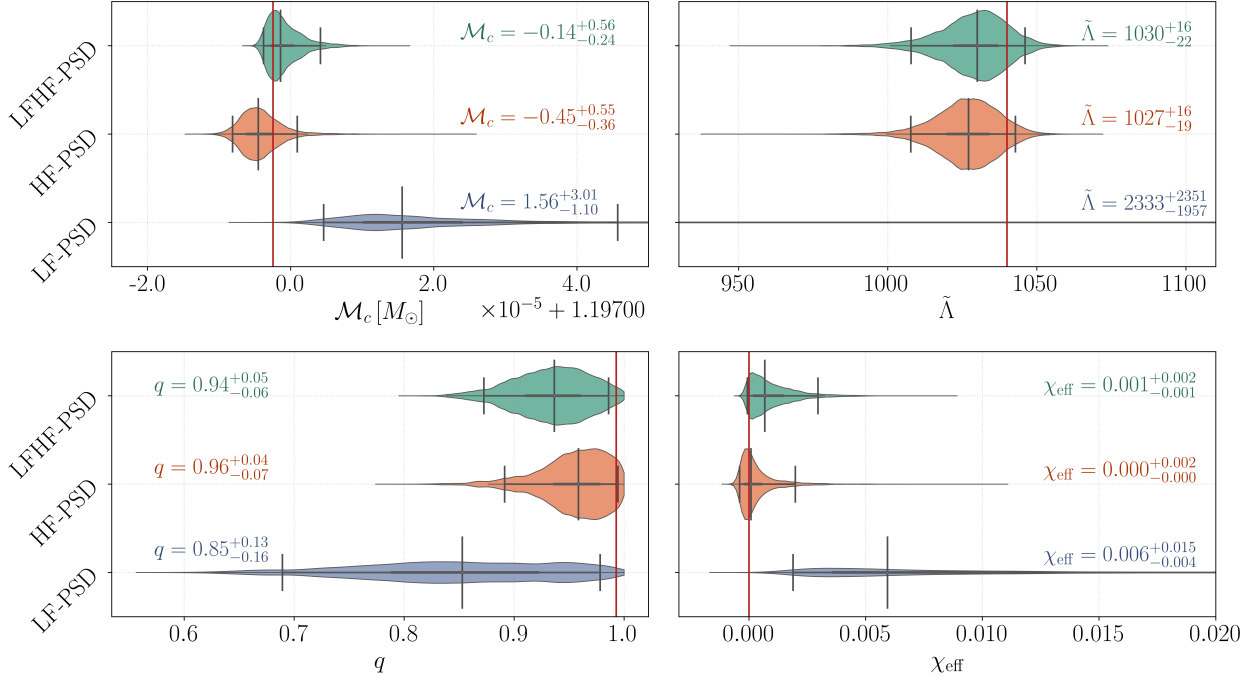


Figure 6.5: Posteriors of \mathcal{M}_c , $\tilde{\Lambda}$, q , and χ_{eff} , for Source C (cf. Table 6.1) and the $\Delta 10\text{km}$ configuration, recovered with the different PSDs. The vertical black lines show the median and the 90% confidence interval, while the black horizontal line indicates the support of the posterior; the red line shows the parameter's injected value. For \mathcal{M}_c , the reported median and quantile values have an offset $\times 10^{-5} + 1.19700 M_\odot$.

one source, Source C, and one detector configuration, $\Delta 10\text{km}$, performing the analysis from a starting frequency $f_{\text{low}} = 10 \text{ Hz}$.

The posteriors for \mathcal{M}_c , q , $\tilde{\Lambda}$, and χ_{eff} are shown in Fig 6.5, where we also report the median and the 5% and 95% quantiles for each parameter. The PSD optimized at low frequencies yields much worse results than the other ones, with a 90% confidence interval 2.5 times larger in the case of mass ratio. $\tilde{\Lambda}$ is not recovered with the LF-PSD, while it is constrained with an accuracy of almost 4% in the other cases. $\tilde{\Lambda}$ represents an extreme case, since its contribution enters the gravitational-wave phase mainly at high frequencies, from a few hundreds Hz and above [365, 366], and therefore is affected by the shape of LF-PSD, as shown in Fig 6.6, more than other parameters. In general, we obtain a much worse parameter recovery when using the LF-PSD alone, meaning that, if the preferred solution of a xylophone implementation is not available, the high-frequency optimized PSD is favorable, in particular if we want to constrain $\tilde{\Lambda}$.

6.3.3 Effect of varying minimum frequency

A big achievement of the ET is to improve the sensitivity at low frequencies. Therefore, in this section, we will study the impact of choosing different starting frequencies in the PE analysis. We note that lowering the starting frequency by only a few Hz has a huge impact on the duration of the waveform and therefore on the computational cost of the analysis. We analyze injections with the parameters of Source B, for two different configurations, $\Delta 10\text{km}$ and $2\text{L}-45^\circ 15\text{km}$. In each case, we perform PE

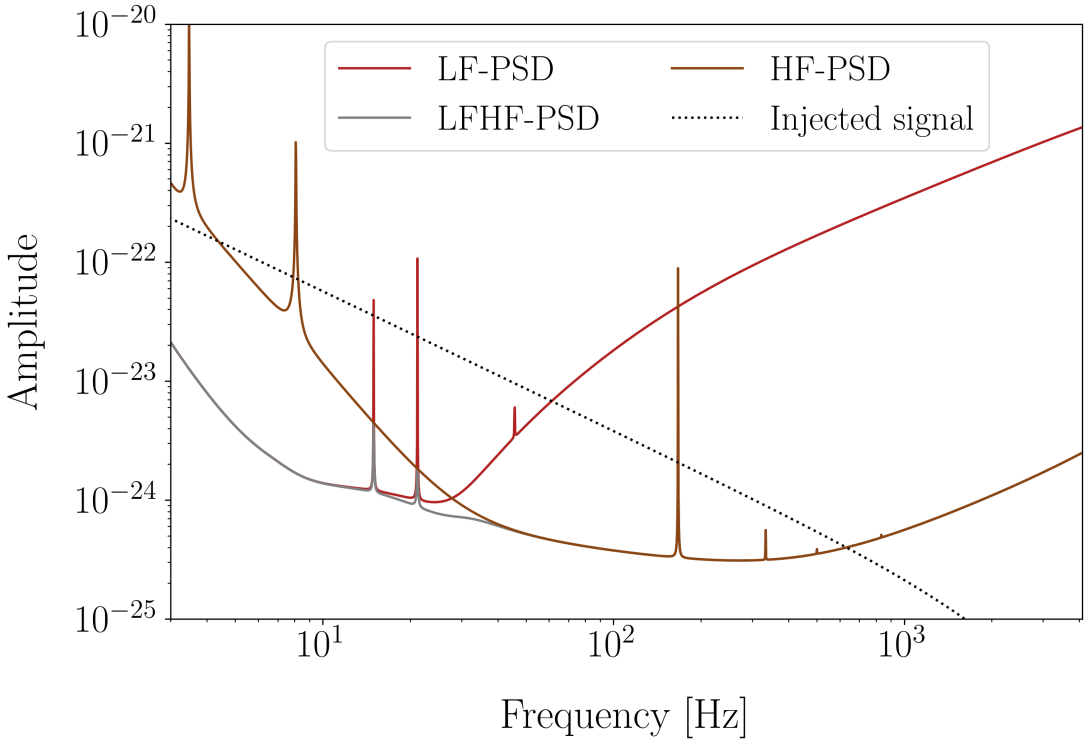


Figure 6.6: Comparison between the amplitude spectral densities corresponding to the PSD optimized at low frequencies (LF-PSD), in red, the PSD optimized at high frequencies (HF-PSD), in brown, and the one of the xylophone configuration (LFHF-PSD), in grey, with a typical injected GW signal (dotted line). All the PSDs shown refer to a detector with 10 km arm length. The sensitivity of the LF-PSD becomes too low at high frequencies to allow to detect the signal above ~ 100 Hz.

studies with the following starting frequencies: 6, 7, 8, 9, 10, and 20 Hz. In this case, the analysis is performed in zero noise since we want to focus on the impact of f_{low} without risking to take into account possible fluctuations induced by the noise realizations. In fact, specific noise realizations can cause a shift in the posterior recovered for $\tilde{\Lambda}$. This shift is usually within 5% of the actual $\tilde{\Lambda}$ value, and, therefore, goes unnoticed in the analysis performed with current detectors. However, we showed that for ET the precision with which $\tilde{\Lambda}$ can be measured improves noticeably. This means that, due to these shifts, we might end up seeing the injected values lying outside the 90% confidence interval of the posterior when simulations involve Gaussian noise (as discussed also in Sec. 5.4.3). When real ET data will be analyzed in the future, this is a point that must be evaluated very carefully. For our purposes, up to now, we compared only results obtained with the same f_{low} , and, as long as we use the same noise seed, we expect a possible fluctuation to affect all the runs in the same way, and, therefore, to be not relevant in our comparison. Here, however, we use different starting frequencies, leading to longer signals and more cycles being analyzed. In this case, the outcome of noise fluctuations can be different for the different f_{low} used. To quantify this, in Table 6.4 we report the median and 90% interval values of the posteriors on $\tilde{\Lambda}$, obtained from analysis both in Gaussian and zero noise, with the same seed but different f_{low} . While we see fluctuations in the median values recovered from

Gaussian-noise runs, in the zero-noise case the median is almost constant. Therefore, to compare $\tilde{\Lambda}$ recovery with different starting frequencies, we look at zero-noise injections. Figure 6.7 shows the posteriors and their 90% width for the different f_{low} values. We see a clear improvement when going to lower frequencies, especially for the recovery of chirp mass. The plot also highlights how, in general, the 2L-45° 15km configuration yields tighter constraints on the parameters' posteriors, but we stress again that the main impact is given by the arm length, not the configuration per se.

	f_{low}	Gaussian noise	zero noise
2L-45° 15km	7 Hz	$279.31^{+9.55}_{-11.35}$	$287.90^{+8.35}_{-9.54}$
	8 Hz	$292.90^{+8.40}_{-8.33}$	$287.36^{+9.01}_{-9.59}$
	9 Hz	$278.63^{+9.75}_{-10.72}$	$287.65^{+8.95}_{-10.92}$
	10 Hz	$285.74^{+11.15}_{-13.26}$	$287.40^{+9.03}_{-10.96}$
	20 Hz	$296.72^{+10.46}_{-11.66}$	$286.18^{+12.01}_{-14.42}$
$\Delta 10\text{km}$	7 Hz	$277.27^{+11.87}_{-13.52}$	$287.29^{+10.95}_{-12.59}$
	8 Hz	$292.95^{+9.15}_{-9.77}$	$287.11^{+11.21}_{-12.79}$
	9 Hz	$274.62^{+12.78}_{-14.09}$	$285.51^{+11.71}_{-13.97}$
	10 Hz	$273.16^{+15.18}_{-17.09}$	$285.51^{+11.71}_{-13.97}$
	20 Hz	$280.09^{+13.76}_{-17.10}$	$285.21^{+14.56}_{-17.86}$

Table 6.4: Recovered $\tilde{\Lambda}$ values with 90% intervals, comparing Gaussian-noise and zero-noise runs for different values of f_{low} .

6.4 Summary

We performed PE studies to compare the different proposed designs for ET. We focus on BNS systems, in particular, to find out how well the tidal effects will be measured. We compare different detector shapes, considering a single triangular detector and two L-shaped ones. In the latter case, we investigate both the cases of aligned or misaligned detectors. Moreover, ET will be composed of two interferometers, one optimized at high and one at low frequencies. We compared results obtained using the different PSDs, the low- and high- frequency one, as well as the xylophone PSD, obtained by combining the two. Finally, we looked at how the PE results improve when using lower cutoff frequencies, investigating $f_{\text{low}} = 20, 10, 9, 8, 7, 6$ Hz. We find that:

- (i) The shape and alignment of the detectors have very little influence on the recovery of parameters.
- (ii) The chosen arm length, instead, plays an important role, as expected given its effect on the PSD. This means that, when comparing the currently proposed configurations, the $\Delta 10\text{km}$ one

performs worse, but this is merely due to the fact that it has a shorter arm length with respect to the 2L ones. When comparing the different configurations, and assuming the same arm length, we find no significant difference in the results.

- (iii) The constraints recovered with the LF-PSD are much worse than the other ones, especially with respect to $\tilde{\Lambda}$. This is expected since with the LF-PSD the signal above a hundred Hz is not detectable.
- (iv) Noise fluctuations have a very strong impact on the $\tilde{\Lambda}$ measurement, causing the posteriors' median values to shift. With ET, $\tilde{\Lambda}$ will be measured with a very high accuracy, therefore, although such shifts are of the order of a few percent, they can be enough for the injected value to lie outside the support of the posterior.
- (v) Regarding the different cutoff frequencies, we studied two different detector configurations, $\Delta 10\text{km}$ and $2\text{L-}45^\circ 15\text{km}$, and find no substantial difference between them. The parameters posteriors become clearly tighter when going to lower frequencies. This is particularly evident in the case of \mathcal{M}_c posteriors, but an improvement is also present for $\tilde{\Lambda}$, although only of about 20%.

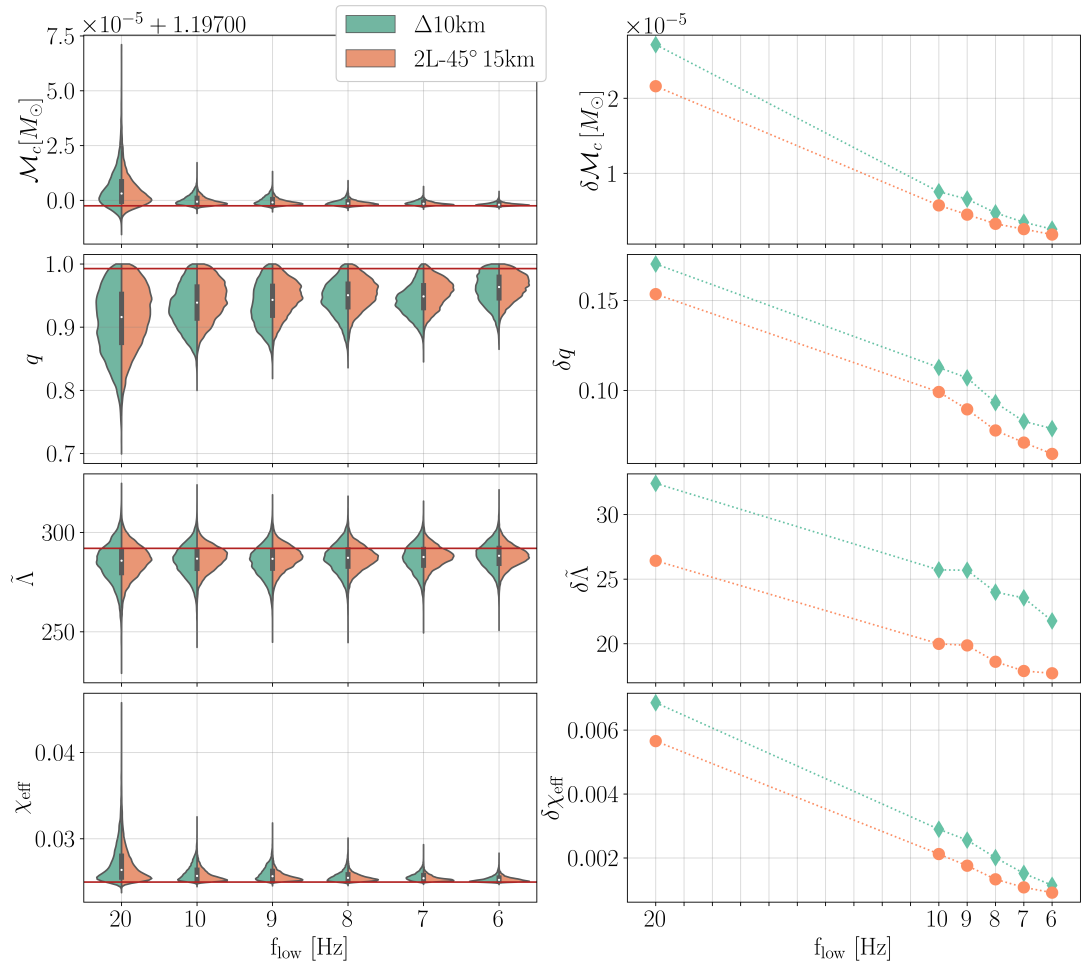
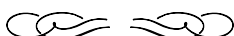


Figure 6.7: *Left:* Posterior distributions for \mathcal{M}_c , q , $\tilde{\Lambda}$, and χ_{eff} for the different choices of f_{low} and for Source B (cf. Table 6.1), in green for the Δ configuration with 10 km arms, in orange for the $2L-0^\circ$ with 15 km arms. The red horizontal lines correspond to the parameters' injected values. *Right:* Width of the 90% confidence interval for each parameter, as a function of the value of f_{low} .

Chapter 7



Conclusions

Since their prediction in Einstein's theory of general relativity, gravitational waves took a hundred years to be actually detected. Nevertheless, the wait was well rewarded since measuring GWs did not only provide a strong confirmation of the predictions of GR, but also offered a new way to study fundamental interactions. The information extracted from GW signals allows us to probe the theory of general relativity in the strong-field regime, as well as to study the equation of state describing the extremely dense matter inside neutron stars. In this thesis, we investigated both these aspects. In particular, we also turned our attention to next-generation detectors, which are expected to increase sensitivity by roughly a factor 10 and to extend the detection bandwidth both at lower and higher frequencies with respect to current detectors. We studied how this will help us constrain the EOS of neutron stars' matter, both by measuring the tidal parameters from the GWs emitted during the inspiral phase and by including the information from a potential postmerger signal. The high sensitivity of future detectors, however, comes also with downsides: the computational cost of the analyses will increase, thus it is necessary to find alternative techniques in order to make the analyses feasible; furthermore, the high precision with which we will be able to measure the sources' parameters will enhance the effect of systematic errors, induced, for example, by the waveform models employed to analyze the data.

Testing general relativity using higher-order modes in gravitational waves

The GW signal emitted by compact binary coalescences has a multipolar structure. Although, usually, the higher-order modes are suppressed with respect to the fundamental one, their contribution becomes non-negligible for binaries with specific features, like large total mass or considerably different component masses. Evidence for the presence of higher-order modes was found in the two high-mass-ratio events GW190412 and GW190814.

In Chapter 3, we developed a method to probe GR by testing whether the amplitude of subdominant modes are consistent with the values predicted by general relativity. We introduced, in the

expression for GWs multipole expansion, some coefficients $c_{\ell m}$ that parametrize possible deviations in the amplitude of the (ℓ, m) mode with respect to GR predictions. We analyzed signals in a Bayesian framework, which allows us both to recover the value of $c_{\ell m}$ with a standard parameter estimation analysis, together with all the other parameters of the source, and to perform hypothesis ranking between the GR model and our modified non-GR one. We focused on the two subdominant modes that are expected to be the strongest, $(\ell, m) = (2, 1), (3, 3)$. We tested our method on simulated signals and then we applied it to the real events GW190412 and GW190814, finding no evidence for violations of GR. Finally, we investigated correlations between the parameters we introduced and the inclination angle, which cause bimodality in the $c_{\ell m}$ posteriors, especially for the $(3, 3)$ mode. Because of this effect, conclusions about possible violations of GR should be inferred only from the hypothesis ranking results.

Comparing gravitational waveform models for binary black hole mergers

The increased sensitivity of future-generation detectors will enhance the effect of systematic errors on GW data analysis. For parameter estimation, one of the main source of systematics lies in the waveform models employed. As discussed in Sec. 2.1, different waveform models are built with different approximations, which can lead to biases in the analyses.

In Chapter 4, we analyzed the 13 heaviest events with a significant SNR in GWTC-3 employing a *hypermodes* approach, which allows us to directly sample over different waveform approximants and to compute probabilities for them, identifying possible preferences among the models. We did not find any model to be overall preferred or disfavored with respect to the other ones, and for most of the events we recovered similar probabilities for all approximants. Only three events show a strong preference for some of the models: GW190521, GW191109_010717, and GW200129_065458. However, the favored models are not the same in the three cases, and, due to their short duration or data quality issues, we cannot draw strong conclusions from these three events only. We did not identify any trends of the models' probabilities with respect to the parameters of the source or the signal SNR. However, we uncovered an interesting correlation with precession: in the three events significantly favoring some models, the preferred ones are always the models that recover evidence for precession for that event. This is not related to how precession is treated in the different approximants, given that the preferred models are different every time, but, in general, the fact that a model recovers precession results in a higher probability for that model.

Including the postmerger for binary neutron stars

After the coalescence, depending on its EOS and total mass, a BNS system can promptly collapse to a BH or form a NS remnant, in which case a GW signal is emitted. This postmerger signal carries information about the NS's EOS, in a different density and temperature regime with respect to the inspiral. Current detectors are strongly limited by quantum shot noise in the kilohertz band, where the postmerger signal is expected to lie. However, future detectors, with their increased sensitivity, are expected to start detecting postmerger signals.

In Chapter 5, we presented a frequency-domain model to describe the GW signal emitted during

the full coalescence of a BNS system. For the inspiral and merger part we employed one of the state-of-the-art models, while the postmerger is described with a three-parameter Lorentzian. Postmerger physics includes a variety of processes, which results in a complicated signal morphology with a rich structure; for simplicity, we describe only the main emission peak.

The goal is to employ our model in parameter estimation analyses. We developed two versions of the model: one, called FREE-PM, in which the Lorentzian parameters are treated as free parameters and recovered within a Bayesian framework together with all the other parameters of the source; in the other one, named QU-PM, the Lorentzian parameters are instead determined from the binary's parameters through some quasi-universal relations. In the latter case, we focused on the measurement of the tidal deformability since it represents the parameter containing the most information about the EOS, given that chirp mass is usually determined with a high accuracy. We expect that the additional information coming from the signal emitted during the postmerger phase leads to tighter constraints on the tidal deformability.

When analyzing high-SNR simulated signals in zero noise, our FREE-PM model recovers well the Lorentzian parameters, especially the one corresponding to the frequency of the main emission peak, and the QU-PM model yields more precise measurements of the tidal deformability parameter with respect to the results obtained with a model without postmerger, as expected. However, we found that noise fluctuations can significantly impact our results. Moreover, when analyzing signals obtained by injecting NR simulations, our model, based on a simple Lorentzian, struggles to recover the complicated postmerger morphology. Therefore, both versions of our model need to be improved, in order to be applied to the analysis of real signals.

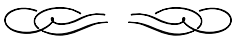
In addition, we compared different networks of future detectors, to assess their performance in postmerger studies. We showed that NEMO, a proposed detector in Australia with improved sensitivity at high frequencies, if approved, will greatly help the detection and study of postmerger signals with second-generation detectors, thanks to its high sensitivity in the kilohertz band.

Studying binary neutron stars with the Einstein Telescope

Third-generation detectors are expected to provide very accurate measurements of the parameters of compact binaries that emit GWs. For the Einstein Telescope, different designs have been proposed: a triangular detector, effectively composed of three V-shaped interferometers with a 60° opening angle between the arms, and two L-shaped interferometers, either with aligned or misaligned arms. In all cases, different arm lengths are possible.

In Chapter 6, we studied how the different designs influence the results of parameter estimation analysis for BNS systems, focusing especially on the recovery of the tidal deformability parameter. We showed that the shape and alignment of the detector do not affect the final result, but the arm length does, which is expected given that a longer arm length results in a higher sensitivity.

Moreover, ET is planned to be built underground and to employ cryogenic technologies, significantly improving the sensitivity at low frequencies and allowing us to detect signals down to a few Hz. We showed the benefits of gaining sensitivity at this end of the detector bandwidth: we analyzed signals starting from different frequencies between 6 and 20 Hz, finding a strong improvement in the measurement of the binary parameters, especially for the chirp mass.



Public summary

When we talk about gravity, the first thing that will probably come to mind is an apple falling on the head of poor Sir Isaac Newton. This lucky accident, according to the myth, led him to the formulation of his theory of gravity. Newton's law of gravitation could describe well the phenomena observed on Earth, where gravity is usually quite weak, but, with time, more sophisticated experiments led to observations that his theory could not explain. All the limitations in Newton's theory were overcome in *general relativity*, a relativistic theory of gravity developed by Albert Einstein a century later, in 1915.

General relativity brought some major perspective changes in the description of gravity. First of all, we now talk of *spacetime*: each event is assigned spacetime coordinates, meaning that it is determined not only by its position in the three-dimensional space we are used to, but also by a time coordinate. In simpler words, the idea is that when you organize a party, you decide the location, but you also need to set the time. Secondly, in Newton's theory, gravity is a force attracting one body to another, according to their mass. In general relativity, instead, gravity is related to the spacetime geometry. Let us picture the spacetime as an elastic fabric: if one places a mass on it, the fabric gets deformed, bending around the massive object (see Fig. S.1). The more *compact* the object, i.e., the more massive for a given size, the stronger the produced curvature will be. Now, if you place a marble on this fabric, it will move following the curvature produced by the first, more massive object, and eventually fall onto it. This is the basic idea of general relativity: masses deform the spacetime geometry producing curvature, and this geometry is what determines how massive objects move. From a mathematical point of view, this is elegantly described by the Einstein field equations.

In this context, gravitational waves are ripples in the spacetime fabric, produced by masses when they accelerate. Consider the situation where we have a compact object, producing its curvature in spacetime, and then we suddenly remove it: without the compact object, the curvature will disappear, but this process is not instantaneous. Similarly, when a massive object moves, the spacetime deformations it produces move with it. The spacetime adapting to the changing curvature that follows an accelerating mass is what produces these waves in spacetime, which propagate with the speed of light. To visualize it, a useful analogy is picturing the ripples produced on the surface of a pond when you throw a rock in the water.

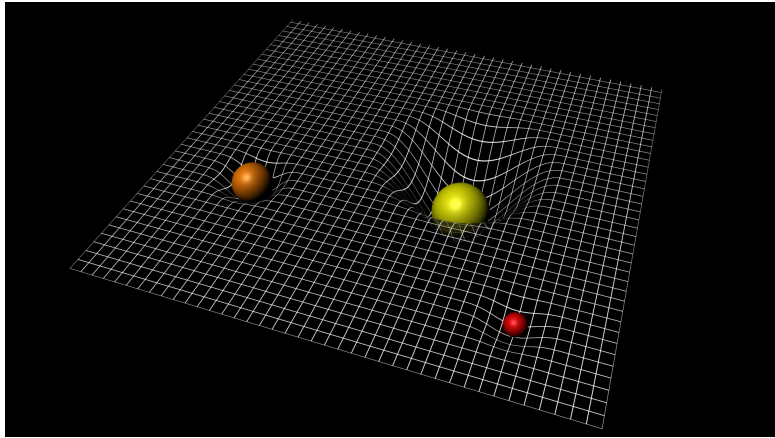


Figure S.1: Artistic representation of the curvature induced in spacetime by objects with different compactness, with the yellow one being the most compact one. *Credit:ESA–C.Carreau*

How do we detect gravitational waves?

When gravitational waves pass by, they periodically stretch and compress spacetime, and this gives us the opportunity to detect them. Current gravitational-wave detectors, such as LIGO, Virgo, and KAGRA, are laser interferometers: basically, they are made of two laser beams that are shone at an input point and that travel along what are called “arms” of the interferometer, usually in perpendicular directions, for a few kilometers; a mirror is placed at the end of each arm, hence each laser beam is reflected back, and the two beams recombine at the output. Light has a wave nature, so each laser beam includes a series of minima and maxima (see left panel of Fig. S.2). When the two beams recombine, interference effects happen: if one beam is at a maximum and one at minimum, for example, the two beams “cancel out” and the output is zero; this effect is called destructive interference (see Fig. S.2). The idea of interferometric detectors is that the instrument at rest, i.e., when there are no gravitational waves passing by, is set to have a specific output, for example a destructive interference. When a gravitational wave arrives, one arm gets stretched and the other one compressed, hence changing the length of the path that the two lasers need to travel. Therefore, when they recombine, we will not have destructive interference anymore, but the output will change in time based on the effect of the passing gravitational wave.

So far so good, but here is the problem: the change in the arms’ length induced by gravitational waves is usually very small, of the order of 0.0000000000000001 meters or smaller. For comparison, the diameter of a human hair is usually 0.000001 meters. Laser interferometry allows us to measure very small changes in the length of the arms, but there are multiple sources of noise that make this measurement difficult. Moreover, the spacetime fabric is very rigid and not easy to deform, therefore only catastrophic events, which involve extremely high velocities and large masses, produce gravitational waves whose effect we can observe. Among such catastrophic events, in this thesis we focus on the coalescence of binaries of compact objects, like neutron stars or black holes, which we briefly describe below.

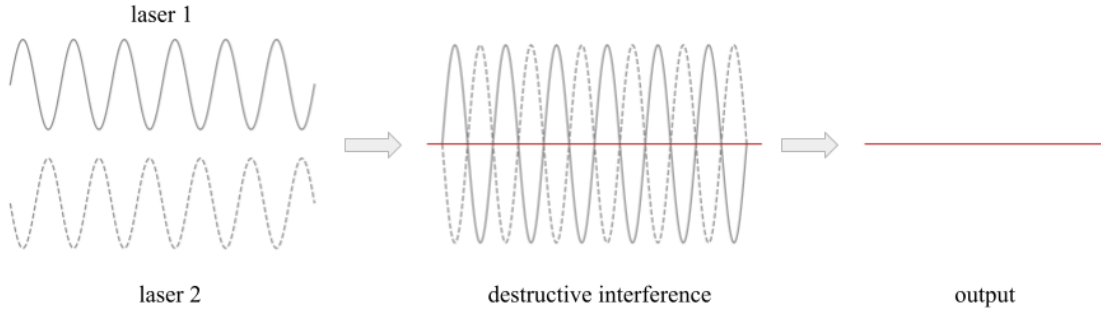


Figure S.2: Schematic representation of destructive interference between two laser beams. The two lasers, *laser 1* and *laser 2*, are made by a series of minima and maxima in their amplitude (*left*). When they recombine at the output of the interferometer, one can set the detector in such a way that, at rest, the minima of one laser perfectly corresponds to the maxima of the other one (*center*), and therefore the combined output, shown in red, is zero (*right*).

Sources of gravitational waves

Stars, like our Sun, are essentially clouds of hydrogen, which is so compressed in the core of the star that it burns, creating helium through nuclear reactions. This hydrogen-burning process releases an enormous amount of energy, which is what makes the stars shine, but also provides an essential source of energy to contrast the inward pressure of gravity, due to the star's own mass, that would make it collapse onto itself. Eventually, all the hydrogen in the star will be transformed into helium: at this point the nuclear fusion process, lacking its fundamental ingredient, stops, and there is no more “outward” pressure to contrast the gravitational one, thus the star begins to collapse. However, this results in the helium atoms being compressed and squashed together, the temperature increases, and it can become so high that also helium starts burning, producing heavier elements. This new nuclear reaction provides further energy to prevent the star's gravitational collapse.

Stellar evolution is a process in which heavier and heavier elements are produced, and the energy released by these nuclear reactions balances the pressure of gravity, preventing the collapse of the star (see Fig. S.3). However, at a certain point, the star runs out of fuel: for the most massive stars, for example, this happens when the element produced in the core is iron. Due to its nuclear structure, iron requires additional energy in order to burn into other elements, thus the nuclear reactions that supplied the star with internal energy stop, and the star begins to collapse onto itself.

Depending on the mass of its core, the star can have different fates. For more massive cores, the final product is a *black hole*. Black holes are exceptionally compact objects, which deform the space-time to such an extent that anything, even light, getting too close to them—that is, going beyond what is called the black hole “event horizon”—cannot escape from the curvature generated and are forced to fall into the black hole. Something different happens for less massive cores, roughly with a mass less than three times the mass of the Sun: when the star's core starts to collapse, the protons and electrons of its atoms are squashed together and they form neutrons. The interactions between neutrons provide the pressure that stops the collapse and eventually supports the final product, a *neutron star*.

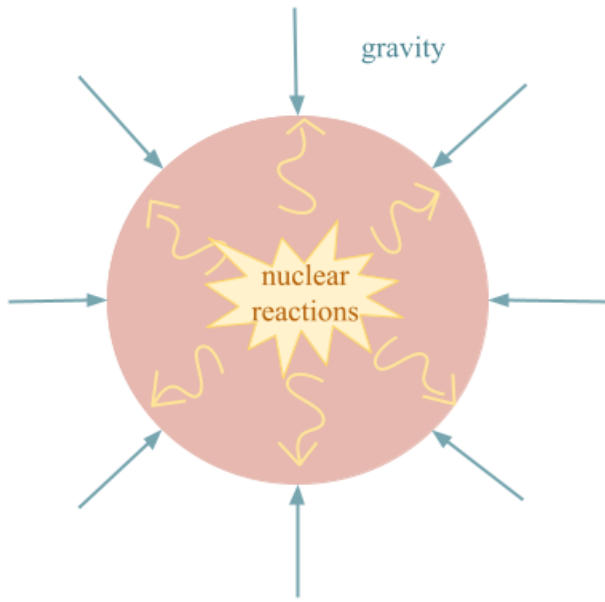


Figure S.3: Representation of the balance in a star between the inward pressure of gravity and the outward pressure produced by the energy released in nuclear reactions.

A *compact binary* is a system of compact objects, like two neutron stars, two black holes, or a neutron star and a black hole, orbiting around each other. While orbiting, the system releases energy through gravitational waves; however, this implies that the system loses energy, and consequently the orbit shrinks, with the two objects moving closer and closer. Smaller orbits, on the other hand, mean higher orbital velocities, and higher velocities result in more energy radiated via gravitational waves. Therefore, the system loses even more energy, the orbit gets even smaller and faster, more energy is emitted via gravitational waves, and so on, until the two objects get so close that they finally merge. During this whole coalescence process, a gravitational-wave signal is emitted, whose features depend on the properties of the system.

What can we study?

By analyzing gravitational-wave signals we can extract information about the parameters of the binary system that emitted them. For example, we can estimate which was the mass of the two objects, or how far from Earth the source was. This is particularly useful to understand the population properties of binary black hole or neutron star systems, in order to answer questions like “How many of them do we expect in the Universe?”, or “What mass do they usually have?”. We also investigate how binary systems are formed, since different formation channels will result in specific differences in some of the parameters.

However, with gravitational waves we can also take a step further and investigate more general and fundamental aspects of physics. They allow us to study how the extremely dense matter inside neutron stars behaves, as we shall see in more detail later. Furthermore, gravitational waves offer

us an extremely useful tool to probe the theory of general relativity. We can design methods to test specific features in the gravitational-wave signals and check whether they are in agreement with the predictions of general relativity.

What we observed so far

The first detection of a gravitational-wave signal happened on 14 September 2015: the two LIGO interferometers in the United States measured a signal produced by the coalescence of two black holes. After that, the number of detections kept increasing, and on 17 August 2017, for the first time, a signal produced by a binary neutron star system was detected, GW170817.

Gravitational wave events are named after the time at which they are observed: the prefix “GW”, for “gravitational wave”, followed by two digits for the year, two for the month, and two for the day.

Until now, we have observed 90 events in total, and currently the detectors are taking data again. With the increasing number of detections, we also started observing events outside the expected “vanilla” population, i.e., with less common or unexpected features, such as very heavy or very different component masses. All the events detected so far were generated by the coalescence of a compact binary system, but some of them already started to challenge our current understanding of the theory underlying these processes, for example, about how binary black holes are formed. Until now, however, no evidence of violations of general relativity has been found.

How do we analyze data?

As mentioned, the gravitational-wave signal emitted by a coalescing compact binary system depends on the properties of the objects in the binary, such as their masses. Therefore, we can study these objects by estimating the parameters that describe their features from the emitted gravitational waves. In order to accomplish this, we need three main ingredients: the measured gravitational-wave data, a model to describe them, and an idea of the range in which the parameters lie, called *prior*.

Gravitational-waveform models describe how we expect the gravitational-wave signal to look like during the coalescence process, until the merger of the two objects and possibly also after that. An example of a gravitational waveform provided by one of these models is shown in Fig. S.4. Usually, these waveform models take as input the parameters of the source and supply as output the emitted gravitational-wave signal (see Fig. S.5).

In order to estimate the source parameters for a given event, the basic idea is that we pick some values for the parameters in the prior range, we use our waveform model to generate the gravitational-wave signal that would be emitted by a source with the chosen parameters, and we compare it with the measured data. We repeat the process for many values in the prior range, and finally we find which parameters produce the gravitational waveform that best describes our data.

Waveform models represent an essential ingredient in the analysis of gravitational-wave data. Creating these models is however not an easy task: in principle, to get the exact form of the gravitational-wave signal, one should solve the Einstein field equations. This cannot be done analytically, so one must resort to some approximations. However, different approximations can be employed to build waveform models, and thus different models exist, which can yield different results in the analysis.

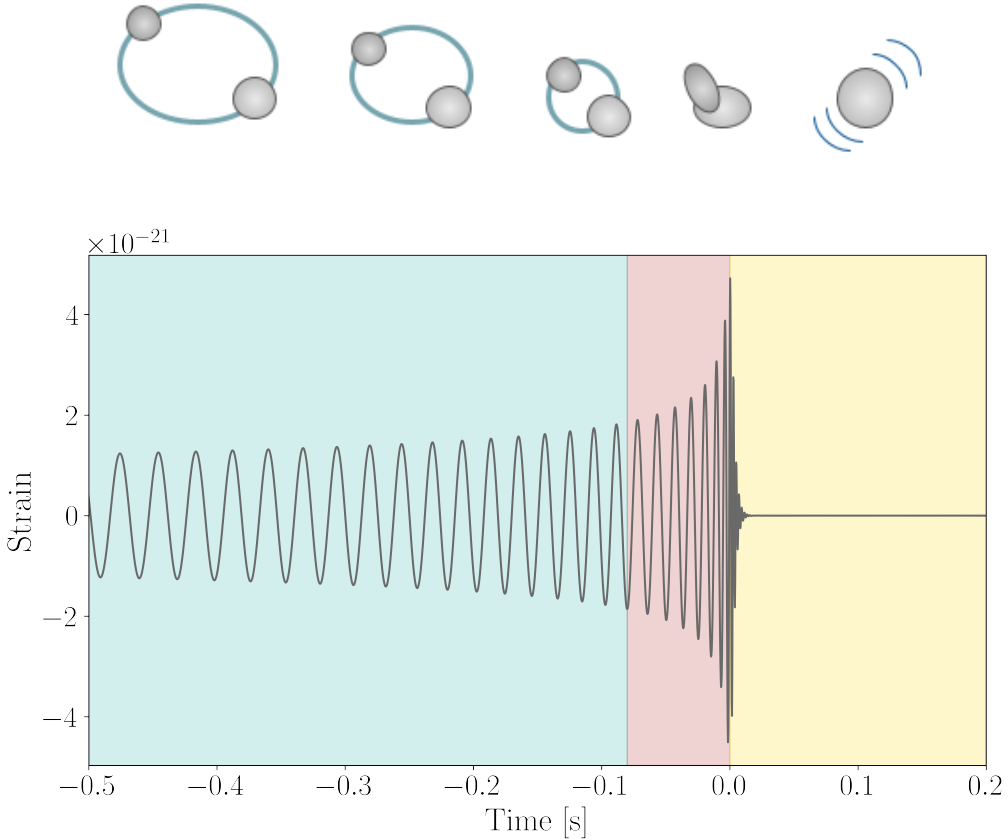


Figure S.4: Example of a gravitational-wave signal emitted by a binary black hole coalescence. The green area corresponds to the inspiral phase, when the two black holes are still orbiting one around each other. The red one, instead, corresponds to the phase when the two objects plunge into each other and merge. Finally, the yellow area shows the signal emitted by the *remnant*, i.e., the object formed after the merger.

About future detectors

Currently, there exist four gravitational-wave interferometers, two in the United States, one in Italy, and one in Japan, and a fifth one is undergoing construction in India. Another detector exists in Germany, GEO600, which is however used mainly to develop and test new technologies. We saw that measuring gravitational waves is not an easy task, given how small the signal is. There exist specific methods to tackle the multiple sources of noise, and there is a constant effort to improve the sensitivity of the detectors, i.e., to make them capable of measuring smaller and smaller signals. Currently, this is accomplished by implementing changes to the existing detectors. However, in order to obtain even higher sensitivities, some technological improvements planned for the future will require the construction of new interferometers, which are therefore called “future-generation”, or “third-generation”, detectors. As of now, the plan for third-generation detectors includes the Einstein Telescope in Europe and the Cosmic Explorer in the United States.

Third-generation detectors, with their increased sensitivity, are expected to measure many more events, in a wider frequency range. This, of course, will provide us with an unprecedented opportunity to study compact binary systems, and possibly also different gravitational-wave sources, but it

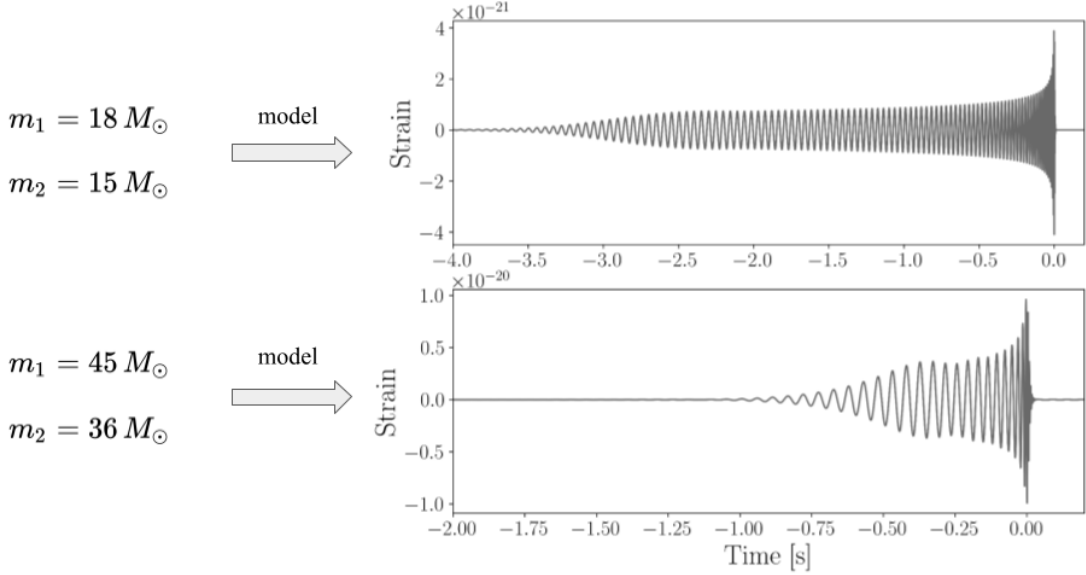


Figure S.5: Example of gravitational-wave signals produced by the same waveform model for different values of masses of the two compact objects in the binary. For simplicity, masses are usually measured in terms of the mass of the Sun, M_{\odot} .

will come with some disadvantages: we will measure so many signals that some of them will overlap, therefore making it difficult to analyze data for a specific source; the signals will be very loud, and therefore we will start seeing the effect of systematic biases induced by our analysis methods; finally, due to both their number and loudness, the detections will require a huge amount of computational resources to be analyzed.

Testing general relativity

As mentioned, with gravitational waves we can probe the theory of general relativity. Different tests with this purpose exist, which investigate various aspects of gravitational waves, but until now none of them highlighted any violation of general relativity. In this thesis, we proposed a new test that looks at the higher-order modes in gravitational-wave signals. Let us think of a guitar: when one plucks its strings, the sound produced has a fundamental mode, but also higher overtones. The same thing happens with gravitational waves, where we have a fundamental mode, called *quadrupolar*, but also higher harmonics, as in sound waves. Usually, the fundamental mode is the strongest one, and for most of the signals emitted by binary systems the higher harmonics are not significant. However, when the source system has specific features, for example, when the masses of the two objects in the binary are very different, the higher-order modes provide a stronger contribution to the emitted signal and we can measure them.

General relativity predicts exactly how this higher-order modes signal will be, therefore we developed a method to check whether the amplitude of the two strongest harmonics is consistent with the predictions of general relativity. In particular, in our test we measure a possible deviation from the

amplitude value predicted by general relativity, but we also compare a general-relativity waveform model with a model that allows such deviations in the amplitude of the higher-order modes, finding which one is favored by the data. We apply this test to two real events, GW190412 and GW190814, the two observations from sources with the largest difference between component masses, and find no evidence of general relativity violations.

Comparing waveform models

As we discussed, building waveform models requires some approximations. Employing models with different approximations generates, in the results of many analyses, differences that will become noticeable, and therefore a potential issue, with future-generation detectors. We presented a study in which we analyze some of the events detected so far with four different models and we try to identify possible preferences among them. This would serve as an indicator of which model employs the best approximation for some kinds of events, or which one includes the best description of a given effect.

Overall, we do not find a model constantly favored (or disfavored) over the others. We recover a strong preference for some models only for three events: although the preferred models are not the same, we find that, in all cases, they are the ones that recover evidence of an effect called *precession*. Imagine the two compact objects orbiting around each other as if they were moving on a table: the table is what we call “orbital plane”. If the table is not still but wobbling, we have precession (see Fig. S.6). This effect leaves a well-defined imprint in the emitted gravitational waves, and its presence would give us important information about the way in which the binary system formed. In our work, we do not find a correlation between the source parameters and the preference for some models, but, in general, the fact that a model recovers precession results in a higher probability for that model.

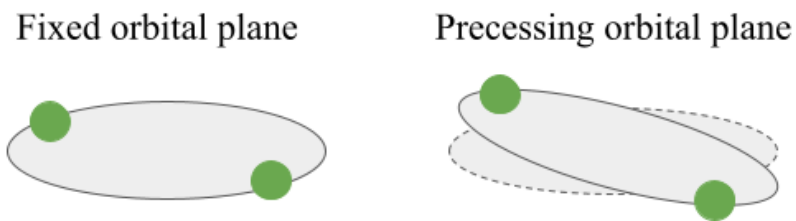


Figure S.6: Schematic representation of the orbital plane precession effect.

Studying neutron stars

The matter inside neutron stars reaches extremely high densities, as if we were compressing the mass of one million space shuttles into a tablespoon. Matter with such densities cannot be reproduced in laboratory experiments, hence studying the properties of neutron stars is extremely important in order to try and understand how this exceptionally dense matter behaves, i.e., its *equation of state*. The equation of state of neutron stars’ matter determines their macroscopic properties, such as their mass and radius. For a given value of mass, an equation of state will tell us exactly what the radius of the neutron star is. However, we still don’t know which is the equation of state of this very dense matter.

Various theoretical models exist, which lead to different predictions: if we take ten physicists, each one with their own equation of state model, and ask them what is the radius of a neutron star with a mass two times the mass of the Sun, we will get ten different answers. Gravitational waves offer us a unique tool to study this equation of state: the properties of the neutron stars in a binary system influence the gravitational-wave signal emitted during the coalescence, therefore, by analyzing this signal, we can recover their parameters and place constraints on the equation of state. For example, let us suppose that we measure the mass to be two solar masses and the radius between 10 and 11 kilometers; if we have an equation of state model predicting a radius of 15 kilometers for a star with two solar masses, we would know that the model is wrong.

Unfortunately, while mass can be measured from gravitational-wave signals with great accuracy, the same does not hold for radius, since it is not one of the quantities that directly determine the emitted gravitational-wave signal. The other quantity that we can estimate from gravitational waves is the *tidal deformability* parameter. While black holes are essentially a place in spacetime where gravity is so strong that nothing can escape from the curvature they produce, in the case of neutron stars the presence of matter plays an important role. To understand the concept of tidal deformability, let us resort to the analogy with ocean tides. The Moon orbits around the Earth, and it generates its own gravitational field. The Moon's gravitational pull is different in different regions on Earth, depending on their position with respect to the Moon. The difference between the Moon's gravitational pull at a specific location and its average gravitational pull on Earth generates some so-called *tidal forces*, which stretch the Earth's body in one direction and squash it in the other. This is what causes the ocean high and low tides, because water is pulled from (or pushed towards) the Earth. In principle, this phenomenon affects also the land, but since it is more difficult to move, we just do not notice. A similar thing happens with neutron stars in a binary system: each one of them has its own gravitational field and generates a tidal field on the other one, deforming it.

How much the matter in a neutron star is deformed by these tidal forces is described by the tidal deformability parameter, and it depends on how the neutron star matter behaves, i.e., on its equation of state, just like land behaves differently than seawater. The relation between the mass and tidal deformability of a neutron star is uniquely determined by its equation of state. Therefore, since we can determine the mass of the neutron stars in a binary from the emitted gravitational-wave signal, if we can obtain also an estimate of their tidal deformability we can constrain the equation of state. Unfortunately, the tidal deformability is not easy to determine, since its effect on the emitted gravitational waves is much weaker than the one of mass.

Postmerger studies

We usually try to estimate the mass and tidal deformability of the neutron stars in a binary system from the gravitational-wave signal emitted during the *inspiral* phase, i.e., when the two neutron stars are still orbiting around each other. However, this is not the end of the story. We mentioned earlier that at some point the two neutron stars will get so close that they plunge one into the other, in what we call *merger*. After that, different scenarios are possible: the formation of a black hole, of a massive and fast-rotating neutron star remnant, or, less commonly, of a stable neutron star. The fate of the binary after the merger is determined by the binary total mass and, above all, by the equation of

state.

If a massive neutron star remnant is formed, it survives at most a few seconds before collapsing into a black hole, but during this time it emits a gravitational-wave signal that can provide us with a wealth of information about the equation of state. Unfortunately, studying this *postmerger* signal is not easy: first of all, it usually involves frequencies between 2000 and 4000 Hertz, and our current detectors are not sensitive enough at such high frequencies. Moreover, a lot of different physical processes are involved in this phase, and we do not have a complete theoretical model to describe it.

In this thesis, we developed a waveform model to describe the gravitational-wave signal emitted during the inspiral, merger, and postmerger phases of a binary neutron star system coalescence. For the inspiral and merger, we employ one of the state-of-the-art models commonly used to analyze signals emitted by binary neutron star systems. Regarding the postmerger phase, instead, its signal is predicted to show a very complex structure with multiple peaks, but, for simplicity, we model only the peak describing the emission of the fundamental mode. We employed our model to analyze simulated data for future detectors, and we found that it helps put tighter constraints on the tidal deformability parameter with respect to a model without postmerger, and also to estimate the main emission frequency of the postmerger gravitational-wave signal. However, when analyzing signals with more complex structures, and therefore more similar to possible real data, our simple model struggles to recover the postmerger signal, and therefore we need to improve it before we can actually use it to analyze data from real events.

Current detectors are not sensitive enough to observe postmerger signals, but future ones are expected to start detecting them. Therefore, we also compared various futures detectors, assessing their performance in the study of the equation of state from postmerger signals.

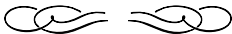
Possible impact of Einstein Telescope designs

Einstein Telescope is expected to have a sensitivity ten times higher than current detectors. The technological improvements needed to reach such conditions require the construction of a new site. The Einstein Telescope collaboration has been investigating different design options for the new detector, among which the shape it should have. Currently, the main candidates are a triangular shape, or two L-shaped detectors, i.e., with two perpendicular arms, either with the same orientation or not. For each shape, the detector arms can also have different lengths. The construction of a detector with these different designs will require different technologies, different costs, and so on, but an important question is whether it will impact the scientific outcome. The influence of the detector design on several analyses has been investigated. In this thesis, we presented a detailed study of the impact of the different designs on the estimation of binary neutron stars parameters, in particular of the tidal deformability. We showed that the detector's shape and alignment play a little role, but longer detector arms will supply more precise measurements of the parameters, as expected since longer arms yield a higher sensitivity.

Moreover, one of the main achievements of the Einstein Telescope will be to gain sensitivity at low frequencies, below 20 Hertz, where current detectors are strongly limited. If we can observe the coalescence of a binary system starting at low frequencies, it means we can observe it for more time, and therefore obtain more information. In our study, we concretely showed, and quantified, how

analyzing signals starting from lower frequencies will improve the estimate of the binary's parameters.

We often hear that “gravitational waves opened a new window on the Universe”: indeed, they offer us a new way to look (or better, to listen) at the Universe, providing us with information that cannot be obtained through electromagnetic observations—let us just think about black holes. Through gravitational waves we can investigate many different phenomena, but also more fundamental issues, like probing the theory of general relativity or understanding the extremely dense matter inside neutron stars. In this thesis, we worked on both these topics, focusing not only on what we can study with current detectors but also on the impact of future ones.



Openbare samenvatting

Wanneer we het over zwaartekracht hebben, is het eerste dat waarschijnlijk in gedachten zal komen, een appel die op het hoofd van de arme Sir Isaac Newton valt. Volgens de mythe leidde dit gelukkige ongeluk hem tot de formulering van zijn zwaartekrachttheorie. Newton's wet van de zwaartekracht kon goed de fenomenen verklaren die op aarde werden waargenomen, waar de zwaartekracht doorgaans vrij zwak is, maar met de tijd leidden meer geavanceerde experimenten tot waarnemingen die zijn theorie niet kon verklaren. Alle beperkingen in Newton's theorie werden een eeuw later in 1915 overwonnen in de *algemene relativiteitstheorie*, een relativistische theorie van zwaartekracht ontwikkeld door Albert Einstein.

Algemene relativiteit bracht enkele belangrijke perspectiefveranderingen in de beschrijving van zwaartekracht. Allereerst spreken we nu van *ruimtetijd*: elk evenement krijgt ruimtetijdcoördinaten toegewezen, wat betekent dat het niet alleen wordt bepaald door zijn positie in de driedimensionale ruimte waaraan we gewend zijn, maar ook door een tijdcoördinaat. In eenvoudiger bewoordingen, het idee is dat wanneer je een feest organiseert, je niet alleen de locatie kiest, maar ook de tijd instelt. Ten tweede, in de theorie van Newton is zwaartekracht een kracht die het ene lichaam naar het andere trekt, afhankelijk van hun massa. In de algemene relativiteitstheorie daarentegen is zwaartekracht gerelateerd aan de ruimtetijd-geometrie. Laten we ons de ruimtetijd voorstellen als een elastische stof: als je er een massa op plaatst, wordt de stof vervormd en buigt om het massieve object heen (zie Fig. Sn.1). Hoe *compacter* het object is, dat wil zeggen, hoe massiever voor een gegeven grootte, hoe sterker de geproduceerde kromming zal zijn. Nu, als je een knikker op deze stof plaatst, zal het bewegen in overeenstemming met de kromming die wordt veroorzaakt door het eerste, meer massieve object, en uiteindelijk erop vallen. Dit is het basisidee van de algemene relativiteit: massa's vervormen de ruimtetijd-geometrie en produceren kromming, en deze geometrie bepaalt hoe massieve objecten bewegen. Vanuit een wiskundig oogpunt wordt dit elegant beschreven door de vergelijkingen van Einstein.

In deze context zijn zwaartekrachtsgolven rimpelingen in de ruimtetijdstof, geproduceerd door massa's wanneer ze versnellen. Stel je de situatie voor waarin we een compact object hebben, dat zijn kromming in de ruimtetijd produceert, en dan plotseling weghalen: zonder het compacte object zal de kromming verdwijnen, maar dit proces is niet onmiddellijk. Op dezelfde manier, wanneer een massief object beweegt, bewegen de ruimtetijdvervormingen die het produceert met zich mee. De

ruimtetijd die zich aanpast aan de veranderende kromming die volgt op een versnellende massa, is wat deze golven in de ruimtetijd produceert, die zich met de snelheid van het licht voortplanten. Om het te visualiseren, is een nuttige analogie om je voor te stellen de rimpelingen die worden geproduceerd op het oppervlak van een vijver wanneer je een steen in het water gooit.

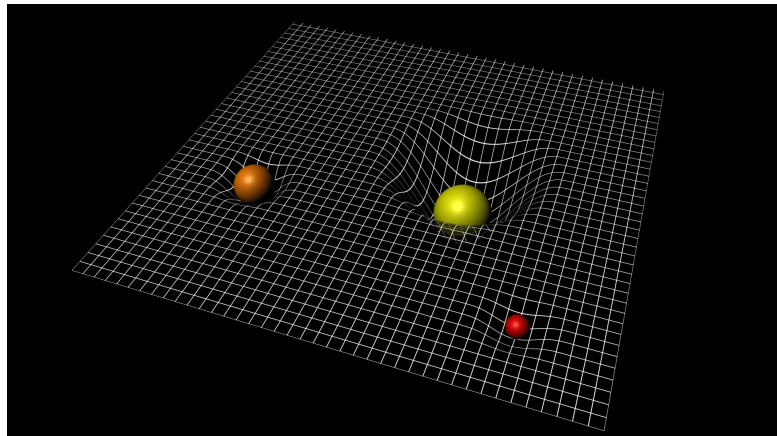


Figure Sn.1: Artistieke weergave van de kromming veroorzaakt in de ruimtetijd door objecten met verschillende compactheid, waarbij de gele het meest compacte is. *Credit:ESA-C.Carreau*

Hoe detecteren we zwaartekrachtgolven?

Wanneer zwaartekrachtgolven passeren, rekken en comprimeren ze periodiek de ruimtetijd, en dit geeft ons de kans om ze te detecteren. Huidige zwaartekrachtgolfdetectoren, zoals LIGO, Virgo en KAGRA, zijn laserinterferometers: in feite bestaan ze uit twee laserstralen die worden uitgezonden naar een invoerpunt en die langs zogenaamde “armen” van de interferometer reizen, meestal in loodrechte richtingen, over enkele kilometers; aan het einde van elke arm bevindt zich een spiegel, waardoor elke laserstraal wordt teruggekaatst, en de twee stralen komen weer samen bij de uitvoer. Licht heeft een golfkarakter, dus elke laserstraal omvat een reeks minima en maxima (zie het linkerpaneel van Fig. Sn.2). Het idee van interferometrische detectoren is dat het instrument in rust, dat wil zeggen wanneer er geen zwaartekrachtgolven passeren, is ingesteld op een specifieke uitvoer, bijvoorbeeld destructieve interferentie. Wanneer een zwaartekrachtgolf arriveert, wordt de ene arm uitgerekt en de andere samengedrukt, waardoor de lengte van het pad dat de twee lasers moeten afleggen verandert. Daarom hebben we bij de recombinatie geen destructieve interferentie meer, maar de uitvoer zal in de tijd veranderen op basis van het effect van de passerende zwaartekrachtgolf.

Tot zover gaat het goed, maar hier is het probleem: de verandering in de lengte van de armen die wordt veroorzaakt door zwaartekrachtgolven is meestal zeer klein, van de orde van $0,000000000000000001$ meter of kleiner. Ter vergelijking, de diameter van een menselijk haar is meestal $0,000001$ meter. Laserinterferometrie stelt ons in staat om zeer kleine veranderingen in de lengte van de armen te meten, maar er zijn meerdere bronnen van ruis die deze meting moeilijk maken. Bovendien is de structuur van de ruimtetijd zeer rigide en niet gemakkelijk te vervormen, daarom produceren alleen catastrofale gebeurtenissen, die gepaard gaan met extreem hoge snelheden en grote massa's, zwaartekrachtgolven waarvan het effect we kunnen waarnemen. Onder dergelijke catastrofale gebeurtenissen richten we

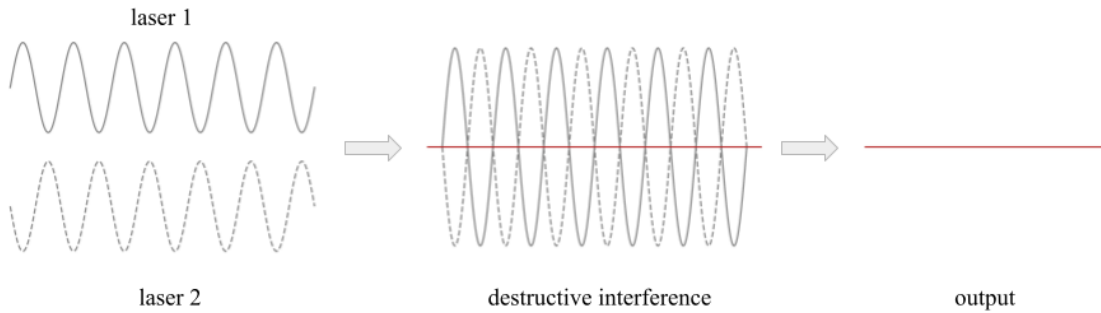


Figure Sn.2: Schematische weergave van destructieve interferentie tussen twee laserstralen. De twee lasers, *laser 1* en *laser 2*, bestaan uit een reeks minima en maxima in hun amplitude (*links*). Wanneer ze weer samenkommen aan de uitvoer van de interferometer, kan men de detector zodanig instellen dat, in rust, de minima van de ene laser perfect overeenkomen met de maxima van de andere (*midden*), en daarom is de gecombineerde uitvoer, weergegeven in rood, nul (*rechts*).

ons in deze scriptie op de samensmelting van dubbele compacte objecten, zoals neutronensterren of zwarte gaten, die we hieronder kort beschrijven.

Bronnen van zwaartekrachtsgolven

Sterren, zoals onze Zon, zijn in wezen wolken van waterstof, die zo samengeperst zijn in de kern van de ster dat het brandt en helium creëert door middel van nucleaire reacties. Dit waterstofverbrandingsproces geeft een enorme hoeveelheid energie vrij, wat de sterren doet schijnen, maar ook een essentiële energiebron biedt om de inwaartse druk van de zwaartekracht tegen te gaan, te wijten aan de massa van de ster zelf, die ervoor zou zorgen dat de ster in zichzelf instort. Uiteindelijk zal alle waterstof in de ster worden omgezet in helium: op dit punt stopt het nucleaire fusieproces, omdat het zijn fundamentele ingrediënt mist, en is er geen “uitwendige” druk meer om de gravitationele druk tegen te gaan, waardoor de ster begint in te storten. Dit resulteert echter in samengeperste heliumatomen die tegen elkaar botsen, de temperatuur stijgt en kan zo hoog worden dat ook helium begint te branden en zwaardere elementen produceert. Deze nieuwe nucleaire reactie levert meer energie om het gravitationele instorten van de ster te voorkomen.

Stereovolutie is een proces waarin steeds zwaardere elementen worden geproduceerd, en de energie die vrijkomt bij deze nucleaire reacties balanceert de zwaartekrachtdruk, waardoor de instorting van de ster wordt voorkomen (zie Fig. Sn.3). Op een bepaald punt raakt de ster echter door zijn brandstof heen: voor de meest massieve sterren gebeurt dit wanneer het element dat in de kern wordt geproduceerd ijzer is. Vanwege de nucleaire structuur heeft ijzer extra energie nodig om in andere elementen te branden. Hierdoor stoppen de nucleaire reacties die de ster van interne energie voorzagen, en begint de ster in zichzelf te storten.

Afhankelijk van de massa van de kern kan de ster verschillende uitkomsten hebben. Voor kernen met meer massa is het eindproduct een *zwart gat*. Zwarte gaten zijn uitzonderlijk compacte objecten die de ruimtetijd zodanig vervormen dat alles, zelfs licht, dat te dichtbij komt (dat wil zeggen, voorbij wat de ‘waarnemingshorizon’ van het zwarte gat wordt genoemd) niet kan ontsnappen aan de

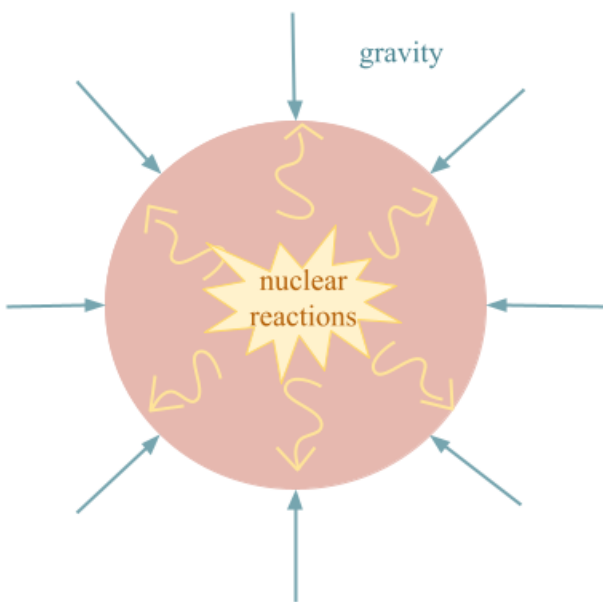


Figure Sn.3: Weergave van het evenwicht tussen de inwaartse druk van de zwaartekracht en de uitwaartse druk die wordt geproduceerd door de energie die vrijkomt bij nucleaire reacties.

gegenereerde kromming en gedwongen wordt in het zwarte gat te vallen. Iets anders gebeurt voor ker nen met iets minder massa, ongeveer met een massa minder dan drie keer die van de zon: wanneer de kern van de ster begint in te storten, worden de protonen en elektronen van zijn atomen samengeperst en vormen ze neutronen. De interacties tussen neutronen zorgen voor de druk die het ineenstorten stopt en uiteindelijk het eindproduct ondersteunt, namelijk een neutronenster.

Een compact dubbelsysteem bestaat uit twee compacte objecten, zoals twee neutronensterren, twee zwarte gaten, of een neutronenster en een zwart gat, die om elkaar heen draaien. Terwijl ze draaien, geeft het systeem energie af via zwaartekrachtgolven; dit betekent echter dat het systeem energie verliest, en als gevolg daarvan krimpt de baan, waarbij de twee objecten steeds dichter bij elkaar komen. Kleinere banen betekenen daarentegen een hogere omloopsnelheid, en hogere snelheden resulteren in meer energie die wordt uitgestraald via zwaartekrachtgolven. Daarom verliest het systeem nog meer energie, krimpt de baan nog meer en wordt deze sneller, wordt er nog meer energie uitgestraald via zwaartekrachtgolven, enzovoort, totdat de twee objecten zo dicht bij elkaar komen dat ze uiteindelijk samensmelten. Gedurende dit hele samensmeltingsproces wordt een zwaartekrachtgolfsignaal uitgestraald, waarvan de kenmerken afhangen van de eigenschappen van het systeem.

Wat kunnen we bestuderen?

Door gravitatiegolfsignalen te analyseren, kunnen we informatie extraheren over de parameters van het dubbelsysteem dat ze heeft uitgestraald. Bijvoorbeeld, we kunnen schatten wat de massa was van de twee objecten, of hoe ver de bron van de aarde verwijderd was. Dit is bijzonder nuttig om de populatiekenmerken van binaire systemen van zwarte gaten of neutronensterren te begrijpen, om vragen

te beantwoorden zoals “Hoeveel van hen verwachten we in het universum?” of “Welke massa hebben ze meestal?”. We onderzoeken ook hoe binaire systemen worden gevormd, aangezien verschillende vormingskanalen specifieke verschillen tussen sommige van de parameters zullen opleveren.

Met gravitatiegolven kunnen we echter ook een stap verder gaan en meer algemene en fundamentele aspecten van de natuurkunde onderzoeken. Ze stellen ons in staat om te bestuderen hoe het extreem dichte materiaal binnen neutronensterren zich gedraagt, zoals we later in meer detail zullen zien. Bovendien bieden gravitatiegolven een uiterst nuttig hulpmiddel om de theorie van de algemene relativiteit te onderzoeken. We kunnen methoden ontwerpen om specifieke kenmerken in de gravitatiegolfsignalen te testen en te controleren of ze overeenkomen met de voorspellingen van de algemene relativiteit.

Wat we tot nu toe hebben gedetecteerd

De eerste detectie van een gravitatiegolfsignaal vond plaats op 14 september 2015: de twee LIGO-interferometers in de Verenigde Staten maten een signaal dat werd geproduceerd door de samensmelting van twee zwarte gaten. Daarna bleef het aantal detecties toenemen, en op 17 augustus 2017 werd voor het eerst een signaal gedetecteerd dat werd geproduceerd door een binaire neutronenster, GW170817.

Gravitatiegolfgebeurtenissen worden genoemd naar het tijdstip waarop ze worden waargenomen: het voorvoegsel “GW”, voor “gravitatiegolf”, gevolgd door twee cijfers voor het jaar, twee voor de maand en twee voor de dag.

Tot nu toe hebben we in totaal 90 gebeurtenissen waargenomen, en momenteel nemen de detectoren weer gegevens op. Met het toenemende aantal detecties begonnen we ook gebeurtenissen te observeren buiten de verwachte “standaard” populatie, dat wil zeggen, met minder voorkomende of onverwachte kenmerken, zoals zeer zware of zeer verschillende componentmassa’s. Alle tot nu toe gedetecteerde gebeurtenissen werden gegenereerd door de samensmelting van een compact binair systeem, maar sommige van hen begonnen al onze huidige begrip van de theorie achter deze processen uit te dagen, bijvoorbeeld over hoe binaire zwarte gaten worden gevormd. Tot nu toe is er echter geen bewijs gevonden van schendingen van de algemene relativiteit.

Hoe analyseren we gegevens?

Zoals we eerder hebben vermeld, hangt het gravitatiegolfsignaal dat wordt uitgezonden door een samensmelzend binair systeem af van de eigenschappen van de compacte objecten in het systeem, zoals hun massa’s. Daarom kunnen we deze objecten bestuderen door de parameters die hun kenmerken beschrijven te schatten op basis van de uitgezonden gravitatiegolven. Om dit te bereiken, hebben we drie belangrijke ingrediënten nodig: de gemeten gravitatiegolfgegevens, een model om ze te beschrijven, en een idee van het bereik waarin de parameters liggen, de zogenaamde “prior”.

Gravitatiegolfvormmodellen beschrijven hoe we verwachten dat het gravitatiegolfsignaal eruit zal zien tijdens het samensmeltingsproces, tot aan de merger van de twee objecten en mogelijk ook daarna. Een voorbeeld van een gravitatiegolfvorm die wordt geleverd door een van deze modellen wordt getoond in Fig. Sn.4). Gewoonlijk nemen deze golfvormmodellen de parameters van de bron als invoer en

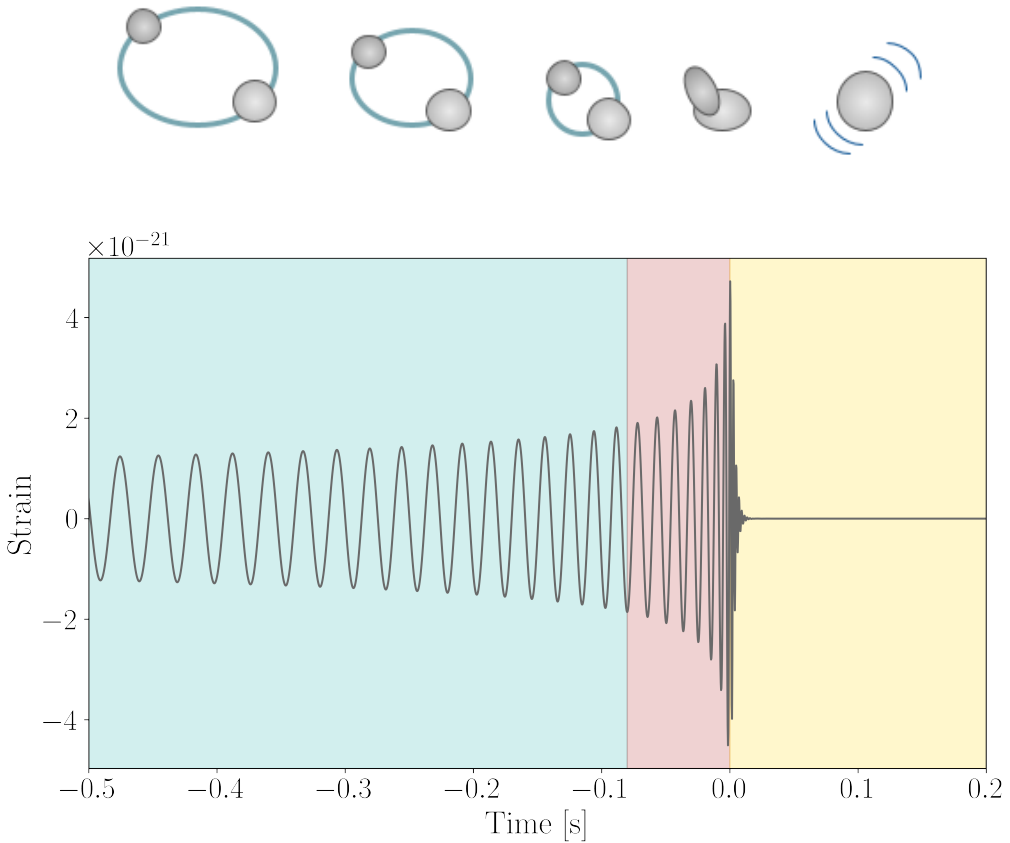


Figure Sn.4: Voorbeeld van een gravitatiegolfsignaal uitgezonden door de samensmelting van een binair zwart gat. Het groene gebied komt overeen met de inspiral, wanneer de twee zwarte gaten nog steeds om elkaar heen draaien. Het rode gebied daarentegen komt overeen met de fase waarin de twee objecten in elkaar storten en samensmelten. Tenslotte toont het gele gebied het signaal dat wordt uitgezonden door het *overblijfsel*, dat wil zeggen het object dat wordt gevormd na de samensmelting.

leveren ze als uitvoer het uitgezonden gravitatiegolfsignaal (zie Fig. S.5).

Om de bronparameters voor een bepaalde gebeurtenis te schatten, is het basisidee dat we enkele waarden voor de parameters in het vooraf bepaalde bereik kiezen, ons golfvormmodel gebruiken om het gravitatiegolfsignaal te genereren dat zou worden uitgezonden door een bron met de gekozen parameters, en we vergelijken het met de gemeten gravitatiegolfgegevens. We herhalen het proces voor veel waarden in het vooraf bepaalde bereik, en uiteindelijk vinden we welke parameters het gravitatiegolfsignaal produceren dat onze gegevens het beste beschrijft.

Golfvormmodellen vormen een essentieel ingrediënt in de analyse van gravitatiegolfgegevens. Het creëren van deze modellen is echter geen gemakkelijke taak: in principe zou men om de exacte vorm van het gravitatiegolfsignaal te krijgen, de Einstein-veldvergelijkingen moeten oplossen. Dit kan niet analytisch worden gedaan, dus men moet zijn toevlucht nemen tot enkele benaderingen. Er kunnen echter verschillende benaderingen worden gebruikt om golfvormmodellen te construeren, en dus bestaan er verschillende modellen die verschillende resultaten kunnen opleveren in de analyse.

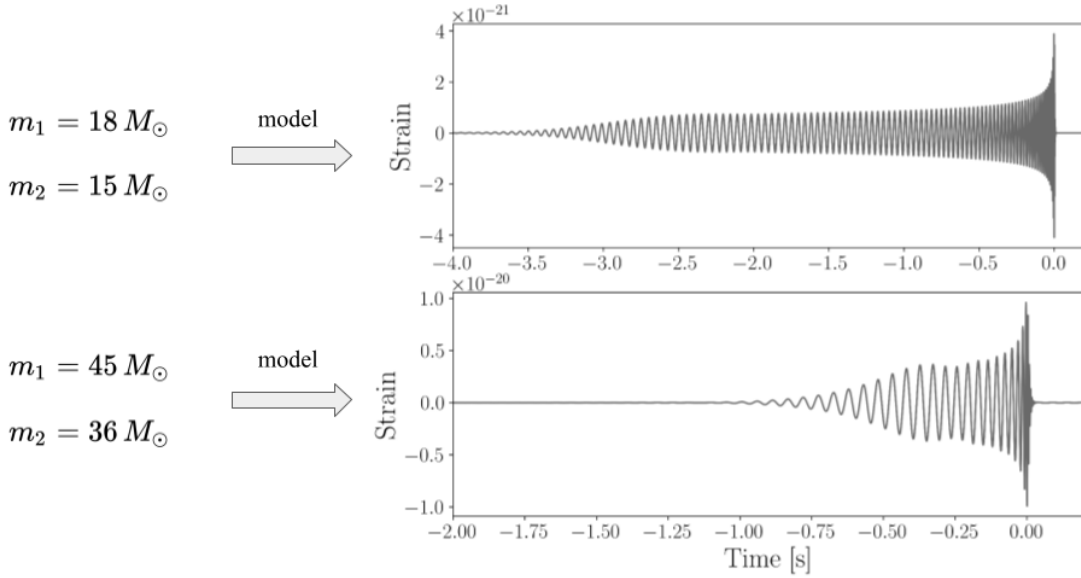


Figure Sn.5: Voorbeeld van gravitatiegolfsignalen geproduceerd door hetzelfde golfvormmodel voor verschillende waarden van de massa's van de twee compacte objecten in het binaire systeem. Voor eenvoud worden massa's meestal gemeten in termen van de massa van de Zon, M_{\odot} .

Over toekomstige detectoren

Op dit moment bestaan er vier gravitatiegolfinterferometers, twee in de Verenigde Staten, één in Italië en één in Japan, en er wordt momenteel een vijfde gebouwd in India. Er bestaat nog een detector in Duitsland, GEO600, die echter hoofdzakelijk wordt gebruikt om nieuwe technologieën te ontwikkelen en te testen. We hebben gezien dat het meten van gravitatiegolven geen eenvoudige taak is, gezien hoe zwak het signaal is. Er bestaan specifieke methoden om de verschillende bronnen van ruis aan te pakken, en er is voortdurende inspanning om de gevoeligheid van de detectoren te verbeteren, dat wil zeggen, om ze in staat te stellen steeds zwakkere signalen te meten. Momenteel wordt dit bereikt door wijzigingen aan te brengen in de bestaande detectoren. Echter, om nog hogere gevoeligheden te bereiken, zullen sommige geplande technologische verbeteringen voor de toekomst de bouw van nieuwe interferometers vereisen, die daarom "toekomstige generatie" of "derde generatie" detectoren worden genoemd. Op dit moment omvat het plan voor detectoren van de derde generatie de Einstein Telescoop in Europa en de Cosmic Explorer in de Verenigde Staten.

Detectoren van de derde generatie, met hun verhoogde gevoeligheid, worden verwacht veel meer gebeurtenissen te zullen meten, over een breder frequentiebereik. Dit zal ons natuurlijk een ongekende kans bieden om compacte binaire systemen te bestuderen, en mogelijk ook verschillende bronnen van gravitatiegolven, maar het zal enkele nadelen met zich meebrengen: we zullen zoveel signalen meten dat sommige ervan zullen overlappen, waardoor het moeilijk wordt om gegevens voor een specifieke bron te analyseren; de signalen zullen erg luid zijn, en daarom zullen we het effect beginnen te zien van systematische vertekeningen veroorzaakt door onze analysemethoden; zowel het aantal als het volume van de detecties zal een enorme hoeveelheid rekenkracht vereisen om te worden geanalyseerd.

Het testen van de algemene relativiteit

Zoals eerder vermeld, kunnen we met gravitatiegolven de theorie van de algemene relativiteit onderzoeken. Er bestaan verschillende tests met dit doel, die verschillende aspecten van gravitatiegolven onderzoeken, maar tot nu toe heeft geen van hen enige schending van de algemene relativiteit aangetoond. In dit proefschrift hebben we een nieuwe test voorgesteld die kijkt naar de hogere modi in gravitatiegolfsignalen. Laten we denken aan een gitaar: wanneer men de snaren plukt, heeft het geproduceerde geluid een grondtoon, maar ook boventonen. Hetzelfde gebeurt met gravitatiegolven, waar we een grondtoon hebben, de zogenaamde “kwadrapool”, maar ook hogere harmonischen, zoals bij geluidsgolven. Gewoonlijk is de grondtoon de sterkste, en voor de meeste signalen die worden uitgezonden door binaire systemen, zijn de hogere harmonischen niet significant. Echter, wanneer het bronssysteem specifieke kenmerken heeft, bijvoorbeeld wanneer de massa's van de twee objecten in het binaire systeem zeer verschillend zijn, leveren de hogere modi een sterkere bijdrage aan het uitgezonden signaal en kunnen we ze meten.

De algemene relativiteit voorspelt precies hoe dit signaal van hogere modi zal zijn, daarom hebben we een methode ontwikkeld om te controleren of de amplitude van de twee sterkste harmonischen overeenkomt met de voorspellingen van de algemene relativiteit. In het bijzonder meten we in onze test een mogelijke afwijking van de amplitudewaarde voorspeld door de algemene relativiteit, maar we vergelijken ook een golfvormmodel van de algemene relativiteit met een model dat dergelijke afwijkingen in de amplitude van de hogere modi toestaat, waarbij we vaststellen welk model wordt ondersteund door de gegevens. We passen deze test toe op twee echte gebeurtenissen, GW190412 en GW190814, de twee waarnemingen van bronnen met het grootste verschil tussen de componentmassa's, en vinden geen bewijs van schendingen van de algemene relativiteit.

Vergelijken van golfvormmodellen

Zoals we hebben besproken, vereist het bouwen van golfvormmodellen enkele benaderingen. Het gebruik van modellen met verschillende benaderingen leidt tot verschillen in de resultaten van veel analyses, die merkbaar zullen worden en daarom een potentieel probleem vormen met detectoren van de toekomstige generatie. We hebben een studie gepresenteerd waarin we enkele van de tot nu toe gedetecteerde gebeurtenissen analyseren met vier verschillende modellen, en we proberen mogelijke voorkeuren tussen hen te identificeren. Dit zou dienen als een indicator van welk model de beste benadering gebruikt voor bepaalde soorten gebeurtenissen, of welk model de beste beschrijving van een bepaald effect bevat.

Over het algemeen vinden we geen model dat consequent wordt beoordeeld (of benadeeld) ten opzichte van de anderen. We stellen alleen een sterke voorkeur vast voor sommige modellen voor drie gebeurtenissen: hoewel de voorkeursmodellen niet hetzelfde zijn, vinden we dat ze in alle gevallen de modellen zijn die bewijs aanleveren voor een effect dat ‘precessie’ wordt genoemd “precessie” herstellen. Stel je de twee compacte objecten voor die om elkaar heen draaien alsof ze op een tafel bewegen: de tafel is wat we het “baanvlak” noemen. Als de tafel niet stil staat maar wiebelt, hebben we precessie (zie Fig. Sn.6). Dit effect laat een goed gedefinieerde afdruk achter in de uitgezonden gravitatiegolven, en de aanwezigheid ervan zou ons belangrijke informatie geven over de manier waarop het binaire

systeem is gevormd. In ons werk vinden we geen correlatie tussen de bronparameters en de voorkeur voor bepaalde modellen, maar over het algemeen leidt het feit dat een model precessie toelaat tot een hogere waarschijnlijkheid voor dat model.

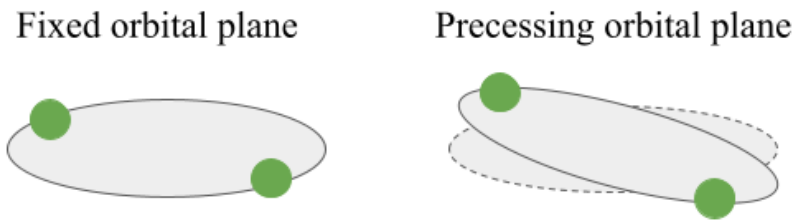


Figure Sn.6: Schematische voorstelling van het effect van precessie in het baanvlak.

Het bestuderen van neutronensterren

De materie binnen neutronensterren bereikt extreem hoge dichthesden, alsof we de massa van één miljoen spaceshuttles in een eetlepel zouden samenpersen. Materie met zulke dichthesden kan niet worden gereproduceerd in laboratoriumexperimenten, daarom is het bestuderen van de eigenschappen van neutronensterren uiterst belangrijk om te proberen begrijpen hoe deze uitzonderlijk dichte materie zich gedraagt, dat wil zeggen, de *toestandsvergelijking*. De toestandsvergelijking van de materie in neutronensterren bepaalt hun macroscopische eigenschappen, zoals hun massa en straal. Voor een bepaalde massa vertelt een toestandsvergelijking ons precies wat de straal van de neutronenster is. We weten echter nog steeds niet wat de toestandsvergelijking is van deze zeer dichte materie. Er bestaan verschillende theoretische modellen, die leiden tot verschillende voorspellingen: als we tien natuurkundigen nemen, elk met hun eigen model van de toestandsvergelijking, en hen vragen wat de straal is van een neutronenster met een massa twee keer de zonsmassa, krijgen we tien verschillende antwoorden. Gravitatiegolven bieden ons een uniek instrument om deze toestandsvergelijking te bestuderen: de eigenschappen van de neutronensterren in een binaire systeem beïnvloeden het gravitatiegolfsignaal dat wordt uitgezonden tijdens de samensmelting, dus door dit signaal te analyseren, kunnen we de parameters herstellen en beperkingen opleggen aan de toestandsvergelijking. Stel bijvoorbeeld dat we de massa met grote nauwkeurigheid meten als twee zonsmassa's en de straal tussen 10 en 11 kilometer; als we een toestandsvergelijking hebben die een straal voorspelt van 15 kilometer voor een ster met twee zonsmassa's, zouden we weten dat het model fout is.

Helaas kan de straal niet met dezelfde nauwkeurigheid worden gemeten als de massa uit gravitatiegolfsignalen, omdat het niet een van de grootheden is die rechtstreeks het uitgezonden gravitatiegolfsignaal bepalen. De andere grootheid die we uit gravitatiegolven kunnen schatten, is de *vervormbaarheidsparameter*. Terwijl zwarte gaten in wezen een plaats zijn in de ruimtetijd waar de zwaartekracht zo sterk is dat niets kan ontsnappen aan de kromming die ze produceren, speelt in het geval van neutronensterren de aanwezigheid van materie een belangrijke rol. Om het concept van getijdevervormbaarheid te begrijpen, kunnen we terugvallen op de analogie met oceaantijden. De Maan draait om de Aarde en genereert zijn eigen zwaartekrachtsveld. De zwaartekracht van de

Maan is verschillend in verschillende regio's op Aarde, afhankelijk van hun positie ten opzichte van de Maan. Het verschil tussen de zwaartekracht van de Maan op een specifieke locatie en zijn gemiddelde zwaartekracht op Aarde genereert zogenaamde *getijdenvelden*, die het lichaam van de Aarde in de ene richting uitrekken en in de andere richting samendrukken. Dit veroorzaakt de hoge en lage getijden in de oceaan, omdat het water van de aarde wordt getrokken (of er naartoe wordt geduwd). In principe heeft dit fenomeen ook invloed op het land, maar omdat het moeilijker te verplaatsen is, merken we het gewoonlijk niet. Iets soortgelijks gebeurt met neutronensterren in een binair systeem: elk van hen heeft zijn eigen zwaartekrachtveld en genereert een getijdenveld op de andere, waardoor het wordt vervormd.

Hoeveel de materie in een neutronenster wordt vervormd door deze getijdenvelden wordt beschreven door de vervormbaarheidsparameter en die hangt af van hoe de materie van de neutronenster zich gedraagt, dat wil zeggen, van zijn toestandsvergelijking, net zoals land zich anders gedraagt dan zeewater. De relatie tussen de massa en de getijdevervormbaarheid van een neutronenster wordt uniek bepaald door zijn toestandsvergelijking. Daarom kunnen we, aangezien we de massa van de neutronensterren in een binaire systeem kunnen bepalen uit het uitgezonden gravitatiegolfsignaal, als we ook een schatting kunnen krijgen van hun getijdevervormbaarheid, de toestandsvergelijking inperken. Helaas is de getijdevervormbaarheid niet gemakkelijk te bepalen, omdat het effect ervan op de uitgezonden gravitatiegolven veel zwakker is dan dat van de massa.

Studies na samensmelting

We proberen doorgaans de massa en getijdevervormbaarheid van de neutronensterren in een binair systeem te schatten aan de hand van het zwaartekrachtsgolfsignaal dat wordt uitgezonden tijdens de *inspiral* fase, dat wil zeggen wanneer de twee neutronensterren nog steeds om elkaar heen cirkelen. Dit is echter niet het einde van het verhaal. Eerder vermeldden we dat op een gegeven moment de twee neutronensterren zo dicht bij elkaar komen dat ze samensmelten, wat we een *merger* noemen. Daarna zijn verschillende scenario's mogelijk: de vorming van een zwart gat, een massieve, snel roterende overblijvende neutronenster, of, minder vaak, een stabiele neutronenster. Het lot van het binaire systeem na de merger wordt bepaald door de totale massa van de binaire systeem en, vooral, door de toestandsvergelijking.

Als er een massieve neutronenster overblijft, overleeft deze hoogstens enkele seconden voordat hij instort tot een zwart gat, maar in deze tijd zendt hij een zwaartekrachtsgolfsignaal uit dat ons veel informatie kan verschaffen over de toestandsvergelijking. Helaas is het bestuderen van dit *post-samensmeltingssignaal* niet eenvoudig: ten eerste gaat het meestal om frequenties tussen 2000 en 4000 Hertz, en onze huidige detectoren zijn niet gevoelig genoeg voor dergelijke hoge frequenties. Bovendien zijn er veel verschillende fysische processen betrokken bij deze fase, en hebben we geen volledig theoretisch model om het te beschrijven.

In dit proefschrift hebben we een golfvormmodel ontwikkeld om het zwaartekrachtsgolfsignaal te beschrijven dat wordt uitgezonden tijdens de inspiral, merger en postmerger fase van een samensmelting van binaire neutronensterren. Voor de inspiral en mergersfase gebruiken we een van de state-of-the-art modellen die doorgaans worden gebruikt om signalen te analyseren die worden uitgezonden door binaire neutronensterrensysteem. Het post-samensmeltingssignaal wordt voorspeld een zeer

complex structuur te vertonen met meerdere pieken, maar voor eenvoud hebben we slechts de piek gemodelleerd die de emissie van de fundamentele modus beschrijft. We gebruiken ons model om gesimuleerde gegevens te analyseren voor toekomstige detectoren, en we ontdekken dat het helpt om strakkere beperkingen te leggen op de vervormbaarheidspараметer en ook om de belangrijkste emissiefrequentie van het post-samensmeltingssignaal te schatten. Wanneer we echter signalen analyseren met complexere structuren, en dus meer lijken op mogelijke echte gegevens, worstelt ons eenvoudige model om het post-samensmeltingssignaal te beschrijven, en daarom moeten we het verbeteren voordat we het daadwerkelijk kunnen gebruiken om gegevens van echte gebeurtenissen te analyseren.

Huidige detectoren zijn niet gevoelig genoeg om post-samensmeltingssignalen waar te nemen, maar toekomstige detectoren worden verwacht ze te gaan detecteren. Daarom hebben we ook toekomstige detectoren vergeleken en hun prestaties beoordeeld in een studie van de toestandsvergelijking aan de hand van post-samensmeltingssignalen.

Eventuele impact van ontwerpen van de Einstein Telescoop

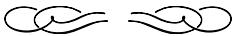
De Einstein Telescoop wordt verwacht een gevoelighed te hebben die tien keer hoger is dan die van de huidige detectoren. De technologische verbeteringen die nodig zijn om deze omstandigheden te bereiken, vereisen de bouw van een nieuwe locatie. De Einstein Telescoop samenwerking heeft verschillende ontwerp mogelijkheden voor de nieuwe detector onderzocht, waaronder de vorm die het zou moeten hebben. Momenteel zijn de belangrijkste kandidaten een driehoekige vorm of twee L-vormige detectoren, dat wil zeggen, met loodrechte armen, met dezelfde oriëntatie of niet. Voor elk ontwerp kunnen de armen van de detector ook verschillende lengtes hebben. De bouw van een detector met deze verschillende ontwerpen zal verschillende technologieën, kosten, enzovoort vereisen, maar een belangrijke vraag is of dit van invloed zal zijn op het wetenschappelijke resultaat. De invloed van het ontwerp van de detector op verschillende analyses is onderzocht. In dit proefschrift hebben we een gedetailleerde studie gepresenteerd van de impact van de verschillende ontwerpen op de schatting van de parameters van binaire neutronensterren, met name van de getijdevervormbaarheid. We hebben laten zien dat de vorm en uitlijning van de detector een kleine rol spelen, maar langere armen van de detector zullen nauwkeurigere metingen van de parameters opleveren, zoals verwacht, aangezien langere armen een hogere gevoelighed opleveren.

Bovendien zal een van de belangrijkste prestaties van de Einstein Telescoop zijn om gevoelighed te krijgen bij lage frequenties, onder de 20 Hertz, waar huidige detectoren sterk beperkt zijn. Als we de coalescentie van een binaire systemen kunnen observeren die bij lage frequenties beginnen, betekent dit dat we ze langer kunnen observeren en dus meer informatie kunnen verkrijgen. In onze studie laten we concreet zien en kwantificeren we hoe het analyseren van signalen die bij lagere frequenties beginnen, de schatting van de parameters van het binaire systeem zal verbeteren.

We horen vaak dat “gravitatiegolven een nieuw venster op het heelal hebben geopend”: inderdaad, ze bieden ons een nieuwe manier om naar het heelal te kijken (of beter gezegd, te luisteren), en voorzien ons van informatie die niet kan worden verkregen via elektromagnetische observaties—laten

Openbare samenvatting

we gewoon denken aan zwarte gaten. Via gravitatiegolven kunnen we veel verschillende verschijnselen onderzoeken, maar ook meer fundamentele kwesties, zoals het testen van de algemene relativiteitstheorie of het begrijpen van extreem dichte materie in neutronensterren. In dit proefschrift hebben we aan beide onderwerpen gewerkt, met de focus niet alleen op wat we kunnen bestuderen met huidige detectoren, maar ook op de impact van toekomstige detectoren.



Sintesi per il pubblico

Quando parliamo di gravità, probabilmente la prima cosa che ci viene in mente è una mela che cade sulla testa del povero Sir Isaac Newton. Questo fortunato incidente, secondo il mito, lo portò alla formulazione della sua teoria della gravità. La legge della gravitazione di Newton poteva descrivere bene i fenomeni osservati sulla Terra, dove di solito la gravità è abbastanza debole, ma, nel tempo, esperimenti più sofisticati portarono a osservazioni che questa teoria non riusciva a spiegare. Tutte le limitazioni nella teoria di Newton furono superate nella *relatività generale*, una teoria relativistica della gravità sviluppata da Albert Einstein un secolo più tardi, nel 1915.

La relatività generale portò alcuni importanti cambiamenti di prospettiva nella descrizione della gravità. Innanzitutto, ora parliamo di *spaziotempo*: ad ogni evento vengono assegnate delle coordinate spaziotemporali, ovvero è determinato non solo dalla posizione nello spazio tridimensionale a cui siamo abituati, ma anche da una coordinata temporale. In parole semplici, quando si organizza una festa, si decide il luogo, ma bisogna anche fissare l'orario. In secondo luogo, nella teoria di Newton, la gravità è una forza che attrae un corpo ad un altro, a seconda della loro massa. In relatività generale, invece, la gravità è legata alla geometria dello spaziotempo. Immaginiamo lo spaziotempo come un tessuto elastico: se ci mettiamo sopra una massa, il tessuto si deforma, piegandosi attorno all'oggetto massivo (vedi Fig. Si.1). Più *compatto* è l'oggetto, cioè più è massivo per una data dimensione, più forte sarà la curvatura prodotta. Ora, se appoggiamo una biglia su questo tessuto, essa si muoverà seguendo la curvatura prodotta dal primo oggetto, più massivo, e alla fine cadrà su di esso. Questa è l'idea di base della relatività generale: le masse deformano la geometria dello spaziotempo generando una curvatura, e questa geometria è quello che determina come gli oggetti massivi si muovono. Da un punto di vista matematico, ciò è elegantemente descritto dalle equazioni del campo di Einstein.

In questo contesto, le onde gravitazionali sono increspature nel tessuto dello spaziotempo, prodotte dalle masse quando accelerano. Consideriamo la situazione in cui abbiamo un oggetto compatto, che produce la sua curvatura nello spaziotempo, e poi all'improvviso lo rimuoviamo: senza l'oggetto compatto, la curvatura sparirà, però questo processo non è istantaneo. Analogamente, quando un oggetto massivo si muove, le deformazioni dello spaziotempo che produce si muovono con esso. Lo spaziotempo che si adatta alla curvatura che cambia, come conseguenza di una massa che accelera, è ciò che produce queste onde sullo spaziotempo, che si propagano con la velocità della luce. Per visualizzarlo, un'analogia utile è immaginare le increspature sulla superficie di uno stagno prodotte

quando si getta un sasso nell'acqua.

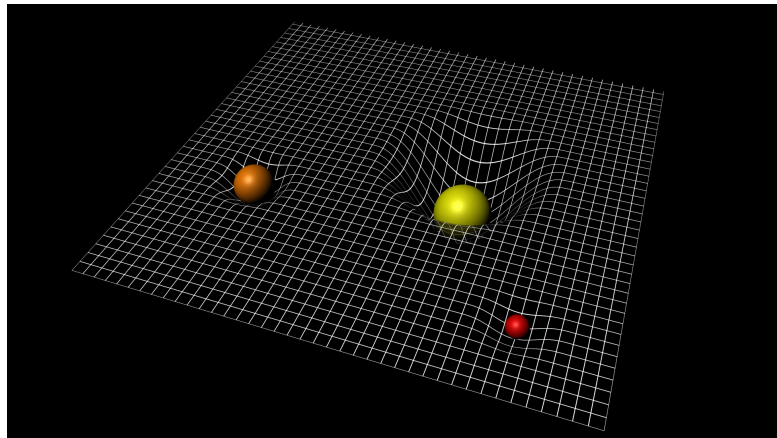


Figure Si.1: Rappresentazione artistica della curvatura nello spaziotempo da oggetti con compattezze diverse, dove quello giallo è il più compatto. *Credit:ESA-C.Carreau*

Come si rilevano le onde gravitazionali?

Le onde gravitazionali, quando passano, allungano e comprimono lo spaziotempo periodicamente, e questo ci fornisce l'opportunità di rilevarle. Gli attuali rivelatori di onde gravitazionali, come LIGO, Virgo e KAGRA, sono interferometri laser: sostanzialmente, sono composti da due raggi laser, emessi a un punto di entrata, i quali viaggiano lungo quelli che vengono chiamati “bracci” dell’interferometro, di solito in direzioni perpendicolari, per qualche kilometro; alla fine di ciascun braccio è posizionato uno specchio, quindi ogni raggio laser viene riflesso indietro e i due raggi si ricombinano all’uscita. La luce ha una natura ondulatoria, quindi ogni raggio laser include una serie di minimi e massimi (vedi pannello a sinistra della Fig. Si.2). Quando i due raggi si ricombinano, si creano effetti d’interferenza: se, per esempio, un raggio è a un massimo e l’altro a un minimo, i due raggi si “cancellano” e l’ampiezza dell’onda risultante è zero; questo effetto viene chiamato interferenza distruttiva (vedi Fig. Si.2). L’idea degli interferometri laser è che lo strumento a riposo, cioè quando non passano onde gravitazionali, è impostato in modo tale da avere un’uscita specifica, per esempio un’interferenza distruttiva. Quando arriva un’onda gravitazionale, un braccio viene allungato e l’altro compresso, cambiando di conseguenza la lunghezza del percorso che i due raggi devono compiere. Pertanto, quando si ricombinano, non si avrà più un’interferenza distruttiva, ma l’uscita cambierà nel tempo a seconda dell’effetto del passaggio dell’onda gravitazionale.

Fin qui tutto bene, ma c’è un problema: il cambiamento nella lunghezza dei bracci indotta dalle onde gravitazionali è estremamente piccolo, dell’ordine di 0.00000000000000000001 metri o meno. Per fare un confronto, il diametro di un cappello umano è tipicamente 0.000001 metri. L’interferometria laser ci permette di misurare cambiamenti nella lunghezza dei bracci molto piccoli, ma ci sono varie fonti di rumore che rendono difficile questa misura. Inoltre, il tessuto dello spaziotempo è molto rigido e non si deforma facilmente, quindi soltanto eventi catastrofici, che coinvolgono velocità estremamente elevate e masse molto grandi, generano onde gravitazionali di cui possiamo rilevare l’effetto. Tra questi eventi catastrofici, in questa tesi ci concentriamo sulla coalescenza di sistemi binari di oggetti

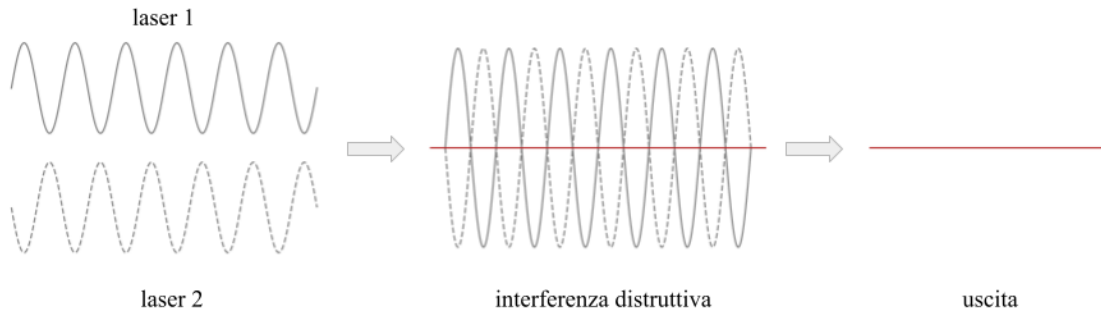


Figure Si.2: Rappresentazione schematica dell’interferenza distruttiva tra due raggi laser. I due laser, *laser 1* e *laser 2*, sono composti da una serie di minimi e massimi nella loro ampiezza (*sinistra*). Quando si ricombinano all’uscita dell’interferometro, si può impostare il rivelatore in modo tale che, a riposo, i minimi di un raggio laser corrispondano perfettamente con i massimi dell’altro (*centro*), e di conseguenza l’onda risultante all’uscita, mostrata in rosso, sia zero (*destra*).

compatti, come stelle di neutroni o buchi neri, descritti brevemente di seguito.

Sorgenti di onde gravitazionali

Le stelle, come il nostro Sole, sono essenzialmente nubi d’idrogeno, talmente compresso nel nucleo della stella da bruciare, creando elio tramite delle reazioni nucleari. Questo processo di combustione dell’idrogeno rilascia un’enorme quantità di energia, che è ciò che fa brillare la stella, ma fornisce anche una fonte di energia essenziale per contrastare la pressione della gravità, dovuta alla massa della stella stessa, che la farebbe collassare su sé stessa. Alla fine, tutto l’idrogeno nella stella sarà stato trasformato in elio: a questo punto il processo di fusione nucleare si ferma, dato che manca del suo ingrediente fondamentale, e non c’è più alcuna pressione verso l’esterno che contrasti quella gravitazionale, pertanto la stella inizia a collassare. Tuttavia, questo comporta la compressione e agglomerazione degli atomi di elio, con un conseguente aumento della temperatura che può diventare talmente elevata che anche l’elio inizia a bruciare, producendo elementi più pesanti. Questa nuova reazione nucleare fornisce ulteriore energia per prevenire il collasso gravitazionale della stella.

L’evoluzione stellare è un processo in cui vengono prodotti elementi sempre più pesanti e l’energia rilasciata da queste reazioni nucleari bilancia la pressione della gravità, prevenendo il collasso della stella (vedi Fig. Si.3). Tuttavia, a un certo punto la stella esaurisce il combustibile: per le stelle più massive, questo succede quando l’elemento prodotto nel nucleo è il ferro. A causa della sua struttura nucleare, il ferro necessita di energia aggiuntiva per bruciare in altri elementi, perciò le reazioni nucleari che avevano fornito energia interna alla stella si fermano, e la stella inizia a collassare su sé stessa.

A seconda della massa del suo nucleo, la stella può avere destini diversi. Per i nuclei più massivi, il prodotto finale è un *buco nero*. I buchi neri sono oggetti eccezionalmente compatti, che deformano lo spazio tempo talmente tanto che qualsiasi cosa, persino la luce, che arriva troppo vicino a loro—cioè, che supera quello che viene chiamato “orizzonte degli eventi” del buco nero—non può sfuggire alla curvatura generata dal buco nero ed è costretta a cadervi dentro. Qualcosa di diverso succede per nuclei meno massivi, con una massa minore di approssimativamente tre volte la massa del Sole: quando il

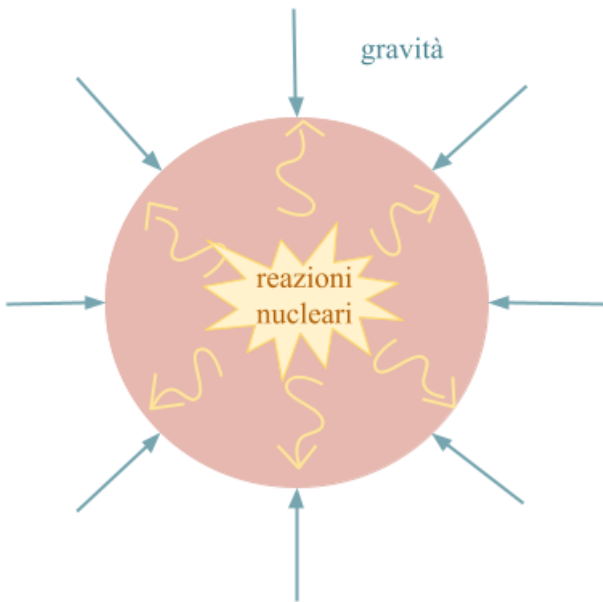


Figure Si.3: Rappresentazione dell'equilibrio in una stella tra la pressione verso l'interno della gravità e la pressione verso l'esterno prodotta dall'energia rilasciata nelle reazioni nucleari.

nucleo della stella inizia a collassare, i protoni e gli elettroni dei suoi atomi vengono schiacciati insieme e formano neutroni. Le interazioni tra neutroni forniscono la pressione che ferma il collasso ed infine supportano il prodotto finale, una *stella di neutroni*.

Una *binaria compatta* è un sistema di oggetti compatti, come due stelle di neutroni, due buchi neri, o una stella di neutroni e un buco nero, che orbitano uno attorno all'altro. Mentre orbitano, il sistema emette energia attraverso onde gravitazionali; tuttavia, questo implica che il sistema perde energia, e di conseguenza l'orbita si restringe, con i due oggetti che si muovono sempre più vicini. Orbite più piccole, d'altra parte, significano velocità orbitali più elevate, e velocità più elevate risultano in più energia emessa sotto forma di onde gravitazionali. Pertanto, il sistema perde ancora più energia, l'orbita diventa ancora più piccola e veloce, più energia viene emessa attraverso onde gravitazionali e così via, finché i due oggetti si avvicinano talmente tanto che alla fine si fondono. Durante tutto questo processo di coalescenza viene emesso un segnale di onde gravitazionali le cui caratteristiche dipendono dalle proprietà del sistema.

Cosa possiamo studiare?

Analizzando segnali di onde gravitazionali possiamo estrarre informazioni riguardo ai parametri del sistema binario che li ha emessi. Per esempio, possiamo stimare quale era la massa dei due oggetti, o a che distanza dalla Terra si trovava la sorgente. Ciò è particolarmente utile per capire le proprietà delle popolazioni di sistemi binari di buchi neri o stelle di neutroni, per rispondere a domande come “Quanti di questi sistemi ci aspettiamo che ci siano nell’Universo?”, oppure “Che massa hanno tipicamente?”. Possiamo anche studiare come i sistemi binari vengono formati, dato che diversi meccanismi

di formazione risultano in specifiche differenze in alcuni dei parametri.

Tuttavia, con le onde gravitazionali possiamo anche compiere un passo ulteriore ed indagare aspetti più generali e fondamentali della fisica. Ci permettono di studiare come si comporta la materia estremamente densa all'interno delle stelle di neutroni, come vedremo in maggior dettaglio di seguito. Inoltre, le onde gravitazionali ci offrono uno strumento estremamente utile per testare la teoria della relatività generale. Possiamo ideare vari metodi per testare specifiche caratteristiche nei segnali di onde gravitazionali e verificare se sono in accordo con le previsioni della relatività generale.

Cosa abbiamo osservato finora

La prima rivelazione di un segnale di onde gravitazionali avvenne il 14 settembre 2015: i due interferometri LIGO negli Stati Uniti misurarono un segnale prodotto dalla coalescenza di due buchi neri. In seguito, il numero di rivelazioni continuò ad aumentare e il 17 agosto 2017 venne rilevato, per la prima volta, un segnale prodotto da un sistema binario di stelle di neutroni, GW170817.

Gli eventi di onde gravitazionali vengono chiamati in base al momento in cui sono stati osservati: “GW”, per “onda gravitazionale” (in inglese “gravitational wave”), seguito da due cifre per l'anno, due per il mese e due per il giorno.

Fino ad oggi, abbiamo osservato 90 eventi in totale e al momento i rivelatori stanno nuovamente acquisendo dati. Con l'aumentare del numero di rivelazioni, abbiamo anche iniziato a osservare eventi al di fuori della cosiddetta popolazione “vanilla”, cioè eventi con caratteristiche meno comuni o inaspettate, come masse dei componenti del sistema binario molto pesanti o molto diverse tra loro. Tutti gli eventi osservati finora sono stati generati dalla coalescenza di un sistema binario compatto, ma alcuni di loro hanno già iniziato a mettere alla prova la nostra attuale comprensione della teoria alla base di questi processi, per esempio riguardo a come vengono formate le binarie di buchi neri. Tuttavia, finora non è stata trovata alcuna evidenza di violazioni della relatività generale.

Come analizziamo i dati?

Come menzionato, il segnale di onde gravitazionali emesso da un sistema binario in coalescenza dipende dalle proprietà degli oggetti compatti nella binaria, come le loro masse. Pertanto, possiamo studiare questi oggetti stimando i parametri che descrivono le loro caratteristiche dalle onde gravitazionali emesse. Per realizzare ciò, ci servono tre ingredienti principali: i dati di onde gravitazionali misurati, un modello per descriverli e un'idea dell'intervallo in cui si trovano i parametri, chiamato *prior*.

I modelli di forme d'onda gravitazionali descrivono come ci aspettiamo che sia il segnale emesso durante il processo di coalescenza, fino alla fusione e possibilmente anche dopo. Un esempio di forma d'onda gravitazionale fornito da uno di questi modelli è mostrato in Fig. Si.4. Solitamente, i modelli di forma d'onda prendono in entrata i parametri della sorgente e forniscono il segnale di onda gravitazionale emesso (vedi Fig. Si.5).

Per stimare le proprietà della sorgente per un dato evento, l'idea di base è che scegliamo dei valori per i parametri nell'intervallo del prior, usiamo il nostro modello di forma d'onda per generare il segnale di onda gravitazionale che sarebbe emesso da una sorgente con quei parametri e lo confrontiamo con i dati misurati. Ripetiamo il processo per molteplici valori nell'intervallo del prior e alla fine troviamo

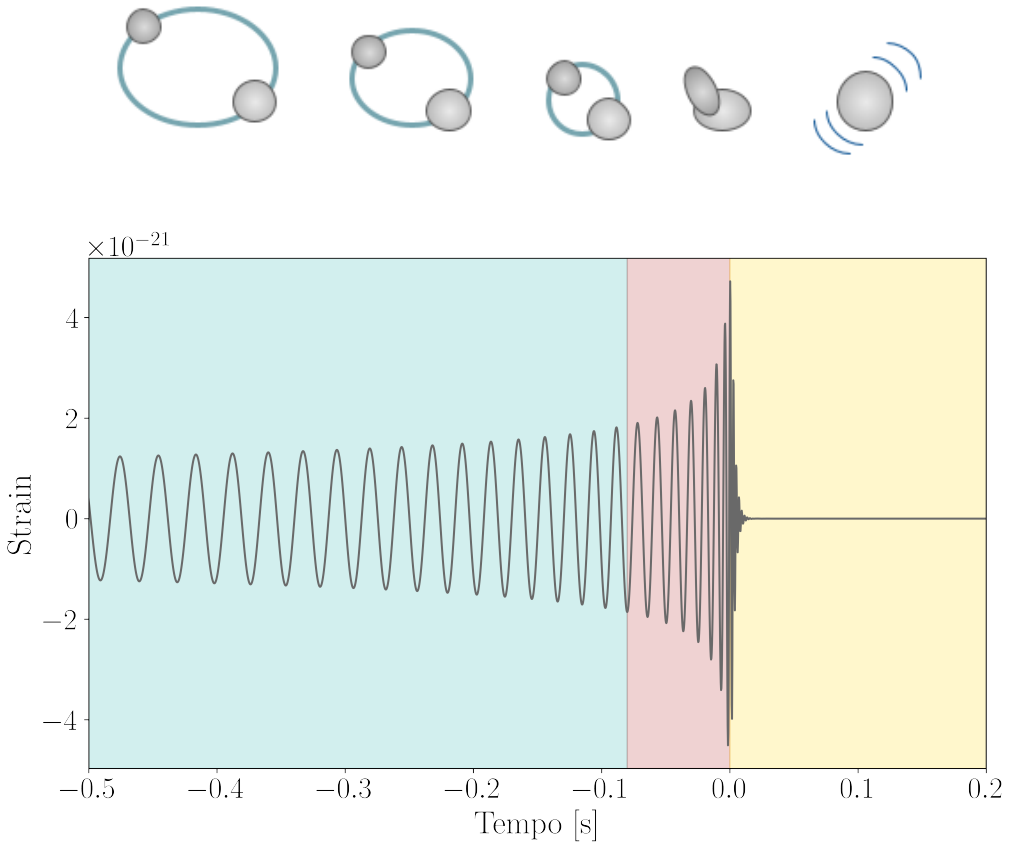


Figure Si.4: Esempio di segnale di onda gravitazionale nel tempo (chiamato *strain* dalla deformazione che produce), emesso dalla coalescenza di una binaria di buchi neri. L'area verde corrisponde alla fase di inspiral, quando i due buchi neri stanno ancora orbitando l'uno attorno all'altro. Quella rossa, invece, corrisponde alla fase in cui i due oggetti si tuffano l'uno nell'altro e si fondono. Infine, l'area gialla mostra il segnale emesso dal *remnant*, cioè l'oggetto formato dopo la fusione.

quali parametri producono la forma d'onda gravitazionale che descrive meglio i nostri dati.

I modelli di forma d'onda rappresentano un ingrediente fondamentale nell'analisi dati delle onde gravitazionali. Creare questi modelli, tuttavia, non è un compito facile: in teoria, per ottenere l'esatta forma del segnale di onda gravitazionale, si dovrebbero risolvere le equazioni del campo di Einstein. Dato che non si possono risolvere analiticamente, però, bisogna ricorrere a delle approssimazioni. Tuttavia, diverse approssimazioni possono essere impiegate per costruire modelli di forma d'onda, e quindi esistono diversi modelli che possono portare a diversi risultati nelle analisi.

Rivelatori futuri

Attualmente, esistono quattro interferometri per le onde gravitazionali, due negli Stati Uniti, uno in Italia e uno in Giappone, e un quinto è in costruzione in India. Esiste un altro rilevatore in Germania, GEO600, che però viene principalmente utilizzato per sviluppare e testare nuove tecnologie. Abbiamo visto che misurare le onde gravitazionali non è un compito semplice, visto quanto è piccolo il segnale. Esistono metodi specifici per affrontare le varie sorgenti di rumore e c'è uno sforzo costante per

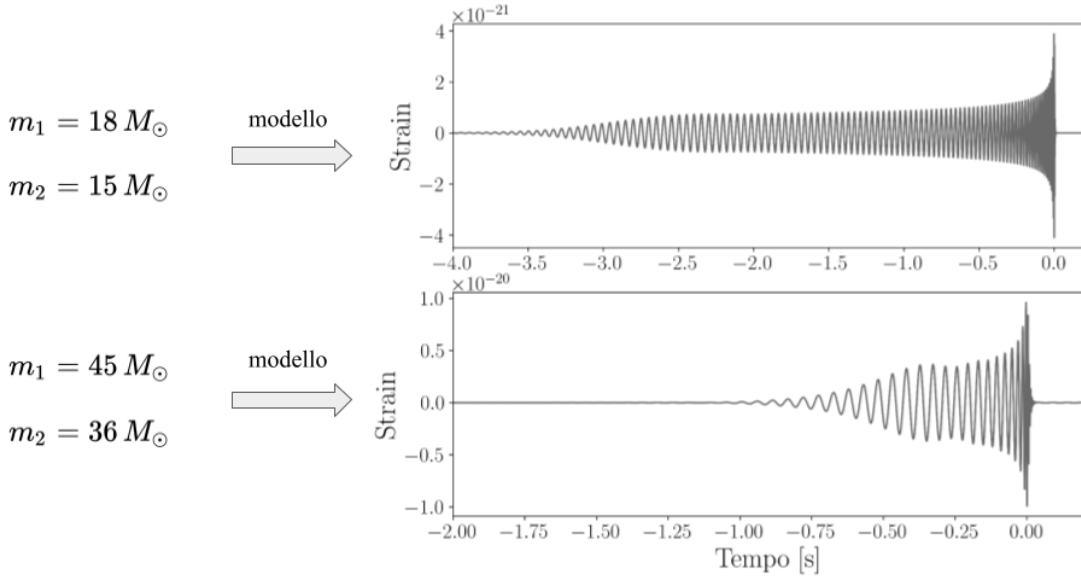


Figure Si.5: Esempio di segnali di onde gravitazionali prodotti dallo stesso modello di forma d'onda per diversi valori delle masse dei due oggetti compatti nella binaria. Per semplicità, le masse sono tipicamente misurate in termini della massa del Sole, M_\odot .

migliorare la sensibilità dei rivelatori, cioè per renderli capaci di misurare segnali sempre più piccoli. Al momento, ciò viene realizzato implementando cambiamenti sui rivelatori esistenti. Tuttavia, per ottenere sensibilità ancora maggiori, alcuni miglioramenti tecnologici pianificati per il futuro richiederanno la costruzione di nuovi interferometri, che di conseguenza vengono chiamati rivelatori di “futura generazione” o di “terza generazione”. Ad ora, il piano per rivelatori di terza generazione include Einstein Telescope in Europa e Cosmic Explorer negli Stati Uniti.

Si prevede che i rivelatori di terza generazione, con la loro aumentata sensibilità, misureranno molti più eventi, in un intervallo di frequenze più esteso. Questo, naturalmente, ci offrirà un’opportunità senza precedenti di studiare i sistemi binari compatti, e verosimilmente anche altre sorgenti di onde gravitazionali, ma avrà anche degli svantaggi: misureremo così tanti segnali che alcuni di essi si sovrapporranno, rendendo quindi difficile analizzare i dati per una specifica sorgente; i segnali saranno molto forti, di conseguenza inizieremo a vedere l’effetto di errori sistematici indotti dai nostri metodi di analisi; infine, visto sia il loro numero che la forza, le rivelazioni richiederanno un’enorme quantità di risorse computazionali per essere analizzate.

Testare la relatività generale

Come menzionato, con le onde gravitazionali possiamo verificare la teoria della relatività generale. Esistono diversi test con questa finalità, che esaminano vari aspetti delle onde gravitazionali, ma finora nessuno di essi ha evidenziato violazioni della relatività generale. In questa tesi, abbiamo proposto un nuovo test che esamina le armoniche di ordine superiore nei segnali di onde gravitazionali. Pensiamo a una chitarra: quando pizzichiamo le sue corde, il suono prodotto ha un’armonica fondamentale, ma

anche toni superiori. La stessa cosa accade con le onde gravitazionali, dove abbiamo una frequenza fondamentale, chiamata quadrupolare, ma anche armoniche superiori, come nelle onde sonore. Solitamente, la radiazione fondamentale è la più forte, e per la maggior parte dei segnali emessi da sistemi binari le armoniche superiori non sono significative. Tuttavia, quando il sistema sorgente ha caratteristiche specifiche, per esempio quando le masse dei due oggetti nella binaria sono molto diverse tra loro, le armoniche superiori forniscono un contributo maggiore al segnale emesso e possiamo misurarle.

La relatività generale predice esattamente come sarà il segnale emesso da queste armoniche superiori, perciò abbiamo sviluppato un metodo per verificare se l'ampiezza delle due armoniche più forti è coerente con le predizioni della relatività generale. In particolare, nel nostro test misuriamo possibili deviazioni dal valore di ampiezza previsto dalla relatività generale, ma compariamo anche un modello di forma d'onda che segue la relatività generale con un modello che invece permette queste deviazioni nell'ampiezza delle armoniche superiori, trovando qual è quello preferito dai dati. Abbiamo applicato questo test a due eventi reali, GW190412 e GW190814, le due osservazioni da sorgenti con la maggiore differenza tra le masse dei componenti, e non abbiamo trovato evidenza di violazioni della relatività generale.

Confrontare modelli di forme d'onda

Abbiamo visto che costruire modelli di forme d'onda richiede delle approssimazioni. Utilizzare modelli con diverse approssimazioni genera, nei risultati di varie analisi, differenze che diventeranno apprezzabili, e quindi un potenziale problema, con i rivelatori di futura generazione. Abbiamo presentato uno studio in cui analizziamo alcuni degli eventi rivelati finora con quattro diversi modelli, e proviamo a identificare possibili preferenze tra di essi. Questo servirebbe come indicatore di quale modello impiega l'approssimazione migliore per certi tipi di eventi, o quale include la migliore descrizione di un determinato effetto.

Nel complesso, non troviamo un modello costantemente favorito (o sfavorito) rispetto agli altri. Abbiamo trovato una forte preferenza per alcuni modelli solamente per tre eventi: nonostante i modelli preferiti non siano gli stessi, abbiamo constatato che, in tutti i casi, sono quelli che trovano evidenza di un effetto chiamato *precessione*. Immaginiamo i due oggetti compatti che orbitano l'uno attorno all'altro come se si muovessero su un tavolo: il tavolo è quello che chiamiamo “piano orbitale”. Precessione significa che il tavolo non è fermo ma oscilla (vedi Fig. Si.6). Questo effetto lascia un'impronta ben definita nelle onde gravitazionali emesse e la sua presenza ci fornirebbe importanti informazioni riguardo al modo in cui il sistema binario si è formato. Nel nostro lavoro, non abbiamo trovato una correlazione tra i parametri della sorgente e la preferenza per alcuni modelli, però, in generale, il fatto che un modello trovi precessione risulta in una probabilità maggiore per quel modello.

Studiare le stelle di neutroni

La materia all'interno delle stelle di neutroni raggiunge densità estremamente elevate, come se stessimo comprimendo la massa di un milione di space shuttles in un cucchiaio. La materia con queste alte densità non può essere riprodotta negli esperimenti di laboratorio, perciò studiare le proprietà delle stelle di neutroni è estremamente importante per provare a capire come questa materia eccezionalmente

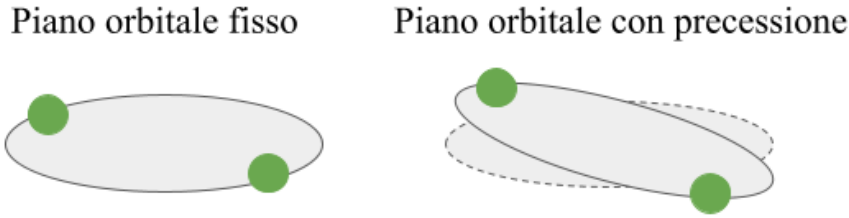


Figure Si.6: Rappresentazione schematica dell'effetto di precessione del piano orbitale.

densa si comporta, cioè la sua *equazione di stato*. L'equazione di stato della materia delle stelle di neutroni determina le loro proprietà macroscopiche, come la massa e il raggio. Per un determinato valore di massa, un'equazione di stato ci dirà esattamente qual è il raggio della stella di neutroni. Tuttavia, ancora non sappiamo quale sia l'equazione di stato di questa materia così densa. Esistono vari modelli teorici, che portano a previsioni differenti: se prendiamo dieci fisici, ognuno con il proprio modello di equazione di stato, e chiediamo loro quale sia il raggio di una stella di neutroni con una massa due volte la massa del Sole, otterremo dieci risposte diverse. Le onde gravitazionali ci offrono uno strumento unico per studiare quest'equazione di stato: le proprietà delle stelle di neutroni in un sistema binario influenzano il segnale di onda gravitazionale emesso durante la coalescenza, pertanto, analizzando questo segnale, possiamo recuperare i loro parametri e porre vincoli sull'equazione di stato. Ad esempio, supponiamo di misurare che la massa sia circa due volte la massa del Sole e il raggio tra 10 e 11 kilometri; se abbiamo un'equazione di stato che prevede un raggio di 15 kilometri per una stella di due masse solari, sapremo che quel modello è sbagliato.

Sfortunatamente, mentre la massa può essere misurata dai segnali di onde gravitazionali con grande precisione, lo stesso non vale per il raggio, dato che non è una delle quantità che determinano direttamente il segnale emesso. L'altra quantità che possiamo stimare dalle onde gravitazionali è il parametro di *deformazione mareale* (*tidal deformability* in inglese). Mentre i buchi neri sono sostanzialmente un luogo nello spaziotempo in cui la gravità è così forte che nulla può sfuggire alla curvatura che producono, nel caso delle stelle di neutroni la presenza di materia gioca un ruolo importante. Per capire il concetto di deformazione mareale, ricorriamo all'analogia con le maree degli oceani. La Luna orbita attorno alla Terra e genera un proprio campo gravitazionale. L'attrazione gravitazionale della Luna è diversa in diverse regioni sulla Terra, a seconda della loro posizione rispetto alla Luna. La differenza tra l'attrazione gravitazionale della Luna in un luogo specifico e la sua attrazione gravitazionale media sulla Terra genera delle cosiddette forze mareali, che allungano il corpo terrestre in una direzione e lo comprimono nell'altra. Questo è ciò che causa le alte e basse maree degli oceani, perché l'acqua viene allontanata dalla (o spinta verso la) Terra. In teoria, questo fenomeno riguarda anche la terraferma, ma, dato che è più difficile da muovere, semplicemente non ce ne accorgiamo. Una cosa simile succede con le stelle di neutroni in un sistema binario: ognuna di loro ha il proprio campo gravitazionale e genera un campo di marea sull'altra, deformandola.

Quanto la materia in una stella di neutroni viene deformata da queste forze mareali è descritto dal parametro di deformazione mareale, e dipende da come si comporta la materia della stella di neutroni,

cioè dalla sua equazione di stato, proprio come la terraferma si comporta diversamente dall’acqua del mare. La relazione tra la massa e il parametro di deformazione mareale di una stella di neutroni è determinata unicamente dalla sua equazione di stato. Di conseguenza, dato che possiamo determinare la massa delle stelle di neutroni in una binaria dal segnale di onda gravitazionale emesso, se riusciamo a ottenere anche una stima della loro deformazione mareale possiamo porre dei vincoli sull’equazione di stato. Purtroppo, la deformazione mareale non è facile da determinare, poiché il suo effetto sulle onde gravitazionali emesse è molto più debole di quello della massa.

Studi sul postmerger

Solitamente cerchiamo di stimare la massa e la deformazione mareale delle stelle di neutroni in un sistema binario dal segnale di onde gravitazionali emesso durante la fase di *inspiral*, cioè quando le due stelle di neutroni stanno ancora orbitando l’una attorno all’altra. Tuttavia, la storia non finisce qui. Abbiamo menzionato prima che a un certo punto le due stelle di neutroni arrivano così vicine che si fondono, in quello che chiamiamo *merger* (o *fusione*). Dopo di ciò, diversi scenari sono possibili: la formazione di un buco nero, di una stella di neutroni massiva e ad alta rotazione, oppure, meno comunemente, di una stella di neutroni stabile. Il destino di una binaria dopo il merger è determinato dalla massa totale della binaria e, soprattutto, dall’equazione di stato.

Se dopo la fusione viene prodotta una stella di neutroni massiva, questa sopravvive al massimo pochi secondi prima di collassare in un buco nero, ma durante questo tempo emette un segnale di onde gravitazionali che ci può fornire moltissime informazioni sull’equazione di stato. Sfortunatamente, studiare questo segnale di postmerger non è facile: innanzitutto, solitamente avviene a frequenze tra 2000 e 4000 Hertz, e i nostri attuali rivelatori non sono abbastanza sensibili a queste alte frequenze. Inoltre, molti processi fisici diversi sono coinvolti in questa fase e non abbiamo un modello teorico completo per descriverla.

In questa tesi, abbiamo sviluppato un modello di forma d’onda per descrivere il segnale di onda gravitazionale emesso durante le fasi di inspiral, merger e postmerger della coalescenza di un sistema binario di stelle di neutroni. Per l’inspiral e il merger, utilizziamo uno dei modelli all’avanguardia comunemente usato per analizzare segnali emessi da binarie di stelle di neutroni. Riguardo alla fase di postmerger, invece, si prevede che il suo segnale mostri una struttura molto complessa con molteplici picchi, ma, per semplicità, modelliamo solo il picco che descrive l’emissione del modo fondamentale. Abbiamo utilizzato il nostro modello per analizzare dati simulati per i rivelatori futuri e abbiamo constatato che aiuta a porre limiti più stringenti sul parametro di deformazione mareale rispetto ad un modello senza postmerger e anche a stimare la frequenza di emissione principale del postmerger. Ciononostante, quando si analizzano segnali con strutture più complesse, e quindi più simili a possibili dati reali, il nostro semplice modello fatica a recuperare il segnale di postmerger e perciò dobbiamo migliorarlo prima di poterlo effettivamente usare nell’analisi di dati da eventi reali.

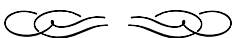
I rivelatori attuali non sono abbastanza sensibili per osservare segnali di postmerger, però ci aspettiamo che quelli futuri inizino a rivelarli. Pertanto, abbiamo anche confrontato vari rivelatori futuri, per determinare la loro prestazione nello studio dell’equazione di stato da segnali di postmerger.

Possibile impatto del design di Einstein Telescope

Si prevede che Einstein Telescope avrà una sensibilità dieci volte superiore a quella dei rivelatori attuali. I miglioramenti tecnologici necessari per raggiungere queste condizioni richiedono la costruzione di un nuovo sito. La collaborazione di Einstein Telescope sta studiando diverse opzioni per il design del nuovo rivelatore, tra cui la forma che dovrebbe avere. Al momento, i principali candidati sono una forma triangolare oppure due detector a forma di L, cioè con due bracci perpendicolari, con lo stesso orientamento oppure no. Per ogni forma, i bracci del rivelatore possono anche avere lunghezze diverse. La costruzione di un rivelatore con questi diversi design richiederà tecnologie diverse, costi diversi e così via, ma una domanda importante è se avrà un impatto sul risultato scientifico. L'influenza del design del rivelatore è stata studiata per diverse analisi. In questa tesi, abbiamo presentato uno studio dettagliato dell'impatto dei diversi design sulla stima dei parametri di una binaria di stelle di neutroni, in particolare della deformazione mareale. Abbiamo mostrato che la forma e l'orientamento del rivelatore ricoprono poca importanza, ma bracci del rivelatore più lunghi ci faranno ottenere misure dei parametri più precise, come previsto dato che bracci più lunghi implicano una maggiore sensibilità.

In aggiunta, una delle principali conquiste di Einstein Telescope sarà di guadagnare sensibilità a basse frequenze, sotto i 20 Hertz, dove i detector attuali sono fortemente limitati. Se possiamo osservare la coalescenza di un sistema binario partendo da basse frequenze, significa che possiamo osservarla per più tempo e quindi ottenere più informazioni. Nel nostro studio, abbiamo mostrato concretamente e quantificato come analizzare i segnali partendo da frequenze più basse migliorerà la stima dei parametri della binaria.

Spesso sentiamo dire che “le onde gravitazionali hanno aperto una nuova finestra sull’Universo”: infatti, ci offrono un nuovo modo di guardare (o meglio, di ascoltare) l’Universo, fornendoci informazioni che non possono essere ottenute da osservazioni elettromagnetiche—basti pensare, per esempio, ai buchi neri. Attraverso le onde gravitazionali possiamo studiare molti fenomeni diversi, ma anche aspetti più fondamentali, come verificare la teoria della relatività generale o capire come si comporta la materia estremamente densa dentro le stelle di neutroni. In questa tesi, abbiamo lavorato su entrambi questi argomenti, concentrandoci non solo su quello che possiamo studiare con i rivelatori attuali, ma anche sull’impatto di quelli futuri.



Curriculum vitae

Personal information

Name: Anna Puecher
Nationality: Italian
Date of birth: 28 November 1994
Email: a.puecher@uu.nl, a.puecher@nikhef.nl, annie.puecher@gmail.com

Education

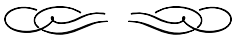
2019-2023: Ph.D in Physics
Nikhef and GRASP, Utrecht University; Prof. dr. C. Van Den Broeck
2016-2019: M.Sc. in Experimental Physics
University of Trento; Prof. G. A. Prodi
2013-2016: B.Sc. in Physics
University of Trento; Prof. W. J. Weber

Publications

- A. Puecher, A. Samajdar, G. Ashton, C. Van Den Broeck, and T. Dietrich. “Comparing gravitational waveform models for binary black hole mergers through a hypermodels approach”. (October 2023). arXiv: 2310.03555 [gr-qc]
- F. Iacovelli, M. Mancarella, C. Mondal, A. Puecher, T. Dietrich, F. Gulminelli, M. Maggiore, and M. Oertel. “Nuclear physics constraints from binary neutron star mergers in the

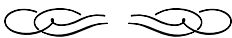
Einstein Telescope era”. *Phys.Rev.D* 108 (2023) 12, 122006. arXiv: 2308.12378 [gr-qc]. DOI:10.1103/PhysRevD.108.122006

- R. W. Kiendrebeogo, A. M. Farah, E. M. Foley, A. Gray, N. Kunert, A. Puecher, *et al.*. “Updated observing scenarios and multi-messenger implications for the International Gravitational-wave Network’s O4 and O5”. *Astrophys.J.* 958 (2023) 2, 158. arXiv: 2306.09234 [astro-ph.HE]. DOI:10.3847/1538-4357/acfc1
- M. C. Tringali, A. Puecher, C. Lazzaro, R. Ciolfi, M. Drago, B. Giacomazzo, G. Vedovato, and G. A. Prodi. “Morphology-independent characterization method of postmerger gravitational wave emission from binary neutron star coalescences”. *Class.Quant.Grav.* 40 (2023) 22, 225008. arXiv: 2304.12831 [gr-qc]. DOI:10.1088/1361-6382/acfc0d
- A. Puecher, A. Samajdar, and T. Dietrich. “Measuring tidal effects with the Einstein Telescope: A design study”. *Phys.Rev.D* 108 (2023) 2, 023018. arXiv: 2304.05349 [astro-ph.IM]. DOI: 10.1103/PhysRevD.108.023018
- M. Branchesi, M. Maggiore, *et al.*. “Science with the Einstein Telescope: a comparison of different designs”. *JCAP* 07 (2023) 068. arXiv: 2303.15923 [gr-qc]. DOI: 10.1088/1475-7516/2023/07/068
- A. Puecher, T. Dietrich, K. W. Tsang, C. Kalaghatgi, S. Roy, Y. Setyawati, and C. Van Den Broeck. “Unraveling information about supranuclear-dense matter from the complete binary neutron star coalescence process using future gravitational-wave detector networks”. *Phys.Rev.D* 107 (2023) 12, 124009. arXiv: 2210.09259 [gr-qc]. DOI: 10.1103/PhysRevD.107.124009
- A. Puecher, C. Kalaghatgi, S. Roy, Y. Setyawati, I. Gupta, B. S. Sathyaprakash, and C. Van Den Broeck. “Testing general relativity using higher-order modes of gravitational waves from binary black holes”. *Phys.Rev.D* 106 (2022) 8, 082003. arXiv: 2205.09062 [gr-qc]. DOI: 10.1103/PhysRevD.106.082003
- P. K. Gupta, A. Puecher, P. T. H. Pang, J. Janquart, G. Koekoek, and C. Van Den Broeck. “Determining the equation of state of neutron stars with Einstein Telescope using tidal effects and r-mode excitations from a population of binary inspirals”. (May 2022). arXiv: 2205.01182 [gr-qc]



Acronyms

2G :	second generation	ISCO :	innermost stable circular orbit
3G :	third generation	KL :	Kullback-Leibler
ASD :	amplitude spectral density	JS :	Jensen-Shannon
BBH :	binary black hole	LAL :	LIGO Algorithms Library
BH :	black hole	LIF :	local inertial frame
BNS :	binary neutron star	LVK :	LIGO-Virgo-KAGRA
CBC :	compact binary coalescence	MCMC :	Markov chain Monte Carlo
CE :	Cosmic Explorer	ML :	maximum likelihood
EFEs :	Einstein field equations	NS :	neutron star
EHT :	Event Horizon Telescope	NR :	numerical relativity
EOB :	effective-one-body	PE :	parameter estimation
EOS :	equation of state	PN :	post-Newtonian
ET :	Einstein Telescope	PSD :	power spectral density
FAR :	false alarm rate	ROQ :	reduced order quadrature
GR :	general relativity	SNR :	signal-to-noise ratio
GW :	gravitational wave	SPA :	stationary phase approximation
GWTC :	Gravitational-Wave Transient Catalog	TOV :	Tolman-Volkov-Oppenheimer
IMBH :	intermediate mass black hole	TT :	transverse-traceless
IMR :	inspiral-merger-ringdown		



Acknowledgments

Time flies, and also for me the time has come to write the word “end” to this amazing chapter of my life. Navigating these four years of Ph.D. has not always been easy, with the usual challenges and also a pandemic getting in the way. However, it has been a wonderful experience, which allowed me to grow on so many levels, and it would not have been the same without the people who accompanied me during this journey.

First of all, I need to thank Chris, who gave me this opportunity in the first place. Thanks for guiding me, allowing me to work on different things, and always offering your advice when I needed it. I am really grateful that I had you as a supervisor, thanks for believing in me.

Anuradha, when I started you taught me basically everything. I am so grateful for your patience, your guidance, and all our chats. I really hope we will keep working together.

Tim, you are not only a great teammate for table soccer, but I also really enjoyed working with you. Thank you for involving me in different projects, and above all for all your help and support.

I definitely need to thank my “Italian PhDs” friends, Sofia, Stefano, and Martino. Our weekly dinners helped me cope with the dark and gray Dutch (prolonged) winters. Thanks, Daniela and Viola, I hope your social dinners will always have plenty of bread. To my DUWO-barbeque friends, Christos, Enzo, Haris, Otto, and Shi: thanks for all the fun times we had together.

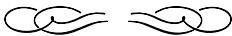
Thanks to all my friends in Italy, especially Silvia, who was always there to listen to my complaints. Thanks, Alessio, also known as Pizz, who somehow managed to prepare a Trento dinner in Amsterdam.

It would not have been the same journey without all my fellow Ph.D. candidates, so thank you Harsh, Justin, Melissa, Pawan, Quirijn, and Thibeau. Peter, it’s been a pleasure “sharing” the office with you. Tomek, I would likely not have survived last year TA-ing without you and your muffins, so thank you, you are really a good friend. Thank you also to all the people in our group, Chinmay, Ka Wa, Soumen, Xisco, Yoshinta, Archisman, Bhooshan, Khun Sang, Marc, Sarah, Sumedha, and all the people I met at Nikhef and Utrecht in these years.

I need to thank my family, who always supported me and made me feel at home every time I came back: my parents, who still wonder what I am actually doing, but support me no matter what; my sister, although she keeps trying to hug me; my brother, who unfortunately I don’t see often, but luckily leaves near the airport; and my grandparents, who always bring a sparkle of joy in my days.

Finally, I have to thank my husband, Andrea, who has seen me at my best and my worst, and has always been by my side anyway: I couldn’t be more grateful I got to share my forever with you.

Bibliography



Bibliography

- [1] Albert Abraham Michelson and Edward Williams Morley. On the Relative Motion of the Earth and the Luminiferous Ether. *Am. J. Sci.*, 34:333–345, 1887.
- [2] A. Einstein. Die grundlage der allgemeinen relativitätstheorie. *Annalen der Physik*, 354(7):769–822, 1916.
- [3] Kazunori Akiyama et al. First M87 Event Horizon Telescope Results. V. Physical Origin of the Asymmetric Ring. *Astrophys. J. Lett.*, 875(1):L5, 2019.
- [4] Kazunori Akiyama et al. First M87 Event Horizon Telescope Results. I. The Shadow of the Supermassive Black Hole. *Astrophys. J. Lett.*, 875:L1, 2019.
- [5] Kazunori Akiyama et al. First M87 Event Horizon Telescope Results. II. Array and Instrumentation. *Astrophys. J. Lett.*, 875(1):L2, 2019.
- [6] Kazunori Akiyama et al. First M87 Event Horizon Telescope Results. III. Data Processing and Calibration. *Astrophys. J. Lett.*, 875(1):L3, 2019.
- [7] Kazunori Akiyama et al. First M87 Event Horizon Telescope Results. IV. Imaging the Central Supermassive Black Hole. *Astrophys. J. Lett.*, 875(1):L4, 2019.
- [8] Kazunori Akiyama et al. First M87 Event Horizon Telescope Results. VI. The Shadow and Mass of the Central Black Hole. *Astrophys. J. Lett.*, 875(1):L6, 2019.
- [9] Joel M. Weisberg and Joseph H. Taylor. Relativistic binary pulsar B1913+16: Thirty years of observations and analysis. *ASP Conf. Ser.*, 328:25, 2005.
- [10] B. P. Abbott et al. Observation of Gravitational Waves from a Binary Black Hole Merger. *Phys. Rev. Lett.*, 116(6):061102, 2016.
- [11] B. P. Abbott et al. GW170817: Observation of Gravitational Waves from a Binary Neutron Star Inspiral. *Phys. Rev. Lett.*, 119(16):161101, 2017.
- [12] B. P. Abbott et al. Gravitational Waves and Gamma-rays from a Binary Neutron Star Merger: GW170817 and GRB 170817A. *Astrophys. J. Lett.*, 848(2):L13, 2017.

Bibliography

- [13] B. P. Abbott et al. Multi-messenger Observations of a Binary Neutron Star Merger. *Astrophys. J. Lett.*, 848(2):L12, 2017.
- [14] R. Abbott et al. GWTC-3: Compact Binary Coalescences Observed by LIGO and Virgo During the Second Part of the Third Observing Run. 11 2021. arXiv:2111.03606 [gr-qc].
- [15] R. Abbott et al. Observation of Gravitational Waves from Two Neutron Star–Black Hole Coalescences. *Astrophys. J. Lett.*, 915(1):L5, 2021.
- [16] R. Abbott et al. GW190412: Observation of a Binary-Black-Hole Coalescence with Asymmetric Masses. *Phys. Rev. D*, 102(4):043015, 2020.
- [17] R. Abbott et al. GW190521: A Binary Black Hole Merger with a Total Mass of $150M_{\odot}$. *Phys. Rev. Lett.*, 125(10):101102, 2020.
- [18] B. P. Abbott et al. GW190425: Observation of a Compact Binary Coalescence with Total Mass $\sim 3.4M_{\odot}$. *Astrophys. J. Lett.*, 892(1):L3, 2020.
- [19] R. Abbott et al. GW190814: Gravitational Waves from the Coalescence of a 23 Solar Mass Black Hole with a 2.6 Solar Mass Compact Object. *Astrophys. J. Lett.*, 896(2):L44, 2020.
- [20] R. Abbott et al. Tests of General Relativity with GWTC-3. 12 2021. arXiv:2112.06861 [gr-qc].
- [21] R. Abbott et al. Tests of general relativity with binary black holes from the second LIGO-Virgo gravitational-wave transient catalog. *Phys. Rev. D*, 103(12):122002, 2021.
- [22] B. P. Abbott et al. Tests of General Relativity with the Binary Black Hole Signals from the LIGO-Virgo Catalog GWTC-1. *Phys. Rev. D*, 100(10):104036, 2019.
- [23] Gabriella Agazie et al. The NANOGrav 15 yr Data Set: Evidence for a Gravitational-wave Background. *Astrophys. J. Lett.*, 951(1):L8, 2023.
- [24] C. J. Moore, R. H. Cole, and C. P. L. Berry. Gravitational-wave sensitivity curves. *Class. Quant. Grav.*, 32(1):015014, 2015.
- [25] R. V. Pound and G. A. Rebka. Apparent weight of photons. *Phys. Rev. Lett.*, 4:337–341, Apr 1960.
- [26] Wei-Tou Ni and Mark Zimmermann. Inertial and gravitational effects in the proper reference frame of an accelerated, rotating observer. *Phys. Rev. D*, 17:1473–1476, Mar 1978.
- [27] Luc Blanchet, Guillaume Faye, Bala R. Iyer, and Siddhartha Sinha. The Third post-Newtonian gravitational wave polarisations and associated spherical harmonic modes for inspiralling compact binaries in quasi-circular orbits. *Class. Quant. Grav.*, 25:165003, 2008. [Erratum: Class.Quant.Grav. 29, 239501 (2012)].
- [28] K. S. Thorne. Multipole Expansions of Gravitational Radiation. *Rev. Mod. Phys.*, 52:299–339, 1980.

- [29] Luc Blanchet, Bala R. Iyer, Clifford M. Will, and Alan G. Wiseman. Gravitational wave forms from inspiralling compact binaries to second postNewtonian order. *Class. Quant. Grav.*, 13:575–584, 1996.
- [30] Lawrence E. Kidder. Using full information when computing modes of post-Newtonian waveforms from inspiralling compact binaries in circular orbit. *Phys. Rev. D*, 77:044016, 2008.
- [31] K. G. Arun, Luc Blanchet, Bala R. Iyer, and Moh'd S. S. Qusailah. The 2.5PN gravitational wave polarisations from inspiralling compact binaries in circular orbits. *Class. Quant. Grav.*, 21:3771–3802, 2004. [Erratum: Class.Quant.Grav. 22, 3115 (2005)].
- [32] Chris Van Den Broeck and Anand S. Sengupta. Phenomenology of amplitude-corrected post-Newtonian gravitational waveforms for compact binary inspiral. I. Signal-to-noise ratios. *Class. Quant. Grav.*, 24:155–176, 2007.
- [33] Chris Van Den Broeck and Anand S. Sengupta. Binary black hole spectroscopy. *Class. Quant. Grav.*, 24:1089–1114, 2007.
- [34] Cameron Mills and Stephen Fairhurst. Measuring gravitational-wave higher-order multipoles. *Phys. Rev. D*, 103(2):024042, 2021.
- [35] Samantha A. Usman, Joseph C. Mills, and Stephen Fairhurst. Constraining the Inclinations of Binary Mergers from Gravitational-wave Observations. *Astrophys. J.*, 877(2):82, 2019.
- [36] B. P. Abbott et al. GWTC-1: A Gravitational-Wave Transient Catalog of Compact Binary Mergers Observed by LIGO and Virgo during the First and Second Observing Runs. *Phys. Rev. X*, 9(3):031040, 2019.
- [37] R. Abbott et al. GWTC-2: Compact Binary Coalescences Observed by LIGO and Virgo During the First Half of the Third Observing Run. *Phys. Rev. X*, 11:021053, 2021.
- [38] R. Abbott et al. GWTC-2.1: Deep Extended Catalog of Compact Binary Coalescences Observed by LIGO and Virgo During the First Half of the Third Observing Run. 8 2021. arXiv:2108.01045 [gr-qc].
- [39] R. Abbott et al. Population Properties of Compact Objects from the Second LIGO-Virgo Gravitational-Wave Transient Catalog. *Astrophys. J. Lett.*, 913(1):L7, 2021.
- [40] R. Abbott et al. Population of Merging Compact Binaries Inferred Using Gravitational Waves through GWTC-3. *Phys. Rev. X*, 13(1):011048, 2023.
- [41] R. Abbott et al. Properties and Astrophysical Implications of the $150 M_{\odot}$ Binary Black Hole Merger GW190521. *Astrophys. J. Lett.*, 900(1):L13, 2020.
- [42] S. E. Woosley, A. Heger, and T. A. Weaver. The evolution and explosion of massive stars. *Rev. Mod. Phys.*, 74:1015–1071, 2002.

Bibliography

- [43] S. E. Woosley and Alexander Heger. The Pair-Instability Mass Gap for Black Holes. *Astrophys. J. Lett.*, 912(2):L31, 2021.
- [44] Michela Mapelli. Formation Channels of Single and Binary Stellar-Mass Black Holes. In *Handbook of Gravitational Wave Astronomy*. 2021.
- [45] Krzysztof Belczynski, Daniel E. Holz, Tomasz Bulik, and Richard O’Shaughnessy. The first gravitational-wave source from the isolated evolution of two 40-100 Msun stars. *Nature*, 534:512, 2016.
- [46] Hans A. Bethe and G. E. Brown. Evolution of binary compact objects which merge. *Astrophys. J.*, 506:780–789, 1998.
- [47] Krzysztof Belczynski, Vassiliki Kalogera, and Tomasz Bulik. A Comprehensive study of binary compact objects as gravitational wave sources: Evolutionary channels, rates, and physical properties. *Astrophys. J.*, 572:407–431, 2001.
- [48] Michal Dominik, Emanuele Berti, Richard O’Shaughnessy, Ilya Mandel, Krzysztof Belczynski, Christopher Fryer, Daniel E. Holz, Tomasz Bulik, and Francesco Pannarale. Double Compact Objects III: Gravitational Wave Detection Rates. *Astrophys. J.*, 806(2):263, 2015.
- [49] Ilya Mandel and Selma E. de Mink. Merging binary black holes formed through chemically homogeneous evolution in short-period stellar binaries. *Mon. Not. Roy. Astron. Soc.*, 458(3):2634–2647, 2016.
- [50] S. E. de Mink and I. Mandel. The chemically homogeneous evolutionary channel for binary black hole mergers: rates and properties of gravitational-wave events detectable by advanced LIGO. *Mon. Not. Roy. Astron. Soc.*, 460(4):3545–3553, 2016.
- [51] Pablo Marchant, Norbert Langer, Philipp Podsiadlowski, Thomas M. Tauris, and Takashi J. Moriya. A new route towards merging massive black holes. *Astron. Astrophys.*, 588:A50, 2016.
- [52] Piero Madau and Martin J. Rees. Massive black holes as Population III remnants. *Astrophys. J. Lett.*, 551:L27–L30, 2001.
- [53] Kohei Inayoshi, Ryosuke Hirai, Tomoya Kinugawa, and Kenta Hotokezaka. Formation pathway of Population III coalescing binary black holes through stable mass transfer. *Mon. Not. Roy. Astron. Soc.*, 468(4):5020–5032, 2017.
- [54] Shrinivas F. Kulkarni, Steve McMillan, and Piet Hut. Stellar black holes in globular clusters. *Nature*, 364:421, 1993.
- [55] Brunetto Marco Ziosi, Michela Mapelli, Marica Branchesi, and Giuseppe Tormen. Dynamics of stellar black holes in young star clusters with different metallicities – II. Black hole–black hole binaries. *Mon. Not. Roy. Astron. Soc.*, 441(4):3703–3717, 2014.

- [56] Carl L. Rodriguez, Meagan Morscher, Bharath PattaBiraman, Sourav Chatterjee, Carl-Johan Haster, and Frederic A. Rasio. Binary Black Hole Mergers from Globular Clusters: Implications for Advanced LIGO. *Phys. Rev. Lett.*, 115(5):051101, 2015. [Erratum: Phys.Rev.Lett. 116, 029901 (2016)].
- [57] Fabio Antonini, Silvia Toonen, and Adrian S. Hamers. Binary black hole mergers from field triples: properties, rates and the impact of stellar evolution. *Astrophys. J.*, 841(2):77, 2017.
- [58] Simon F. Portegies Zwart and Steve L. W. McMillan. The Runaway growth of intermediate-mass black holes in dense star clusters. *Astrophys. J.*, 576:899–907, 2002.
- [59] B. McKernan, K. E. S. Ford, W. Lyra, and H. B. Perets. Intermediate mass black holes in AGN discs - I. Production and growth. *Mon. Not. Roy. Astron. Soc.*, 425(1):460–469, September 2012.
- [60] Giacomo Fragione, Nathan Leigh, and Rosalba Perna. Black hole and neutron star mergers in Galactic Nuclei: the role of triples. *Mon. Not. Roy. Astron. Soc.*, 488(2):2825–2835, 2019.
- [61] Imre Bartos, Bence Kocsis, Zolt Haiman, and Szabolcs Márka. Rapid and Bright Stellar-mass Binary Black Hole Mergers in Active Galactic Nuclei. *Astrophys. J.*, 835(2):165, 2017.
- [62] Nicholas C. Stone, Brian D. Metzger, and Zoltán Haiman. Assisted inspirals of stellar mass black holes embedded in AGN discs: solving the ‘final au problem’. *Mon. Not. Roy. Astron. Soc.*, 464(1):946–954, 2017.
- [63] Carl L. Rodriguez, Michael Zevin, Chris Pankow, Vasiliki Kalogera, and Frederic A. Rasio. Illuminating Black Hole Binary Formation Channels with Spins in Advanced LIGO. *Astrophys. J. Lett.*, 832(1):L2, 2016.
- [64] Theocharis A. Apostolatos, Curt Cutler, Gerald J. Sussman, and Kip S. Thorne. Spin induced orbital precession and its modulation of the gravitational wave forms from merging binaries. *Phys. Rev. D*, 49:6274–6297, 1994.
- [65] Lawrence E. Kidder. Coalescing binary systems of compact objects to postNewtonian 5/2 order. 5. Spin effects. *Phys. Rev. D*, 52:821–847, 1995.
- [66] Patricia Schmidt, Frank Ohme, and Mark Hannam. Towards models of gravitational waveforms from generic binaries II: Modelling precession effects with a single effective precession parameter. *Phys. Rev. D*, 91(2):024043, 2015.
- [67] L. Santamaria et al. Matching post-Newtonian and numerical relativity waveforms: systematic errors and a new phenomenological model for non-precessing black hole binaries. *Phys. Rev. D*, 82:064016, 2010.
- [68] P. Ajith et al. Inspiral-merger-ringdown waveforms for black-hole binaries with non-precessing spins. *Phys. Rev. Lett.*, 106:241101, 2011.

Bibliography

- [69] Mark Hannam, Patricia Schmidt, Alejandro Bohé, Leila Haegel, Sascha Husa, Frank Ohme, Geraint Pratten, and Michael Pürrer. Simple Model of Complete Precessing Black-Hole-Binary Gravitational Waveforms. *Phys. Rev. Lett.*, 113(15):151101, 2014.
- [70] Werner Israel. Event horizons in static vacuum space-times. *Phys. Rev.*, 164:1776–1779, 1967.
- [71] B. Carter. Axisymmetric Black Hole Has Only Two Degrees of Freedom. *Phys. Rev. Lett.*, 26:331–333, 1971.
- [72] B. P. Abbott et al. GW170817: Observation of Gravitational Waves from a Binary Neutron Star Inspiral. *Phys. Rev. Lett.*, 119(16):161101, 2017.
- [73] B. P. Abbott et al. Properties of the binary neutron star merger GW170817. *Phys. Rev. X*, 9(1):011001, 2019.
- [74] B. P. Abbott et al. GW170817: Measurements of neutron star radii and equation of state. *Phys. Rev. Lett.*, 121(16):161101, 2018.
- [75] J. R. Oppenheimer and G. M. Volkoff. On massive neutron cores. *Phys. Rev.*, 55:374–381, 1939.
- [76] Richard C. Tolman. Static solutions of Einstein’s field equations for spheres of fluid. *Phys. Rev.*, 55:364–373, 1939.
- [77] LIGO Scientific Collaboration. LIGO Algorithm Library - LALSuite. free software (GPL), 2018. 10.7935/GT1W-FZ16.
- [78] John Antoniadis et al. A Massive Pulsar in a Compact Relativistic Binary. *Science*, 340:6131, 2013.
- [79] Zaven Arzoumanian et al. The NANOGrav 11-year Data Set: High-precision timing of 45 Millisecond Pulsars. *Astrophys. J. Suppl.*, 235(2):37, 2018.
- [80] A. Bauswein and N. Stergioulas. Unified picture of the post-merger dynamics and gravitational wave emission in neutron star mergers. *Phys. Rev.*, D91(12):124056, 2015.
- [81] James Alexander Clark, Andreas Bauswein, Nikolaos Stergioulas, and Deirdre Shoemaker. Observing Gravitational Waves From The Post-Merger Phase Of Binary Neutron Star Coalescence. *Class. Quant. Grav.*, 33(8):085003, 2016.
- [82] Luciano Rezzolla and Kentaro Takami. Gravitational-wave signal from binary neutron stars: a systematic analysis of the spectral properties. *Phys. Rev.*, D93(12):124051, 2016.
- [83] Kent Yagi and Nicolas Yunes. I-Love-Q Relations in Neutron Stars and their Applications to Astrophysics, Gravitational Waves and Fundamental Physics. *Phys. Rev. D*, 88(2):023009, 2013.
- [84] Kent Yagi, Koutarou Kyutoku, George Pappas, Nicolás Yunes, and Theocharis A. Apostolatos. Effective No-Hair Relations for Neutron Stars and Quark Stars: Relativistic Results. *Phys. Rev. D*, 89(12):124013, 2014.

- [85] Brynmor Haskell, Riccardo Ciolfi, Francesco Pannarale, and Luciano Rezzolla. On the universality of I-Love-Q relations in magnetized neutron stars. *Mon. Not. Roy. Astron. Soc.*, 438(1):L71–L75, 2014.
- [86] Sayan Chakrabarti, Térence Delsate, Norman Gürlebeck, and Jan Steinhoff. I-Q relation for rapidly rotating neutron stars. *Phys. Rev. Lett.*, 112:201102, 2014.
- [87] Andrea Maselli, Vitor Cardoso, Valeria Ferrari, Leonardo Gualtieri, and Paolo Pani. Equation-of-state-independent relations in neutron stars. *Phys. Rev. D*, 88(2):023007, 2013.
- [88] Borja Reina, Nicolas Sanchis-Gual, Raül Vera, and José A. Font. Completion of the universal I-Love-Q relations in compact stars including the mass. *Mon. Not. Roy. Astron. Soc.*, 470(1):L54–L58, 2017.
- [89] Cosima Breu and Luciano Rezzolla. Maximum mass, moment of inertia and compactness of relativistic stars. *Mon. Not. Roy. Astron. Soc.*, 459(1):646–656, 2016.
- [90] Cecilia Chirenti, Gibran H. de Souza, and Wolfgang Kastaun. Fundamental oscillation modes of neutron stars: validity of universal relations. *Phys. Rev. D*, 91(4):044034, 2015.
- [91] Katerina Chatzioannou, Carl-Johan Haster, and Aaron Zimmerman. Measuring the neutron star tidal deformability with equation-of-state-independent relations and gravitational waves. *Phys. Rev. D*, 97(10):104036, 2018.
- [92] Bharat Kumar and Philippe Landry. Inferring neutron star properties from GW170817 with universal relations. *Phys. Rev. D*, 99(12):123026, 2019.
- [93] Anuradha Samajdar and Tim Dietrich. Constructing Love-Q-Relations with Gravitational Wave Detections. *Phys. Rev. D*, 101(12):124014, 2020.
- [94] Luciano Rezzolla, Elias R. Most, and Lukas R. Weih. Using gravitational-wave observations and quasi-universal relations to constrain the maximum mass of neutron stars. *Astrophys. J. Lett.*, 852(2):L25, 2018.
- [95] A. Bauswein and H. Th. Janka. Measuring neutron-star properties via gravitational waves from binary mergers. *Phys. Rev. Lett.*, 108:011101, 2012.
- [96] Sukanta Bose, Kabir Chakravarti, Luciano Rezzolla, B. S. Sathyaprakash, and Kentaro Takami. Neutron-star Radius from a Population of Binary Neutron Star Mergers. *Phys. Rev. Lett.*, 120(3):031102, 2018.
- [97] J. Clark, A. Bauswein, L. Cadonati, H. T. Janka, C. Pankow, and N. Stergioulas. Prospects For High Frequency Burst Searches Following Binary Neutron Star Coalescence With Advanced Gravitational Wave Detectors. *Phys. Rev.*, D90(6):062004, 2014.
- [98] Kentaro Takami, Luciano Rezzolla, and Luca Baiotti. Constraining the Equation of State of Neutron Stars from Binary Mergers. *Phys. Rev. Lett.*, 113(9):091104, 2014.

Bibliography

- [99] Sebastiano Bernuzzi, Tim Dietrich, and Alessandro Nagar. Modeling the complete gravitational wave spectrum of neutron star mergers. *Phys. Rev. Lett.*, 115(9):091101, 2015.
- [100] A. Bauswein, H. T. Janka, K. Hebeler, and A. Schwenk. Equation-of-state dependence of the gravitational-wave signal from the ring-down phase of neutron-star mergers. *Phys. Rev.*, D86:063001, 2012.
- [101] Kenta Hotokezaka, Kenta Kiuchi, Koutarou Kyutoku, Takayuki Muranushi, Yu-ichiro Sekiguchi, Masaru Shibata, and Keisuke Taniguchi. Remnant massive neutron stars of binary neutron star mergers: Evolution process and gravitational waveform. *Phys. Rev.*, D88:044026, 2013.
- [102] A. Bauswein, N. Stergioulas, and H. T. Janka. Revealing the high-density equation of state through binary neutron star mergers. *Phys. Rev.*, D90(2):023002, 2014.
- [103] Kentaro Takami, Luciano Rezzolla, and Luca Baiotti. Spectral properties of the post-merger gravitational-wave signal from binary neutron stars. *Phys. Rev.*, D91(6):064001, 2015.
- [104] Katerina Chatzioannou, James Alexander Clark, Andreas Bauswein, Margaret Millhouse, Tyson B. Littenberg, and Neil Cornish. Inferring the post-merger gravitational wave emission from binary neutron star coalescences. *Phys. Rev.*, D96(12):124035, 2017.
- [105] Georgios Lioutas, Andreas Bauswein, and Nikolaos Stergioulas. Frequency deviations in universal relations of isolated neutron stars and postmerger remnants. *Phys. Rev. D*, 104(4):043011, 2021.
- [106] Michele Maggiore. *Gravitational Waves. Vol. 1: Theory and Experiments*. Oxford University Press, 2007.
- [107] Andreas Freise and Kenneth Strain. Interferometer Techniques for Gravitational-Wave Detection. *Living Rev. Rel.*, 13:1, 2010.
- [108] Peter R. Saulson. Terrestrial gravitational noise on a gravitational wave antenna. *Phys. Rev. D*, 30:732–736, 1984.
- [109] Scott A. Hughes and Kip S. Thorne. Seismic gravity gradient noise in interferometric gravitational wave detectors. *Phys. Rev. D*, 58:122002, 1998.
- [110] Aaron Buikema et al. Sensitivity and performance of the Advanced LIGO detectors in the third observing run. *Phys. Rev. D*, 102(6):062003, 2020.
- [111] J. Aasi et al. Advanced LIGO. *Class. Quant. Grav.*, 32:074001, 2015.
- [112] F. Acernese et al. Advanced Virgo: a second-generation interferometric gravitational wave detector. *Class. Quant. Grav.*, 32(2):024001, 2015.
- [113] Tyson B. Littenberg and Neil J. Cornish. Bayesian inference for spectral estimation of gravitational wave detector noise. *Phys. Rev. D*, 91(8):084034, 2015.
- [114] Derek Davis et al. LIGO detector characterization in the second and third observing runs. *Class. Quant. Grav.*, 38(13):135014, 2021.

- [115] F. Acernese et al. Virgo detector characterization and data quality: tools. *Class. Quant. Grav.*, 40(18):185005, 2023.
- [116] F. Acernese et al. Virgo detector characterization and data quality: results from the O3 run. *Class. Quant. Grav.*, 40(18):185006, 2023.
- [117] T. Akutsu et al. Overview of KAGRA: Calibration, detector characterization, physical environmental monitors, and the geophysics interferometer. *PTEP*, 2021(5):05A102, 2021.
- [118] D. Davis, T. B. Littenberg, I. M. Romero-Shaw, M. Millhouse, J. McIver, F. Di Renzo, and G. Ashton. Subtracting glitches from gravitational-wave detector data during the third LIGO-Virgo observing run. *Class. Quant. Grav.*, 39(24):245013, 2022.
- [119] Samantha A. Usman et al. The PyCBC search for gravitational waves from compact binary coalescence. *Class. Quant. Grav.*, 33(21):215004, 2016.
- [120] F. Aubin et al. The MBTA pipeline for detecting compact binary coalescences in the third LIGO–Virgo observing run. *Class. Quant. Grav.*, 38(9):095004, 2021.
- [121] Kipp Cannon et al. GstLAL: A software framework for gravitational wave discovery. *SoftwareX*, 14:100680, June 2021.
- [122] S. Klimenko, G. Vedovato, M. Drago, F. Salemi, V. Tiwari, G. A. Prodi, C. Lazzaro, K. Ackley, S. Tiwari, C. F. Da Silva, and G. Mitselmakher. Method for detection and reconstruction of gravitational wave transients with networks of advanced detectors. *Phys. Rev. D*, 93:042004, Feb 2016.
- [123] Sergey Klimenko, Gabriele Vedovato, Valentin Necula, Francesco Salemi, Marco Drago, Rhys Poulton, Eric Chassande-Mottin, Vaibhav Tiwari, Claudia Lazzaro, Brendan O’Brian, Marek Szczepanczyk, Shubhanshu Tiwari, and V. Gayathri. cwb pipeline library: 6.4.5, October 2023. Zenodo. <https://doi.org/10.5281/zenodo.10022289>.
- [124] B. P. Abbott et al. Prospects for observing and localizing gravitational-wave transients with Advanced LIGO, Advanced Virgo and KAGRA. *Living Rev. Rel.*, 21(1):3, 2018.
- [125] T. Akutsu et al. Overview of KAGRA: Detector design and construction history. *PTEP*, 2021(5):05A101, 2021.
- [126] Kentaro Somiya. Detector configuration of KAGRA: The Japanese cryogenic gravitational-wave detector. *Class. Quant. Grav.*, 29:124007, 2012.
- [127] Yoichi Aso, Yuta Michimura, Kentaro Somiya, Masaki Ando, Osamu Miyakawa, Takanori Sekiguchi, Daisuke Tatsumi, and Hiroaki Yamamoto. Interferometer design of the KAGRA gravitational wave detector. *Phys. Rev. D*, 88(4):043007, 2013.
- [128] M. Saleem et al. The science case for LIGO-India. *Class. Quant. Grav.*, 39(2):025004, 2022.

Bibliography

- [129] Vicky Kalogera et al. The Next Generation Global Gravitational Wave Observatory: The Science Book. 11 2021. arXiv:2111.06990 [gr-qc].
- [130] M. Punturo et al. The Einstein Telescope: A third-generation gravitational wave observatory. *Class. Quant. Grav.*, 27:194002, 2010.
- [131] Michele Maggiore et al. Science Case for the Einstein Telescope. *JCAP*, 03:050, 2020.
- [132] A. Freise, S. Chelkowski, S. Hild, W. Del Pozzo, A. Perreca, and A. Vecchio. Triple Michelson Interferometer for a Third-Generation Gravitational Wave Detector. *Class. Quant. Grav.*, 26:085012, 2009.
- [133] Stefan Hild, Simon Chelkowski, Andreas Freise, Janyce Franc, Nazario Morgado, Raffaele Flaminio, and Riccardo DeSalvo. A Xylophone Configuration for a third Generation Gravitational Wave Detector. *Class. Quant. Grav.*, 27:015003, 2010.
- [134] S. Hild et al. Sensitivity Studies for Third-Generation Gravitational Wave Observatories. *Class. Quant. Grav.*, 28:094013, 2011.
- [135] B. Sathyaprakash et al. Scientific Potential of Einstein Telescope. In *46th Rencontres de Moriond on Gravitational Waves and Experimental Gravity*, pages 127–136, 8 2011.
- [136] Benjamin P Abbott et al. Exploring the Sensitivity of Next Generation Gravitational Wave Detectors. *Class. Quant. Grav.*, 34(4):044001, 2017.
- [137] David Reitze et al. Cosmic Explorer: The U.S. Contribution to Gravitational-Wave Astronomy beyond LIGO. *Bull. Am. Astron. Soc.*, 51(7):035, 2019.
- [138] Matthew Evans et al. A Horizon Study for Cosmic Explorer: Science, Observatories, and Community. 9 2021. arXiv:2109.09882 [astro-ph.IM].
- [139] Varun Srivastava, Derek Davis, Kevin Kuns, Philippe Landry, Stefan Ballmer, Matthew Evans, Evan D. Hall, Jocelyn Read, and B. S. Sathyaprakash. Science-driven Tunable Design of Cosmic Explorer Detectors. *Astrophys. J.*, 931(1):22, 2022.
- [140] Marica Branchesi et al. Science with the Einstein Telescope: a comparison of different designs. *JCAP*, 07:068, 2023.
- [141] K. Ackley et al. Neutron Star Extreme Matter Observatory: A kilohertz-band gravitational-wave detector in the global network. *Publ. Astron. Soc. Austral.*, 37:e047, 2020.
- [142] Frans Pretorius. Evolution of binary black hole spacetimes. *Phys. Rev. Lett.*, 95:121101, 2005.
- [143] Manuela Campanelli, C. O. Lousto, P. Marronetti, and Y. Zlochower. Accurate evolutions of orbiting black-hole binaries without excision. *Phys. Rev. Lett.*, 96:111101, 2006.
- [144] John G. Baker, Joan Centrella, Dae-II Choi, Michael Koppitz, and James van Meter. Gravitational wave extraction from an inspiraling configuration of merging black holes. *Phys. Rev. Lett.*, 96:111102, 2006.

- [145] Vitor Cardoso, Leonardo Gualtieri, Carlos Herdeiro, and Ulrich Sperhake. Exploring New Physics Frontiers Through Numerical Relativity. *Living Rev. Relativity*, 18:1, 2015.
- [146] Marcus Thierfelder, Sebastiano Bernuzzi, and Bernd Bruegmann. Numerical relativity simulations of binary neutron stars. *Phys. Rev. D*, 84:044012, 2011.
- [147] Bernd Bruegmann, Wolfgang Tichy, and Nina Jansen. Numerical simulation of orbiting black holes. *Phys. Rev. Lett.*, 92:211101, 2004.
- [148] Bernd Bruegmann, Jose A. Gonzalez, Mark Hannam, Sascha Husa, Ulrich Sperhake, and Wolfgang Tichy. Calibration of Moving Puncture Simulations. *Phys. Rev. D*, 77:024027, 2008.
- [149] Bernd Bruegmann. Binary black hole mergers in 3-d numerical relativity. *Int. J. Mod. Phys. D*, 8:85, 1999.
- [150] David Radice and Luciano Rezzolla. THC: a new high-order finite-difference high-resolution shock-capturing code for special-relativistic hydrodynamics. *Astron. Astrophys.*, 547:A26, 2012.
- [151] Y. Zlochower, J. G. Baker, Manuela Campanelli, and C. O. Lousto. Accurate black hole evolutions by fourth-order numerical relativity. *Phys. Rev. D*, 72:024021, 2005.
- [152] <https://www.black-holes.org/code/SpEC.html>.
- [153] Luca Baiotti, Ian Hawke, Pedro J. Montero, Frank Löffler, Luciano Rezzolla, Nikolaos Stergioulas, Jose A. Font, and Ed Seidel. Three-dimensional relativistic simulations of rotating neutron star collapse to a Kerr black hole. *Phys. Rev. D*, 71:024035, 2005.
- [154] Tetsuro Yamamoto, Masaru Shibata, and Keisuke Taniguchi. Simulating coalescing compact binaries by a new code SACRA. *Phys. Rev. D*, 78:064054, 2008.
- [155] Jose A. Font. Numerical Hydrodynamics and Magnetohydrodynamics in General Relativity. *Living Rev. Rel.*, 11:7, 2008.
- [156] Michael Boyle et al. The SXS Collaboration catalog of binary black hole simulations. *Class. Quant. Grav.*, 36(19):195006, 2019.
- [157] Kenta Kiuchi, Kyohei Kawaguchi, Koutarou Kyutoku, Yuichiro Sekiguchi, and Masaru Shibata. Sub-radian-accuracy gravitational waves from coalescing binary neutron stars in numerical relativity. II. Systematic study on the equation of state, binary mass, and mass ratio. *Phys. Rev. D*, 101(8):084006, 2020.
- [158] Tim Dietrich et al. Matter imprints in waveform models for neutron star binaries: Tidal and self-spin effects. *Phys. Rev. D*, 99(2):024029, 2019.
- [159] Scott E. Field, Chad R. Galley, Jan S. Hesthaven, Jason Kaye, and Manuel Tiglio. Fast prediction and evaluation of gravitational waveforms using surrogate models. *Phys. Rev. X*, 4(3):031006, 2014.

Bibliography

- [160] Jonathan Blackman, Scott E. Field, Chad R. Galley, Béla Szilágyi, Mark A. Scheel, Manuel Tiglio, and Daniel A. Hemberger. Fast and Accurate Prediction of Numerical Relativity Waveforms from Binary Black Hole Coalescences Using Surrogate Models. *Phys. Rev. Lett.*, 115(12):121102, 2015.
- [161] Vijay Varma, Scott E. Field, Mark A. Scheel, Jonathan Blackman, Davide Gerosa, Leo C. Stein, Lawrence E. Kidder, and Harald P. Pfeiffer. Surrogate models for precessing binary black hole simulations with unequal masses. *Phys. Rev. Research.*, 1:033015, 2019.
- [162] Luc Blanchet. Gravitational Radiation from Post-Newtonian Sources and Inspiralling Compact Binaries. *Living Rev. Rel.*, 17:2, 2014.
- [163] P. C. Peters. Gravitational Radiation and the Motion of Two Point Masses. *Phys. Rev.*, 136:B1224–B1232, 1964.
- [164] Thibault Damour, Bala R. Iyer, and B. S. Sathyaprakash. A Comparison of search templates for gravitational waves from binary inspiral. *Phys. Rev. D*, 63:044023, 2001. [Erratum: Phys.Rev.D 72, 029902 (2005)].
- [165] Alessandra Buonanno, Bala Iyer, Evan Ochsner, Yi Pan, and B. S. Sathyaprakash. Comparison of post-Newtonian templates for compact binary inspiral signals in gravitational-wave detectors. *Phys. Rev. D*, 80:084043, 2009.
- [166] Luc Blanchet, Guillaume Faye, Quentin Henry, François Larrouturou, and David Trestini. Gravitational-Wave Phasing of Quasicircular Compact Binary Systems to the Fourth-and-a-Half Post-Newtonian Order. *Phys. Rev. Lett.*, 131(12):121402, 2023.
- [167] Thibault Damour, Piotr Jaranowski, and Gerhard Schaefer. Dimensional regularization of the gravitational interaction of point masses. *Phys. Lett. B*, 513:147–155, 2001.
- [168] Luc Blanchet, Thibault Damour, and Gilles Esposito-Farese. Dimensional regularization of the third postNewtonian dynamics of point particles in harmonic coordinates. *Phys. Rev. D*, 69:124007, 2004.
- [169] Thibault Damour, Piotr Jaranowski, and Gerhard Schaefer. Equivalence between the ADM-Hamiltonian and the harmonic coordinates approaches to the third postNewtonian dynamics of compact binaries. *Phys. Rev. D*, 63:044021, 2001. [Erratum: Phys.Rev.D 66, 029901 (2002)].
- [170] Vanessa C. de Andrade, Luc Blanchet, and Guillaume Faye. Third postNewtonian dynamics of compact binaries: Noetherian conserved quantities and equivalence between the harmonic coordinate and ADM Hamiltonian formalisms. *Class. Quant. Grav.*, 18:753–778, 2001.
- [171] Luc Blanchet and Bala R. Iyer. Third postNewtonian dynamics of compact binaries: Equations of motion in the center-of-mass frame. *Class. Quant. Grav.*, 20:755, 2003.
- [172] Yousuke Itoh and Toshifumi Futamase. New derivation of a third postNewtonian equation of motion for relativistic compact binaries without ambiguity. *Phys. Rev. D*, 68:121501, 2003.

- [173] Thibault Damour, Piotr Jaranowski, and Gerhard Schaefer. Dynamical invariants for general relativistic two-body systems at the third postNewtonian approximation. *Phys. Rev. D*, 62:044024, 2000.
- [174] Sebastian Khan, Sascha Husa, Mark Hannam, Frank Ohme, Michael Pürer, Xisco Jiménez Forteza, and Alejandro Bohé. Frequency-domain gravitational waves from nonprecessing black-hole binaries. II. A phenomenological model for the advanced detector era. *Phys. Rev. D*, 93(4):044007, 2016.
- [175] A. Buonanno and T. Damour. Effective one-body approach to general relativistic two-body dynamics. *Phys. Rev. D*, 59:084006, 1999.
- [176] Alessandra Buonanno, Yi Pan, John G. Baker, Joan Centrella, Bernard J. Kelly, Sean T. McWilliams, and James R. van Meter. Toward faithful templates for non-spinning binary black holes using the effective-one-body approach. *Phys. Rev. D*, 76:104049, 2007.
- [177] Thibault Damour, Piotr Jaranowski, and Gerhard Schaefer. On the determination of the last stable orbit for circular general relativistic binaries at the third postNewtonian approximation. *Phys. Rev. D*, 62:084011, 2000.
- [178] Thibault Damour, Bala R. Iyer, and B. S. Sathyaprakash. Improved filters for gravitational waves from inspiraling compact binaries. *Phys. Rev. D*, 57:885–907, Jan 1998.
- [179] Alessandra Buonanno, Yanbei Chen, and Thibault Damour. Transition from inspiral to plunge in precessing binaries of spinning black holes. *Phys. Rev. D*, 74:104005, 2006.
- [180] Alejandro Bohé et al. Improved effective-one-body model of spinning, nonprecessing binary black holes for the era of gravitational-wave astrophysics with advanced detectors. *Phys. Rev. D*, 95(4):044028, 2017.
- [181] Yi Pan, Alessandra Buonanno, Michael Boyle, Luisa T. Buchman, Lawrence E. Kidder, Harald P. Pfeiffer, and Mark A. Scheel. Inspiral-merger-ringdown multipolar waveforms of nonspinning black-hole binaries using the effective-one-body formalism. *Phys. Rev. D*, 84:124052, 2011.
- [182] Andrea Taracchini, Yi Pan, Alessandra Buonanno, Enrico Barausse, Michael Boyle, Tony Chu, Geoffrey Lovelace, Harald P. Pfeiffer, and Mark A. Scheel. Prototype effective-one-body model for nonprecessing spinning inspiral-merger-ringdown waveforms. *Phys. Rev. D*, 86:024011, 2012.
- [183] Thibault Damour, Alessandro Nagar, and Sebastiano Bernuzzi. Improved effective-one-body description of coalescing nonspinning black-hole binaries and its numerical-relativity completion. *Phys. Rev. D*, 87(8):084035, 2013.
- [184] Enrico Barausse and Alessandra Buonanno. Extending the effective-one-body Hamiltonian of black-hole binaries to include next-to-next-to-leading spin-orbit couplings. *Phys. Rev. D*, 84:104027, 2011.

Bibliography

- [185] Andrea Taracchini et al. Effective-one-body model for black-hole binaries with generic mass ratios and spins. *Phys. Rev. D*, 89(6):061502, 2014.
- [186] Stanislav Babak, Andrea Taracchini, and Alessandra Buonanno. Validating the effective-one-body model of spinning, precessing binary black holes against numerical relativity. *Phys. Rev. D*, 95(2):024010, 2017.
- [187] Serguei Ossokine et al. Multipolar Effective-One-Body Waveforms for Precessing Binary Black Holes: Construction and Validation. *Phys. Rev. D*, 102(4):044055, 2020.
- [188] Mohammed Khalil, Alessandra Buonanno, Hector Estelles, Deyan P. Mihaylov, Serguei Ossokine, Lorenzo Pompili, and Antoni Ramos-Buades. Theoretical groundwork supporting the precessing-spin two-body dynamics of the effective-one-body waveform models SEOBNRv5. 3 2023.
- [189] Lorenzo Pompili et al. Laying the foundation of the effective-one-body waveform models SEOBNRv5: improved accuracy and efficiency for spinning non-precessing binary black holes. 3 2023.
- [190] Antoni Ramos-Buades, Alessandra Buonanno, Héctor Estellés, Mohammed Khalil, Deyan P. Mihaylov, Serguei Ossokine, Lorenzo Pompili, and Mahlet Shiferaw. SEOBNRv5PHM: Next generation of accurate and efficient multipolar precessing-spin effective-one-body waveforms for binary black holes. 3 2023.
- [191] Maarten van de Meent, Alessandra Buonanno, Deyan P. Mihaylov, Serguei Ossokine, Lorenzo Pompili, Niels Warburton, Adam Pound, Barry Wardell, Leanne Durkan, and Jeremy Miller. Enhancing the SEOBNRv5 effective-one-body waveform model with second-order gravitational self-force fluxes. 3 2023.
- [192] Michael Pürrer. Frequency domain reduced order model of aligned-spin effective-one-body waveforms with generic mass-ratios and spins. *Phys. Rev. D*, 93(6):064041, 2016.
- [193] Sascha Husa, Sebastian Khan, Mark Hannam, Michael Pürrer, Frank Ohme, Xisco Jiménez Forteza, and Alejandro Bohé. Frequency-domain gravitational waves from nonprecessing black-hole binaries. I. New numerical waveforms and anatomy of the signal. *Phys. Rev. D*, 93(4):044006, 2016.
- [194] Eric Poisson. Gravitational waves from inspiraling compact binaries: The Quadrupole moment term. *Phys. Rev. D*, 57:5287–5290, 1998.
- [195] K. G. Arun, Alessandra Buonanno, Guillaume Faye, and Evan Ochsner. Higher-order spin effects in the amplitude and phase of gravitational waveforms emitted by inspiraling compact binaries: Ready-to-use gravitational waveforms. *Phys. Rev. D*, 79:104023, 2009. [Erratum: Phys.Rev.D 84, 049901 (2011)].
- [196] Balazs Mikoczi, Matyas Vasuth, and Laszlo A. Gergely. Self-interaction spin effects in inspiralling compact binaries. *Phys. Rev. D*, 71:124043, 2005.

- [197] Alejandro Bohé, Sylvain Marsat, and Luc Blanchet. Next-to-next-to-leading order spin-orbit effects in the gravitational wave flux and orbital phasing of compact binaries. *Class. Quant. Grav.*, 30:135009, 2013.
- [198] Parameswaran Ajith et al. Phenomenological template family for black-hole coalescence waveforms. *Class. Quant. Grav.*, 24:S689–S700, 2007.
- [199] Geraint Pratten, Sascha Husa, Cecilio García-Quiros, Marta Colleoni, Antoni Ramos-Buades, Hector Estelles, and Rafel Jaume. Setting the cornerstone for a family of models for gravitational waves from compact binaries: The dominant harmonic for nonprecessing quasicircular black holes. *Phys. Rev. D*, 102(6):064001, 2020.
- [200] Cecilio García-Quiros, Marta Colleoni, Sascha Husa, Héctor Estellés, Geraint Pratten, Antoni Ramos-Buades, Maite Mateu-Lucena, and Rafel Jaume. Multimode frequency-domain model for the gravitational wave signal from nonprecessing black-hole binaries. *Phys. Rev. D*, 102(6):064002, 2020.
- [201] Kostas D. Kokkotas and Bernd G. Schmidt. Quasinormal modes of stars and black holes. *Living Rev. Rel.*, 2:2, 1999.
- [202] S. A. Teukolsky. Rotating black holes - separable wave equations for gravitational and electromagnetic perturbations. *Phys. Rev. Lett.*, 29:1114–1118, 1972.
- [203] Saul A. Teukolsky. Perturbations of a rotating black hole. 1. Fundamental equations for gravitational electromagnetic and neutrino field perturbations. *Astrophys. J.*, 185:635–647, 1973.
- [204] Ajit Kumar Mehta, Praveer Tiwari, Nathan K. Johnson-McDaniel, Chandra Kant Mishra, Vijay Varma, and Parameswaran Ajith. Including mode mixing in a higher-multipole model for gravitational waveforms from nonspinning black-hole binaries. *Phys. Rev. D*, 100(2):024032, 2019.
- [205] Geraint Pratten et al. Computationally efficient models for the dominant and subdominant harmonic modes of precessing binary black holes. *Phys. Rev. D*, 103(10):104056, 2021.
- [206] Patricia Schmidt, Mark Hannam, and Sascha Husa. Towards models of gravitational waveforms from generic binaries: A simple approximate mapping between precessing and non-precessing inspiral signals. *Phys. Rev. D*, 86:104063, 2012.
- [207] Patricia Schmidt, Mark Hannam, Sascha Husa, and P. Ajith. Tracking the precession of compact binaries from their gravitational-wave signal. *Phys. Rev. D*, 84:024046, 2011.
- [208] E.P. Wigner. *Group Theory: And Its Application to the Quantum Mechanics of Atomic Spectra*. (Academic Press, New York, NY, 1959).
- [209] Michalis Agathos, Jeroen Meidam, Walter Del Pozzo, Tjonne G. F. Li, Marco Tompitak, John Veitch, Salvatore Vitale, and Chris Van Den Broeck. Constraining the neutron star equation of state with gravitational wave signals from coalescing binary neutron stars. *Phys. Rev. D*, 92(2):023012, 2015.

Bibliography

- [210] Thibault Damour, Alessandro Nagar, and Loic Villain. Measurability of the tidal polarizability of neutron stars in late-inspiral gravitational-wave signals. *Phys. Rev. D*, 85:123007, 2012.
- [211] Justin Vines, Eanna E. Flanagan, and Tanja Hinderer. Post-1-Newtonian tidal effects in the gravitational waveform from binary inspirals. *Phys. Rev. D*, 83:084051, 2011.
- [212] Tim Dietrich, Anuradha Samajdar, Sebastian Khan, Nathan K. Johnson-McDaniel, Reetika Dudi, and Wolfgang Tichy. Improving the NRTidal model for binary neutron star systems. *Phys. Rev. D*, 100(4):044003, 2019.
- [213] Tanja Hinderer. Tidal Love numbers of neutron stars. *Astrophys. J.*, 677:1216–1220, 2008.
- [214] Eanna E. Flanagan and Tanja Hinderer. Constraining neutron star tidal Love numbers with gravitational wave detectors. *Phys. Rev. D*, 77:021502, 2008.
- [215] Thibault Damour and Alessandro Nagar. Relativistic tidal properties of neutron stars. *Phys. Rev. D*, 80:084035, 2009.
- [216] Taylor Binnington and Eric Poisson. Relativistic theory of tidal Love numbers. *Phys. Rev. D*, 80:084018, 2009.
- [217] Leslie Wade, Jolien D. E. Creighton, Evan Ochsner, Benjamin D. Lackey, Benjamin F. Farr, Tyson B. Littenberg, and Vivien Raymond. Systematic and statistical errors in a bayesian approach to the estimation of the neutron-star equation of state using advanced gravitational wave detectors. *Phys. Rev. D*, 89(10):103012, 2014.
- [218] Marc Favata. Systematic parameter errors in inspiraling neutron star binaries. *Phys. Rev. Lett.*, 112:101101, 2014.
- [219] J. Veitch and A. Vecchio. Bayesian coherent analysis of in-spiral gravitational wave signals with a detector network. *Phys. Rev. D*, 81:062003, 2010.
- [220] J. Veitch et al. Parameter estimation for compact binaries with ground-based gravitational-wave observations using the LALInference software library. *Phys. Rev. D*, 91(4):042003, 2015.
- [221] John Skilling. Nested sampling for general Bayesian computation. *Bayesian Analysis*, 1(4):833–859, 2006.
- [222] Johannes Buchner. Nested Sampling Methods. *Statistics Surveys*, 17:169–215, January 2023.
- [223] Johannes Buchner. Comparison of Step Samplers for Nested Sampling. In *Physical Sciences Forum*, volume 5 of *Physical Sciences Forum*, page 46, December 2022.
- [224] Nelson Christensen and Renate Meyer. Parameter estimation with gravitational waves. *Rev. Mod. Phys.*, 94(2):025001, 2022.
- [225] N. Metropolis, A. W. Rosenbluth, M. N. Rosenbluth, A. H. Teller, and E. Teller. Equation of state calculations by fast computing machines. *J. Chem. Phys.*, 21:1087–1092, 1953.

- [226] W. K. Hastings. Monte Carlo Sampling Methods Using Markov Chains and Their Applications. *Biometrika*, 57:97–109, 1970.
- [227] W.R. Gilks, S. Richardson, and D. Spiegelhalter. *Markov Chain Monte Carlo in Practice*. Chapman & Hall/CRC Interdisciplinary Statistics. Taylor & Francis, 1995.
- [228] David J Earl and Michael W Deem. Parallel tempering: Theory, applications, and new perspectives. *Physical Chemistry Chemical Physics*, 7(23):3910–3916, 2005.
- [229] Tyson B. Littenberg and Neil J. Cornish. A Bayesian Approach to the Detection Problem in Gravitational Wave Astronomy. *Phys. Rev. D*, 80:063007, 2009.
- [230] Radford M. Neal. Probabilistic inference using markov chain monte carlo methods. 2011.
- [231] Nicolas Lartillot and Hervé Philippe. Computing Bayes Factors Using Thermodynamic Integration. *Systematic Biology*, 55(2):195–207, 04 2006.
- [232] Martyn Plummer, Nicky Best, Kate Cowles, and Karen Vines. Coda: Convergence diagnosis and output analysis for mcmc. *R News*, 6, 11 2005.
- [233] Daniel Foreman-Mackey, David W Hogg, Dustin Lang, and Jonathan Goodman. emcee: the mcmc hammer. *Publications of the Astronomical Society of the Pacific*, 125(925):306, 2013.
- [234] Vivekananda Roy. Convergence diagnostics for markov chain monte carlo. *Annual Review of Statistics and Its Application*, 7:387–412, 2020.
- [235] Andrew Gelman and Donald B. Rubin. Inference from Iterative Simulation Using Multiple Sequences. *Statist. Sci.*, 7:457–472, 1992.
- [236] Peter J. Green. Reversible jump Markov chain Monte Carlo computation and Bayesian model determination. *Biometrika*, 82(4):711–732, 12 1995.
- [237] Barak Zackay, Liang Dai, and Tejaswi Venumadhav. Relative Binning and Fast Likelihood Evaluation for Gravitational Wave Parameter Estimation. 6 2018. arXiv:1806.08792 [astro-ph.IM].
- [238] Liang Dai, Tejaswi Venumadhav, and Barak Zackay. Parameter Estimation for GW170817 using Relative Binning. 6 2018. arXiv:1806.08793 [gr-qc].
- [239] Nathaniel Leslie, Liang Dai, and Geraint Pratten. Mode-by-mode relative binning: Fast likelihood estimation for gravitational waveforms with spin-orbit precession and multiple harmonics. *Phys. Rev. D*, 104(12):123030, 2021.
- [240] C. Prud'homme, D. V. Rovas, K. Veroy, L. Machiels, Y. Maday, A. T. Patera, and G. Turinici. Reliable Real-Time Solution of Parametrized Partial Differential Equations: Reduced-Basis Output Bound Methods . *Journal of Fluids Engineering*, 124(1):70–80, 11 2001.

Bibliography

- [241] Priscilla Canizares, Scott E. Field, Jonathan R. Gair, and Manuel Tiglio. Gravitational wave parameter estimation with compressed likelihood evaluations. *Phys. Rev. D*, 87(12):124005, 2013.
- [242] Rory Smith, Scott E. Field, Kent Blackburn, Carl-Johan Haster, Michael Pürer, Vivien Raymond, and Patricia Schmidt. Fast and accurate inference on gravitational waves from precessing compact binaries. *Phys. Rev. D*, 94(4):044031, 2016.
- [243] Scott E. Field, Chad R. Galley, Frank Herrmann, Jan S. Hesthaven, Evan Ochsner, and Manuel Tiglio. Reduced basis catalogs for gravitational wave templates. *Phys. Rev. Lett.*, 106:221102, 2011.
- [244] Priscilla Canizares, Scott E. Field, Jonathan Gair, Vivien Raymond, Rory Smith, and Manuel Tiglio. Accelerated gravitational-wave parameter estimation with reduced order modeling. *Phys. Rev. Lett.*, 114(7):071104, 2015.
- [245] Hong Qi and Vivien Raymond. Python-based reduced order quadrature building code for fast gravitational wave inference. *Phys. Rev. D*, 104(6):063031, 2021.
- [246] Maxime Barrault, Yvon Maday, Ngoc Cuong Nguyen, and Anthony T. Patera. An ‘empirical interpolation’ method: application to efficient reduced-basis discretization of partial differential equations. *Comptes Rendus Mathematique*, 339(9):667–672, 2004.
- [247] Ajit Kumar Mehta, Alessandra Buonanno, Roberto Cotesta, Abhirup Ghosh, Noah Sennett, and Jan Steinhoff. Tests of general relativity with gravitational-wave observations using a flexible theory-independent method. *Phys. Rev. D*, 107(4):044020, 2023.
- [248] Anna Puecher, Chinmay Kalaghatgi, Soumen Roy, Yoshinta Setyawati, Ish Gupta, B. S. Sathyaprakash, and Chris Van Den Broeck. Testing general relativity using higher-order modes of gravitational waves from binary black holes. *Phys. Rev. D*, 106(8):082003, 2022.
- [249] Soumen Roy, Anand S. Sengupta, and K. G. Arun. Unveiling the spectrum of inspiralling binary black holes. *Phys. Rev. D*, 103(6):064012, 2021.
- [250] Reed Essick and Philippe Landry. Discriminating between Neutron Stars and Black Holes with Imperfect Knowledge of the Maximum Neutron Star Mass. *Astrophys. J.*, 904(1):80, 2020.
- [251] Ingo Tews, Peter T. H. Pang, Tim Dietrich, Michael W. Coughlin, Sarah Antier, Mattia Bulla, Jack Heinzel, and Lina Issa. On the Nature of GW190814 and Its Impact on the Understanding of Supranuclear Matter. *Astrophys. J. Lett.*, 908(1):L1, 2021.
- [252] Siddharth Dhanpal, Abhirup Ghosh, Ajit Kumar Mehta, Parameswaran Ajith, and B. S. Sathyaprakash. A no-hair test for binary black holes. *Phys. Rev. D*, 99(10):104056, 2019.
- [253] Tousif Islam, Ajit Kumar Mehta, Abhirup Ghosh, Vijay Varma, Parameswaran Ajith, and B. S. Sathyaprakash. Testing the no-hair nature of binary black holes using the consistency of multipolar gravitational radiation. *Phys. Rev. D*, 101(2):024032, 2020.

- [254] Shilpa Kastha, Anuradha Gupta, K. G. Arun, B. S. Sathyaprakash, and Chris Van Den Broeck. Testing the multipole structure of compact binaries using gravitational wave observations. *Phys. Rev. D*, 98(12):124033, 2018.
- [255] Shilpa Kastha, Anuradha Gupta, K. G. Arun, B. S. Sathyaprakash, and Chris Van Den Broeck. Testing the multipole structure and conservative dynamics of compact binaries using gravitational wave observations: The spinning case. *Phys. Rev. D*, 100(4):044007, 2019.
- [256] Collin D. Capano and Alexander H. Nitz. Binary black hole spectroscopy: a no-hair test of GW190814 and GW190412. *Phys. Rev. D*, 102(12):124070, 2020.
- [257] Michael Boyle, Lawrence E. Kidder, Serguei Ossokine, and Harald P. Pfeiffer. Gravitational-wave modes from precessing black-hole binaries. 9 2014. arXiv:1409.4431 [gr-qc].
- [258] B. P. Abbott et al. Tests of general relativity with GW150914. *Phys. Rev. Lett.*, 116(22):221101, 2016. [Erratum: Phys.Rev.Lett. 121, 129902 (2018)].
- [259] B. P. Abbott et al. Binary Black Hole Population Properties Inferred from the First and Second Observing Runs of Advanced LIGO and Advanced Virgo. *Astrophys. J. Lett.*, 882(2):L24, 2019.
- [260] B. P. Abbott et al. Tests of General Relativity with GW170817. *Phys. Rev. Lett.*, 123(1):011102, 2019.
- [261] Antoni Ramos-Buades, Patricia Schmidt, Geraint Pratten, and Sascha Husa. Validity of common modeling approximations for precessing binary black holes with higher-order modes. *Phys. Rev. D*, 101(10):103014, 2020.
- [262] H. Jeffreys. *Theory of Probability*. Oxford, Oxford, England, third edition, 1961.
- [263] T. G. F. Li, W. Del Pozzo, S. Vitale, C. Van Den Broeck, M. Agathos, J. Veitch, K. Grover, T. Sidery, R. Sturani, and A. Vecchio. Towards a generic test of the strong field dynamics of general relativity using compact binary coalescence. *Phys. Rev. D*, 85:082003, 2012.
- [264] Stanislav Babak, Antoine Petiteau, and Martin Hewitson. LISA Sensitivity and SNR Calculations. 8 2021. arXiv:2108.01167 [astro-ph.IM].
- [265] Anna Puecher, Anuradha Samajdar, Gregory Ashton, Chris Van Den Broeck, and Tim Dietrich. Comparing gravitational waveform models for binary black hole mergers through a hypermodels approach. 10 2023. arXiv:2310.03555 [gr-qc].
- [266] Michael Pürrer and Carl-Johan Haster. Gravitational waveform accuracy requirements for future ground-based detectors. *Phys. Rev. Res.*, 2(2):023151, 2020.
- [267] Charlie Hoy. Accelerating multimodel Bayesian inference, model selection, and systematic studies for gravitational wave astronomy. *Phys. Rev. D*, 106(8):083003, 2022.

Bibliography

- [268] Héctor Estellés, Marta Colleoni, Cecilio García-Quirós, Sascha Husa, David Keitel, Maite Mateu-Lucena, Maria de Lluc Planas, and Antoni Ramos-Buades. New twists in compact binary waveform modeling: A fast time-domain model for precession. *Phys. Rev. D*, 105(8):084040, 2022.
- [269] Tousif Islam, Avi Vajpeyi, Feroz H. Shaik, Carl-Johan Haster, Vijay Varma, Scott E. Field, Jacob Lange, Richard O’Shaughnessy, and Rory Smith. Analysis of GWTC-3 with fully precessing numerical relativity surrogate models. 9 2023. arXiv:2309.14473.
- [270] Gregory Ashton and Tim Dietrich. The use of hypermodels to understand binary neutron star collisions. *Nature Astron.*, 6(8):961–967, 2022.
- [271] Jonathan Blackman, Scott E. Field, Mark A. Scheel, Chad R. Galley, Christian D. Ott, Michael Boyle, Lawrence E. Kidder, Harald P. Pfeiffer, and Béla Szilágyi. Numerical relativity waveform surrogate model for generically precessing binary black hole mergers. *Phys. Rev. D*, 96(2):024058, 2017.
- [272] Roberto Cotesta, Alessandra Buonanno, Alejandro Bohé, Andrea Taracchini, Ian Hinder, and Serguei Ossokine. Enriching the Symphony of Gravitational Waves from Binary Black Holes by Tuning Higher Harmonics. *Phys. Rev. D*, 98(8):084028, 2018.
- [273] Héctor Estellés, Sascha Husa, Marta Colleoni, David Keitel, Maite Mateu-Lucena, Cecilio García-Quirós, Antoni Ramos-Buades, and Angela Borchers. Time-domain phenomenological model of gravitational-wave subdominant harmonics for quasicircular nonprecessing binary black hole coalescences. *Phys. Rev. D*, 105(8):084039, 2022.
- [274] Gregory Ashton and Colm Talbot. Bilby-MCMC: an MCMC sampler for gravitational-wave inference. *Mon. Not. Roy. Astron. Soc.*, 507(2):2037–2051, 2021.
- [275] Anna Puecher. Data release: Comparing gravitational waveform models for binary black hole mergers - a hypermodels approach, 2023. Zenodo. <https://doi.org/10.5281/zenodo.8251823>.
- [276] J. Lin. Divergence measures based on the Shannon entropy. *IEEE Trans. Info. Theor.*, 37(1):145–151, 1991.
- [277] S. Kullback and R. A. Leibler. On Information and Sufficiency. *The Annals of Mathematical Statistics*, 22(1):79–86, 1951.
- [278] Isobel M. Romero-Shaw, Paul D. Lasky, Eric Thrane, and Juan Calderon Bustillo. GW190521: orbital eccentricity and signatures of dynamical formation in a binary black hole merger signal. *Astrophys. J. Lett.*, 903(1):L5, 2020.
- [279] V. Gayathri, J. Healy, J. Lange, B. O’Brien, M. Szczepanczyk, Imre Bartos, M. Campanelli, S. Klimenko, C. O. Lousto, and R. O’Shaughnessy. Eccentricity estimate for black hole mergers with numerical relativity simulations. *Nature Astron.*, 6(3):344–349, 2022.

- [280] V. Gayathri, J. Healy, J. Lange, B. O'Brien, M. Szczepanczyk, I. Bartos, M. Campanelli, S. Klimenko, C. O. Lousto, and R. O'Shaughnessy. Measuring the Hubble Constant with GW190521 as an Eccentric black hole Merger and Its Potential Electromagnetic Counterpart. *Astrophys. J. Lett.*, 908(2):L34, 2021.
- [281] Yumeng Xu and Eleanor Hamilton. Measurability of precession and eccentricity for heavy binary-black-hole mergers. *Phys. Rev. D*, 107(10):103049, 2023.
- [282] Juan Calderón Bustillo, Nicolas Sanchis-Gual, Alejandro Torres-Forné, and José A. Font. Confusing Head-On Collisions with Precessing Intermediate-Mass Binary Black Hole Mergers. *Phys. Rev. Lett.*, 126(20):201101, 2021.
- [283] Rossella Gamba, Matteo Breschi, Gregorio Carullo, Simone Albanesi, Piero Rettegno, Sebastiano Bernuzzi, and Alessandro Nagar. GW190521 as a dynamical capture of two nonspinning black holes. *Nature Astron.*, 7(1):11–17, 2023.
- [284] V. De Luca, V. Desjacques, G. Franciolini, P. Pani, and A. Riotto. GW190521 Mass Gap Event and the Primordial Black Hole Scenario. *Phys. Rev. Lett.*, 126(5):051101, 2021.
- [285] Masaru Shibata, Kenta Kiuchi, Sho Fujibayashi, and Yuichiro Sekiguchi. Alternative possibility of GW190521: Gravitational waves from high-mass black hole-disk systems. *Phys. Rev. D*, 103(6):063037, 2021.
- [286] Maya Fishbach and Daniel E. Holz. Minding the gap: GW190521 as a straddling binary. *Astrophys. J. Lett.*, 904(2):L26, 2020.
- [287] Alexander H. Nitz and Collin D. Capano. GW190521 may be an intermediate mass ratio inspiral. *Astrophys. J. Lett.*, 907(1):L9, 2021.
- [288] Héctor Estellés et al. A Detailed Analysis of GW190521 with Phenomenological Waveform Models. *Astrophys. J.*, 924(2):79, 2022.
- [289] Rachel C. Zhang, Giacomo Fragione, Chase Kimball, and Vicky Kalogera. On the Likely Dynamical Origin of GW191109 and Binary Black Hole Mergers with Negative Effective Spin. *Astrophys. J.*, 954(1):23, 2023.
- [290] Mark Hannam et al. General-relativistic precession in a black-hole binary. *Nature*, 610(7933):652–655, 2022.
- [291] Vijay Varma, Sylvia Biscoveanu, Tousif Islam, Feroz H. Shaik, Carl-Johan Haster, Maximiliano Isi, Will M. Farr, Scott E. Field, and Salvatore Vitale. Evidence of Large Recoil Velocity from a Black Hole Merger Signal. *Phys. Rev. Lett.*, 128(19):191102, 2022.
- [292] Ethan Payne, Sophie Hourihane, Jacob Golomb, Rhianon Udall, Richard Udall, Derek Davis, and Katerina Chatzioannou. Curious case of GW200129: Interplay between spin-precession inference and data-quality issues. *Phys. Rev. D*, 106(10):104017, 2022.

Bibliography

- [293] Anna Puecher, Tim Dietrich, Ka Wa Tsang, Chinmay Kalaghatgi, Soumen Roy, Yoshinta Setyawati, and Chris Van Den Broeck. Unraveling information about supranuclear-dense matter from the complete binary neutron star coalescence process using future gravitational-wave detector networks. *Phys. Rev. D*, 107(12):124009, 2023.
- [294] Sven Köppel, Luke Bovard, and Luciano Rezzolla. A General-relativistic Determination of the Threshold Mass to Prompt Collapse in Binary Neutron Star Mergers. *Astrophys. J. Lett.*, 872(1):L16, 2019.
- [295] A. Bauswein, T. W. Baumgarte, and H. T. Janka. Prompt merger collapse and the maximum mass of neutron stars. *Phys. Rev. Lett.*, 111(13):131101, 2013.
- [296] Luca Baiotti, Bruno Giacomazzo, and Luciano Rezzolla. Accurate evolutions of inspiralling neutron-star binaries: prompt and delayed collapse to black hole. *Phys. Rev. D*, 78:084033, 2008.
- [297] Sebastiano Bernuzzi. Neutron Star Merger Remnants. *Gen. Rel. Grav.*, 52(11):108, 2020.
- [298] Luca Baiotti and Luciano Rezzolla. Binary neutron star mergers: a review of Einstein’s richest laboratory. *Rept. Prog. Phys.*, 80(9):096901, 2017.
- [299] Peter T. H. Pang et al. NMMA: A nuclear-physics and multi-messenger astrophysics framework to analyze binary neutron star mergers. 5 2022. arXiv:2205.08513 [astro-ph.HE].
- [300] Peter Hammond, Ian Hawke, and Nils Andersson. Thermal aspects of neutron star mergers. *Phys. Rev. D*, 104(10):103006, 2021.
- [301] Carolyn Raithel, Vasileios Paschalidis, and Feryal Özel. Realistic finite-temperature effects in neutron star merger simulations. *Phys. Rev. D*, 104(6):063016, 2021.
- [302] Elias R. Most, Alexander Haber, Steven P. Harris, Ziyuan Zhang, Mark G. Alford, and Jorge Noronha. Emergence of microphysical viscosity in binary neutron star post-merger dynamics. 7 2022. arXiv:2207.00442 [astro-ph.HE].
- [303] Wolfgang Kastaun and Filippo Galeazzi. Properties of hypermassive neutron stars formed in mergers of spinning binaries. *Phys. Rev. D*, 91(6):064027, 2015.
- [304] B. P. Abbott et al. Search for Post-merger Gravitational Waves from the Remnant of the Binary Neutron Star Merger GW170817. *Astrophys. J. Lett.*, 851(1):L16, 2017.
- [305] B. P. Abbott et al. Search for gravitational waves from a long-lived remnant of the binary neutron star merger GW170817. *Astrophys. J.*, 875(2):160, 2019.
- [306] Andreas Bauswein, Niels-Uwe F. Bastian, David B. Blaschke, Katerina Chatzioannou, James A. Clark, Tobias Fischer, and Micaela Oertel. Identifying a first-order phase transition in neutron star mergers through gravitational waves. *Phys. Rev. Lett.*, 122(6):061102, 2019.

- [307] Elias R. Most, L. Jens Papenfort, Veronica Dexheimer, Matthias Hanauske, Stefan Schramm, Horst Stöcker, and Luciano Rezzolla. Signatures of quark-hadron phase transitions in general-relativistic neutron-star mergers. *Phys. Rev. Lett.*, 122(6):061101, 2019.
- [308] Daniel M. Siegel, Riccardo Ciolfi, Abraham I. Harte, and Luciano Rezzolla. Magnetorotational instability in relativistic hypermassive neutron stars. *Phys. Rev. D*, 87(12):121302, 2013.
- [309] Mark G. Alford, Luke Bovard, Matthias Hanauske, Luciano Rezzolla, and Kai Schwenzer. Viscous Dissipation and Heat Conduction in Binary Neutron-Star Mergers. *Phys. Rev. Lett.*, 120(4):041101, 2018.
- [310] David Radice. General-Relativistic Large-Eddy Simulations of Binary Neutron Star Mergers. *Astrophys. J. Lett.*, 838(1):L2, 2017.
- [311] Masaru Shibata and Kenta Kiuchi. Gravitational waves from remnant massive neutron stars of binary neutron star merger: Viscous hydrodynamics effects. *Phys. Rev. D*, 95(12):123003, 2017.
- [312] Roberto De Pietri, Alessandra Feo, José A. Font, Frank Löffler, Francesco Maione, Michele Pasquali, and Nikolaos Stergioulas. Convective Excitation of Inertial Modes in Binary Neutron Star Mergers. *Phys. Rev. Lett.*, 120(22):221101, 2018.
- [313] Paul J. Easter, Paul D. Lasky, Andrew R. Casey, Luciano Rezzolla, and Kentaro Takami. Computing Fast and Reliable Gravitational Waveforms of Binary Neutron Star Merger Remnants. *Phys. Rev. D*, 100(4):043005, 2019.
- [314] Matteo Breschi, Sebastiano Bernuzzi, Francesco Zappa, Michalis Agathos, Albino Perego, David Radice, and Alessandro Nagar. kiloHertz gravitational waves from binary neutron star remnants: time-domain model and constraints on extreme matter. *Phys. Rev. D*, 100(10):104029, 2019.
- [315] Paul J. Easter, Sudarshan Ghonge, Paul D. Lasky, Andrew R. Casey, James A. Clark, Francisco Hernandez Vivanco, and Katerina Chatzioannou. Detection and parameter estimation of binary neutron star merger remnants. *Phys. Rev. D*, 102(4):043011, 2020.
- [316] Theodoros Soultanis, Andreas Bauswein, and Nikolaos Stergioulas. Analytic models of the spectral properties of gravitational waves from neutron star merger remnants. *Phys. Rev. D*, 105(4):043020, 2022.
- [317] Matteo Breschi, Sebastiano Bernuzzi, Kabir Chakravarti, Alessandro Camilletti, Aviral Prakash, and Albino Perego. Kilohertz Gravitational Waves From Binary Neutron Star Mergers: Numerical-relativity Informed Postmerger Model. 5 2022. arXiv:2205.09112 [gr-qc].
- [318] Matteo Breschi, Rossella Gamba, Ssohrab Borhanian, Gregorio Carullo, and Sebastiano Bernuzzi. Kilohertz Gravitational Waves from Binary Neutron Star Mergers: Inference of Postmerger Signals with the Einstein Telescope. 5 2022. arXiv:2205.09979 [gr-qc].
- [319] Marcella Wijngaarden, Katerina Chatzioannou, Andreas Bauswein, James A. Clark, and Neil J. Cornish. Probing neutron stars with the full premerger and postmerger gravitational wave signal from binary coalescences. *Phys. Rev. D*, 105(10):104019, 2022.

Bibliography

- [320] Ka Wa Tsang, Tim Dietrich, and Chris Van Den Broeck. Modeling the postmerger gravitational wave signal and extracting binary properties from future binary neutron star detections. *Phys. Rev. D*, 100(4):044047, 2019.
- [321] Gregory Ashton et al. BILBY: A user-friendly Bayesian inference library for gravitational-wave astronomy. *Astrophys. J. Suppl.*, 241(2):27, 2019.
- [322] I. M. Romero-Shaw et al. Bayesian inference for compact binary coalescences with bilby: validation and application to the first LIGO–Virgo gravitational-wave transient catalogue. *Mon. Not. Roy. Astron. Soc.*, 499(3):3295–3319, 2020.
- [323] Tim Dietrich, David Radice, Sebastiano Bernuzzi, Francesco Zappa, Albino Perego, Bernd Brügmann, Swami Vivekanandji Chaurasia, Reetika Dudi, Wolfgang Tichy, and Maximiliano Ujevic. CoRe database of binary neutron star merger waveforms. *Class. Quant. Grav.*, 35(24):24LT01, 2018.
- [324] <http://www.computational-relativity.org/>, 2018. CoRe Database webpage.
- [325] Nikolaos Stergioulas, Andreas Bauswein, Kimon Zagkouris, and Hans-Thomas Janka. Gravitational waves and nonaxisymmetric oscillation modes in mergers of compact object binaries. *Mon. Not. Roy. Astron. Soc.*, 418:427, 2011.
- [326] Maximilian Kölsch, Tim Dietrich, Maximiliano Ujevic, and Bernd Bruegmann. Investigating the mass-ratio dependence of the prompt-collapse threshold with numerical-relativity simulations. *Phys. Rev. D*, 106(4):044026, 2022.
- [327] Ben Margalit and Brian D. Metzger. Constraining the Maximum Mass of Neutron Stars From Multi-Messenger Observations of GW170817. *Astrophys. J. Lett.*, 850(2):L19, 2017.
- [328] H. T. Cromartie et al. Relativistic Shapiro delay measurements of an extremely massive millisecond pulsar. *Nature Astron.*, 4(1):72–76, 2019.
- [329] Pauli Virtanen, Ralf Gommers, Travis E. Oliphant, Matt Haberland, Tyler Reddy, David Cournapeau, Evgeni Burovski, Pearu Peterson, Warren Weckesser, Jonathan Bright, Stéfan J. van der Walt, Matthew Brett, Joshua Wilson, K. Jarrod Millman, Nikolay Mayorov, Andrew R. J. Nelson, Eric Jones, Robert Kern, Eric Larson, C J Carey, İlhan Polat, Yu Feng, Eric W. Moore, Jake VanderPlas, Denis Laxalde, Josef Perktold, Robert Cimrman, Ian Henriksen, E. A. Quintero, Charles R. Harris, Anne M. Archibald, Antônio H. Ribeiro, Fabian Pedregosa, Paul van Mulbregt, and SciPy 1.0 Contributors. SciPy 1.0: Fundamental Algorithms for Scientific Computing in Python. *Nature Methods*, 17:261–272, 2020.
- [330] Alex Nitz, Ian Harry, Duncan Brown, Christopher M. Biwer, Josh Willis, Tito Dal Canton, Collin Capano, Thomas Dent, Larne Pekowsky, Andrew R. Williamson, Soumi De, Miriam Cabero, Bernd Machenschalk, Duncan Macleod, Prayush Kumar, Steven Reyes, dfinstad, Francesco Paninarale, Sumit Kumar, Thomas Massinger, Márton Tápai, Leo Singer, Sebastian Khan, Stephen

- Fairhurst, Gareth S Cabourn Davies, Alex Nielsen, Shashwat Singh, Koustav Chandra, shasvath, and veronica villa. `gwastro/pycbc`: Release v2.0.1 of pycbc, January 2022. Zenodo. <https://doi.org/10.5281/zenodo.5825666>.
- [331] Lisa Barsotti, Ed McCuller, Matthew Evans, and Peter Fritschel. The A+ design curve. <https://dcc.ligo.org/LIGO-T1800042/public>, 2018.
- [332] Matthew Evans, Jan Harms, and Salvatore Vitale. Exploring the Sensitivity of Next Generation Gravitational Wave Detectors. <https://dcc.ligo.org/LIGO-P1600143/public>, 2016.
- [333] Yuta Michimura, Kentaro Komori, Yutaro Enomoto, Koji Nagano, and Kentaro Somiya. Example sensitivity curves for the KAGRA upgrade, 2020.
- [334] John Miller, Lisa Barsotti, Salvatore Vitale, Peter Fritschel, Matthew Evans, and Daniel Sigg. Prospects for doubling the range of advanced ligo. *Phys. Rev. D*, 91:062005, Mar 2015.
- [335] Joshua S. Speagle. dynesty: a dynamic nested sampling package for estimating Bayesian posteriors and evidences. *Mon. Not. Roy. Astron. Soc.*, 493(3):3132–3158, 2020.
- [336] Sergey Koposov, Josh Speagle, Kyle Barbary, Gregory Ashton, Johannes Buchner, Carl Scheffler, Ben Cook, Colm Talbot, James Guillochon, Patricio Cubillos, Andrés Asensio Ramos, Ben Johnson, Dustin Lang, Ilya, Matthieu Dartailh, Alex Nitz, Andrew McCluskey, Anne Archibald, Christoph Deil, Dan Foreman-Mackey, Danny Goldstein, Erik Tollerud, Joel Leja, Matthew Kirk, Matt Pitkin, Patrick Sheehan, Phillip Cargile, ruskin23, Ruth Angus, and Tansu Daylan. `joshspeagle/dynesty`: v1.2.2, April 2022. Zenodo. <https://doi.org/10.5281/zenodo.6456387>.
- [337] Justin Janquart. RelativeBilbying: a package for relative binning with bilby. <https://github.com/lemnis12/relativebilbying>, 2022.
- [338] Kenta Kiuchi, Kyohei Kawaguchi, Koutarou Kyutoku, Yuichiro Sekiguchi, Masaru Shibata, and Keisuke Taniguchi. Sub-radian-accuracy gravitational waveforms of coalescing binary neutron stars in numerical relativity. *Phys. Rev. D*, 96(8):084060, 2017.
- [339] Kyohei Kawaguchi, Kenta Kiuchi, Koutarou Kyutoku, Yuichiro Sekiguchi, Masaru Shibata, and Keisuke Taniguchi. Frequency-domain gravitational waveform models for inspiraling binary neutron stars. *Phys. Rev. D*, 97(4):044044, 2018.
- [340] Tanja Hinderer et al. Effects of neutron-star dynamic tides on gravitational waveforms within the effective-one-body approach. *Phys. Rev. Lett.*, 116(18):181101, 2016.
- [341] Anna Puecher, Anuradha Samajdar, and Tim Dietrich. Measuring tidal effects with the Einstein Telescope: A design study. *Phys. Rev. D*, 108(2):023018, 2023.
- [342] B. P. Abbott et al. Estimating the Contribution of Dynamical Ejecta in the Kilonova Associated with GW170817. *Astrophys. J. Lett.*, 850(2):L39, 2017.

Bibliography

- [343] Costantino Pacilio, Andrea Maselli, Margherita Fasano, and Paolo Pani. Ranking Love Numbers for the Neutron Star Equation of State: The Need for Third-Generation Detectors. *Phys. Rev. Lett.*, 128(10):101101, 2022.
- [344] Andrea Maselli, Andrea Sabatucci, and Omar Benhar. Constraining three-nucleon forces with multimessenger data. *Phys. Rev. C*, 103(6):065804, 2021.
- [345] Andrea Sabatucci, Omar Benhar, Andrea Maselli, and Costantino Pacilio. Sensitivity of neutron star observations to three-nucleon forces. *Phys. Rev. D*, 106(8):083010, 2022.
- [346] Francesco Iacovelli, Michele Mancarella, Stefano Foffa, and Michele Maggiore. Forecasting the Detection Capabilities of Third-generation Gravitational-wave Detectors Using GWFAST. *Astrophys. J.*, 941(2):208, 2022.
- [347] Natalie Williams, Geraint Pratten, and Patricia Schmidt. Prospects for distinguishing dynamical tides in inspiralling binary neutron stars with third generation gravitational-wave detectors. *Phys. Rev. D*, 105(12):123032, 2022.
- [348] Matteo Breschi, Sebastiano Bernuzzi, Daniel Godzieba, Albino Perego, and David Radice. Constraints on the Maximum Densities of Neutron Stars from Postmerger Gravitational Waves with Third-Generation Observations. *Phys. Rev. Lett.*, 128(16):161102, 2022.
- [349] Henrik Rose, Nina Kunert, Tim Dietrich, Peter T. H. Pang, Rory Smith, Chris Van Den Broeck, Stefano Gandolfi, and Ingo Tews. Revealing the strength of three-nucleon interactions with the proposed Einstein Telescope. *Phys. Rev. C*, 108(2):025811, 2023.
- [350] Duncan Meacher, Kipp Cannon, Chad Hanna, Tania Regimbau, and B. S. Sathyaprakash. Second Einstein Telescope Mock Data and Science Challenge: Low Frequency Binary Neutron Star Data Analysis. *Phys. Rev. D*, 93(2):024018, 2016.
- [351] Shichao Wu and Alexander H. Nitz. Mock data study for next-generation ground-based detectors: The performance loss of matched filtering due to correlated confusion noise. *Phys. Rev. D*, 107(6):063022, 2023.
- [352] Rory Smith et al. Bayesian Inference for Gravitational Waves from Binary Neutron Star Mergers in Third Generation Observatories. *Phys. Rev. Lett.*, 127(8):081102, 2021.
- [353] B. S. Sathyaprakash, B. F. Schutz, and C. Van Den Broeck. Cosmography with the Einstein Telescope. *Class. Quant. Grav.*, 27:215006, 2010.
- [354] Chris Van Den Broeck. Compact binary coalescence and the science case for Einstein Telescope. In *12th Marcel Grossmann Meeting on General Relativity*, pages 1682–1685, 3 2010.
- [355] W. Zhao, C. Van Den Broeck, D. Baskaran, and T. G. F. Li. Determination of Dark Energy by the Einstein Telescope: Comparing with CMB, BAO and SNIa Observations. *Phys. Rev. D*, 83:023005, 2011.

- [356] M. Punturo et al. The third generation of gravitational wave observatories and their science reach. *Class. Quant. Grav.*, 27:084007, 2010.
- [357] B. Sathyaprakash et al. Scientific Objectives of Einstein Telescope. *Class. Quant. Grav.*, 29:124013, 2012. [Erratum: Class.Quant.Grav. 30, 079501 (2013)].
- [358] C. Van Den Broeck. Astrophysics, cosmology, and fundamental physics with compact binary coalescence and the Einstein Telescope. *J. Phys. Conf. Ser.*, 484:012008, 2014.
- [359] B. S. Sathyaprakash et al. Extreme Gravity and Fundamental Physics. 3 2019. arXiv:1903.09221 [astro-ph.HE].
- [360] Alexander H. Nitz and Tito Dal Canton. Pre-merger Localization of Compact-binary Mergers with Third-generation Observatories. *Astrophys. J. Lett.*, 917(2):L27, 2021.
- [361] Man Leong Chan, Chris Messenger, Ik Siong Heng, and Martin Hendry. Binary Neutron Star Mergers and Third Generation Detectors: Localization and Early Warning. *Phys. Rev. D*, 97(12):123014, 2018.
- [362] Wen Zhao and Linqing Wen. Localization accuracy of compact binary coalescences detected by the third-generation gravitational-wave detectors and implication for cosmology. *Phys. Rev. D*, 97(6):064031, 2018.
- [363] Francisco Hernandez Vivanco, Rory Smith, Eric Thrane, Paul D. Lasky, Colm Talbot, and Vivien Raymond. Measuring the neutron star equation of state with gravitational waves: The first forty binary neutron star merger observations. *Phys. Rev. D*, 100(10):103009, 2019.
- [364] Gonçalo Castro, Leonardo Gualtieri, Andrea Maselli, and Paolo Pani. Impact and detectability of spin-tidal couplings in neutron star inspirals. *Phys. Rev. D*, 106(2):024011, 2022.
- [365] Tim Dietrich, Tanja Hinderer, and Anuradha Samajdar. Interpreting Binary Neutron Star Mergers: Describing the Binary Neutron Star Dynamics, Modelling Gravitational Waveforms, and Analyzing Detections. *Gen. Rel. Grav.*, 53(3):27, 2021.
- [366] Ian Harry and Tanja Hinderer. Observing and measuring the neutron-star equation-of-state in spinning binary neutron star systems. *Class. Quant. Grav.*, 35(14):145010, 2018.

